AGGREGATION IN COLLOIDS AND AEROSOLS

by

FLINT G. PIERCE

B.S., Kansas State University, 1994
B.S., Kansas State University, 1994

AN ABSTRACT OF A DISSERTATION

submitted in partial fulfillment of the requirements for the degree

DOCTOR OF PHILOSOPHY

Department of Physics
College of Arts and Sciences

KANSAS STATE UNIVERSITY
Manhattan, Kansas

2007

Abstract

This work is the result of a wide range of computer simulation research into the aggregation behavior of dispersed colloidal and aerosol particles in a number of different environments from the continuum to the free-molecular. The goal of this research has been to provide a bridge between experimental and theoretical researchers in this field by simulating the aggregation process within a known model. To this end, a variety of inter-particle interactions has been studied in the course of this research, focusing on the effect of these interactions on the aggregation mechanism and resulting aggregate structures. Both Monte Carlo and Brownian Dynamics codes have been used to achieve this goal. The morphologies of clusters that result from aggregation events in these systems have been thoroughly analyzed with a range of diverse techniques, and excellent agreement has been found with other researchers in this field. Morphologies of these clusters include fractal, gel, and crystalline forms, sometimes within the same structure at different length scales. This research has contributed to the fundamental understanding of aggregation rates and size distributions in many physical system, having allowed for the development of improved models of the aggregation and gelation process. Systems studied include DLCA and BLCA in two and three dimension, free-molecular diffusional (Epstein) system, selective aggregation in binary colloids, ssDNA mediated aggregation in colloidal systems, and several others.

AGGREGATION IN COLLOIDS AND AEROSOLS

by

FLINT G. PIERCE

B.S., Kansas State University, 1994
B.S., Kansas State University, 1994

A DISSERTATION

submitted in partial fulfillment of the requirements for the degree

DOCTOR OF PHILOSOPHY

Department of Physics
College of Arts and Sciences

KANSAS STATE UNIVERSITY
Manhattan, Kansas

2007

Approved by:

Major Professor
Amit Chakrabarti

Abstract

This work is the result of a wide range of computer simulation research into the aggregation behavior of dispersed colloidal and aerosol particles in a number of different environments from the continuum to the free-molecular. The goal of this research has been to provide a bridge between experimental and theoretical researchers in this field by simulating the aggregation process within a known model. To this end, a variety of inter-particle interactions has been studied in the course of this research, focusing on the effect of these interactions on the aggregation mechanism and resulting aggregate structures. Both Monte Carlo and Brownian Dynamics codes have been used to achieve this goal. The morphologies of clusters that result from aggregation events in these systems have been thoroughly analyzed with a range of diverse techniques, and excellent agreement has been found with other researchers in this field. Morphologies of these clusters include fractal, gel, and crystalline forms, sometimes within the same structure at different length scales. This research has contributed to the fundamental understanding of aggregation rates and size distributions in many physical system, having allowed for the development of improved models of the aggregation and gelation process. Systems studied include DLCA and BLCA in two and three dimension, free-molecular diffusional (Epstein) system, selective aggregation in binary colloids, ssDNA mediated aggregation in colloidal systems, and several others.

Table of Contents

Page - Section

List of Figures

Page - Figure

172-Fig 6.26: kinetics plots for all values of λ_{p0}. The highest value of λ_{p0} (1000) gives z ~ 2 while the lowest (0.1) gives z ~ 0.80.

173-Fig 6.27: Fig 6.26: $\frac{s_{scale}}{t}$ for all values of λ_{p0} plotted to distinguish values of the kinetic exponent. The highest value of λ_{p0} (1000) gives z ~ 2 while the lowest (0.1) gives z ~ 0.80. Symbols indicate same values of λ_{p0} as in Fig 6.26.

174-Fig 6.28: Gel times (squares) and time for kinetic enhancement to occur (circles) for all values of λ_{p0}.

176-Fig 6.29: $s_p^2(t)n(N,t)$ vs. $x = \frac{N}{s_p}$ for $\lambda_{p0} = 10^3$, along with the fit curve to the scaling form.

177-Fig 6.30: z from kinetics and CSD for all values of λ_{p0}

183-Fig 7.1:

a: (top left): Late time snapshots of 20,000 small particles with 100 large particles (number fraction 200:1). Notice the predominance of clusters containing only 1 large particle. The box dimensions are 420 x 420 in units of the *diameter* of the small particles. The current view is set to a 100 x 100 section. The apparent "clusters" of small particles alone are not actually clusters. The simulation allows small particles to touch each other but then diffuse away in later steps.

b: (top right): 20,000 small particles with 200 large particles (number fraction 100:1). In this situation most clusters contain only a few large particles. The box dimensions are 440 x 440. The current view is set to 100 x 100.

c: (bottom left): 20,000 small particles with 2000 large particles (number fraction 10:1). Notice the larger clusters containing several large particles as well as the almost complete absence of monomers. The box dimensions are 740 x 740. The current view is set to 200 x 200.

d: (bottom right): 20,000 small particles with 10,000 large particles (number fraction 2:1) at t = 12,650. Now we see many larger clusters containing several large particles and the complete absence of monomers. The box dimensions are 1450 x 1450. The current view is set to 400 x 400.

186-Fig 7.2: 20,000 small particles with 10,000 large particles (number fraction 2:1) at t = 1,997,850. We observe very large branched clusters containing hundreds of large particles as well as many small particles which at this scale are nearly invisible. The small particles act like glue for the large particles to stick together in clusters. The box dimensions are 1450 x 1450 as is the current view.

187-Fig 7.3: The same simulation as Fig. 7.2, but focused into a current view of 250 x 250. At this level of focus, we can see the small particles that were invisible in Fig. 6.32.

188-Fig 7.4: Fractal dimension of clusters formed with number fraction 2:1 at time t = 38,276 with N_c= 414. The value obtained from the slope of a linear fit to log(M) vs. log(R_g) is 1.46.

188-Fig 7.5: Fractal dimension vs. time in Monte-Carlo steps of clusters formed with number fraction 2:1 for times ranging from 10^4 to 10^6. The fractal dimension varies continuously from nearly 1.4 (similar to 2D DLCA of ~1.45) to a value of 1.54 consistent with 2D RLCA (D_f = 1.55) as the time evolves. All values were derived from a sample of ten runs. Error bars represent standard errors of values. The large standard errors at late times are due to a relatively smaller number of clusters in the system.

190-Fig 7.6: Graph of $N_c^{-1}(t)$ - $N_c^{-1}(0)$ vs. t for n_R = 2 . The straight line fit at the intermediate times yield the kinetic exponent z = 0.74 $\pm$ 0.05.

191-Fig 7.7: Same as in Fig. 7.6 except for n_R = 10. The straight line fit at the intermediate times yield the kinetic exponent z = 0.74 $\pm$ 0.05. Note the slow down in the kinetics at late times.

192-Fig 7.8: Cluster size distributions for various times during the simulation along with the common tangent line. The slope of the tangent line is -2.05 in good agreement with theory.

193-Fig 7.9: Scaled cluster size distributions along with the theoretical form (solid line) expressed in Eq. (1.1) with λ = - 0.35 and α = 1.35.

199-Fig 7.10: Bonding between 2 monomers in a simulation with b_t = 10 and b_n=3. DNA linkers are assumed to be distributed approximately symmetrically over the surface of the monomers, limiting the number of possible "linker" contacts between monomers.

200-Fig 7.11:
a (upper-left): Late-time (t = 24, 444) snapshot of a system at the DNA 'melting' temperature T_m. At this temperature only aggregation events occur and a gel-like morphology is observed. Here b_t = 10, b_n = 3, and f_a = 0.1.
b (upper-right): Same as in a) except T = 1.02T_m and t = 98, 349. In comparison to the aggregation-only morphologies seen at T_m, the clusters here begin to exhibit some compactification and local ordering due to fragmentation and reaggregation.
c (lower-left): Here T = 1.04T_m and t = 93, 905. A higher degree of compactification is observed, and local ordering becomes more clear. Some of the clusters have begun to dissolve as can be seen by the presence of monomers and smaller clusters.
d (lower-right): Now T= 1.05T_m and t = 949, 489. Fragmentation is highly pronounced here as can be seen by the proliferation of small clusters. The whole system is on the verge of dissolution.

202-Fig 7.12: Evolution of the fractal dimension D_f with time in the case of an overall area fraction of f_a = 0.10 with bonding configuration b_t=10 and b_n=3 at the melting temperature T_m. The clusters begin to form with a fractal dimension close to that of 2d-DLCA value (D_f = 1.4) and evolve toward a higher value, closer to the 2d-RLCA value

(D_f = 1.55). A "characteristic" error bar is shown. Error bars for other data points are of similar magnitude.

204-Fig 7.13: Same as in Fig. 7.12 except T = 1.04T_m. The compactification of the clusters seen in Fig. 7.11c is reflected in the increasing value of the fractal dimension D_f. It begins at a value close to the accepted 2d-DLCA value of 1.4 and continues to rise past 1.6, indicating the formation of more compact clusters at late times. Beyond this temperature, steady-state clusters are too small for fractal dimension curves to have much meaning. A "characteristic" error bar is shown. Error bars for other data points are of similar magnitude.

205-Fig 7.14: Plot of the number of monomers left in the system at late times vs. the scaled temperature $(T-T_m)/T_m$ for the bonding configuration b_t=10 and b_n=3 for various area fractions. Notice the sharp temperature profiles.

207-Fig 7.15: Here we fix the area fraction at f_a = 0.01 and vary b_t and b_n. The dissolution temperature increases as one increases b_t. When b_n = 1, the value of b_t does not change the dissolution phase-diagram appreciably when b_n = 1. Even for b_n > 1, the effect of b_t on the dissolution phase diagram is still marginal.

208-Fig 7.16: Kinetics graph showing a log-log plot of inverse cluster number vs. time (slope = z , the kinetic exponent) for the case of area fraction f_a = 0.01 and bonding configuration b_t = 10, b_n = 3 at various temperatures. As can be seen in the graph, all curves start with $z \approx 0.85$. As time progresses, the higher temperature kinetics reach steady-state values, whereas the kinetic behavior is complicated at intermediate temperatures showing the appearance of inflection points.

209-Fig 7.17: Same as in Fig 6.46, but for area fraction f_a = 0.10. At lower temperatures the early time value of $z \approx 0.84$ increases to a higher value of $z \approx 1$ at intermediate times. This is consistent with the cluster crowding picture for 2d DLCA. Again, higher

temperature kinetics reach steady-state values, whereas the kinetic behavior is complicated at intermediate temperatures.

210-Fig 7.18: Kinetics curves for an overall area fraction of $f_a = 0.01$ and $b_n = 3$. Here b_t is varied from 3 to 10. For values of $b_t > 8$, inflections points can be seen in the kinetic graphs.

211-Fig 7.19: A plot of the coordination number (with opposite-typed particles) for an overall area fraction of $f_a = 0.01$ and bond configuration $b_t=10$ and $b_n=3$ at an intermediate temperature of $1.03T_m$. Inflection points occur in similar positions to those seen in the kinetics data (t = 400 ,4000, 40000) shown by the triangles.

213-Fig 7.20: Kinetics curves for an overall area fraction of $f_a = 0.01$ with $b_t = 6$ and $b_n = 3$. Here the temperature is varied from T_m to $1.03T_m$. The dashed horizontal line indicates the inverse cluster number corresponding to an average cluster size of 4. The triangles represent two points on either side of the peak (at t = 1977 and t = 426080, respectively) in the kinetics curve where the average cluster size in the system are similar to each other.

214-Fig 7.21:
a (left): A sample section of the system morphology for the case referred to in Fig. 7.20 with t = 1977. The aggregates here are small but appear as the "stringy" precursors of DLCA-like aggregates.
b (right): A sample section of the system morphology for the case referred to in Fig. 7.21 with t = 426080. The aggregates here are more compact than the previous case, and a proliferation of tetramers is apparent. The inset represents a possible stable bonding configuration (for $b_t = 6$ and $b_n = 3$) leading to these 4-particle clusters.

217-Fig 7.22: log-log plot of the steady-state scaled value of the average cluster size vs. overall area fraction in the case of $T = 1.003T_m$ with a bonding configuration of $b_t=3$ and $b_n=1$. A best fit line passes very near all data points, indicating the fact that scaling does

work well in this case. The line has a slope of 1, yielding a fragmentation kernel exponent α of –1, assuming λ = 0, and z = 1.

218-Fig 7.23: Same as in Fig. 7.22 except T = 1.05T_m with a bonding configuration of b_t = 10 b_n=3. The line has a slope of 1, yielding a fragmentation kernel exponent α of –1, assuming λ=0, and z=1.

222-Fig 7.24: the $\alpha - 2\alpha$ for several choices of α and ε.

223-Fig 7.25:

(a)-top left: $\alpha = 6, \varepsilon = 4, f_v = 0.05$ Small compact clusters - a few monomers

(b)-top right: $\alpha = 6, \varepsilon = 7, f_v = 0.05$ Small, slightly branched clusters - no monomers

(c)-bottom left: $\alpha = 6, \varepsilon = 4, f_v = 0.20$ Large, thick, slightly branched clusters - a few monomers

(d)-bottom right: $\alpha = 6, \varepsilon = 7, f_v = 0.20$ Large, thin, highly branched clusters - no monomers

224-Fig 7.26:

(a)-top left: $\alpha = 12, \varepsilon = 4, f_v = 0.05$ Small compact clusters - large number monomers

(b)-top right: $\alpha = 12, \varepsilon = 7, f_v = 0.05$ Small, slightly branched clusters - no monomers

©-bottom left: $\alpha = 12, \varepsilon = 4, f_v = 0.20$ Large, thick, slightly branched clusters -moderate number monomers (thinner than for $\alpha = 6$)

(d)-bottom right: $\alpha = 12, \varepsilon = 7, f_v = 0.20$ Large, thin, highly branched clusters present - no monomers (thinner than for $\alpha = 6$)

226-Fig 7.27:

a) top: size $N = 1148$ cluster for $\alpha = 6, \varepsilon = 7, f_v = 0.20$ Notice the crystal ordering at small length scales and the branched fractal structure at large length scales.

b) bottom: size $N = 891$ cluster for $\alpha = 12, \varepsilon = 7, f_v = 0.20$ at $t = 1600$ similarly showing different morphologies at different length scales. With increased α(decreased range), the structures are more ramified as evidenced by thinner branches.

227,228-Fig 7.28:

a) top: Structure factor for cluster from Fig 7.27a

b) bottom: Structure factor for cluster from Fig 7.27b

List of Tables

Acknowledgements

This work would not have been possible without the tireless efforts of Dr. Amit Chakrabarti and Dr. Chris Sorensen, whose devotion to my education as a scientist was beyond compare. I am thankful for the way in which they have helped me look at the world in which we live with an eye toward fundamental understanding. My thanks can never be enough for the countless hours of discussion we have shared.

I am constantly thankful for a loving wife and baby girl who give reason to my life and hope for the future. Their patience and understanding during many near-sleepless nights of study and research have been a great blessing to me. They have always been by my side and continue to be my treasures.

I wish to also thank my father and mother for giving me the discipline and encouragement I needed to pursue my goal of becoming a physicist. Their help has never waivered, especially during the times when the responsibilities of life became diffiult to bear. Their example encourages me to strive to be a better person.

I cannot forget to thank my research group, colleagues that I have come to know and appreciate including Rajan Dhaubhadel, Tahereh Mokhtari, and Matt Berg. The discussions we have had about many topics in physics have often been the spark that I needed to see the next step clearly.

Finally, if there is any thanks in my heart, it is to my Lord and Savior, Jesus Christ. He has been my friend, guide, and comfort in times were filled with both sadness and joy. Without Him, my life would be without purpose. I am thankful for the faith and hope He brings to me.

Chapter 1 - Introduction

1.1 Aggregation Defined:

Aggregation is defined as "the act of gathering something together" [1]. In this sense, the process of aggregation is a universal concept which each of us is intimately familiar with. Our experience of this process is as varied as the observation of gelatin forming from a cooling aqueous solution of its granulated powder [2] to the gathering of bubbles on the surface of soapy water in a bathtub. From the manufacture of chemical and pharmaceutical products to the formation of visible soot floating in smoke or planets from nebular dust, aggregation is an important process to be able to predict, control, and at times prevent [3-11].

In its simplest form, aggregation has few requisite components. The first and most obvious is a collection of dispersed condensed-phase (solid or liquid) particles. The second is a system volume in which these particles are dispersed. This volume can contain (though not a requirement) a medium in either a liquid or gaseous state. Finally, some potential(s) of interaction must exist between the dispersed particles, whether short or long-ranged, in order to drive them together.

1.2 Scope of Thesis:

The scope of this work is the process of aggregation in aerosols and colloids. Aerosols are collections of finely dispersed particulate matter in a gaseous medium. Colloids, similarly, are finely divided matter suspended in a continuous medium in such a way as to not settle out easily. Our goal has been to understand the aggregation process

in these systems in order to provide a bridge between the abundance of experimental work and theoretical models in these fields. Computer simulations have been the tool by which much of this goal has been achieved. In pursuit of this understanding, we have modeled a large number of physical systems.

Within the aerosol field, we have come to understand the process of aggregation of particles with nonspecific interactions such as the van der Waals potential in both two and three dimensions. We now have a better understanding of the morphologies of structural forms that result from aggregation of particles within this regime. Specifically we have a clearer picture of how simple interactions can produce large ramified structures like fractal aggregates. We further understand how these aggregates can grow from a cluster-dilute to cluster-dense state leading ultimately to gelation and the increase of the fractal dimension at larger length scales. Additionally, through a lucid but robust scaling model, the kinetic growth exponents and aggregation kernel homogeneities are now predictable for a large range of systems.

Inside the world of colloids, we have explored the specific interactions that can mediate the aggregation of dispersed matter. We have studied the aggregation of particles whose interactions are binary in nature, allowing only dissimilar type particles to aggregate. Excellent agreement has been found with the morphological forms seen in experiment. We have developed a simplified predictive model for the aggregation of colloidal particles ligated with single-stranded DNA (ssDNA) that is also corroborated by experiment, showing the sharp temperature profiles that make these systems potential diagnostic tools. Finally, we have studied the effects of interaction range and depth as they relate to such physical systems as proteins aggregating in highly screened salt

solutions. Our results are in good agreement with both the theoretical work of others and experimental findings.

Ultimately, though many questions about the aggregation process have been answered by this work, many more questions have been brought to light. In this vein, the dual goals of science are met, both the furtherance of understanding and illumination to show the next step forward. It is left to others to take those next steps.

1.3 Organization of Thesis:

In Chapter 1 we introduce the goals and scope of the research contained within the body of this work.

Chapter 2 is devoted to the regimes of particle motion, from continuum to free-molecular, from diffusive to ballistic. The parameters that determine the aggregation regime are thoroughly studied. We discuss the crossover that can occur between regimes as a result of particle growth. The importance of particle volume fraction and its relation to nearest-neighbor separation in determining the motional regime is addressed. Limiting cases of Diffusion Limited Cluster Aggregation (DLCA) and Ballistic Limited Cluster Aggregation (BLCA) are introduced.

In Chapter 3 we present the various interactions that can mediate the aggregation of particles. First, we introduce the ubiquitous van der Waals potential between molecular species (essentially points) and particles (modeled as spheres). We then study the standard Lennard-Jones potential and the nature of both its attractive and repulsive components. Finally, we discuss the combined effect of screened coulomb repulsion and vdW attraction between particles as described by the DLVO potential, a useful model for

charged colloidal particles in solutions of various salt concentrations. Finally, the simplified model of Reaction Limited Cluster Aggregation (RLCA) is presented.

Chapter 4 introduces the simulation methods used in our aggregation simulations. These methods include standard Monte Carlo (MC), Metropolois MC, and Brownian Dynamics (BD). The concepts of random particle placement, periodic boundary conditions, the link-cell method, and the unfolding process are all presented and discussed. We analyze the various procedures for dealing with particle and cluster motion in both the diffusional and ballistic settings.

In Chapter 5, basic aggregation concepts are introduced. The Smoluchowski coagulation equation and its associated aggregation and fragmentation kernels are discussed, specifically as they relate to the motional regimes. The concepts of fractal geometry and the ramified nature of aerosol and colloidal aggregates is presented. We additionally address the gelation process which results from the aggregation of fractal clusters to the point at which the system becomes cluster-dense. Finally, we relate the above concepts to the kinetics and resulting size distributions of aggregating systems.

Chapter 6 contains the results of our research into aerosol aggregation. Here we discuss the kinetics, morphologies, and size distributions of Diffusion Limited Cluster Aggregation in both two and three dimensions, from initially dilute to dense. We then proceed to explain the curious behavior of aggregates in the "Epstein Regime", a free-molecular regime in which particles move diffusionally between collisions with each other rather than ballistically. Finally, we evaluate the effect of regime crossover from the ballistic to the Epstein regimes that occurs as a result of cluster growth.

In Chapter 7, we present the results from our colloidal aggregation studies. These include selective aggregation between particles in a binary system, DNA mediated aggregation of colloidal particles with a highly temperature-sensitive potential, and a study of the effect of range and potential depth as it relates to the aggregation of proteins in solutions with high salt concentration.

Chapter 8 gives a brief summary of some of our results.

1.4 Interactions:

Particle and/or external interactions are ultimately responsible for the aggregation process. Immediately following their creation or dispersion within a system, interacting particles can begin to aggregate into larger clusters.

In the absence of an external potential, if no interaction exists between particles or alternatively, an overall repulsive interaction exists, aggregation can be prevented, and the system can be held indefinitely in its original monodisperse state. The second of these cases is seen in some of the colloidal gold suspensions created by Faraday; they are stable (i.e. unaggregated) despite being formed more than 150 years ago [12].

A variety of interactions can exist between dispersed particles. Gravitational potentials can affect aggregating systems, modifying the kinetics and morphologies of the clusters formed [13-15]. Particle charge, dipole moment, and higher order moments are also known to play a significant role under certain conditions [16-18]. For high volume fraction systems, as in binary mixtures of hard spheres, aggregation can still proceed due to entropic considerations, leading to a variety of superlattice structures [19,20]. Specific short-range chemical interactions including complementary chemical species such as

DNA linkers provide a means to tailor nanoparticle interactions for the purpose of creating novel structures and are increasingly being utilized [21-23].

One attractive interaction that always exists between suspended particles, even those lacking any permanent electrical or magnetic moment, is that provided by London dispersion forces, the so-called van der Waals interaction [24]. It is this interaction and its accompanying force that are often principally responsible for aggregation phenomena, especially those that occur in the gas-phase (i.e. aerosols).

This work addresses a number of these interactions.

1.5 Current Work:

This work is a result of the highly varied simulation research done by the author into a wide range of aggregation phenomena occurring in particulate systems. Much of this work has been done in the continuum regime, where particles exist in a liquid or dense gaseous medium. For this regime, a variety of interactions has been studied in 2D and 3D, including near-permanent vdW, specific lock-key chemical bonding, and DNA hybridization [9,25,26]. Simulations have also been performed to model systems in the free-molecular regime of particle motion in a rarified gas as well as the crossover between the continuum and the free-molecular [27,28].

Chapter 2 - Regimes of Particle Motion:

In this chapter we discuss the system parameters that lead to various types of cluster motion between collisions. The concept of drag is presented as is its form for both the continuum and free-molecular regimes. The Knudsen number is shown to be a means of determining the relationship between the dispersed particles and the medium in which they are dispersed. An application of Newton's laws is used to illustrate the importance of length scale on the ideas of ballistic or diffusional motion of clusters. Motional regime crossover is shown to occur due to cluster growth. The importance of the concept of "mobility radius" for nonspherical clusters is covered. The nearest neighbor distance is shown to affect whether particle motion between collisions is diffusional or ballistic. Finally, the limiting cases of DLCA and BLCA are discussed.

2.1 Drag:

Drag affects the motion of all dispersed particles in systems for which a medium is present. The effect of drag represents a momentum exchange interaction between the particle and medium molecules. The drag coefficient (f) and mobility (μ) of a particle are related to the diffusion constant D through the Einstein relation [29]:

$$D = k_B T \mu = \frac{k_B T}{f} \tag{2.1}$$

.f can be either Stokes-Einstein type scaling as r (radius) as in a continuum fluid or Epstein scaling as A_{CS} (cross sectional area) as in a rarefied free-molecular gas [30,31].

2.2 Continuum Regime:

If the system medium is a liquid or dense gas or one at sufficiently low temperature, the path of medium molecules impinging on the surface of the dispersed particle will be severely affected by those leaving the surface; this produces a “stick” boundary condition at the particle surface and is known as the *continuum* [3,30,32,33].

2.3 Free-Molecular Regime:

If the particles are dispersed into a rarefied gas or one at sufficiently high temperature, the path of impinging medium molecules is essentially unaffected by those leaving the particle surface. The result is a *free-molecular* type of drag with “slip” boundary condition at the particle surface [3,30].

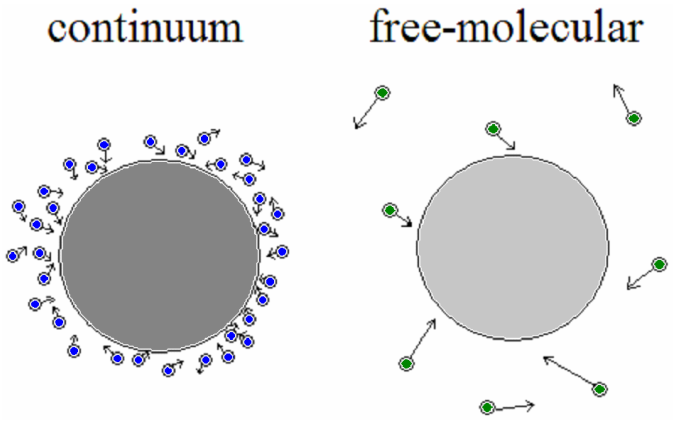

Fig 2.1: Visualization of the continuum and free-molecular regimes. For the continuum, medium molecules "interfere" with each other's trajectories near the particle surface. For the free-molecular, they do not.

2.4 Knudsen Number:

We can distinguish between these two conditions through the use of the Knudsen number:

$$Kn = \frac{\lambda_g}{r_p} \tag{2.2}$$

$$\lambda_g = \frac{1}{2^{\frac{5}{2}} \pi r_g{}^2 n_g} \tag{2.3}$$

λ_g = gas (medium molecule) mean free path

r_g = medium molecule radius

n_g = medium molecule number density

r_p = radius of the dispersed particle

When $Kn \succ\succ 1$, the result is a free-molecular condition, where *medium molecules* move in essentially straight lines (ballistically) for distances much greater than the particle radius. When $Kn \prec\prec 1$, medium molecules collide many times and have randomly fluctuating velocity vectors for distances on the order of the particle radius or less.

2.4 Diffusive vs. Ballistic Motion:

An important point that must be stressed is that the diffusive or ballistic nature of the motion of molecules or particles *depends on the length scale used*. Over some small length scale, the motion of *any* particle or molecule not experiencing external forces is ballistic due to the conservation of momentum. For such a particle, there exists a distance beyond which collisions with other molecules/particles significantly alters this

straight-line path, and the velocity vector becomes uncorrelated with its original direction, the so called *persistence length*. Beyond this point, the motion will be diffusive.

This concept can be clarified via an expression of Newton's law for a particle dispersed in a medium under the influence of thermal forces *only*. As an example, consider a particle of mass m and position **r**(t) initially at rest (starting at the origin) in a medium. Then:

$$m\frac{d^2\mathbf{r}}{dt^2} = -f\frac{d\mathbf{r}}{dt} + \xi(t) \tag{2.4}$$

where f is the drag coefficient of the particle, and **ξ**(t) is the stochastic thermal force acting on the particle due to the medium. The stochastic nature of ξ(t) combined with the fluctuation-dissipation theorem gives in d-dimensional space:

$$<\xi(t)> = 0 \tag{2.5}$$

$$<\xi(t)\xi(t')> = 2dk_BTf\delta(t-t') = 6k_BTf\delta(t-t') \text{ (for d = 3)} \tag{2.6}$$

since the drag force acting on a particle moving through the medium at velocity **v**(t) and the *random fluctuations* (stochastic force) acting on the particle have the same source, that of the temperature dependent Maxwell-Boltzmann distribution of medium molecules incident on the particle surface. If we rewrite equation (2.4) in terms of **v**(t), we have:

$$\frac{d\mathbf{v}}{dt} = -\lambda\mathbf{v} + \mathbf{g}(t) \tag{2.7}$$

where $\lambda = \frac{f}{m}$ and $\mathbf{g}(t) = \frac{\xi(t)}{m}$. A standard solution to this differential equation is:

$$\mathbf{v}(t) = \mathbf{v}(0)e^{-\lambda t} + e^{-\lambda t}\int_0^t \mathbf{g}(t')e^{\lambda t'}dt' \tag{2.8}$$

$$\mathbf{r}(t) = \int_0^t \left[\mathbf{v}(0)e^{-\lambda t'} + e^{-\lambda t'} \int_0^{t'} \mathbf{g}(t'')e^{\lambda t''} dt'' \right] dt' = \mathbf{v}(0)\frac{1-e^{-\lambda t}}{\lambda} + \int_0^t \left\{ e^{-\lambda t'} \int_0^{t'} \mathbf{g}(t'')e^{\lambda t''} dt'' \right\} dt' \quad (2.9)$$

The second term can be evaluated using integration by parts:

$$\int u dv = uv - \int v du \quad \text{with} \quad u = \left[\int_0^{t'} \mathbf{g}(t'')e^{\lambda t''} dt'' \right]_0^t \quad \text{and} \quad dv = e^{-\lambda t'} dt'$$

Then $du = \mathbf{g}(t')e^{\lambda t'} dt'$ and $v = \dfrac{1-e^{-\lambda t}}{\lambda}$ so that second term becomes:

$$\frac{1-e^{-\lambda t}}{\lambda} \left[\int_0^{t'} \mathbf{g}(t'')e^{\lambda t''} dt'' \right]_0^t - \frac{1}{\lambda} \int_0^t (1-e^{-\lambda t'}) \mathbf{g}(t')e^{\lambda t'} dt'$$

$$\frac{1-e^{-\lambda t}}{\lambda} \int_0^t \mathbf{g}(t')e^{\lambda t'} dt' + \frac{1}{\lambda} \int_0^t \mathbf{g}(t') dt' - \frac{1}{\lambda} \int_0^t \mathbf{g}(t')e^{\lambda t'} dt'$$

$$\frac{1}{\lambda} \int_0^t \left[1 - e^{\lambda(t'-t)} \right] \mathbf{g}(t') dt'$$

Yielding:

$$\mathbf{r}(t) = \frac{1}{\lambda} \left\{ \mathbf{v}(0)(1-e^{-\lambda t}) + \int_0^t \left[1 - e^{\lambda(t'-t)} \right] \mathbf{g}(t') dt' \right\} \quad (2.10)$$

Of course, since **g**(t) is not deterministic, there will be no exact analytic expression for **r**(t). Computer simulations circumvent this problem by *sampling* the solution from a properly defined distribution. Still, from the above expression we can derive the mean-sqare displacement $<\mathbf{r}^2(t)>$. We use the knowledge that there is no correlation between the initial velocity of the particle and the thermal force:

$$< \mathbf{v}(0)\mathbf{g}(t) > = 0 \quad (2.11)$$

and that for a Maxwell-Boltzmann velocity distribution:

$$< \mathbf{v}^2(0) > = \frac{3k_B T}{m} \tag{2.12}$$

Then:

$$< \mathbf{r}^2(t) > = \frac{1}{\lambda^2}\left\{\frac{3k_B T}{m}(1-e^{-\lambda t})^2 + \int_0^t\int_0^t \left[1-e^{\lambda(t'-t)}\right]\left[1-e^{\lambda(t''-t)}\right] < \mathbf{g}(t)\mathbf{g}(t') > dt'\,dt''\right\} \tag{2.13}$$

The second term inside the brackets is:

$$\frac{6k_B T\lambda}{m}\int_0^t [1-e^{\lambda(t'-t)}]^2\,dt' = \frac{6k_B T\lambda}{m}(t + \frac{2}{\lambda}e^{-\lambda t} - \frac{1}{2\lambda}e^{-2\lambda t} - \frac{3}{2\lambda})$$

Combining terms we obtain:

$$< \mathbf{r}^2(t) > = \frac{3k_B T}{m\lambda}(-\frac{2}{\lambda} + \frac{2}{\lambda}e^{-\lambda t} + 2t) \tag{2.14}$$

Specifically, we are interested in the short time $(t \approx 0)$ and long time $(t \succ\succ 0)$ behavior.

For short times, an expansion of the exponential in the above expression yields to first order:

$$< \mathbf{r}^2(t) > \approx \frac{3k_B T}{m}t^2 \tag{2.15}$$

This corroborates our picture of the *ballistic* nature of particles on small time scales since $\mathbf{r}_{rms}(t) \propto t$.

For large times, the linear term dominates the behavior of the mean square displacement and:

$$< \mathbf{r}^2(t) > \approx \frac{6k_B T}{m\lambda}t = \frac{6k_B T}{f}t = 6Dt \tag{2.16}$$

$$D = \frac{k_B T}{f} \tag{2.17}$$

yielding *diffusional* particle motion as expected.

2.6 Calculating Drag:

In most practical situations, the particle mass is much greater than the medium molecular mass $\left(m_p \succ\succ m_g\right)$, and the velocity of particles is much less than that of the medium molecules $\left(v_p \prec\prec v_g\right)$. An example of this is a system of nm or larger dispersed particles in thermal equilibrium with its medium (particles are not "blown" into the fluid at high velocity). With these conditions, the drag force acting on spherical particles is given by the following forms, dependent on the value of Kn [30]:

$$\mathbf{F}_D = -\frac{4}{3}\pi\delta n_g m_g v_g r_p{}^2 \mathbf{v}_p \quad \left(Kn \succ\succ 1\right) \text{ "free molecular"} \tag{2.18}$$

$$\mathbf{F}_D = -6\pi\eta r_p \mathbf{v}_p \quad \left(Kn \prec\prec 1\right) \text{ "continuum"} \tag{2.19}$$

δ = accommodation coefficient

= 1 for specular reflections, 1.442 for diffuse reflections

$$= 1 + \frac{\pi}{8}\alpha \ \left(\alpha = 0.91\right) = 1.36 \text{ [3,34]} \tag{2.20}$$

A specular reflection is one in which an impinging medium molecule rebounds from the particle surface in agreement with the law of reflection $\left(\theta_{incident} = \theta_{reflected}\right)$. A diffuse reflection is one in which the impinging molecule rebounds from the surface with an uncorrelated direction $\left(\theta_{incident} \neq \theta_{reflected}\right)$. Occasionally, α is referred to as the accommodation coefficient rather than δ.

$n_g = \dfrac{P}{k_B T}$ (if medium is "ideal" gas) = medium molecule number density

m_g = medium molecular mass

$v_g = \sqrt{\frac{3k_BT}{m}}$ = medium molecule rms thermal velocity

η = viscosity of fluid

r_p = dispersed particle radius

v_p = dispersed particle rms velocity ($= \sqrt{\frac{3k_BT}{m_p}}$ if thermal)

m_p = dispersed particle mass

The free-molecular drag in an ideal gas simplifies to:

$$F_D = 7.26\delta P\sqrt{\frac{m_g}{k_BT}}r_p{}^2 v_p = f_{freemol}v_p \tag{2.21}$$

For the continuum, Fuchs gives the viscosity as [30]:

$$\eta = 0.3502 n_g m_g v_g \lambda_g = 0.1365\frac{\sqrt{k_BTm_g}}{d_g{}^2} \tag{2.22}$$

so that continuum expression simplifies to:

$$F_D = 2.573\sqrt{k_BTm_g}\,\frac{r_p}{d_g{}^2}v_p = f_{cont}v_p \tag{2.23}$$

2.7 Regime Crossover:

A crossover between the free molecular and the continuum drag is seen in the Cunningham slip correction, which describes the way the frictional coefficient for a spherical particle changes in the intermediate Kn regime [35]. It is especially useful for

the Kn range $0.1 < Kn < 10$, where the extremes of the range represent an $\approx 10\%$ error in using the free-molecular or continuum result alone. For the Cunninham correction:

$$f = \frac{f_{cont}}{C(Kn)} \tag{2.24}$$

$$C(Kn) = 1 + 1.257Kn + 0.4e^{-\frac{1.1}{Kn}} \tag{2.25}$$

$$\sim 1.0 \text{ for } Kn \approx 0 \text{ (continuum)}$$

$$\sim 1.257\text{Kn for } Kn \succ\succ 1 \text{ (free-molecular)}$$

for $Kn \prec\prec 1$ we find:

$$f = f_{cont}$$

and for Kn >> 1:

$$f = \frac{6\pi\eta r_p}{1.257Kn} = 5.251 n_g m_g v_g r_p{}^2 = 9.096P\sqrt{\frac{m_g}{k_B T}} r_p{}^2$$

Using Sorensen's value for $\delta \approx 1.36$, we see that the above formula can be written as:

$$f_{freemol} = 6.69\delta P\sqrt{\frac{m_g}{k_B T}} r_p{}^2 \tag{2.26}$$

in good agreement with the Fuchs formula.

In Fig. 2.2 we show a graph of the continuum and free-molecular drag coefficients (conveniently scaled) as well as the Cunningham corrected form which allows a smooth transition from one regime into the other. The range $0.1 < Kn < 10$ obviously requires the Cunningham corrected form to give realistic values:

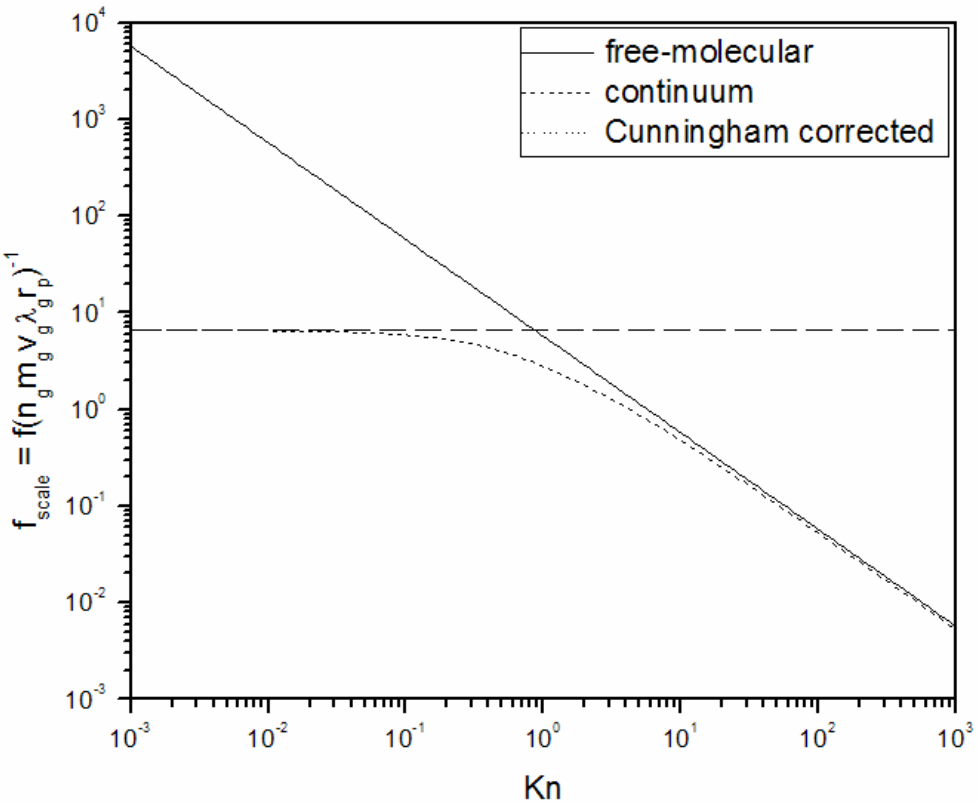

Fig 2.2: Crossover from continuum to free-molecular drag as given by the Cunningham correction.

2.8 Special Considerations:

In the free molecular regime, the drag force acting on a particle is proportional to the square of the particle's radius. This can be seen as a proportionality to the cross sectional area of the particle in the medium, and this is the interpretation we use. This definition will clearly be useful for *nonspherical* objects like the aggregates formed from collisions of hard spheres within each motional regime, where the definition of an aggregate's "radius" is not altogether obvious.

For the free molecular regime, we can "define" a mobility radius r_m of any particle given by:

$$A_{CS} = \pi r_m^{\,2} \tag{2.27}$$

where A_{CS} is the cross sectional area of the particle in the direction of motion through the gas as seen by the gas molecules. Of course, how this mobility radius scales with mass will be an important consideration that we will return to.

In the continuum, the drag force acting on a particle is proportional to the particle radius. When we consider aggregates of particles, the concept of a mobility radius will again be useful, and we will again have to determine the way this mobility radius scales with the aggregate mass.

2.9 Nearest Neighbor Distance (R_{nn}):

In many cases, it is important to know the average separation distance between clusters of particles, the so-called nearest neighbor distance, R_{nn}. As an analogy one might consider a crystalline system where R_{nn} would represent the equilibrium lattice spacing.

To find an expression for R_{nn}, we use the cluster volume fraction f_{vc}, the ratio between the *volume occupied by the clusters* within the system and the system volume itself. For N_c clusters of "radius" R_p within a system of volume V_{system}:

$$f_{vc} = \frac{4\pi}{3}\frac{N_c R_p^{\,3}}{V_{system}} \tag{2.28}$$

Noting that initially, for the N_0 monomers of radius r_0 of which the system is composed:

$$f_{v0} = \frac{4\pi}{3}\frac{N_0 r_0^{\,3}}{V_{system}} \tag{2.29}$$

We can then rewrite:

$$f_{vc} = f_{v0}\frac{N_c}{N_0}\left(\frac{R_p}{r_0}\right)^3 = f_{v0}\frac{1}{N}\left(\frac{R_p}{r_0}\right)^3 \tag{2.30}$$

N being the average cluster size. Alternatively, we note that in an ideal sense, the highest volume fraction for a system of clusters of size R_p is:

$$f_{vc,\max} = f_{cp} = \frac{\pi}{\sqrt{18}} \approx 0.74 \tag{2.31}$$

This occurs when $R_{nn} = 2R_p$ (clusters just touching), and for this case we consider clusters to have come in contact and formed a system spanning network.

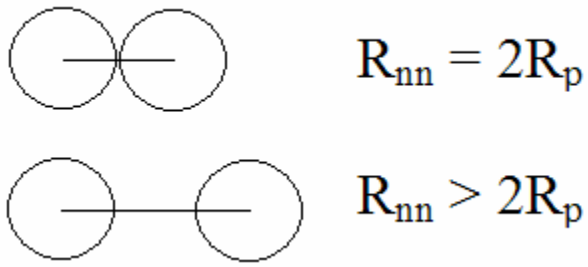

Fig 2.3: Visualization of R_{nn} in relation to the particle size R_p

If we then increase R_{nn}, the volume of the system will have gone up by R_{nn}^3 while the volume of clusters *will have remained unchanged*. Thus the volume fraction will fall off as R_{nn}^{-3}. We have then:

$$f_{vc} = f_{cp}\left(\frac{2R_p}{R_{nn}}\right)^3 \tag{2.32}$$

Combining the above 2 expressions for f_{vc}, we find for size N clusters that:

$$R_{nn} = 2\left(\frac{f_{v0}}{f_{cp}}\right)^{-\frac{1}{3}} N^{\frac{1}{3}} r_0 \tag{2.33}$$

Two simple and useful relationships are:

$$R_{nn} \propto f_{v0}{}^{-\frac{1}{3}} \tag{2.34}$$

$$R_{nn} \propto N^{\frac{1}{3}} \tag{2.35}$$

We see then that initially, since most systems are considered to start as an ensemble of monomers ($N(t=0)=1$) and since $f_{cp}{}^{-\frac{1}{3}} \approx 1$:

$$R_{nn,scale}(t=0) = \frac{R_{nn}(t=0)}{2r_0} \approx f_{v0}{}^{-\frac{1}{3}} \tag{2.36}$$

2.10 Diffusion Limited Cluster Aggregation (DLCA):

Common examples of aggregating systems are dispersions of nm-μm scale polystyrene spheres in coulomb-screened aqueous solutions and carbon monomers (tens to hundreds of nm in diameter) in a post-explosion reaction chamber [8,9]. Such systems begin aggregating from a monodisperse or nearly monodisperse size distribution of monomers at low volume fraction within a system. When, as in these cases, the collision of particles with each other is a *result of their mutual diffusion*, the resulting type of aggregation is termed "diffusion-limited" [36-38]. In addition to this, DLCA (Diffusion Limited Cluster Aggregation) refers to the idea that as collisions between particles occur and a distribution of cluster sizes is formed, the resulting clusters themselves diffuse to have further collisions.

Other conditions are required for DLCA. In DLCA, the position at which two clusters aggregate must be *uncorrelated* with their respective starting positions; this assumes the system is well described as "dilute". As seen above, the diffusion constant of a particle can be either of the Einstein or Epstein type. DLCA aggregation produces aggregates with complex *fractal* morphologies (discussed below), exhibiting a fractal dimension of ~1.8 in 3D and ~ 1.45 in 2D [39]. In 3-dimensions, continuum DLCA aggregates grow with mass increasing linearly with time[40], while Epstein DLCA aggregates grow at a slightly slower rate (discussed below)[27].

2.11 Ballistic Limited Cluster Aggregation (BLCA):

BLCA is similar to DLCA except that the motions of clusters between collisions with each other are along linear trajectories. Such can be the case in high Kn systems like those that occur in a gaseous medium with adequately high T or low P. BLCA aggregation also produces fractal aggregates, but with slightly different morphologies than those of DLCA, the fractal dimension in 3D being ~ 1.9 [41-43]. It is characterized by a nearly quadratic increase in average cluster mass with time (discussed below).

Chapter 3 - Interactions:

Chapter 3 is a discussion of the various potentials that govern the interaction of dispersed particles. The first and perhaps most important, the van der Waals potential, is fully explored including its full form for spherical particles. The need for a repulsive potential is then discussed. Here, the familiar Lennard-Jones (LJ) form is presented as is the nature of its attractive and repulsive components. Next, the DLVO potential is studied, including its relationship to physical parameters such as salt concentration and particle surface potential in a liquid. Finally, the Reaction Limited Cluster Aggregation (RLCA) model is presented as a simplified way to model systems in which a finite energy barriers exists to particle aggregation.

3.1 van der Waals:

3.1.1 Origin of vdW:

Even in the absence of obvious particle interactions (charge, magnetic, chemical bonding, etc.), one potential *always* exists between any two particles at small distances as a result of the atomic nature of matter. Atoms are essentially positively charged nuclei with a cloud of negative electrons moving around them at high velocities within various orbitals. Due to the orbital motion of the electrons, at any point in time, an atom possesses a fluctuating instantaneous electric dipole moment. As two atoms approach each other, these instantaneous dipoles begin to influence each other's electronic oscillations in such a way as to produce an overall attractive potential between the atoms. Unlike strong permanent dipole-dipole interactions this interaction does not lead to a

fixed alignment of these temporary dipoles but rather a partial alignment *on average*. The potential between two atoms has the same distance dependence as that of thermally averaged $\left(U << k_B T\right)$ freely rotating permanent dipole-dipole interactions [24], and is of the form:

$$E_{vdw} = -\frac{C_{vdw}}{r^6} \tag{3.1}$$

where C_{vdw} depends on the nature of the particular atoms involved and r is the distance between them. Specifically:

$$C_{vdw} = \frac{3}{2}\alpha_{01}\alpha_{02}\frac{1}{\left(4\pi\varepsilon_0\right)^2}\frac{1}{I_1^{-1} + I_2^{-1}} \tag{3.2}$$

where:

$\alpha_{01}, \alpha_{02} \approx 4\pi\varepsilon_0 r_i^3$ = electronic polarizabilities of atoms 1 and 2

r_i = radius of atom 1 or 2

$\varepsilon_0 = 1.25664 \cdot 10^{-6}\frac{F}{m}$ = permittivity of free space

I_1, I_2 = Ionization potentials of atoms 1 and 2

For identical atoms [24,44]:

$$C_{vdw} = \frac{3}{4}\frac{\alpha_0^{\,2} I}{\left(4\pi\varepsilon_0\right)^2} \tag{3.3}$$

3.1.2 vdW for Particles:

As a first approximation, the interaction between two particles of finite size can be seen as the sum of the pairwise interactions between their constituent atoms. For two identical spherical particles, one can proceed by treating the particles as continuous in the following way:

$$d^2E_{vdw} = -\frac{C\rho^2 dV_1 dV_2}{r_{12}^{\ 6}} \tag{3.4}$$

C is a material dependent interaction constant related to C_{vdw} (above), ρ is the density of the material making up the particles, and r_{12} is the distance between infinitesimal volume elements within the respective spheres. That is, the 2nd order differential element of vdW energy is dependent on the properties of the material involved and the pairwise separation between the constituent pieces. Then the total vdW energy between the spheres is given as the double volume integration:

$$E_{vdw} = \int_{V1}\int_{V2} -\frac{C\rho^2}{r_{12}^{\ 6}} dV_1 dV_2 \tag{3.5}$$

The result is:

$$E_{vdw} = -\frac{H}{12}\left[\frac{1}{x^2-1} + \frac{1}{x^2} + 2\ln\left(1-\frac{1}{x^2}\right)\right] \tag{3.6}$$

where $x = \frac{r}{d}$, r the distance between particle centers, and d the diameter of the particles.

H is known as the Hamaker constant and is a property of the material making up the spheres. It is related to C_{vdw} by:

$$H = \frac{C_{vdw}\pi^2}{v_0^{\ 2}} \tag{3.7}$$

where v_0 is the volume of an individual atom. C is related to C_{vdw} by:

$$C_{vdw} = Cm_0^{\ 2} \tag{3.8}$$

where $m_0 = \rho v_0$ is the mass of an individual atom.

3.1.3 vdW Dependence on Material:

A log-log plot of the vdW energy (positive for convenience) along with the *large distance* r^{-6} dependence is shown in Fig 3.1 for the example of spherical gold particles at T = 300K.

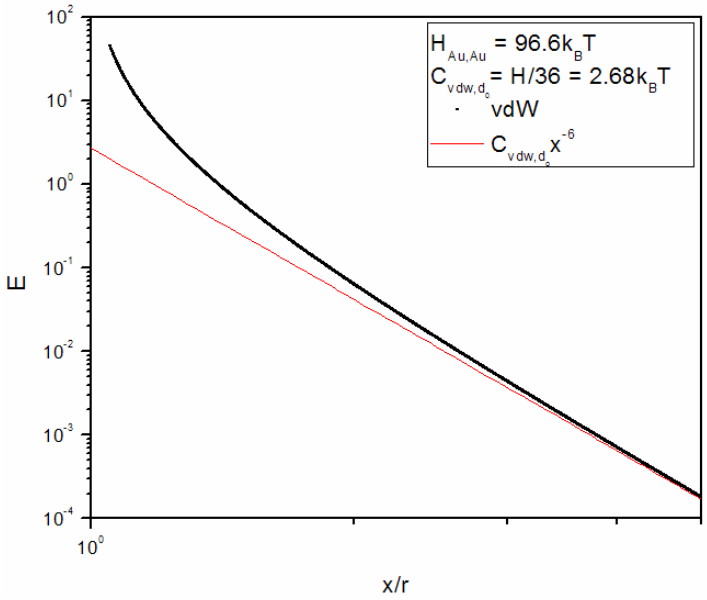

Fig 3.1: vdW energy for two gold spherical particles

The value of the Hamaker constant (thus the interaction energy) depends strongly on the type of material involved. Metallic materials (i.e. Au, Ag, Cu) tend to have the highest values for Hamaker constants; this, of course, is related to the polarizability of the atoms and the ionization potential as given above. For instance, Au has a Hamaker constant (in vacuum) of $\sim 40 \cdot 10^{-20}$ J ($\sim 97 k_B T$ at T = 300K) [24]. Fused silica, on the other hand, has a value of $\sim 6.6 \cdot 10^{-20}$ J ($\sim 16 k_B T$ at T = 300K).

The vdW energy is often sufficient to hold small particles together near contact in a vacuum and many other media. At a separation distance of 1 atomic diameter ($\approx 1A$), two 5nm (diameter) fused silica spheres have an interaction energy of $\approx 25.5 k_B T \left(T = 300K\right)$, whereas the binding energy climbs to $\approx 155 k_B T$ for gold spheres

of the same dimensions. These binding energies are normally large enough to keep particles from separating as a result of thermal fluctuations.

3.1.4 vdW for the Medium:

One must take into account that there are also van der Waals interactions between medium molecules and between the medium molecules and dispersed particles. These interactions can reduce the binding energies between dispersed particles, effectively reducing their Hamaker constant. For two particles of material 1 dispersed in a medium of material 2, the *relative* Hamaker constant governing the vdW interaction of the particles ,H_{121}, is given by the following combing rule:

$$H_{121} = \left(\sqrt{H_{11}} - \sqrt{H_{22}}\right)^2 \text{ [24]} \tag{3.9}$$

where H_{ii} is the Hamaker constant of two portions material i interacting with each other in a vacuum. In this case, if $H_{11} \approx H_{22}$, the aggregation process can be significantly diminished or eliminated altogether. This concept is related to the idea of solvation, indicating that the more "similar" two substances are, the better their tendency to dissolve in each other.

3.1.5 Size Scaling of vdW:

Note that the vdW energy between two spheres *does not scale* with their volume but is a universal function of x. The vdw *force* on the other hand does scale with the particle size, and is not a universal function of x. Instead the force is given below (and plotted in Fig 3.2) as:

$$F_{vdw} = -\frac{dE_{vdw}}{dr} = -\frac{\partial E_{vdw}}{\partial x}\frac{\partial x}{\partial r} = -\frac{H}{6d}\frac{1}{x^3(x^2-1)^2} \tag{3.10}$$

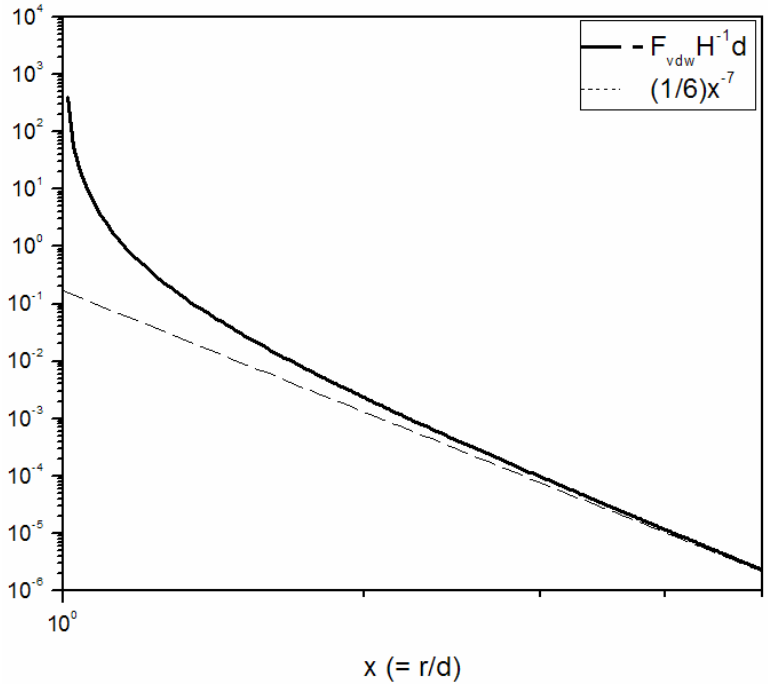

Fig 3.2: Normalized vdW force between two spherical particles

Here we have plotted in log-log scale the universal function $-F_{vdw}H^{-1}d$ along with the dependence on x^{-7} at large distances. From the Eq 3.10 we see that when the size of the interacting spheres is decreased by some factor *while keeping x constant*, the *force* holding the spheres together *increases* by this same factor, despite the fact that the *energy* remains constant. We see then why F_{vdw} can hold micron and smaller sized particles together more easily (leading to aggregation) than they can cm or greater sized particles. F_{vdw} is simply too weak to hold large particles together.

3.2 Repulsive Potentials:

3.2.1 Need for repulsion:

Accurate model interaction potentials between particles must include this vdW attractive energy. Of equal importance is the need to incorporate a strong repulsive potential at particle contact. Repulsion must be included in any realistic model to prevent the unphysical collapse of the interacting particles into themselves or into each other. Two 5nm spherical Au particles may attract each other strongly near contact as a result of vdW forces, but they will not collapse or deform on contact. Rather, they will remain at a center to center distance of approximately 1 particle diameter due to a strong repulsive interaction between the electronic orbitals of the contact atoms in respective particles. This repulsion is responsible for the minimum separation distance between atoms within each particle, the lattice spacing. Au atoms attract each other at distances greater than their equilibrium lattice spacing but become strongly repulsive at distances even a fraction less than this.

3.2.2 Lennard-Jones Potential:

3.2.2.1 LJ Form:

The most commonly used model for the combination of vdW attraction and near-contact repulsion between atoms or molecules is that of the Lennard-Jones (LJ) potential [45]:

$$E_{LJ} = 4\varepsilon\left[\left(\frac{r}{\sigma}\right)^{-12} - \left(\frac{r}{\sigma}\right)^{-6}\right] \tag{3.11}$$

Here ε is the depth of the LJ potential well, r is the particle center to center distance, and σ is the LJ "diameter" of the interacting particles; σ is not identical but related to the lattice spacing of the solid made of this atomic(molecular) species. This potential is demonstrated graphically in Fig 3.3 for several values of ε and σ:

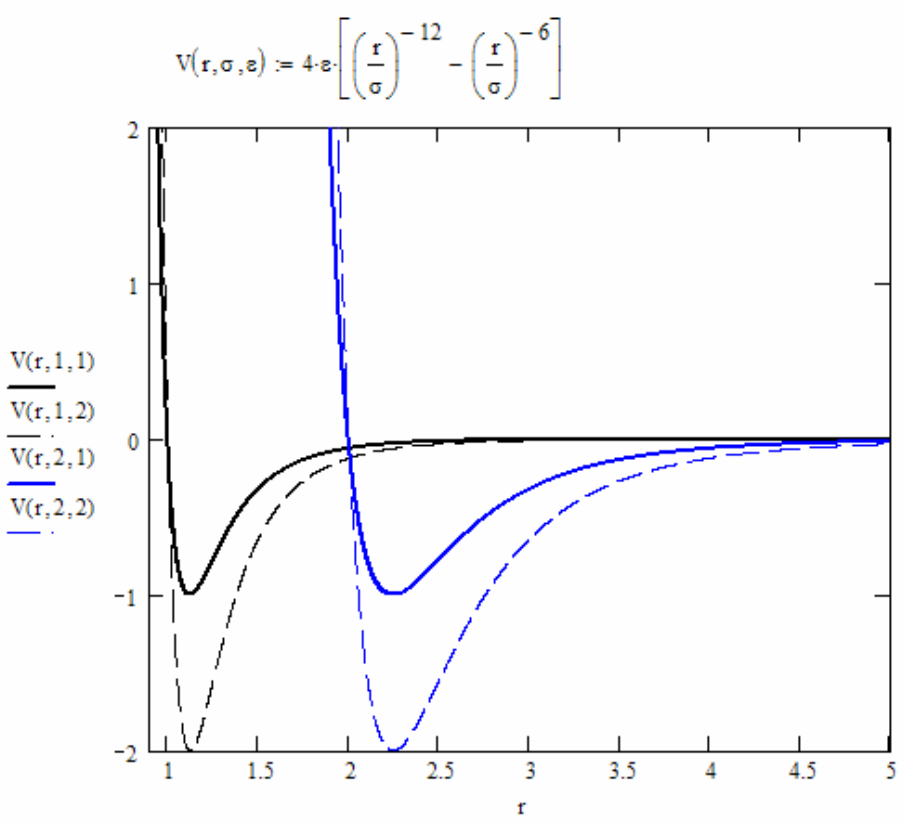

Fig 3.3: LJ potential for several values of σ and ε.

For the LJ potential, the minimum occurs at $r_{eq} = 2^{\frac{1}{6}}\sigma$; this distance can be identified as the equilibrium separation of two interacting LJ particles. The value of the potential at r_{eq} is considered the binding energy of two LJ particles, ε. For the purpose of computer simulations, it is common to set a cutoff range for the LJ potential on the order of 2.5σ. At this distance, the magnitude of the potential has fallen to 1.6% of the binding energy.

For $r \succ\succ \sigma$, $E_{LJ} \approx -4\varepsilon\left(\frac{r}{\sigma}\right)^{-6}$, and we see the same r dependence as that of the far range of the vdW interaction, as expected.

3.2.2.2 Origin of the repulsive term:

The r^{-12} repulsive term is itself *nonphysical* in origin [24,46]. In fact, the actual repulsive near-contact potential likely has an exponential term due to the origin of the repulsion, electron cloud densities, which contain exponential functions of distance (as in Hydrogenic wave functions). The r^{-12} repulsive term is used for two reasons. First, it represents a realistic "sharp" repulsion with decreasing distance like that observed for real particles. Secondly, the mathematical form for the equilibrium position and binding energy are simpler than for the exponential choice. In reality, no simple analytical form exists for the repulsive term as it requires an exact solution of the Schrodinger Equation for the atoms(molecules) in question.

3.2.2.3 Utility:

The use of the Leonard-Jones form, or the fitting of actual molecular interaction potentials to this form is replete in the literature. It has proven to be a successful and valuable tool in characterizing the physical properties and phase behavior of many substances [47-52].

3.2.3 Chemical Considerations and the DLVO potential:

3.2.3.1 Surface Charging in a Liquid Medium:

In many applications, particles are dispersed into a liquid phase medium. When this occurs, the particles may become charged as a result of various inter/re-actions with the medium molecules. An example of this is the surface charging of a dispersion of polystyrene spheres in water. When in an aqueous medium, the spheres can obtain an equilibrium negative surface charge density (σ_s) as a result of the reaction of their surface groups (often carboxyl, COOH) with the surrounding water molecules; H^+ is liberated

into solution (counterions) leaving negative carboxylate (COO^-) groups behind. The system, of course, maintains its charge neutrality. In general, when dispersed particles gain a surface charge density, surface groups on the particles are either *chemically reacting* to release ions into solution or accept them from solution or they are *adsorbing* ions from solution. The dispersed particles all obtain a charge density of like sign. The surrounding layer of counterions leads to a *screened* coulomb repulsion between the particles. Of course, the vdW interaction between particles remains attractive.

3.2.3.2 DLVO Potential:

The total interaction between two charged spheres is known as the DLVO (Derjaguin Landau Verwey Overbeek) potential, and accounts for both the effects of the surface charging (with accompanying counterion charge distribution) and vdW interactions. For low surface potentials (below ~ 25mV), the DLVO potential between two spheres is given by [24, 53]:

$$E_{DLVO} = \pi \varepsilon_0 \varepsilon_r d_0 \Psi_0^{\,2} \frac{e^{-\kappa(x-1)}}{x} + E_{vdW} \tag{3.12}$$

$\varepsilon = \varepsilon_0 \varepsilon_r$ = dielectric constant of solvent

d_0 = diameter of spherical particles

Ψ_0 = surface potential of particles

$\kappa = k_D d_0$ = reduced debye wave number

k_D^{-1} = Debye screening length

$= C[\text{salt}]^{-1/2}$

$C = 0.304\text{nmM}^{1/2}$ for 1:1 electrolytes (NaCl, KOH, etc.)

$= 0.176\text{nmM}^{1/2}$ for 1:2 & 2:1 electrolytes ($CaCl_2$, etc.)

$= 0.152\text{nmM}^{1/2}$ for 2:2 electrolytes ($CaSO_4$, etc.)

To explore the behavior of the DLVO potential as a function of the above parameters we define:

$$E_{DLVO}(x,H,J,\kappa) = J\frac{e^{-\kappa(x-1)}}{x} - \frac{H}{12}\left[\frac{1}{x^2-1} + \frac{1}{x^2} + 2\ln\left(1-\frac{1}{x^2}\right)\right] \tag{3.13}$$

The first term represents the screened coulomb repulsion between like-charged particles, and the second is the van der Waals attraction between the particles. In Fig 3.4 we graph several examples:

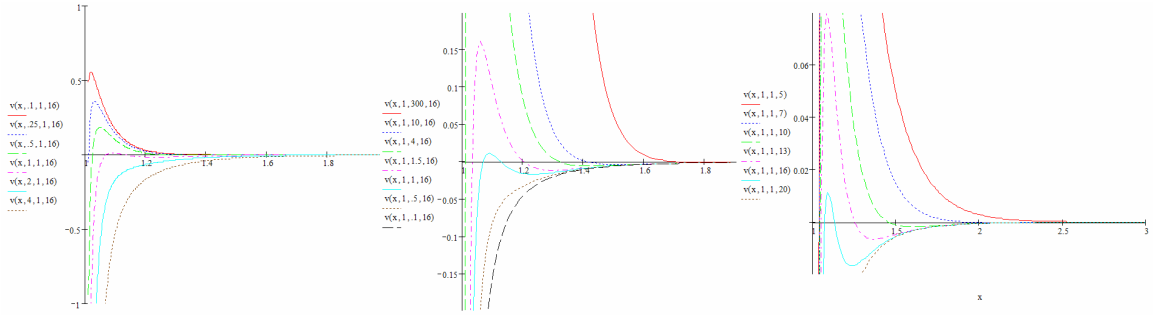

Fig 3.4: several examples of the DLVO potential with various parameters.

We can see from the left pane that an increase in the Hamaker constant H of the particles decreases the height of the coulomb barrier, eventually eliminating it altogether. At this point the particles would fall toward contact with each other despite their similar charge. This is similar to the DLCA process as defined above.

From the center pane, we observe that an increase in J (due to increase in ε, d_0, or Ψ_0) results in an increase in coulomb repulsion, at some point completely halting the aggregation mechanism. If particles do make it past this repulsive peak, they fall inevitably toward the primary vdW minimum at contact. Since the peak height may

exceed k_BT, this may have a low probability of occurrence ($p \approx e^{-\frac{E_{peak}}{k_BT}}$). A reduction in J results in a loss of the Coulomb barrier and again results in DLCA-like conditions.

At intermediate J values, a shallow secondary minimum [24,53-55] in the potential curve can exist in which particles can possibly exist in a metastable (reversible) state; the effects of this minimum have been studied by a number of researchers [54,55].

Finally, with an increase in screening constant κ, the coulomb repulsion can be shielded significantly, eventually being overwhelmed by the vdW attraction of the particles at short distances, leading to DLCA-type aggregation once again.

These parameters can be seen as affecting the "solubility" of dispersed particles in the solvent.

3.2.3.3 Reaction Limited Cluster Aggregation (RLCA):

As shown above, the similar charging of monomers in a liquid can lead to a Coulomb barrier in the approach of two dispersed particles to their primary energy mimimum location, that of contact. The above theory is useful in that it give a physical connection to known system parameters.

A different, but simple and useful way to approach the problem of an aggregation barrier is to set an aggregation "probability" for particles to bind when they come in contact, p_{stick} [56-63]. For $p_{stick} = 1$, the situation is the same as DLCA, that is complete and irreversible merging of the host clusters upon particle contact. For $p_{stick} = 0.001$, particles must *on average* come in contact 1000 times before they are allowed to be merged into a single entity. This is analgous to a DLVO potential with a repulsive peak of height ~ 7kT, since the probability for a particle to make it past this peak and be bound

to another particle is on the order of $p_{stick} = e^{-7} \sim 9.12 \cdot 10^{-4}$. It is known that for $p_{stick} \geq 0.01$, clusters formed have essentially the same fractal dimension as that of standard DLCA clusters and are characterized by an average size that grows linearly with time whereas for $p_{stick} < 0.001$, the clusters are more compact, having a higher fractal dimension (2.0-2.1 in 3D) and grow with a limited time-range exponential kinetics [56-59,64]. Additionally, RLCA growth mechanisms tend to produce systems with a higher degree of polydispersity than DLCA systems [64].

Chapter 4 - Simulation Methods:

In Chapter 4 we explain the various methods of computer simulation used in these studies. The idea of random variable assignment, especially as it relates to uniform spherical distributions is discussed. The Monte Carlo (MC) method is defined, and its application to aggregation simulations is thoroughly explained, including the various methods by which diffusional and ballistic motion of particles can be properly dealt with in code. The utility of periodic boundary conditions (PBC) and the link-cell method are discussed. The algorithms for building cluster lists and unfolding clusters in systems with PBC are presented. We show how non-contact particle interactions can be incorporated into MC via the Metropolis MC methodology. Finally, Brownian Dynamics programming and its relationship to the Langevin Equation is studied; the BD algorithm by which particle motion takes place is then presented.

4.1 Code:

The majority of the work included in this study was done using an Off-Lattice Monte Carlo (OLMC) code written in the C programming language by the author. Several variants of this code were created for diverse purposes, including Metropolis Monte Carlo algorithms and multiple-bonding programs. Additional work was done using a Brownian Dynamics code written and modified by the author.

4.2 Random Variable Assignment:

Simulation requires the assignment of particle positions, velocity vectors, etc. based on uniform random distributions. The placement of N_0 particles randomly within a d-dimension box of side L is easily achieved as:

$$\forall_{i=1..d,j=1..N_0}\left\{x_i(j) = L \cdot rand(0-1)\right\} \tag{4.1}$$

This assignment will produce a "uniform" density of points within the box, as required since a d-dimensional volume element is:

$$dV = \prod_i dx_i$$

, and dV is not a function of the x_i's.

A problem can arise, however, during the assignment of random velocity vectors in 3D. In this case, one normally wishes to generate velocities whose directions are randomly distributed in *orientation*, which we term *spherically random*. A simplistic approach would be to set the velocities as follows:

$$\theta = \pi \cdot rand(0-1)$$
$$\phi = 2\pi \cdot rand(0-1)$$

$$v_x = v\sin(\theta)\cos(\phi)$$
$$v_y = v\sin(\theta)\sin(\phi)$$
$$v_z = v\cos(\theta)$$

Such a distribution of velocities is shown in Fig 4.1 for 10^4 such velocity vectors:

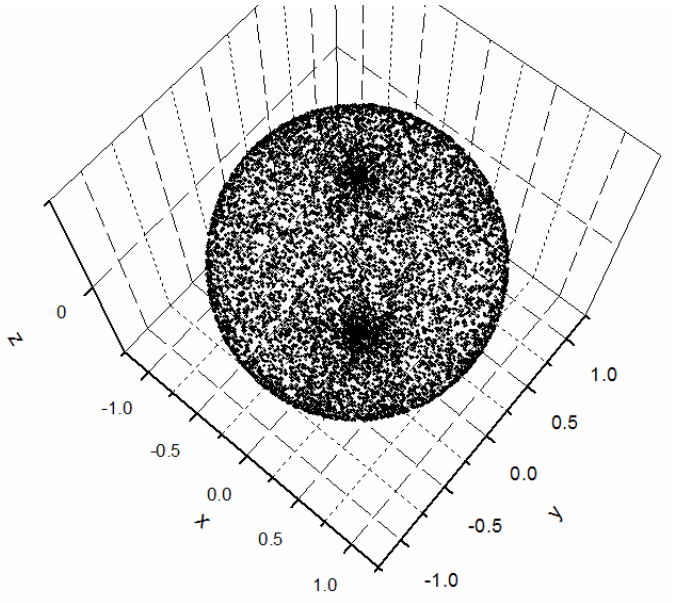

Fig 4.1: Random selection of θ leads to spherical nonuniformity for velocity vectors

It is not difficult to see that there is a definite spherical *nonuniformity* in the distribution, one which favors placement near the poles. The problem arises from the fact that we desire a random choice of *solid angle*. The differential element of solid angle is:

$$d\Omega = \sin(\theta)d\theta d\phi = d\left[-\cos(\theta)\right]d\phi \neq d\theta d\phi \tag{4.2}$$

For a random solid angle, we need to pick θ not from a uniform distribution in its range (0,π), but rather –cos(θ) over its range (-1,1). Since cos(θ) is symmetric, we can alternatively choose cos(θ) randomly between -1 and 1. We then do:

$$A = 2rand(0-1)-1 \tag{4.3}$$

which gives A uniformly distributed in the range (-1,1).

Then we have:

$$\theta = \cos^{-1}(A) \tag{4.4}$$

Since dΩ is not a function of φ, the choice of φ from a uniform distribution 0-2π is correct. With this correction in the choice of θ we obtain a uniform spherical distribution as desired and shown in Fig 4.2 for 10^4 velocity vectors :

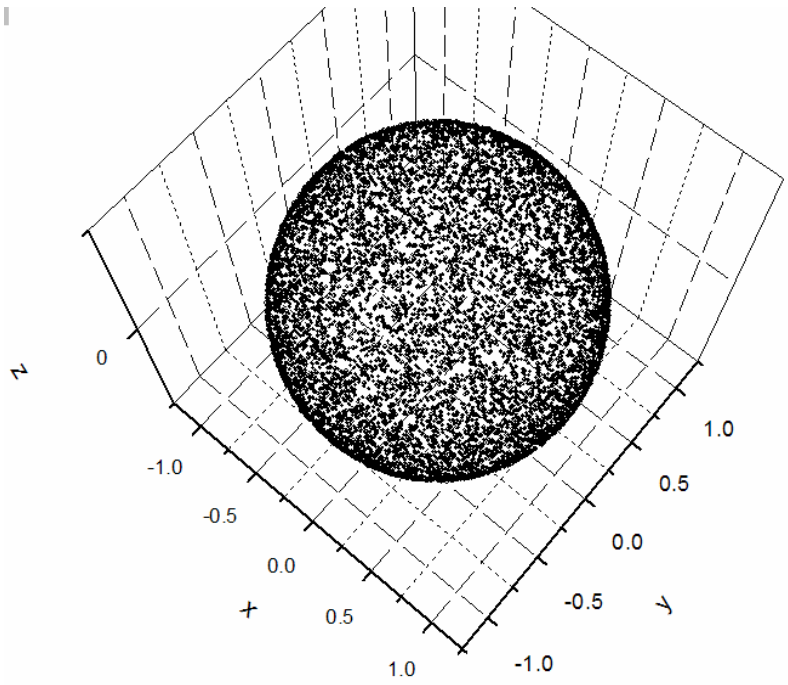

Fig 4.2: Correct selection of random solid angle leads to spherical uniformity

4.3 Monte Carlo Simulations:

4.3.1 Advantages and Disadvantages:

The heart of the Monte Carlo (MC) simulation is its use of random selection to solve problems that are analytically intractable. Typically one or several variable quantities are selected with some probability from a distribution in an iterative fashion. MC methods are therefore *nondeterministic* in their solution of physical problems. MC algorithms are well suited to represent the stochastic behavior of physical phenomena such as Brownian diffusion that occur as a result of random thermal fluctuations in

medium molecules and dispersed particles. The use of MC techniques in simulation greatly simplifies the complexity of the process by allowing one to ignore all but the essential details. For example, an MC simulation of the conformations of a linear alkane chain can allow for random fluctuations of orientational (dihedral) angles while leaving bond-lengths and bond angles fixed. This is not true of MD (molecular dynamics) simulations, which use Newton's laws to track the motion of each individual particle and must *explicitly* contain information for all acting potentials. MC uses statistics to solve problems instead of exact solutions; this is both an advantage and disadvantage.

4.3.2 Standard MC Aggregation Algorithm:

4.3.2.1 Initial Placement:

In a standard MC aggregation simulation, the system is initialized with a set of N_0 monomers of diameter $d_0 = 1$ placed randomly (as above) within a periodic d-dimensional box (d =2 or 3) of sufficient size L to produce a desired initial volume fraction, f_{v0}:

$$f_{v0} = N_0 \frac{\pi}{4} \cdot \frac{{d_0}^2}{L^2} \text{ (d = 2)} \tag{4.5}$$

$$f_{v0} = N_0 \frac{\pi}{6} \cdot \frac{{d_0}^3}{L^3} \text{ (d = 3)} \tag{4.6}$$

Particles are forbidden to overlap, and if such occurs during placement, the particle is reset to a new random location until there is no overlap.

4.3.2.2 Periodic Boundary Conditions (PBC):

Periodic boundary conditions (PBC) exist to allow a finite system to avoid inherent wall-effects which can alter physical system properties and *mimic* the behavior

of truly infinite systems. If solid walls are used in a simulation, the collision rates of particles near the walls will vary greatly from those within the bulk of the system, as will movement measurements such as diffusion constants. The information obtained from such a simulation will therefore be complicated by the wall's presence. In a PBC implementation, when a particle's movement places it outside the system box, its coordinates are readjusted so that it remains within the box, entering the system on the opposite side. An example is illustrative. Consider a particle with initial (x,y,z) coordinates (13.8, 1.6, 24.7) in a 3D system with box length L = 25. If it moves such that its new coordinates are (13.9, 1.3, 25.1), PBC will require that the z coordinate is altered from 25.1 to 25.1- L = 0.1. Each or several of the coordinates can be adjusted in such a way as needed concurrently. Fig 4.3 is an image of one such move in 2D; the particle starts in the position colored blue and moves to new position colored red according to PBC:

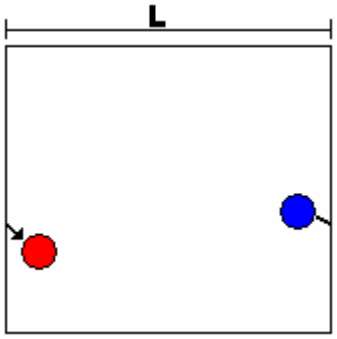

Fig 4.3: Movement of particle across a periodic boundary

An additional consideration with PBC is the calculation of distances between particles. Instead of simply:

$$r_{ij} = \sqrt{(x_i - x_j)^2 + (y_i - y_j)^2 + (z_i - z_j)^2}$$

we write:

$$r_{ij} = \sqrt{\Delta x_{ij,\min}{}^2 + \Delta y_{ij,\min}{}^2 + \Delta z_{ij,\min}{}^2} \tag{4.7}$$

where:

$$\begin{aligned} \Delta x_{ij,\min} &= \left| x_i - x_j \right| \quad for \quad \left| x_i - x_j \right| \le \frac{L}{2} \\ &= \left| x_i - x_j - L \right| \quad for \quad \left(x_i - x_j \right) \ge \frac{L}{2} \\ &= \left| x_j - x_i - L \right| \quad for \quad \left(x_j - x_i \right) \ge \frac{L}{2} \end{aligned} \tag{4.8}$$

$\Delta y_{ij,min}$ and $\Delta z_{ij,min}$ are defined in a similar fashion. These definitions ensure that the distance calculated between particles is the *minimum* distance between any of the pair's periodic images. Fig 4.4 is a 2D example of this problem. The minimum distance (dmin) calculated between the red particle and all of the blue particle periodic images is clearly seen to be the one labeled as determined by the above procedure:

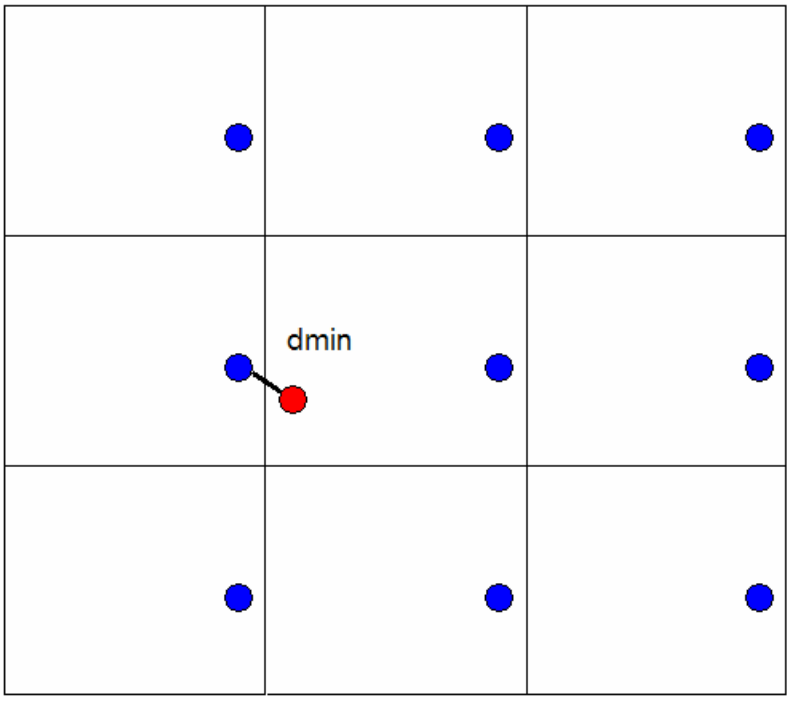

Fig 4.4: Calculating minimum separation distance using PBC

4.3.2.3 Link-Cell Method:

Often during a simulation, the position of a particle relative to other particles must be found. This occurs during the calculation of potentials/forces between particles. It also occurs in the case of cluster movement, since overlap of particles is forbidden, and the updated positions of particles within a moving cluster must obey this constraint. In general, a cluster moves a very small distance relative to the size of the system in one simulation time step. Additionally, many potentials have a cutoff range that is not much larger than the particle size. It therefore becomes highly inefficient to calculate the position of a moving particle relative to *all* other system particles; it is only a particle's *local neighborhood* that will affect its motion. As an example, if a system contains 10^4 particles, without the use of some reduction technique, $\left(\frac{1}{2}\right)10^4\left(10^4-1\right) \approx 5\cdot 10^7$ relative distance calculations will need to be performed for *each* period of $\Delta t_{MC} = 1$. As clusters form and grow, the number of calculations can decrease, since (in the absence of restructuring) the relative positions of particles within a cluster will not change and thus do not need to be calculated. It is not difficult to see, though, that the number of requisite calculations reduces a viable system size down to a few thousand particles at best, even with the fastest multiple processor systems available today.

Thankfully, such a technique for reducing the number of required calculations does exist [65]. This is termed the link-cell method. It is nearly universal in its implementation in both MC and molecular/Brownian dynamics simulations. The basic premise of the method is that the number of calculations can be reduced by *gridding* the

L^d sized system into d-dimensional grids of size L_c^d (side-length L_c). L_c is chosen such that it is on the order of either the movement size of a particle in one simulation time step or the range of the particle interaction potential (if one is used). Long-range interaction potentials such as the Coulomb force require special techniques, sometimes including reciprocal space calculations such as the Ewald Sum. L_c is chosen with the above constraints and such that $N_{side} = \frac{L}{L_c}$ is the integral number of cells on one side of the simulation box. The advantage of the link-cell method is that particle interactions need only calculated *between particles within the same and neighboring cells*.

For example, if in a 3D system L = 100, $L_c = 2$, there will be $N_{side} = 50$ cells per side of the simulation box and a total of $N_{box} = N_{side}^3 = 125{,}000$ total cells within the system. In this case, the cutoff range will not exceed 2 units. For each particle's movement within the system, its position then must be calculated relative to only those particles in its own cell and the 26 neighboring cells. The average computational time reduction factor is then on the order of $\frac{125{,}000}{27} \approx 4600$, an enormous savings. A 2D example of this process is shown in Fig 4.5 for a system of 40 particles. In this case, L = 16, $L_c = 2$; L_c is set by the cutoff distance for some potential which is drawn as a circle around the particle in question (green). For this particle, only 5 calculations of relative positions need to be made (indicated by black lines), instead of the 39 required if the link-cell method is not used:

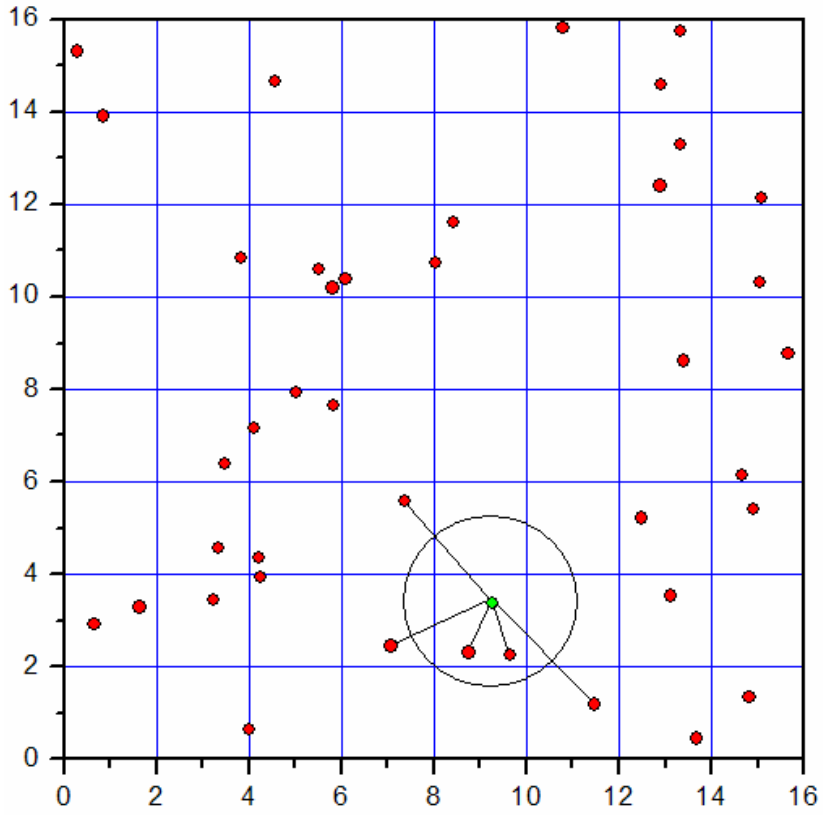

Fig 4.5: The Link-cell method drastically reduces the number of required distance calculations between system particles. In this case 5 calculations are required instead of 39.

The use of the link-cell method does require a certain overhead, however. For each cell within the system, an ordered list of particles contained must be maintained. In our implementation, each cell has a *first* and a *last*. Additionally, each system particle has a *next* and a *prev* (previous) within the list. By convention, when particles are initially placed randomly in the system, these lists are constructed, being updated as needed as the system evolves and particles move from cell to cell. Below is *pseudocode* for both the initial particle placement and subsequent particle movement from one cell to another:

Particle Placement in cells:

Cycle through all system particles i:

For particle i:

Find (x,y,z):

x = rand(0-1)*L

y,z = ….

Find (cx,cy,cz):

cx = int(x/L_c) + 1

cy,cz …

Check if first[cx,cy,cz] exists (≠0):

if so:

lastp=last[cx,cy,cz]

next[lastp]=i

next[i]=0

prev[i]=lastp

last[cx,cy,cz]=i

if not:

first[cx,cy,cz]=i

last[cx,cy,cz]=i

prev[i]=0

next[i]=0

This process is efficient in that *as* particles are being placed, the link-cell lists are constructed. A check can also be placed in the above algorithm to guarantee that no two particles are placed too closely to each other (to prevent overlap). With these lists, no

matter which direction we wish to step through the cell lists, we can do so unambiguously.

Below is pseudocode for the process of moving a particle from one cell to another:

Particle i moving from cell (cxo,cyo,czo) to (cxn,cyn,czn):

```
Assign:
    ofirst = first[cxo,cyo,czo]
    olast = last[cxo,cyo,czo]
    oprev = prev[i]
    onext = next[i]
    nfirst = first[cxo,cyo,czo]
    nlast = last[cxo,cyo,czo]
Check if first[cxn,cyn,czn] = 0
    if so:
        first[cxn,cyn,czn] = i
        last[cxn,cyn,czn] = i
        next[i] = 0
        prev[i] = 0
    if not:
        last[cxn,cyn,czn] = i
        next[i] = 0
        prev[i] = nlast
        next[nlast] = i
```

Check if ofirst = i

if so:

first[cxo,cyo,czo] = onext

prev[onext] = 0

Check if olast = i

if so:

last[cxo,cyo,czo] = oprev

next[oprev] = 0

If i≠ofirst and i≠olast

next[oprev] = onext

prev[onext] = oprev

Note that when a particle moves from one cell to another, it is always added to the *end* of the new cell's link list (becoming the last of that cell). If the new cell it is moving into is empty, it will also become the first of that cell. As can be seen from the three cases above, care must be taken in extracting a particle from its current cell's link list to ensure that the list remains continuous after removal of the particle.

The above process can appear quite intricate and computationally costly, but for large systems, the savings in computing time far outway the cost of managing the link-cell lists. Proof of this lies in the fact that this technique allows simulations of systems of millions of particles, for which the number of distance calculations required *per MC time step* would be on the order of 10^{12} without, an unreasonably high value for currently available computing resources.

4.3.2.4 Cluster Lists:

The geometry of the aggregation process in a system with PBC can be complicated to unravel. To make the movement of clusters and calculation of cluster properties easier, it is common practice to keep an ordered list of all the particles belonging to each cluster. This allows the program to iteratively proceed through all of the particles within a given cluster. In this regard, each particle within the system is assigned a *clustleader* and a *clustlast*. Since the simulation begins with a set monomers, the clustleader and clustlast values for each particle are initialized to the particle number itself. Each particle also has a *clustnext* which indicates the particle immediately after the current one in the cluster list. This is initialized to 0 for each particle. When a cluster is moved, comes in contact with a second cluster, and merge with it, several things must happen:

1) The *clustlead* of each particle in the stationary cluster gets assigned the value of the *clustlead* of the moving cluster.

2) The *clustnext* for the *clustlast* of the moving cluster is set to the *clustlead* of the stationary cluster.

3) The *clustlast* for each particle in the moving cluster gets assigned the value of the *clustlast* of the stationary cluster.

4.3.2.5 Unfolding:

In many cases, a growing cluster in a PBC system can extend beyond the edge of one side of the simulation box and into the other side. This is particularly likely at late times in the simulation when the number of clusters $N_c \to 1$, or as the system nears gelation, the formation of a system spanning cluster. Due to this, the calculation of certain physical parameters can be done improperly if the "in-box" coordinates of such a

cluster's particles are used. An example of this might be the determination of a cluster's center of mass. In order to circumvent this problem, a process called unfolding is typically done, where, starting at the lead particle of the cluster, a routine is performed to find what the coordinates of each cluster particle would be in order for the cluster to be a continuous geometrical structure, their so-called *unfolded coordinates* . This can be a complex process. In MD or BD (Brownian Dyamics) simulations, one *must* perform this unfolding on system clusters every time one wishes to know such properties, since relative positions of particles within clusters are constantly changing.

The following is pseudocode for a cluster unfolding algorithm.

Unfolding Algorithm:

a) Starting at leading particle, cycle through all particles in cluster using cluster list (clustnext of each particle).

-The unfolded coordinates of the lead particle in the cluster are defined as its box coordinates.

b) Scan current cell and neighboring cells (using PBC) for particles within the cluster that are within a contact cutoff range $r_{contact}$ of current particle.

c) For any particle that meets these criteria, adjust its *unfolded* coordinates as needed (adding or subtracting multiples of the system size L) to bring it within a contact cutoff range of current particle's unfolded coordinates.

d) Once a particle's unfolded coordinates are so adjusted, mark it as *complete.*

e) Continue cycling through particles in cluster until all particles are marked as complete. At this point, cluster is unfolded

For MC simulations, the complexity of the unfolding process can be almost entirely removed. Each time two clusters are merged into a single entity, the relative positions of the *contacting* particles within the moving and stationary clusters can be determined. From this information, the unfolded coordinates of all particles within the stationary cluster can be calculated. In this way, the "unfolding" of the cluster is done *during* cluster formation, eliminating the need to do it in later steps.

Fig 4.6 is an image of a large, late-time cluster of size $N = 8475$ in both its boxed and unfolded state. The cluster is one of two within a system with $f_{v0} = 0.01$ and $N_0 = 10^4$ at $t = 5479$. At $t = 1241$, a system spanning cluster was formed (gel). The differences in appearance between the two images are striking; notice that the unfolded cluster extends far beyond the box boundaries.

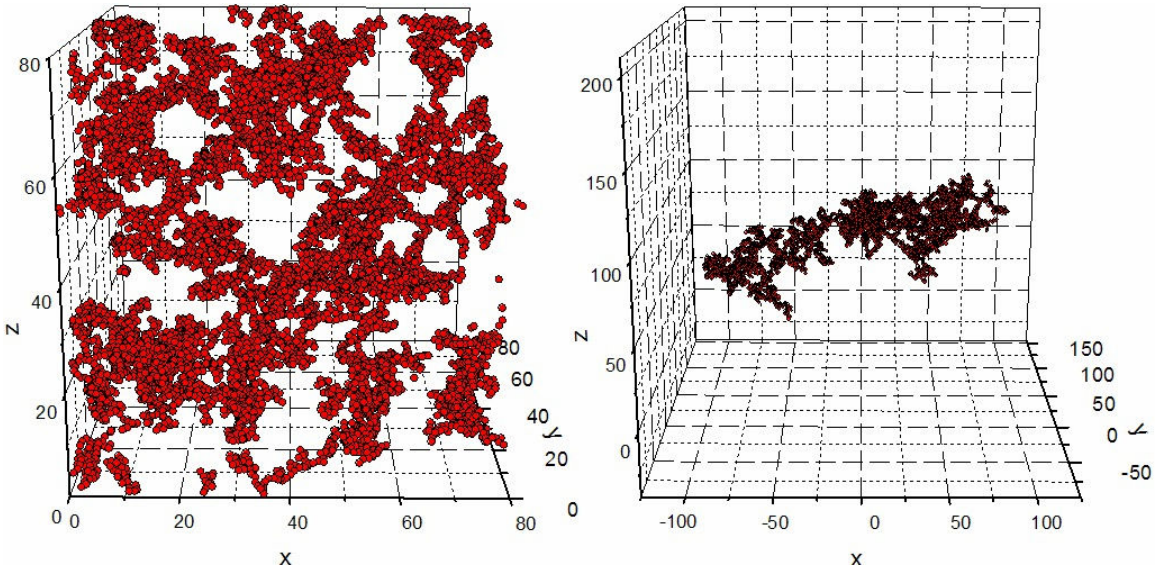

Fig 4.6: N = 8475 gelled cluster in both "box" and unfolded coordinates.

4.3.2.6 Cluster Motion:

After placement, a particle (or cluster of particles) is chosen with some probability p_{choose} from the list of N_c clusters and is moved a distance r_{move} with probability p_{move} in a specified direction. There are several ways for this to occur. We take examples from two motional regimes, the ballistic and diffusional.

4.3.2.6.1 Ballistic:

The simplest case of cluster movement is that of ballistic motion that can occur in the free-molecular regime. In this case, particles or clusters of particles move along linear trajectories between collisions with each other. Such motion can occur when particles are dispersed in a zero-g vacuum or at a low medium gas pressure (discussed below).

The simulated motion of a ballistic cluster can occur in one of two ways. In both cases, the randomly placed monomers are assigned spherically random velocity vectors. During each MC step, a cluster is chosen randomly with uniform probability:

$$p_{choose} = \frac{1}{N_c} \tag{4.9}$$

from the list of N_c remaining clusters. By convention, the diameter of monomers is set to $d_0 = 1$, thus defining the unit length for the simulation. Time is incremented by $\frac{1}{N_c}$ for each cluster choice (whether or not cluster is actually moved); after N_c such moves are made, a total of one Monte Carlo time unit ($t_{MC} = 1$) has passed.

In the first ballistic method, the cluster chosen at each MC step is moved a distance d_{clust} along its current trajectory. d_{clust} for a monomer is set to a distance of one monomer diameter, d_0. During one MC step, a cluster of size N moves a distance:

$$d_{clust} = \sqrt{\frac{1}{N}} \tag{4.10}$$

based on its thermal velocity relative to that of the monomer. If the movement of the current cluster would lead to the overlap of a particle belonging to the cluster with a particle not contained in the current cluster, d_{clust} is adjusted so that *exact contact* between the two is achieved.

In the second method, the cluster chosen at each MC step is moved a *unitary* distance d_0 *regardless of its size* along its trajectory with a probability p_{move} based on its thermal velocity. Convention sets $p_{move}=1$ for monomers and:

$$p_{move} = \sqrt{\frac{1}{N}} \tag{4.11}$$

for clusters of size N, based again on their relative thermal velocity. As in the first method, d_{clust} is adjusted as needed to prevent overlap of contacting clusters.

In both methods, when clusters come into contact, they are merged into a single cluster which moves as a single entity when it is chosen in subsequent MC steps. Consequently N_c is decremented by 1. After the merge, the newly formed cluster is assigned a new spherically random velocity vector.

The above methods generate the same kinds of aggregates with the same kinetics and associated cluster size distributions. The equivalence of the results of the two methods has been shown in other works [64]. The advantage to one method over the other is purely a matter of computational time required. In the first method, the cluster is *always* moved. Thus a movement of each of the cluster's particles, a test for their overlap, and a calculation of changes in interparticle potentials (if any) must be performed at each MC step. In the second method, only monomers are *always* moved;

the larger the cluster is, the less likely it is to move. Therefore, for large clusters, only infrequently will the numerous calculations required for each cluster particle need to be performed. Therefore the second method is superior for the reduction of computational time, a serious concern in computational physics. A graph of the kinetics for a single run of the two methods is shown in Fig 4.7:

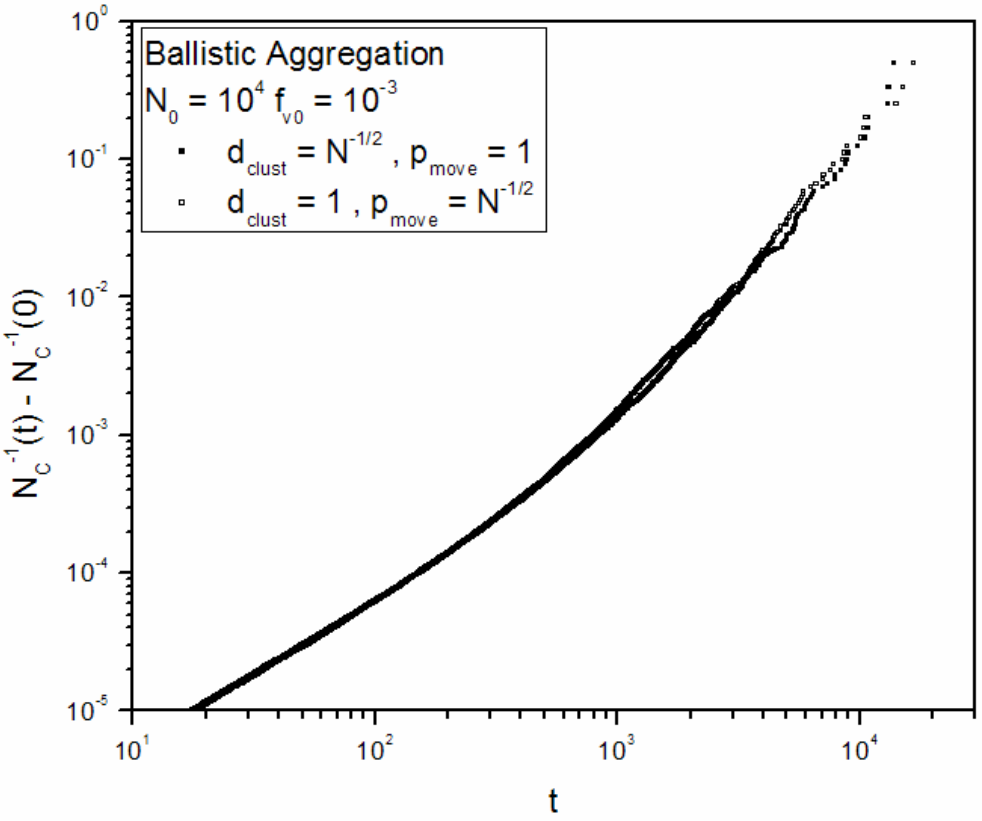

Fig 4.7: Agreement between the two methods for moving ballistic particles in MC

The excellent agreement between the two methods is obvious. Slight differences between the two appear at late simulation times due to the worsening statistics brought on by finite-size effects as $N \to N_0$ and $N_c \to 1$. The run based on the first method completed in 5 min 22 sec on an AMD Athlon XP 3000+ processor, while the second method run finished in 4 min 7 sec. Note that the ratio of run times will increasingly

favor the second method as N_0 increases. This is because the desired end-point of these MC aggregation simulations is often $N_c = 1$, and at late times in the simulation the size of clusters will continue to increase.

4.3.2.6.2 Diffusional:

Similar variances in method also occur in diffusional simulations. As in the ballistic case, the two most frequently used involve adjustments to either d_{clust} or p_{move} based on cluster size. In all diffusional simulations, a chosen cluster is moved in a spherically random direction at each MC step; there are no persistent velocity vectors. The law of diffusion gives us:

$$< x_N{}^2 > = 2dD_N t = d_{clust}{}^2 N_{chosen} p_{move} = d_{clust}{}^2 N_{move} \tag{4.12}$$

That is, the mean square displacement of a diffusional particle is proportional to its diffusion constant and time over which it diffuses. Alternatively, it is proportional to the number of diffusional steps in which the cluster is moved $N_{move} = N_{chosen} p_{move}$ and the square of the size of the step d_{clust}.

In the first diffusional method, a chosen cluster of size N is moved a distance:

$$d_{clust} = \sqrt{\frac{D_N}{D_0}} = \sqrt{\frac{r_0}{R_g}} \propto N^{-\frac{1}{2Df}} \tag{4.13}$$

based on its relative diffusion constant to that of a monomer. p_{move} is set to 1 for all clusters. Then, as defined above:

$$< x_N{}^2 > = \frac{D_N}{D_0} N_{move} \tag{4.14}$$

Since $N_{move} \propto t_{MC}$, we obtain $< x_N{}^2 > \propto Dt$ as required.

In the second method, a chosen cluster of size N is again moved a distance d_{clust} = d_0 regardless of its size. It is moved with a probability $p_{move} = \frac{D_N}{D_0}$. In this case:

$$< x_N^{\,2} > = d_0^{\,2} N_{chosen} \frac{D_N}{D_0} \tag{4.15}$$

Now $N_{chosen} \sim t_{MC}$ so that as needed $< x_N^{\,2} > \propto Dt$.

As for the ballistic case, the second method will be favored for the reduction of computing time, especially as N_0 increases, and for the same reasons.

4.3.3 Metropolis MC:

Whenever a *noncontact* potential exists between dispersed particles or an external potential influences the system, the simulated motion of particles must take these into account. In such a simulation, the ratio of potential energy changes to the available thermal energy becomes important. A change in temperature will lead to different kinetics, morphologies, and size distributions for the structures formed in a real system with the same interaction potentials in effect. A method for incorporating system energetics into MC sampling was first introduced by Nicolas Metropolis in 1953 [66]. It is almost universally referred to as the *Metropolis Monte Carlo Method*.

In Metropolis MC, a system at any point in time exists in a known state S_i (initially S_0) which can include information on particle positions, velocities, etc. This state is characterized by a potential energy U_i (initially U_0). For simulations, it is more efficacious to keep track of a scaled energy parameter $E_i = \frac{U_i}{k_B T}$. At each step of the algorithm, an attempted change in state is made, taking the state from S_i to S_f with

associated scaled potential energies E_i and E_f. The difference in scaled potential energy is then:

$$\Delta E = E_f - E_i \tag{4.16}$$

The probability that the change in state actually occurs is a function of ΔE. There are three possible cases:

$\Delta E < 0$:

Change is accepted and system is transformed into state S_f with energy E_f

$\Delta E > 0$:

Random number C_{rand} in the range (0,1) is generated

Factor $C_E = e^{-\Delta E}$ is calculated

If $C_{rand} < C_E$:

Change is accepted and system is transformed into state S_f with energy E_f

If $C_{rand} > C_E$:

Change is not accepted and system stays in state S_i with energy E_i

The above sampling method gives the proper *Boltzmann Statistics* for physical properties and allows us to calculate thermal average quantities. The probability of the system being in a particular state S_a with scaled energy E_a is:

$$P(S_a) = \frac{e^{-E_a}}{Z} \tag{4.17}$$

Z, the partition function, is defined as:

$$Z = \sum_i N_i e^{-E_i} \tag{4.18}$$

where i runs over all energy states, N_i is the number of states having energy E_i (degeneracy). For instance, if a property of the system is X, then the *Boltzmann Distribution* gives:

$$< X > = \sum_i X_i N_i \frac{e^{-E_i}}{Z} \tag{4.19}$$

X may include properties such as average number of particles per cluster, radius of gyration, etc.

The Metropolis method is useful in many physical situations including systems with gravitational settling, temperature dependent bond energies, and has been used in the current work to model systems whose particles interact with each other.

4.4 Brownian Dynamics (BD):

MC codes have many advantages, but a large number of physical systems are better modeled through an explicit integration of particle equations of motion. Brownian Dynamics is a robust method for achieving this.

4.4.1 Molecular Dynamics (MD):

While Monte Carlo simulations have many advantages, a more rigorous treatment of physical laws governing aggregation is found in Molecular Dynamics (MD). In a strict sense, MD requires a direct knowledge of the interaction energies (forces) between particles within a system as well as the effects of any external potentials acting on the system [51,52]. In many implementations, medium molecules must be treated explicitly, with their own degrees of freedom. From a known set of initial conditions, the motion of all particles within the system can be found by numerical integration of Newton's laws. The time step in such a simulation is small due the strength of forces associated with

particle contact. The time required for a system to evolve from its initial state to a desired final state can be exceedingly high. Processes such as gelation within dispersed particle systems are almost inapproachable via MD simulations. The Brownian Dynamics Methodology described below helps circumvent these problems.

4.4.2 Initial Particle Velocities

In the BD methodology, the system normally begins at a known temperature through the assignment of particle velocities based on a Maxwell-Boltzmann distribution:

$$f_v(v_x, v_y, v_z) = \left(\frac{m}{2\pi k_B T}\right)^{\frac{3}{2}} e^{-\frac{m\left(v_x^2+v_y^2+v_z^2\right)}{2k_B T}} \tag{4.20}$$

The corresponding *speed* distribution is:

$$f(v) = 4\pi\left(\frac{m}{2\pi k_B T}\right)^{\frac{3}{2}} v^2 e^{-\frac{mv^2}{2k_B T}} \tag{4.21}$$

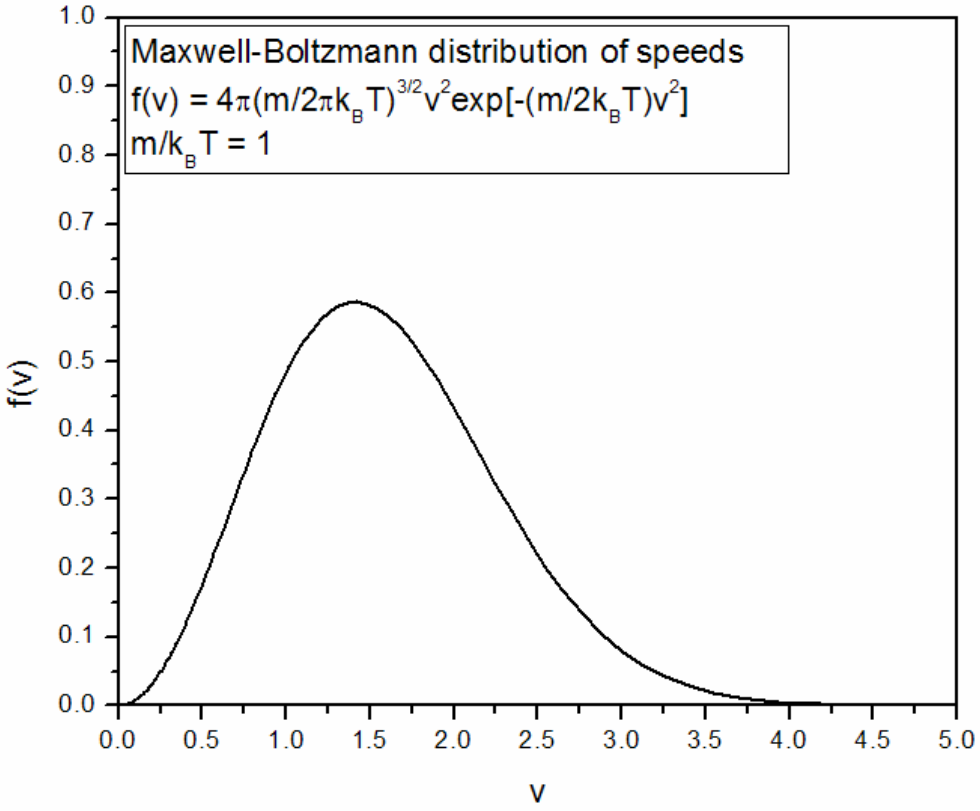

Fig 4.8: The Maxwell-Boltzmann thermal speed distribution

4.4.3 Langevin Equation:

In many physical situations, aggregation occurs under constant temperature conditions. In this case, it is possible to *avoid* the explicit treatment of medium molecules. In addition to all explicit interparticle interactions, the stochastic thermal forces from medium molecular collisions need to be included in such simulations in order to obtain meaningful results. The Langevin equation is a stochastic differential equation that describes the motion of such a particle. It is a statement of Newton's 2nd law for a particle experiencing both deterministic and stochastic thermal forces:

$$m_p \frac{d^2 \mathbf{x}_p}{dt^2} = \mathbf{F}_{drag} + \xi - \nabla U = f_{drag} \frac{d\mathbf{x}_p}{dt} + \xi - \nabla U \qquad (4.22)$$

$\mathbf{x}_p$ = position of dispersed particle

$\mathbf{F}_{drag}$ = drag force on the particle

ξ = stochastic thermal force acting on the particle (as given in Eq. 2.6)

$$< \xi(t)\xi(t') > = 2dk_B T f_{drag}\delta(t-t') \text{ (in d-dimensional space)} \qquad (4.23)$$

$-\nabla U = \mathbf{F}_{pot}$ = sum of the external and interparticle forces

The forces on the particle in the above equation come from three terms. The first is a drag force from the surrounding fluid as described earlier. The second is the *stochastic* thermal force, "stochastic" indicating that there is no spatial or time correlation between values of this force at the beginning and end of any time interval, no matter how small the interval. In a liquid or gas medium the source of this force is the momentum exchange during collisions with medium molecules or other dispersed particles, each particle and medium molecule being given a certain amount of kinetic energy via the equipartition of energy. The final force comes from any potential that the particles interact with each other by or any externally applied potential.

As noted by Einstein [67], the *fluctuation-dissipation* theorem indicates that the source of both the stochastic thermal force, responsible for fluctuations of a particle's position and thus Diffusion, and the drag felt by a particle in moving at a velocity v through the medium have the same origin, that of the Maxwell-Boltzmann distribution of medium molecular velocities in thermal equilibrium at temperature T. This shows up as the drag coefficient f_{drag} in the time correlation of the stochastic force as seen above.

4.4.4 Method and Implementation:

In opposition to MD simulations, the majority of BD implementations *do not* require the explicit integration of medium molecule degrees of freedom. In this case, the

medium is seen as a continuous one whose effects are felt through the drag and thermal force acting on the dispersed particles. Medium effects may also be included *implicitly* through alteration of interparticle forces. An example of this is the adjustment of the *relative* Hamaker constant of two particles in a water medium.

The advantage of the BD methodology is the reduction in the number of integrations that must be performed in order for a system to evolve over a long period of time. Disadvantages also occur in BD. These include the ignoring of any explicit medium interactions such as the adsorption of medium molecules on the surface of dispersed particles. Additionally, BD requires a complicated integration method due to the stochastic nature of the thermal forces. Stochastic integration has been the subject of a wide range of studies [68-72].

In our implementation, the third-order BD algorithm of van Gunsteren and Berendsen has been used [68]. A principal advantage to this algorithm is that, unlike many other implementations, the time step Δt does not have to satisfy the condition:

$$\Delta t \prec\prec \frac{1}{\gamma} \tag{4.24}$$

where $\gamma = \frac{f_{drag}}{m}$

Avoiding the rigorous details of the calculations, the algorithm is as follows:

1) Assign particles positions randomly and velocities from Maxwell-Boltzmann Distribution using the system temperature T_{ref}

2) Calculate associated potential energies $V[x_i(0)]$ and Forces $F(0)$ for each particle

3) In the first step (n=1), for each particle:

Choose $X_0(\Delta t)$ from Gaussian distribution where:

$$< X_o(\Delta t) > = 0$$
$$< X_0{}^2(\Delta t) > = \frac{k_B T_{ref}}{m\gamma^2} C(\gamma\Delta t) \tag{4.25}$$

$$C(x) = 2x - 3 + 4e^{-x} - e^{-2x} \ \{x > 1\}$$
$$C(x) = \frac{2}{3}x^3 - \frac{1}{2}x^4 + \frac{7}{30}x^5 - \frac{1}{12}x^6 + \frac{31}{1260}x^7 - \frac{1}{160}x^8 + \frac{127}{90720}x^9 \ldots \{x < 1\} \tag{4.26}$$

Then the updated positions at $t_1 = t_0 + \Delta t$ (usually $t_0 = 0$) are given by:

$$x(t_1) = x(t_0) + v(t_0)\frac{1 - e^{-\gamma\Delta t}}{\gamma} + \frac{F(t_0)}{m}\frac{\gamma\Delta t - \left(1 - e^{-\gamma\Delta t}\right)}{\gamma^2} + X_0(t) \tag{4.27}$$

Here, x can represent each of the particle coordinates (x,y,z) of the particle in question, each with it's own separate choice of X_0.

4) For all subsequent steps $(n = 2,3\ldots)$ using $x(t_n)$, $x(t_{n-1})$, $X_{n-1}(\Delta t)$, $F(t_{n-1})$:

Find $F(t_n)$ from spatial derivative of potential $V[x(t_n)]$

Find $F'(t_n)$ (time derivative of $F(t_n)$) from:

$$F'(t_n) = \frac{F(t_n) - F(t_{n-1})}{\Delta t} \tag{4.28}$$

Choose Y from Gaussian distribution with:

$$< Y > = 0$$
$$< Y^2 > = \frac{k_B T_{ref}}{m\gamma^2}\frac{E(\gamma\Delta t)}{C(\gamma\Delta t)} \tag{4.29}$$

$C(x)$ defined above

$$E(x) = 16\left(e^x + e^{-x}\right) - 4\left(e^{2x} + e^{-2x}\right) - 24 - 4x\left(e^x - e^{-x}\right) + 2x\left(e^{2x} - e^{-2x}\right)\{x > 1\} \tag{4.30}$$

$$\frac{E(x)}{C(x)} = \frac{1}{2}x^3 + \frac{3}{8}x^4 + \frac{29}{160}x^5 + \frac{43}{640}x^6 + \frac{1831}{89600}x^7 + \frac{381}{71680}x^8 + \frac{235009}{193536000}x^9 \ldots \{x < 1\}$$

(4.31)

Calculate:

$$X_n(-\Delta t) = X_{n-1}(\Delta t)\frac{G(\gamma\Delta t)}{C(\gamma\Delta t)} + Y \tag{4.32}$$

with:

$C(x)$ defined above

$$G(x) = e^x - 2x - e^{-x} \ \{x > 1\} \tag{4.33}$$

$$\frac{G(x)}{C(x)} = \frac{1}{2} + \frac{3}{8}x + \frac{21}{160}x^2 + \frac{19}{640}x^3 + \ldots \{x < 1\} \tag{4.34}$$

Choose $X_n(\Delta t)$ from Gaussian distribution with:

$$\begin{aligned} &< X_n(\Delta t) > = 0 \\ &< X_n{}^2(\Delta t) > = \frac{kT_{ref}}{m\gamma^2} C(\gamma\Delta t) \end{aligned} \tag{4.35}$$

Calculate:

$$\begin{aligned} x(t_n + \Delta t) = x(t_n)(1 + e^{-y}) - x(t_n - \Delta t)e^{-y} + \frac{F(t_n)}{m}\frac{(\Delta t)^2}{y}\left(1 - e^{-y}\right) + \\ \frac{F'(t_n)}{m}\frac{(\Delta t)^3}{y^2}\left[\frac{1}{2}y\left(1 + e^{-y}\right) - (1 - e^{-y})\right] + X_n(\Delta t) + e^{-y}X_n(-y) \quad \{y = \gamma\Delta t > 1\} \end{aligned}$$

(4.36)

and appropriate small y expansions of above exponential functions for y<1

Velocities are calculated from *positions* as:

$$v(t_n) = \left\{\left[x(t_n + \Delta t) - x(t_n - \Delta t)\right] + \frac{F(t_n)}{m\gamma^2}G(\gamma\Delta t) - \frac{F'(t_n)}{m\gamma^3}G(\gamma\Delta t) + \left[X_n(-\Delta t) - X_n(\Delta t)\right]\right\}\frac{H(\gamma\Delta t)}{\Delta t}$$

(4.37)

$$H(x) = \frac{x}{e^{x} - e^{-x}} \{x > 1\} \tag{4.38}$$

$$H(x) = \frac{1}{2} - \frac{1}{12}x^{2} + \frac{7}{720}x^{4} \ldots \{x < 1\} \tag{4.39}$$

This method assumes that there is *no correlation* between the stochastic force and the systematic force (resulting from interparticle/external potentials). This assumption is shown to be good when the temperature calculated from:

$$T = \frac{1}{3Nk_{B}} \sum_{i=1}^{N} m(v_{x}^{2} + v_{y}^{2} + v_{z}^{2}) \tag{4.40}$$

meets the condition:

$$T \approx T_{ref} \tag{4.41}$$

In all implementations, this condition is seen to hold well.

We note that for simplicity, it is standard practice to set m, k_B, T_{ref}, d_0 equal to 1. Energy values (kinetic and potential) are all measured then in units of k_BT and distances in units of the monomer diameter d_0.

This method is third order in Δt. It reduces to the commonly used Verlet MD algorithm in the limit that the drag vanishes [55].

Chapter 5- Aggregation Theory:

In chapter 5 we explain the basic concepts of Aggregation theory. The Smoluchowski coagulation equation is defined, and its kernels (both aggregation and fragmentation) are analyzed for the various particle motional regimes. Steady state cluster sizes as a result of aggregation/fragmentation equilibrium are explained via several examples. The fractal nature of colloidal and aerosol aggregates is elucidated with special attention given to the mass-radius scaling for these ramified structures. Several ways of determining the fractal dimension of aggregates are presented, including the ensemble, onion-shell, and structure factor methods. The inevitable gelation of systems aggregating without any fragmentation kernel is explained, and four possible mathematical descriptions of gelation are derived. Kinetic exponents are shown to be related to the homogeneity of the aggregation kernel, and the scaling law for determining kinetic exponents is presented. Finally, the scaling form for the cluster size distributions (CSD) is presented.

5.1 Smoluchowski (Coagulation) Equation:

Historically, the theoretical basis for aggregation is the famous coagulation (kinetic) equation, dubbed the "Smoluchowki Equation", derived by Marian Smoluchowski in 1916 [73]. In the absence of any fragmentation, the equation has the following form:

$$\frac{\partial n(i,t)}{\partial t} = \frac{1}{2}\sum_{j=1}^{i-1} K(i-j,j)n(i-j,t)n(j,t) - \sum_{j=1}^{\infty} K(i,j)n(i,t)n(j,t) \qquad (5.1)$$

Here n(i,t) is the concentration of clusters of size i as a function of time t. K(i,j) represents the coagulation kernel, or the (concentration independent) rate at which collisions occur between clusters of sizes (number of monomers) i and j. We see in the first term on the right side of the equation, that the concentration of i clusters increases with time due to the collision of smaller clusters combining to form clusters of size i. The factor of ½ is required to correct for the double counting of collisions that is done in the first term. The second term indicates the concentration of size i clusters decreases as these clusters themselves combine with other clusters to form clusters larger than size i. Importantly, we see that the coagulation kernel K is time independent, indicating that the rate at which clusters i and j combine is dependent only on their concentrations (which are time dependent) and time independent geometrical factors contained within the kernel K. This equation is therefore "mean-field"; that is, at no point in time are there are spatial correlations between clusters, regardless of their size. Notably, this equation then *assumes* that the system of particles is dilute. If this were not the case, a cluster's motion could not be sufficiently randomized before collision with another cluster for the kernel to be spatially isotropic. Implicitly, we see that the "structure" of clusters is static once formed and that all clusters of the same size have common morphological properties leading to the same collision kernel.

5.1.1 Kernels:

A difficulty in using the Smoluchowski equation is that few analytical solutions exist for the time-dependent size distributions of clusters for various choices of the coagulation kernel, except for those that are not physically realistic. Complete analytical solutions include those for the following kernels:

$$K(i,j) = C \text{ (constant) [74]} \tag{5.2}$$

$$K(i,j) = i + j \text{ (additive) [75]} \tag{5.3}$$

$$K(i,j) = ij \text{ (multiplicative) [76]} \tag{5.4}$$

From physical considerations, one can think of the kernel as a kind of collisional flux with:

$$K(i,j) = v_{ij} A_{coll,ij} \tag{5.5}$$

where v_{ij} is the relative velocity of clusters i and j, and $A_{coll,ij}$ is the collision cross section of these clusters. As an example, in the free-molecular regime of particle motion, the average thermal velocity (not rms) of particles is given by:

$$v_i = \sqrt{\frac{8k_B T}{\pi m_i}} \tag{5.6}$$

Then the average relative velocity of particles of size i and j is given as:

$$v_{ij} = \sqrt{\frac{8k_B T}{\pi}\left(\frac{1}{m_i} + \frac{1}{m_j}\right)} \tag{5.7}$$

The collision cross section between particles i and j is:

$$A_{coll,ij} = \pi\left(\frac{d_i + d_j}{2}\right)^2 = \frac{\pi}{4}\left(d_i + d_j\right)^2 \tag{5.8}$$

Yielding:

$$K(i,j) = \sqrt{\frac{k_B T \pi}{2}}\sqrt{\frac{1}{m_i} + \frac{1}{m_j}}\left(d_i + d_j\right)^2 \tag{5.9}$$

Friedlander [3] writes this in an equivalent form for spherical particles:

$$K(i,j) = \left(\frac{3}{4\pi}\right)^{\frac{1}{6}}\sqrt{\frac{6k_B T}{\rho}}\sqrt{\frac{1}{V_i} + \frac{1}{V_j}}\left(V_i^{\frac{1}{3}} + V_j^{\frac{1}{3}}\right)^2 \tag{5.10}$$

where V_i is the volume of particle i. The brownian kernel can be derived in a similar fashion (using diffusion constants) as [3]:

$$K(i,j) = \frac{2k_B T}{3\mu}\left(\frac{1}{V_i^{\frac{1}{3}}} + \frac{1}{V_j^{\frac{1}{3}}}\right)\left(V_i^{\frac{1}{3}} + V_j^{\frac{1}{3}}\right) \tag{5.11}$$

where μ is the viscosity of the fluid in which the particles are suspended. Unfortunately, these kernels have no known analytical solution.

The traditional approach to solving the Smoluchowski equation for the above kernels involves the use of a computer to find numerical solutions to the problem. Alternatively, Monte Carlo methods are also used to find solutions to the kinetic equation for various choices of the kernel. This technique involves the creation of a system of particles whose motions are governed by the chosen diffusion constant or that move ballistically (as in a dilute gas). The size distributions are seen to evolve dynamically as the simulation proceeds. We have employed the second of these techniques to each of these conditions within this work.

As we shall see below, the aggregation kernel is well-approximated as time-independent as long as the system remains dilute (no correlations between locations of clusters). As the clusters grow, the system can become crowded, and the mean-field assumption for collision can no longer hold, except possibly with a rescaling based on the cluster volume fraction [40]. In the case of cluster crowding, the form of the kernel inevitably changes, leading to changes in coagulation kinetics, size distributions, and cluster morphologies[9,64].

5.1.2 Cluster Fragmentation:

In addition to the aggregation of particles into clusters, it is also possible for clusters once formed to fragment into pieces. Fragmentation can be a result of a number of causes, including shear forces, cluster-cluster collisions, strong electrostatic interactions, etc. The occurrence of fragmentation is particularly possible when the binding potential between particles is small (a few k_BT). Such fragmentation can lead to the possibility of local ordering and crystallization. As a system evolves, different structural forms can become obvious at different length scales.

When both aggregation and fragmentation occur within a system, one can write a more comprehensive version of the Smoluchowki equation, including the fragmentation kernel explicitly:

$$\frac{\partial n(i,t)}{\partial t} = \frac{1}{2}\sum_{j=1}^{i-1}\left[K(i-j,j)n(i-j,t)n(j,t) - F(i-j,j)n(i,t)\right] - \sum_{j=1}^{\infty}\left[K(i,j)n(i,t)n(j,t) - F(i,j)n(i+j,t)\right] \tag{5.12}$$

where F(i,j) is the concentration independent rate at which a cluster of size i+j fragments into clusters of size i and j. In the same manner as the aggregration kernel K, F is independent of time. This inherently assumes that a cluster's breaking into pieces is not affected or initiated by the presence other clusters, since the population of clusters of various sizes neighboring the cluster in question *will* be time dependent.

In most cases, the fragmentation kernel is assumed to be (like the aggregation kernel previously) a homogeneous function of the size of the fragmenting cluster. In this case, for a multiplicative factor x:

$$F(xi,xj) = x^{\alpha}F(i,j) \tag{5.13}$$

where α is the fragmentation homogeneity, independent of the aggregation homogeneity λ.

If we write the Smoluchowski Equation in continuum form:

$$\frac{\partial n(i,t)}{\partial t} = \frac{1}{2}\int_0^i [K(i-j,j)n(i-j,t)n(j,t) - F(i-j,j)n(i,t)]dj - \int_0^\infty [K(i,j)n(i,t)n(j,t) - F(i,j)n(i+j,t)]dj \tag{5.14}$$

The n's are all functions of t. The moments of the size distribution are defined as:

$$M_i(t) = \sum_{k=1}^{\infty} k^i n(k,t) \tag{5.15}$$

or in continuous form:

$$M_i(t) = \int_0^\infty u^i n(u,t)du \tag{5.16}$$

From the Smoluchowski equation we obtain [77]:

$$\frac{dM_i(t)}{dt} = \frac{1}{2}\int_0^\infty\int_0^\infty [(u+v)^i - (u^i + v^i)][K(u,v)n(u,t)n(v,t) - F(u,v)n(u+v,t)]dudv \tag{5.17}$$

Specifically for the 2nd moment:

$$\frac{dM_2}{dt} = \int_0^\infty\int_0^\infty uv[K(u,v)n(u,t)n(v,t) - F(u,v)n(u+v,t)]dudv \tag{5.18}$$

From the scaling form of the cluster size distribution we have:

$$n(u,t) = \frac{M_1}{{s_p}^2}\phi\left(\frac{u}{s_p}\right) = \frac{M_1}{{s_2}^2}\phi\left(\frac{u}{s_2}\right) \quad (\text{for } s_2 = \frac{M_2}{M_1}) \tag{5.19}$$

For now let $s = s_2$

We define x,y as:

$u = sy,\ v = sx$

$$n(u,t) = \frac{M_1}{s^2}\phi(y),\ n(v,t) = \frac{M_1}{s^2}\phi(x) \tag{5.20}$$

Using the homogeneity of the kernels:

$$K(u,v) = s^{\lambda}K(x,y) \tag{5.21}$$

$$F(u,v) = s^{\alpha}F(x,y) \tag{5.22}$$

we obtain:

$$\frac{dM_2}{dt} = {M_1}^2 s^{\lambda}\int_0^{\infty}\int_0^{\infty}\left[xyK(x,y)\phi(x)\phi(y)\right]dxdy - M_1 s^{\alpha+2}\int_0^{\infty}\int_0^{\infty}xyF(x,y)\phi(x+y)dxdy \tag{5.23}$$

Now let: $K(x,y) = k_a\Psi(x,y),\ F(x,y) = k_f\Omega(x,y)$

where k_a and k_f are the aggregation and fragmentation rate constants, respectively. Then:

$$\frac{dM_2}{dt} = {M_1}^2 s^{\lambda}k_c\int_0^{\infty}\int_0^{\infty}xy\Psi(x,y)\phi(x)\phi(y)dxdy - M_1 s^{\alpha+2}k_f\int_0^{\infty}\int_0^{\infty}xy\Omega(x,y)\phi(x+y)dxdy \tag{5.24}$$

Defining the time independent parameters:

$$\begin{aligned} A &= \int_0^{\infty}\int_0^{\infty}xy\Psi(x,y)\phi(x)\phi(y)dxdy \\ B &= \int_0^{\infty}\int_0^{\infty}xy\Omega(x,y)\phi(x+y)dxdy \end{aligned} \tag{5.25}$$

we have:

$$\frac{dM_2}{dt} = M_1\left(M_1 s^{\lambda}k_c A - s^{\alpha+2}k_f B\right) \tag{5.26}$$

since $s = s_2 = \frac{M_2}{M_1}$ and M_1 is a *constant* by particle conservation, being the total number

of particles within the system:

$$\frac{ds}{dt} = \frac{1}{M_1}\frac{dM_2}{dt} \tag{5.27}$$

thus;

$$\frac{ds}{dt} = M_1 s^{\lambda} k_c A - s^{\alpha+2} k_f B \tag{5.28}$$

If we let $s^* = \frac{s}{s_0}$ and $t^* = \frac{t}{t_0}$ (s_0, t_0 arbitrary constants) we obtain:

$$\frac{s_0}{t_0}\frac{ds^*}{dt^*} = M_1 s^{*\lambda} {s_0}^{\lambda} k_c A - s^{*\alpha+2} {s_0}^{\alpha+2} k_f B \tag{5.29}$$

$$\frac{ds^*}{dt^*} = M_1 t_0 s^{*\lambda} {s_0}^{\lambda-1} k_c A - t_0 s^{*\alpha+2} {s_0}^{\alpha+1} k_f B \tag{5.30}$$

When $\frac{ds^*}{dt^*} \to 0$, s^* goes to its steady state equilibrium value s^*_{equil}. s_0 is an arbitrary constant as defined above, so we specify it as the equilibrium value of s, namely s_{equil}. Now $s_{equil} = s^*_{equil} s_0$, so $s^*_{equil} = 1$. Therefore:

$$s_0 = \left(M_1 \frac{k_c A}{k_f B} \right)^{\frac{1}{\alpha+2-\lambda}} \tag{5.31}$$

t_0 is also an arbitrary constant which we define here as:

$$t_0 = \frac{{s_0}^{1-\lambda}}{M_1 k_c A} \tag{5.32}$$

With these definitions, t_0 becomes a *characteristic* time for the approach of the average cluster size to s_0. The above differential equation then simplifies to:

$$\frac{ds^*}{dt^*} = s^{*\lambda} - s^{*\alpha+2} \tag{5.33}$$

The evolution of the average scaled cluster size can be seen then as a combination of two effects, the aggregation of clusters leading to growth and the fragmentation of larger clusters into smaller ones.

5.1.2.1 Examples:

Example 1: $\lambda = 0, \alpha = 0$

$\lambda = 0$ holds for Brownian diffusion. The choice of $\alpha = 0$ indicates the rate of fragmentation is independent of cluster size (all clusters fragment at the same rate). In this case:

$$\frac{ds^*}{dt^*} = 1 - s^{*2} \tag{5.34}$$

With the appropriate initial and final conditions set on s^*:

$$s^*(t^* = 0) = 0, \;\; s^*(t^* \to \infty) = 1 \tag{5.35}$$

we have:

$$s^* = \frac{e^{2t^*} - 1}{e^{2t^*} + 1} \tag{5.36}$$

Example 2: $\lambda = 0, \alpha = -1$

Here we have aggregation via Brownian diffusion with a fragmentation rate that *decreases* with cluster size. This could be the case for fragmentation that occurs on the surface of a cluster, since the surface/volume ratio decreases with increasing cluster size. In this case:

$$\frac{ds^*}{dt^*} = 1 - s^* \tag{5.37}$$

$$s^* = 1 - e^{-t^*} \tag{5.38}$$

Example 3: $\lambda = 0, \alpha = 1$

Again we look at aggregation via Brownian diffusion but with a fragmentation rate that increases linearly with cluster size. Here the fragmentation rate increases

linearly with the number of particles in a cluster; equivalently it increases linearly with the number of particle-particle bonds. This could occur thermally driven fragmentation of tenuous (low Df) fractal aggregates for which the average coordination number is 2; fragmentation could occur with equal probability at any point within the cluster. Here:

$$\frac{ds^*}{dt^*} = 1 - s^{*3} \tag{5.39}$$

No closed form solution exists for s^* in terms of t^*. However, the inverse form does exist:

$$t^* = \frac{1}{6}\ln\left[\frac{1-s^{*3}}{\left(1-s^*\right)^3}\right] + \frac{1}{\sqrt{3}}\left\{\tan^{-1}\left[\frac{1}{\sqrt{3}}\left(2s^*+1\right)\right] - \frac{\pi}{6}\right\} \tag{5.40}$$

Example 4: $\lambda = \frac{1}{2}, \alpha = 1$

A λ value of $\frac{1}{2}$ is indicative of ballistic type aggregation, where clusters move along linear paths between collisions with each other; $\alpha = 1$ has the same interpretation as previously. Then:

$$\frac{ds^*}{dt^*} = s^{*\frac{1}{2}} - s^* \tag{5.41}$$

$$s^* = \left(1 - e^{-t^*}\right)^2 \tag{5.42}$$

A graph of each of the above relations is shown in Fig 5.1:

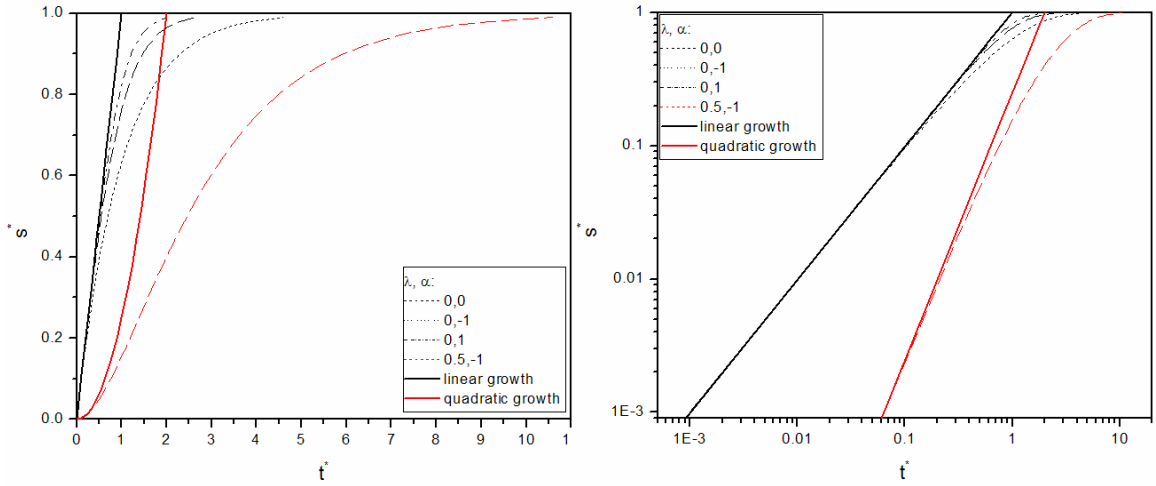

Fig 5.1: Approach to equilibrium mean cluster size with various choices of aggregation and fragmentation homogeneities.

Comparison:

Each of the above combinations of aggregation/fragmentation kernel leads to the same steady state value of $s^* = 1\,(s = s_0)$. For the Brownian aggregation kernels, the approach to this value is the fastest for the choice of $\alpha = 1$ as is clearly seen in the linear plot; since for this case fragmentation can occur at any point within the cluster, the trend follows our intuition. The early time growth of s^* in each case is governed by the aggregation homogeneity, since early on, clusters are small and no significant amount of fragmentation can occur. From the log-log plot one can see that for the Brownian kernels, the early time growth of s^* is linear, while for the ballistic kernel, the initial growth is quadratic, both well known results. Despite this fact, it is the ballistic kernel which, contrary to intuition, is the *slowest* to approach an equilibrium value.

5.2 Fractal aggregates:

5.2.1 Fractal Dimension and Mass Scaling:

For coalescing particles, there is a simple relationship between the linear size and aggregate volume. For non-coalescing particles, the morphology (structure) of aggregates is a complicated matter. This complexity affects the coagulation kernel given above. It is well known that in the dilute limit (low particle volume fraction), aggregation of particles for which there is no fragmentation or restructuring leads to the formation of clusters whose mass to size relationship is a power law with a nonintegral power Df . That is:

$$N = k_0 \left(\frac{R_g}{r_0} \right)^{Df} \tag{5.43}$$

Where N is the mass (number of monomers contained) of the aggregate, k_0 a unitless prefactor on the order of 1 [78], R_g the radius of gyration of the cluster, and r_0 the radius of the monomers making up the aggregate. R_g is calculated for the aggregate as:

$$MR_g^{\,2} = R_g^{\,2} \sum_{i=1}^{N} m_i = \sum_{i=1}^{N} m_i \mathbf{r}_{ic}^{\,2} \tag{5.44}$$

With $\mathbf{r}_{ic} = \mathbf{r}_i - \mathbf{r}_{com}$ the relative displacement from the aggregate center of mass $\mathbf{r}_{com}$.

Df represents a "fractal dimension" for the aggregate, the power in the scaling law by which the mass of the aggregate varies as a function of it's linear size (here R_g). $Df < d$ for aggregates growing in d dimensional space, often significantly less. In the dilute limit for $d = 3$, $Df \approx 1.8$ for continuum regime aggregates (liquid or dense gas medium) and $Df \approx 1.9$ for the free-molecular (rarified gas medium).

Fractal aggregates are extended multi-branched structures with a spiderweb-like appearance. Fractals have the property of self-similarity (often incorrectly termed length

scale invariance) within a size range intermediate between the monomer radius and the radius of gyration. The property of self-similarity indicates that "focusing" on the fractal at different length scales does not alter the morphological appearance of the structures seen. In some sense, the aggregates that form in the continuum and free-molecular regimes are not "strictly" fractals. Perfect mathematical fractal objects have the same form for the relationship between mass and linear size as given above. Additionally, they have ideal length-scale invariance, indicating that focusing in on a subsection of the fractal at certain length scales can produce an image that *exactly* matches that found at higher length scales [79]. Such is the case of the famous Koch curve and Serpinski triangle (shown in Fig 5.2).

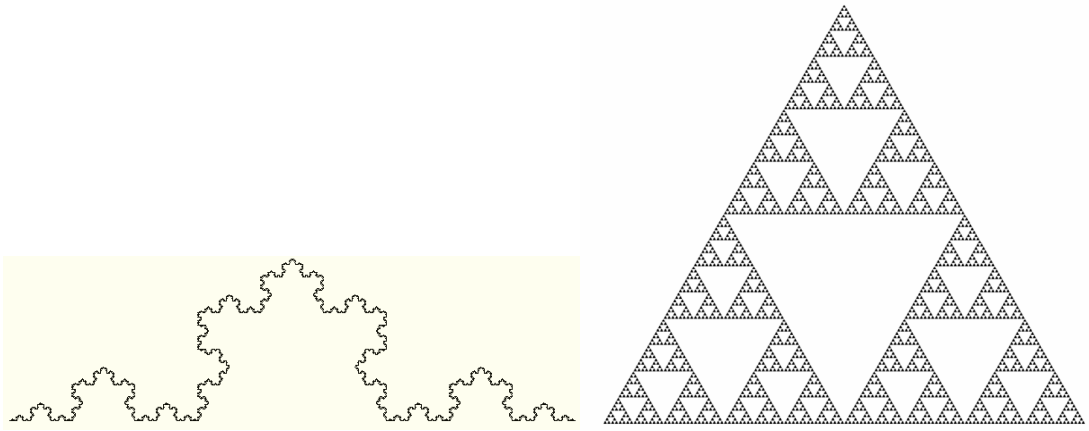

Fig 5.2: Koch curve and Serpinski triangle

Of course, fractal aggregates produced by diffusion or ballistic motion of particles do not have this property, due to the statistical nature of their motion.

From the above relationship we can determine the density profile of the aggregate. We first write the above mass radius relationship in a slightly different way:

$$M = k_p \left(\frac{R_p}{r_0} \right)^{Df} \tag{5.45}$$

Where k_p is a unitless constant related to k_0 and R_p is the "perimeter radius" of the fractal. R_p can be seen as a kind of enclosing radius for the aggregate, whose relationship to R_g is derived below. We could also write, for all $r < R_p$:

$$m(r) = k_p \left(\frac{r}{r_0} \right)^{Df} \tag{5.46}$$

to mean that the mass of the aggregate enclosed within a radius r goes as the above power law. Using this equation we see that the density ρ(r) can be given in 3D as:

$$\rho(r) = \frac{dm(r)}{dV} = \frac{1}{4\pi r^2} \frac{dm(r)}{dr} = \frac{k_p Df}{4\pi {r_0}^{Df}} r^{Df-3} \tag{5.47}$$

We can derive the relationship between R_p and R_g since for a continuous object:

$${R_g}^2 = \frac{\int_V r^2 \rho(r) dV}{\int_V \rho(r) dV} \tag{5.48}$$

From this we see that:

$${R_g}^2 = \frac{Df}{Df+2} {R_p}^2 \tag{5.49}$$

or:

$$R_p = \sqrt{\left(1 + \frac{2}{Df}\right)} R_g \tag{5.50}$$

Now $k_p \left(\frac{R_p}{r_0} \right)^{Df} = k_0 \left(\frac{R_g}{r_0} \right)^{Df}$ so that:

$$k_p = \left(1 + \frac{2}{Df}\right)^{-\frac{Df}{2}} k_0 \tag{5.51}$$

As an example, for continuum regime fractals, $k_0 \approx 1.3$ [78], which yields $k_p \approx 0.67$ for $Df = 1.8$.

5.2.2 Determination of Fractal Dimension:

It is desirable to be able to determine the fractal dimension of aggregates formed during the evolution of the system from its initial monomer state. The calculation of the fractal dimension of a system of aggregates can be done in a number of ways.

5.2.2.1 Ensemble Method:

As a system evolves, a size distribution of aggregates will develop from it's initially monodisperse (single size) state. At late times, a wide variety of cluster sizes will exist in the system. For this ensemble of aggregates, the above M to R_g relationship will hold (see equation ….). Thus, if we plot log M vs. log R_g for each cluster in the system, data points will lie on or around a best fit line:

$$\log(M) = Df \log\left(R_g\right) + \left(\log k_0 - Df \log r_0\right) \tag{5.52}$$

From the slope and intercept of the line we obtain Df and k_0. In reality, there will be some spread around this best fit line. The following plot (Fig 5.3) shows an example of this procedure for a continuum regime DLCA system with monomer volume fraction $f_v = 0.001$ and initial particle number $N_0 = 10{,}000$ at a point in which there are $N_c = 120$ clusters remaining in the system:

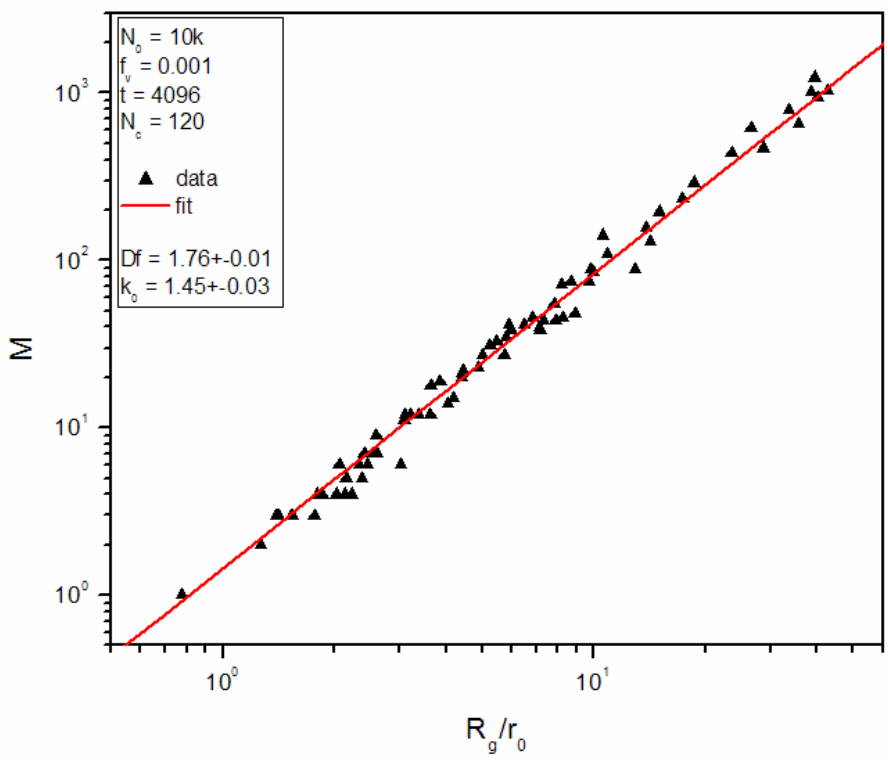

Fig 5.3: ensemble method of determining Df for a DLCA fractal aggregate

As can easily be seen, the power law behavior is quite evident, despite the spread around the best fit line. The slope of ~1.8 is in agreement with that of continuum regime aggregates, as is the value of the fractal prefactor k_0.

5.2.2.2 Onion-shell Method:

An alternative method for calculating the fractal dimension is to determine for each aggregate the relationship between the radius of a sphere whose center coincides with the center of mass of the aggregate and the mass enclosed within that sphere over a range of radii. From a log-log plot of this relationship, we can again determine the fractal dimension Df:

$$\log[m(r)] = k_p + Df \log\left(\frac{r}{r_0}\right) \tag{5.53}$$

The disadvantage to this method is that for each value of r chosen, the counting procedure must be performed for each aggregate within the system. This process requires significantly more computational time than the first method.

5.2.2.3 Structure Factor Method:

The above are real-space techniques for the determination of Df. As a companion tool to that used by experimental researchers in this field, a reciprocal-space method is often employed to determine Df from simulation data. This method is analagous to the experimental technique of static light scattering, namely the static structure factor. An excellent summary of this method is given in a review article by Sorensen [77]. For static light scattering, the important quantity is the scattered light intensity as a function of the scattered wave vector **q**. The scattered wave vector **q** is defined as:

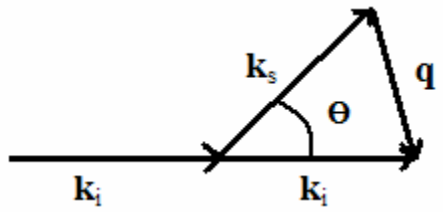

Fig 5.4: incident and scattered wave vectors.

$$\mathbf{q} = \mathbf{k}_i - \mathbf{k}_s \tag{5.54}$$

$\mathbf{k}_i$ = incident wave vector

$\mathbf{k}_s$ = scattered wave vector

$$|\mathbf{k}_i| = |\mathbf{k}_s| = \frac{2\pi}{\lambda} \tag{5.55}$$

$$|\mathbf{q}| = \frac{4\pi}{\lambda}\sin\left(\frac{\theta}{2}\right) \tag{5.56}$$

With the assumption of single-scattering by the monomers, *no multiple-scattering* occurs within the system. That is, all particles respond only to the incident EM field, not the scattered fields from other particles. In this case we have for the unitless scattering intensity I:

$$I(\mathbf{q}) = \left|\sum_{i=1}^{N_0} e^{-i\mathbf{q}\cdot\mathbf{r}_i}\right|^2 \tag{5.57}$$

$$I(q) = < I(\mathbf{q}) >_{spherical} \tag{5.58}$$

$\mathbf{r}_i$ = position of particle i

N_0 = total number of particles

The structure factor is then defined as:

$$S(q) = \frac{I(q)}{N_0{}^2} \tag{5.59}$$

The behavior of the structure factor is highly dependent on the range of q; q^{-1} is used to determine the structure of the system of particle over various length scales. Whenever a group of particles are within a distance on the order of q^{-1} of each other, they are effectively in phase ($\mathbf{q}\cdot(\mathbf{r}_i - \mathbf{r}_j) < 1$), and the scattering intensity goes as the square of the number of particles within the volume $V_q \sim q^{-3}$. For an average particle number density n, this gives the number of particles contained within this volume as:

$$N_q = nV_q \tag{5.60}$$

and:

$$I(q) \propto N_q{}^2 = \left(nV_q\right)^2 \propto n^2 q^{-6} \tag{5.61}$$

When particles (or clusters of particles) are further than q^{-1} from each other, they scatter with a *random* phase with respect to each other and the intensity goes as the number of particles (or clusters) adding randomly as is the case for Brownian motion for which $< x^2 > \propto N$ (# of steps). Thus for n_q contributing particles or clusters of particles:

$$I(q) \propto n_q \tag{5.62}$$

In summary:

$$I(q) = n_q N_q{}^2 \tag{5.63}$$

As a consequence of the Ewald-Oseen extinction theorem, only the *fluctuations in density* within the scattering volume give rise to scattering at nonzero angles [77]. An infinite lattice, for instance, has no nonzero angle scattering. This fluctuation in density is seen to occur at a *surface*, where the local environment of the scatterers differs from that of scatterers within the bulk. n_q then represents the number of q^{-1} sized groups needed to cover the surface of an object.

The lowest q *limit* of S(q) for an aggregate or system of aggregates can be understood by considering the entire system of N_0 monomers being contained within a single volume $(n_q = 1)$ of linear size $q^{-1} > L$, where L is the linear size of the container. These N_0 monomers will be in phase with each other, giving $N_q = N_0{}^2$. Then:

$$I(q) = n_q N_q{}^2 = N_0{}^2 \tag{5.64}$$

and

$$S(q) = \frac{I(q)}{N_0{}^2} = 1 \tag{5.65}$$

For small q values, one can rewrite the integral form of the structure factor to obtain a useful expansion. We write the density the density function as [77]:

$$n(\mathbf{r}) = \frac{\sum_{i}^{N_0} \delta(\mathbf{r} - \mathbf{r}_i)}{N_0} \tag{5.66}$$

Then:

$$S(\mathbf{q}) = \iint n(\mathbf{r}) n(\mathbf{r}') e^{i\mathbf{q}\cdot(\mathbf{r}-\mathbf{r}')} d\mathbf{r} d\mathbf{r}' = \left| \int n(\mathbf{r}) e^{i\mathbf{q}\cdot\mathbf{r}} d\mathbf{r} \right|^2 \tag{5.67}$$

In an isotropic setting, we can express the structure factor as a function of the scalar value q instead of the vector **q**:

$$S(q) = 4\pi \int g(u) \frac{\sin(qu)}{qu} u^2 du \tag{5.68}$$

with the density autocorrelation function $g(\mathbf{r})$:

$$g(\mathbf{r}) = \int n(\mathbf{r} - \mathbf{r}') n(\mathbf{r}') d\mathbf{r}' \tag{5.69}$$

An expansion of S(q) to 2nd order in q is then:

$$S(q) \approx 1 - \frac{q^2}{6} \int u^2 g(u) d\mathbf{u} = 1 - \frac{1}{3} q^2 R_g{}^2 \tag{5.70}$$

Thus when S(q) has fallen to a value of $\approx \frac{2}{3}$, $q \approx \frac{1}{R_g}$. This low-q range is known as the Guinier regime [80].

For a *solid* 3D object of linear size and $q^{-1} < R$, the number of scatterers within a q^{-3} volume goes as $N_q \propto nq^{-3}$, with n being the number density of scatterers within the object. The number of such q^{-3} volumes on the surface of the object goes as $n_q \propto \left(\frac{R}{q^{-1}} \right)^2$. Then:

$$I(q) \propto n^2 R^2 q^{-4} \tag{5.71}$$

and

$$S(q) \propto \frac{n^2}{N_0^{\,2}} R^2 q^{-4} \propto q^{-4} \tag{5.72}$$

For the structure factor of a sphere, cube, or any other regular 3D object, one obtains a -4 slope for its q-space S(q) envelope within this q-range as confirmed by experiment and simulation. This is a demonstration of Porod's law for a sphere or any other 3D object, a well-known result [80,81].

Let us consider the scattering from a single *fractal* cluster of gyration radius R_g [77]. As above, for $q^{-1} > R_g$, we have $S(q) = 1$. With an increase of q to the range $r_0 < q^{-1} < R_g$, we have a completely different scenario. In general, a fractal cluster may possess possibly different mass (D_m) and surface (D_s) fractal dimensions defined by:

$$N = k_o \left(\frac{R_g}{r_o} \right)^{Dm} \quad (\text{N = number of particles within the aggregate}) \tag{5.73}$$

$$N = k_s \left(\frac{R_g}{r_o} \right)^{Ds} \quad (\text{N}_\text{s} = \text{number of particles on the surface of the aggregate, } \text{k}_\text{s} \text{ constant}) \tag{5.74}$$

Consider a volume of linear size q^{-1} within the above defined q-range. Within it, there will be contained $N_{m,q}$ monomers:

$$N_{m,q} = k_m \left(\frac{q^{-1}}{r_0} \right)^{Dm} \quad (k_m = k_p \text{ used in perimeter radius relation above}) \tag{5.75}$$

We then determine the number of such q^{-1} sized regions on the surface of the aggregate:

$$n_{s,q} = k_s \left(\frac{R_g}{q^{-1}} \right)^{Ds} \tag{5.76}$$

which follows from the above definition of surface fractal dimension and the self-similarity property of fractals.

We see then that:

$$I(q) = n_{s,q} N_{m,q}{}^2 = k_s k_m{}^2 \left(qR_g\right)^{-2Dm+Ds} \left(\frac{R_g}{r_0} \right)^{2Dm} = k_s N^2 \left(qR_g\right)^{-2Dm+Ds} \tag{5.77}$$

However, in the case of fractal aggregates, $D_m = D_s = D_f$. This is tantamount to saying that every scatterer within a fractal aggregate exists on the surface, yielding:

$$I(q) = k_s N^2 \left(qR_g\right)^{-Df} \propto q^{-Df} \tag{5.78}$$

$$S(q) = k_s \frac{N^2}{N_0{}^2} \left(qR_g\right)^{-Df} \propto q^{-Df} \tag{5.79}$$

Often, scattering is done not from a single fractal aggregate, but rather from a system of aggregates. For a *system* of N_c randomly located (uncorrelated) aggregates with average nearest-neighbor separation R_{nn} and size R_g for the q range $q^{-1} < R_g < R_{nn}$ we have:

$$I_{system}(q) = \sum_{i=1}^{N_c} I_i(q) \tag{5.80}$$

That is, due to their random placement, each cluster contributes to the scattering, as if all the clusters represent a fluctuation in density. If we constrain our analysis to that of nearly monodisperse systems we have:

$$I_{system}(q) = N_c I_{clust}(q) \tag{5.81}$$

$$N_c = \frac{N_0}{N} \tag{5.82}$$

or:

$$I_{system}(q) = k_s N_0 N\left(qR_g\right)^{-2Dm+Ds} = k_s N_0 N\left(qR_g\right)^{-Df} \tag{5.83}$$

$$S_{system}(q) = k_s \frac{N}{N_0}\left(qR_g\right)^{-Df} \tag{5.84}$$

Therefore, a system of aggregates can also display the q^{-Df} behavior with the above condition on q met.

Another important q range for a system of aggregates is $R_{nn} < q^{-1} < L$. Within this range, each q^{-3} volume will contain on average nq^{-3} monomers, n being the number density of monomers in the system. n is related to the particle volume fraction as:

$$n = \frac{f_{v0}}{v_0} \text{ (v}_0 \text{ = monomer volume)} \tag{5.85}$$

Within each volume, all monomers will scatter in phase so that:

$$I(q) \propto \left(nq^{-3}\right)^2 = \frac{{f_{v0}}^2}{{v_0}^2} q^{-6} \tag{5.86}$$

In this case, it is only the surface groups which contribute to the scattering, as each q^{-3} within the bulk will be large enough to contain a statistically average number of particles, thus not representing a density fluctuation. The number of these q^{-3} volumes that lie on the surface of the system of linear size L is:

$$n_q = \frac{L^2}{q^{-2}} = L^2 q^2 \tag{5.87}$$

Each of these n_q volumes will scatter randomly with respect to each other. Therefore:

$$I(q) \propto \left(L^2 q^2\right)\left(\frac{{f_{v0}}^2}{{v_0}^2} q^{-6}\right) \propto q^{-4} \tag{5.88}$$

One sees that within this range of q, the scattering follows the same behavior as that of the 3D container.

For a system of aggregates, the q-range $R_g < q^{-1} < R_{nn}$ also exhibits interesting behavior in $S(q)$. In this case, the q^{-3} volume can enclose $N_q = N$ particles. There will be $n_q = N_c$ (number of clusters) contributing; each system cluster will contribute due to the random (uncorrelated) location of clusters within the system. For a monodisperse system, $N_c = \frac{N_0}{N}$. Thus:

$$I_{system}(q) \approx \frac{N_0}{N} N^2 = N_0 N \tag{5.89}$$

$$S_{system}(q) \approx \frac{N_0 N}{{N_0}^2} = \frac{N}{N_0} = \frac{1}{N_c} \tag{5.90}$$

both independent of q. We then expect to see a plateau in S(q) due to cluster growth as the system evolves for this q range. This is demonstrated in the graph of the evolving structure factor (Fig 5.5) for an aggregating system of 10^4 monomers at a volume fraction of 0.01:

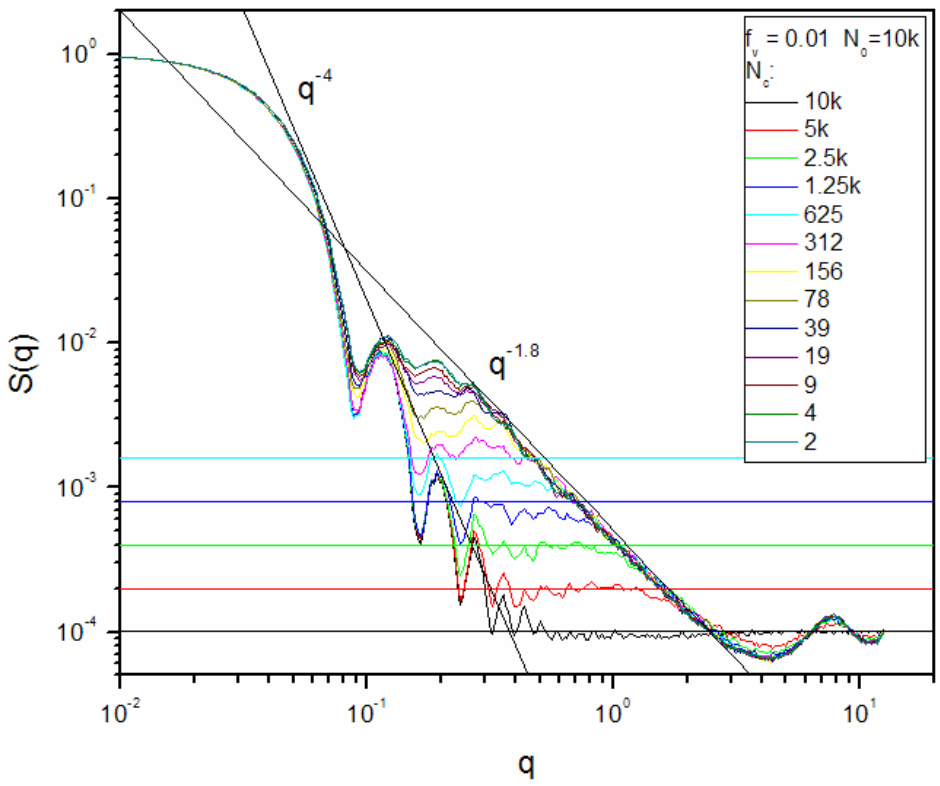

Fig 5.5: Evolving Structure factor of DLCA system with $f_v = 0.01$ showing aggregate Df. Plateaus indicate the number of clusters present at the time.

We do observe, as expected the q^{-4} and q^{-Df} ($Df = 1.8$) behavior in the proper ranges of q, with the extent of the q^{-Df} range increasing as R_g evolves. We also see the plateau at $S(q) \approx \frac{1}{N_c}$ (colored horizontal lines) for the first few simulation times. However, as the system evolves, $R_g \to R_{nn}$, and the condition $R_g < q^{-1} < R_{nn}$ becomes more difficult to meet. The agreement between the plateau prediction and that observed in S(q) therefore begins to fail. For very low f_v systems, this is less of an issue, as $R_g \prec\prec R_{nn}$ for a significant period of time as demonstrated in Fig 5.6 & 5.7 for the lower volume fraction $f_v = 0.001$.

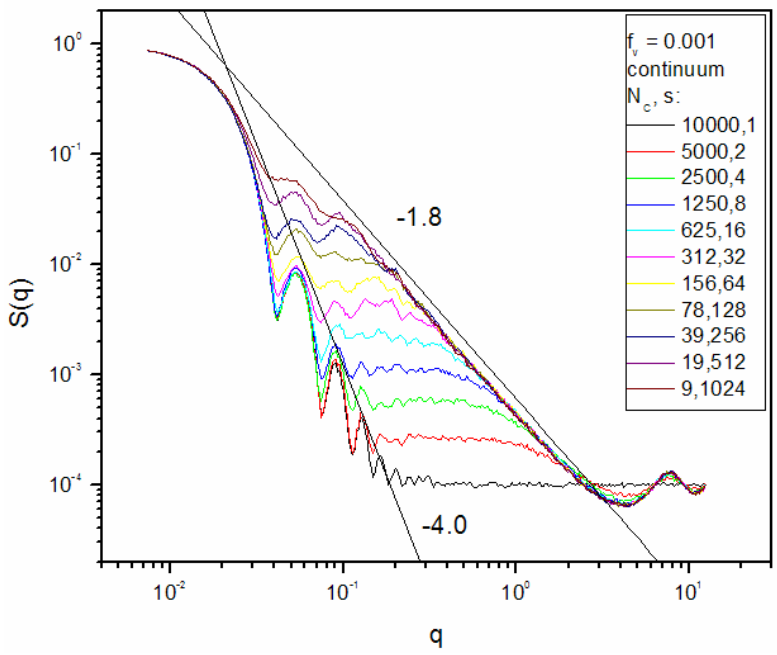

Fig 5.6: Evolving Structure factor of DLCA system with $f_v = 0.001$ showing aggregate Df. Plateaus indicate the number of clusters present at the time.

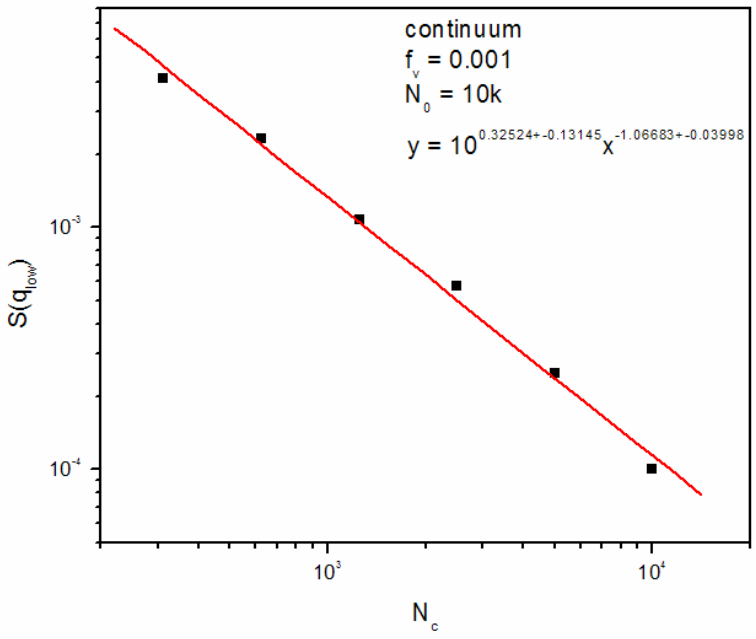

Fig 5.7: Plot of S(q) at plateau vs. N_c for system in Fig 5.5. -1 power law follows theory.

As expected, the plateau value for $S(q) \approx \frac{1}{N_c}$ for the first several simulation times shown.

For $q^{-1} < r_0$, we must be careful. In simulation studies, the particles often have *no internal structure* below the monomer size. That is, the monomer is seen as having a single property, a diameter $d = 2r_0 = 1$. In this case, for non-lattice scatterers, $n_q = N_s = N_0$. The number of scatterers contained within each q^{-3} volume is $N_q = 1$. Thus:

$$I(q) = 1^2 \cdot N_0 = N_0 \tag{5.91}$$

$$S(q) = \frac{1}{N_0} \tag{5.92}$$

both independent of q.

In Fig 5.8 we display the structure factor of a box filled with monomers both on a square lattice and randomly placed for $f_v = 0.01$.

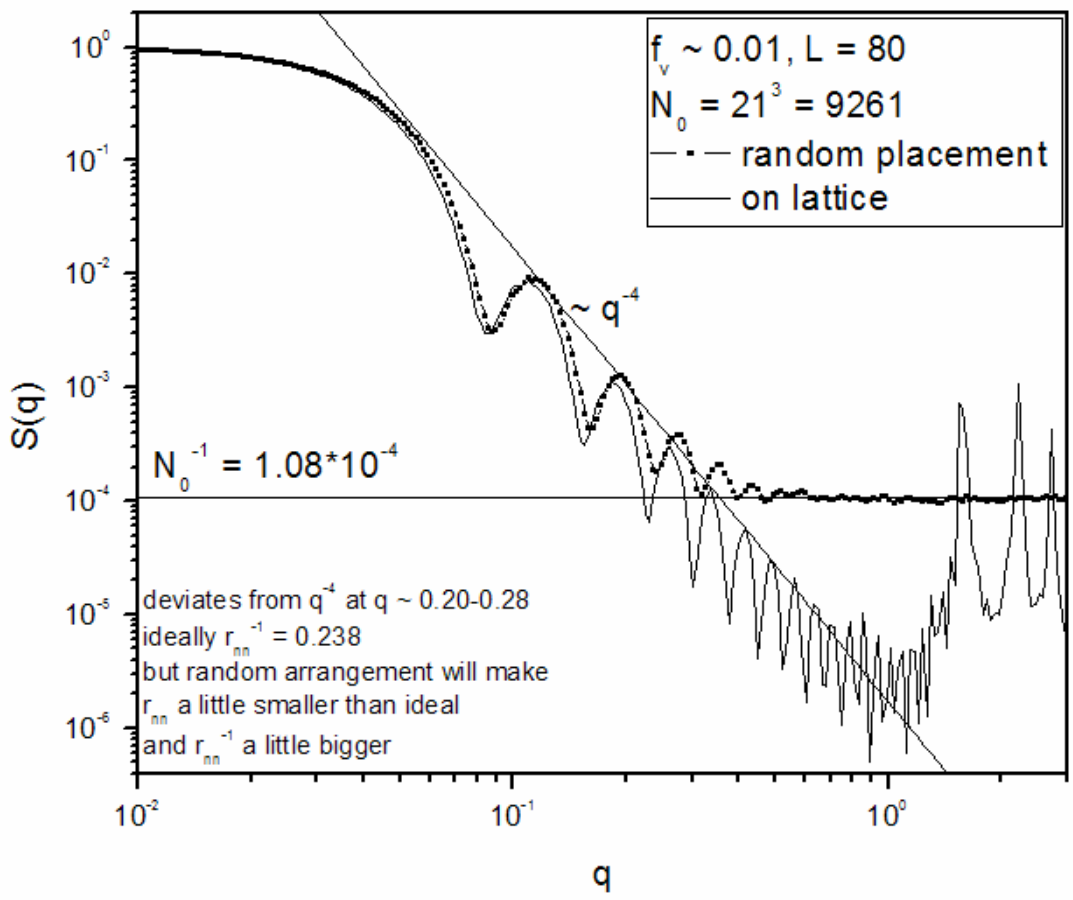

Fig 5.8: S(q) of cubes filled randomly with 9261 points and with points placed on a lattice with lattice spacing 4.

We note that as predicted, for both cases $S(q) \approx 1$ for $q < L^{-1}(0.0125)$.

For our lattice of points, the value of R_g of the system is 41.95 treating all lattice points with equal weight, leading to an expectation of $S(q) = \frac{2}{3}$ at $q = \frac{1}{41.95} = 0.0238$; we find $S(0.026) \approx 0.67$, in good agreement. For the randomly placed points, R_g takes on a value of ≈ 40.19, and we expect $S(q) = \frac{2}{3}$ at $q = \frac{1}{40.19} = 0.0248$; the actual q value where this occurs is ≈ 0.027, again agreeing well.

For $r_{nn} < q^{-1} < L$, $S(q) \propto q^{-4}$ in both cases. This q^{-4} dependence continues on until approximately the position of the first Bragg peak for the case of the lattice-placed scatterers at $q = \frac{2\pi}{a}(a = 4) \approx 1.57$. This continued agreement is due to the fact (as stated above) that only the surface contributes to the scattering in the lattice case, the bulk scatterers possessing a homogeneous environment.

For the case of random placement of scatterers, when $q \approx 0.2 - 0.3$, $q \approx r_{nn,ideal}^{-1}$, effectively the entire system represents fluctuations in the density and thus all scatterers contribute to the scattering. Therefore $S(q) \approx \frac{1}{N_0} \approx 1.08 \cdot 10^{-4}$, as expected.

Additionally, in the case of the randomly placed scatterers, $S(q) \approx \frac{1}{N_0}$ for $q^{-1} < r_0$, due to the lack of structure within the scatterers, as discussed previously.

For *experimental* systems, the monomers do have structure, that of solid 3D objects. In this case, each monomer scatters with $I_{mon}(q) \propto q^{-4}$. Again, all the scatterers will essentially lie on the surface so that for a single aggregate of N monomers:

$$I_{clust}(q) \propto Nq^{-4} \tag{5.93}$$

or for a system of aggregates containing N_0 monomers:

$$I_{system}(q) \propto N_0 q^{-4} \tag{5.94}$$

It is then clear that the structure can provide a wealth of information about fractal aggregates and in many ways, this is the preferred method of analyzing their complex structures.

5.3 Gelation:

One consequence to the fact that $Df < d$ is that as fractal aggregates grow, they begin to occupy more system volume. That is, an aggregate fills more "space" than the sum of its monomers. In Fig. 5.9 we see such a *space-filling* 3D fractal aggregate made up of 2339 monomers formed from an initial monomer volume fraction of 0.001 under continuum diffusion limited conditions:

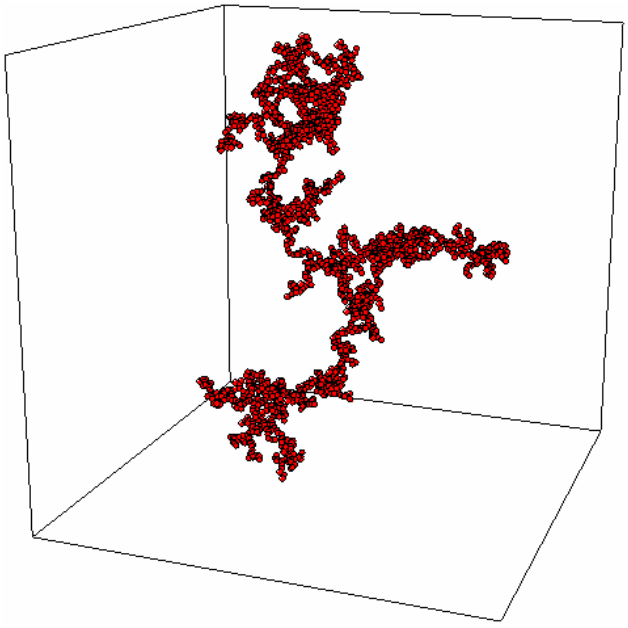

Fig 5.9: 3D DLCA fractal aggregate with N = 2339. Fractals *fill more space* than their constituent particles

Let us take $d = 3$ as an example. If the initial state of the system is a random dispersion of N_0 monomers, the initial volume fraction can be given as:

$$f_{v0} = \frac{N_0 v_0}{V_{system}} \tag{5.95}$$

where $v_0 = \frac{4\pi}{3} r_0^{\,3}$ is the volume of a monomers of radius r_0. The "effective" volume of an aggregate containing N monomers is:

$$v_N = \frac{4\pi}{3} R_{p,N}^{\,3} = \frac{4\pi}{3}\left(1+\frac{2}{Df}\right)^{\frac{3}{2}} R_{g,N}^{\,3} \tag{5.96}$$

Assuming that the system remains monodisperse for all times (all N_c aggregates within a system are of the same size N), we have the effective cluster volume fraction of the system:

$$f_{vc} = \frac{N_c v_N}{V_{system}} \tag{5.97}$$

Using the above relation:

$$N = k_p\left(\frac{R_{p,N}}{r_0}\right)^{Df} = k_0\left(\frac{R_{g,N}}{r_0}\right)^{Df} \tag{5.98}$$

and combining, we have:

$$f_{vc} = \frac{N_0}{V_{system}}\frac{v_N}{N} = \frac{N_0}{V_{system}}\left(\frac{4\pi}{3k_0}\right)\left(1+\frac{2}{Df}\right)^{\frac{3}{2}} r_0^{\,Df} R_{g,N}^{\,3-Df} = \frac{f_{v0}}{k_0}\left(1+\frac{2}{Df}\right)^{\frac{3}{2}}\left(\frac{R_{g,N}}{r_0}\right)^{3-Df} \tag{5.99}$$

Since $Df < 3$, the growth of $R_{g,N}$ with time inevitably leads to the increase of the effective volume fraction of the system, due to it's power law of $3 - Df > 0$. In the absence of fragmentation and restructuring, and with a sufficient number of monomers in the system, it is inescapable that a single system spanning cluster will form. This process is known as gelation. It has been observed both experimentally[9] and in simulation[40].

The term gelation is often ambiguously used for both the formation of a system-spanning cluster and the state of a system in which all particles are incorporated into a

single system-spanning cluster. Of course, these are not identical, and caution must be used in determining which of these states is implied.

5.3.1 Conditions for Gelation:

The conditions required for gelation can be defined in a number of ways. We present four cases.

5.3.1.1 Case 1: $R_{nn} = 2R_p$

In case 1, the condition for gelation relates the average perimeter radius R_p of the aggregates to the average nearest-neighbor separation of the aggregates in the system R_{nn}:

$$R_{nn} = 2R_p \tag{5.100}$$

$$R_{nn,ideal} = 2\left(\frac{f_{v0}}{f_{cp}}\right)^{-\frac{1}{3}}\left(\frac{N_0}{N_c}\right)r_0 = 2\left(\frac{f_{v0}}{f_{cp}}\right)^{-\frac{1}{3}} Nr_0 \tag{5.101}$$

As stated above, this is the ideal case, where the clusters exist on a close-packed lattice. In other words, $R_{nn,ideal} > R_{nn,actual}$. Due to the random initial placement of monomers and the stochastic nature of the thermal motion (ballistic or diffusional), the positions of the clusters at any point in time will not be on a lattice, but rather random. We can then say that:

$$R_{nn} = 2\beta\left(\frac{f_{v0}}{f_{cp}}\right)^{-\frac{1}{3}} Nr_0 \tag{5.102}$$

where $\beta < 1$, though on the order of 1. We then have the tools necessary to find the conditions on N and R_g for gelation in case 1.

We find:

$$N_{gel} = k_0^{\frac{3}{3-Df}} f_{v0}^{-\frac{Df}{3-Df}} \left[\beta^3 \left(1 + \frac{2}{Df} \right)^{-\frac{3}{2}} f_{cp} \right]^{\frac{Df}{3-Df}} = C_{N,gel} \left[\beta^3 \left(1 + \frac{2}{Df} \right)^{-\frac{3}{2}} f_{cp} \right]^{\frac{Df}{3-Df}} \quad (5.103)$$

$$R_{g,gel} = r_0 k_0^{\frac{1}{3-Df}} f_{v0}^{-\frac{1}{3-Df}} \left[\beta^3 \left(1 + \frac{2}{Df} \right)^{-\frac{3}{2}} f_{cp} \right]^{\frac{1}{3-Df}} = C_{R,gel} \left[\beta^3 \left(1 + \frac{2}{Df} \right)^{-\frac{3}{2}} f_{cp} \right]^{\frac{1}{3-Df}} \quad (5.104)$$

5.3.1.2 Case 2: $R_{nn} = 2R_g$

For case 2, we consider that gelation may not occur as soon as clusters touch each other at their perimeters but rather interdigitate to the point where $R_{nn} \approx 2R_g$. It is likely, for low fractal dimension aggregates that such interpenetration will happen before aggregation actually occurs. For this case we find:

$$N_{gel} = C_{N,gel} \left[\beta^3 f_{cp} \right]^{\frac{Df}{3-Df}} \quad (5.105)$$

$$R_{g,gel} = C_{R,gel} \left[\beta^3 f_{cp} \right]^{\frac{1}{3-Df}} \quad (5.106)$$

5.3.1.3 Case 3: $f_{vc} = 1$

In case 3, the condition for gelation is seen as the point at which the volume of the clusters becomes the same as the system volume. In other words, the entire system becomes occupied by clusters ($f_{vc} = 1$). For this case:

$$N_{gel} = C_{N,gel} \left[\left(1 + \frac{2}{Df} \right)^{-\frac{3}{2}} \right]^{\frac{Df}{3-Df}} \quad (5.107)$$

$$R_{g,gel} = C_{R,gel} \left[\left(1 + \frac{2}{Df} \right)^{-\frac{3}{2}} \right]^{\frac{1}{3-Df}} \quad (5.108)$$

5.3.1.4 Case 4: $f_{vc} = f_{3d,perc}$

Finally, case 4 identifies that gelation is similar to site percolation, the formation of a system spanning cluster[82]. In 3 dimensions, a site volume fraction of $f_{3d,perc} \approx 0.312$ leads to percolation of the system half of the time. For these conditions, "gelation" will be seen to occur when $f_{vc} = f_{3d,perc}$ or:

$$N_{gel} = C_{N,gel}\left[f_{3d,perc}\left(1+\frac{2}{Df}\right)^{-\frac{3}{2}} \right]^{\frac{Df}{3-Df}} \tag{5.109}$$

$$R_{g,gel} = C_{R,gel}\left[f_{3d,perc}\left(1+\frac{2}{Df}\right)^{-\frac{3}{2}} \right]^{\frac{1}{3-Df}} \tag{5.110}$$

Each of the above cases leads to a different prediction for N_{gel} and $R_{g,gel}$ for a particular set of system conditions, though in each case we have N_{gel}, $R_{g,gel}$ being a power law of the initial volume fraction with identical powers respectively for all cases . As an example, we take $\beta = 1$, $k_0 = 1.3$, $Df = 1.8$. We display these prediction in Fig. 5.10.

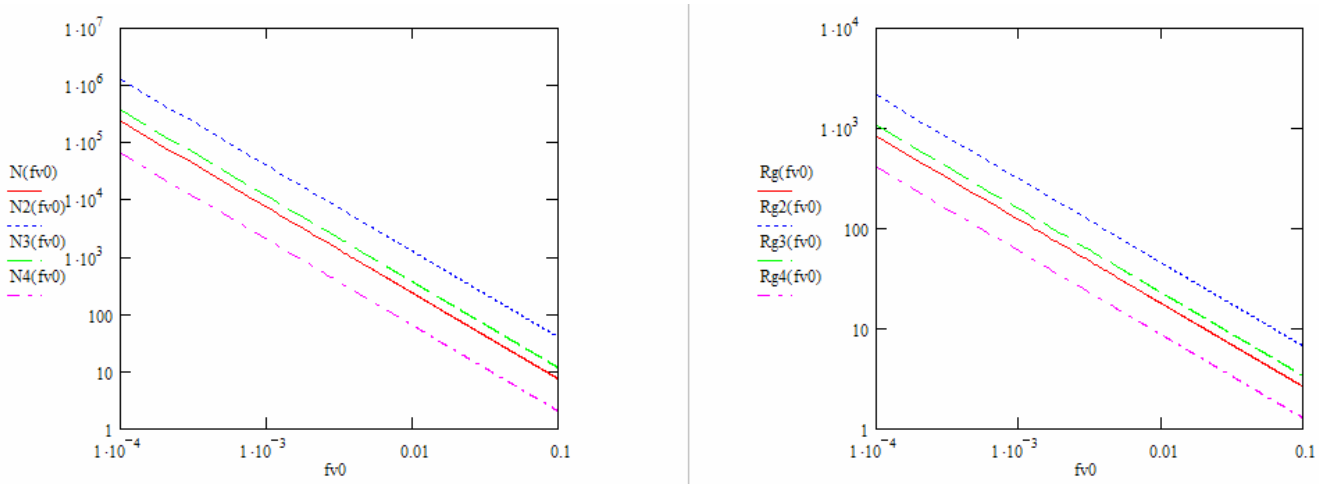

Fig 5.10: N_{gel} and $R_{g,gel}$ predictions vs. f_v for each of the four gelling conditions.

We note that the predictions from lowest to highest for N_{gel} and $R_{g,gel}$ vary by no more than about a factor of 10.

5.4 Aggregation Kinetics:

5.4.1 Kinetic Exponent from Homogeneity:

For aggregation between like-sized clusters, the Smoluchowski equation gives the following simplified form for size k clusters:

$$\frac{dn_k}{dt} = -K(k,k){n_k}^2 \tag{5.111}$$

We note that for this case:

$$n_k(t) = \frac{n_1(0)}{k(t)} \tag{5.112}$$

and

$$k(t=0) = 1 \tag{5.113}$$

Also, for homogeneous aggregation we can write that:

$$K(ki,kj) = k^{\lambda}K(i,j) \text{ (by homogeneity)} \tag{5.114}$$

$$K(k,k) = k^{\lambda}K(1,1) = C_0k^{\lambda} \tag{5.115}$$

$$\frac{d\left(\frac{n_1(0)}{k}\right)}{dt} = -C_0k^{\lambda}\left[\frac{n_1(0)}{k}\right]^2 \tag{5.116}$$

$$-\frac{n_1(0)}{k^2}\frac{dk}{dt} = -C_0{n_1}^2(0)k^{\lambda-2} \tag{5.117}$$

$$k^{-\lambda}dk = C_0n_1(0)dt \tag{5.118}$$

$$\frac{1}{1-\lambda} k'^{1-\lambda}\Big|_1^k = C_0 n_1(0) t \tag{5.119}$$

$$k = \left[1 + (1-\lambda) C_0 n_1(0) t\right]^{\frac{1}{1-\lambda}} = \left[1 + \frac{C_0 n_1(0)}{z} t\right]^z \tag{5.120}$$

with:

$$z = \frac{1}{1-\lambda} \tag{5.121}$$

For small t we expand k to a series:

$$k \approx 1 + C_0 n_1(0) t + \frac{1}{2} \frac{z-1}{z} C_0{}^2 n_1{}^2(0) t^2 + \ldots \approx 1 + C_0 n_1(0) t \tag{5.122}$$

or:

$$k - 1 \propto t \tag{5.123}$$

Thus, regardless of the homogeneity of the aggregation, for early times, a plot of $k-1$ should be linear with t.

As $t \to \infty$:

$$k \approx \left[\frac{C_0 n_1(0)}{z}\right]^z t^z = C_z t^z \tag{5.124}$$

We see that after a sufficient time, the average cluster size increases as a power law of t with a kinetic exponent z, thereby connecting the homogeneity of the coagulation kernel with the kinetics of the coagulation.

5.4.2 Kinetics for Various Regimes:

The values of the homogeneity and kinetic exponent are functions of the regime of particle motion.

For continuum regime diffusion limited cluster-cluster aggregation (DLCA or Brownian diffusion between collisions), we use the above form of the brownian kernel to determine the initial aggregation rate for the ensemble of monomers at the beginning of aggregation. For spherical particles, $K(1,1)$ is independent of particle size v_i, i.e. $K(N,N) = K(1,1)$. By homogeneity then $\lambda = 0$ and consequently $z = 1$. From the above equation(5.11) we obtain:

$$K(1,1) = \frac{8k_B T}{3\eta} \tag{5.125}$$

where η is the viscosity of the medium. For Monte Carlo DLCA simulations, a monomer is typically allowed to diffuse one diameter in one time step. By the diffusion equation:

$$< x^2 > = 2dDt \text{ (in d dimensions)} \tag{5.126}$$

$$< x^2 > = 6Dt \text{ (in 3D)} \tag{5.127}$$

One obtains:

$$D_0 = \frac{1}{6} \text{ (in units of } \frac{d_0^{\,2}}{t_{MC}}) \tag{5.128}$$

for monomers.

Since the monomer diffusion constant in physical units is:

$$D_0 = \frac{k_B T}{6\pi\eta r_0} \tag{5.129}$$

we see that:

$$K(1,1) = 16\pi r_0 D_0 = \frac{8}{3}\pi r_0 = \frac{4}{3}\pi \tag{5.130}$$

since for all single sized simulations $d_0 = 2r_0 = 1$. For the initial size distribution of monomers (assuming binary collisions):

$$\frac{dn_1}{dt} = -K(1,1)n_1{}^2 \tag{5.131}$$

In simulation studies of aggregation kinetics, it is often the scaled average size which is used as a measure of aggregate growth with time. The scaled average size is defined as:

$$s_{scale} = \frac{1}{N_c(t)} - \frac{1}{N_0} \tag{5.132}$$

The advantage of this parameter is that its initial value is 0 and for N_0 large, $s_{scale} \to 1$ as aggregation proceeds $\left(N_c(t) \to 1\right)$. It is related to the average size $s_1(t) = \frac{N_0}{N_c(t)}$ as:

$$s_1 - 1 = N_0 s_{scale} \tag{5.133}$$

Initially, the size distribution is a monodisperse collection of monomers so for early times:

$$s - 1 \approx \frac{1 - \frac{n_1(t)}{n_1(0)}}{1 + \frac{n_1(t)}{n_1(0)}} \tag{5.134}$$

Then for the time derivative:

$$\frac{ds_{scale}}{dt} = -2\frac{L^3}{N_0{}^2}\left[1 + \frac{n_1(t)}{n_1(0)}\right]^{-2}\frac{dn_1}{dt} \tag{5.135}$$

and

$$\frac{ds_{scale}}{dt}(t=0) = -\frac{1}{2}\frac{L^3}{N_0{}^2}\frac{dn_1}{dt}(t=0) = \frac{1}{2}\frac{L^3}{N_0{}^2}\frac{4\pi}{3}n_1{}^2(0) = \frac{2\pi}{3L^3} = \frac{4f_{v0}}{N_0} \tag{5.136}$$

Fig 5.11 is of s_{scale} for a range of volume fractions along with the early time linear theoretical prediction. Agreement between the two improves with decreasing volume fraction. This, of course, is due to the fact that the use of the Brownian kernel assumes

that collisions are *diffusion limited*, that is, the motion of clusters *between collisions* is well described as diffusional. In the dilute limit, the angular probability distribution of collisions between particles lacks any correlation to the initial particle positions. For high initial volume fractions, this condition does not hold well, and one observes significant deviation from the simplified theory, especially at late times.

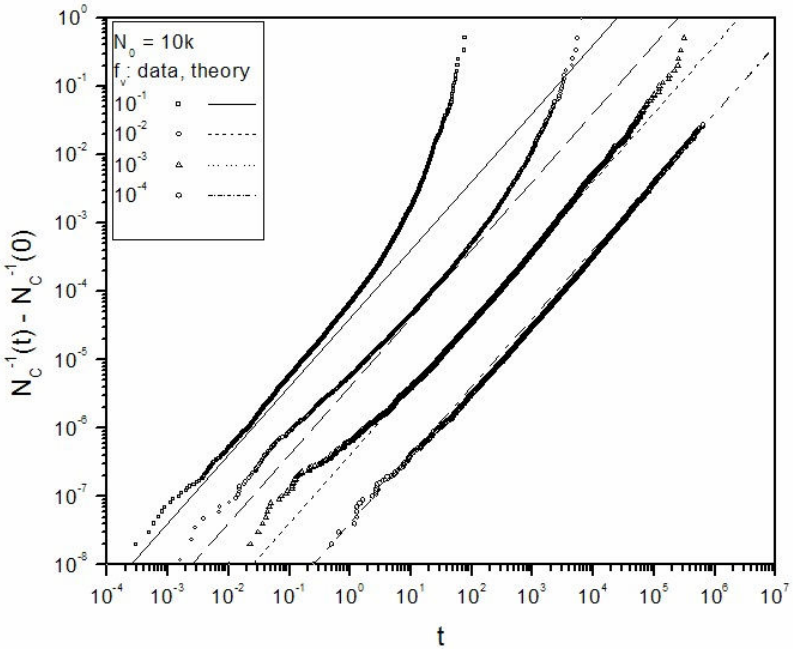

Fig 5.11: Kinetics graphs for various values of f_v. Theory predicts well the initial aggregation rate. Higher volume fractions deviate from this linear behavior at increasingly earlier times.

For low volume fractions, the agreement is quite good over a large range of time, as can be seen from the kinetics for $f_v = 10^{-4}$. In any case, for a large enough system, regardless of the volume fraction, there will be a time at which the aggregation kinetics *speeds up* $(z > 1)$ [40,64]. We see this kinetic increase for each of the first three simulated volume fractions above; to observe this for $f_v = 10^{-4}$ requires a larger system

size. The increase in z is due to the fact that as fractal clusters grow, they continue to occupy more system volume, leading to inevitable gelation as discussed above. Near the onset of gelation, the dilute limit assumption of position uncorrelated collisions cannot hold; this leads to an inevitable change in the kernel homogeneity and consequently the kinetic exponent.

5.4.3 Kinetics for Fractal Aggregates:

The resulting aggregates for the above volume fractions are fractal in nature. It is somewhat surprising that the Brownian prediction for the aggregation of *spherical* particles fits the results for fractal aggregates so well (especially at very low volume fractions). For continuum diffusion limited aggregation of clusters the kernel is shown below; it holds for both spherical and nonspherical clusters, though for nonspherical aggregates, the meaning of R is not immediately clear:

$$K(i,j) = \frac{2k_B T}{3\mu}\left(\frac{1}{R_i} + \frac{1}{R_j}\right)\left(R_i + R_j\right) = 4\pi D_{ij} R_{ij} \tag{5.137}$$

In any case, for collisions between like sized clusters $\left(R_i \approx R_j\right)$, the kernel is *independent* of particle size and the exact scaling law between the mass and radius. Therefore, $K(i,i) = K(1,1)$, $\lambda = 0$, and $z = 1$ for spherical, fractal, or other type aggregates in the *diffusion limited* regime. This is precisely what we see in the above graphs.

A simple scaling rule, based on the assumption of collsions between like-sized clusters is that:

$$K \propto N^{\lambda} \propto v_{clust-clust} A_{coll} \text{ (free molecular)} \tag{5.138}$$

$$\propto D_{clust-clust} R_{coll} \text{ (diffusional)} \tag{5.139}$$

In the free molecular regime, the Maxwell-Boltzmann distribution determines cluster velocities:

$$< v_{clust} >= \sqrt{\frac{8k_B T}{\pi m}} \text{ and } v_{rms} = \sqrt{\frac{3k_B T}{m}} \tag{5.140}$$

$$v_{clust-clust} \propto \frac{1}{\sqrt{N}} \tag{5.141}$$

$$A_{coll} \propto R_g{}^2 \propto N^{\frac{2}{Df}} \text{ [83]} \tag{5.142}$$

This is a general result holding for fractal $(Df < 3)$ or solid $(Df = 3)$ objects.

For spherical aggregates (coalescing particles on collision):

$$K \propto N^{-\frac{1}{2}} N^{\frac{2}{3}} = N^{\frac{1}{6}} \tag{5.143}$$

$$\lambda = \frac{1}{6} \rightarrow z = \frac{6}{5} = 1.2 \tag{5.144}$$

For Fractal aggregates:

$$K \propto N^{-\frac{1}{2}} N^{\frac{2}{Df}} = N^{\frac{2}{Df}-\frac{1}{2}} \tag{5.145}$$

Aggregates formed at the dilute limit within the free molecular regime are known to have $Df \approx 1.9$ [41-43]. Therefore:

$$\lambda = \frac{2}{Df} - \frac{1}{2} \approx 0.55 \rightarrow z \approx 2.2 \tag{5.146}$$

We see then that the kinetic exponent in the free molecular regime is highly dependent on the morphology of the resulting aggregates through the value of Df. Specifically, the higher the fractal dimension, the lower the homogeneity and resulting kinetic exponent. This is perhaps not altogether surprising since low Df objects are branched, extended

objects with large collision cross sections, and are more likely to collide than compact high Df aggregates of the same mass.

Fig 5.12 is a graph of s_{scale} vs. t (log-log) for a free-molecular ballistic system of 10^5 monomers at a volume fraction of 10^{-3}:

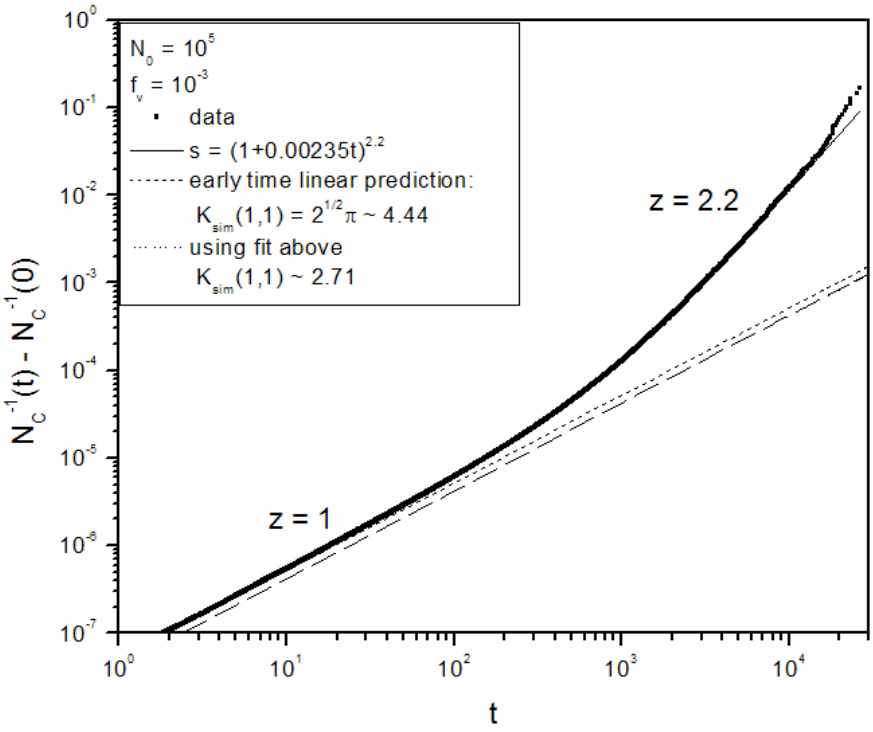

Fig 5.12: kinetics for a ballistic system at $f_v = 0.001$ showing both early time linearity and late time nearly quadratic kinetics.

At early times, $s_{scale} \propto t$ as the low t limit of the aggregate growth above predicts. When $s > 2$, $s_{scale} \approx \frac{1}{N_0}$, and the system begins to transition over to a $z \approx 2.2$ as predicted.

Fitting to the theoretical curve for s over all time works quite well, though the value of K(1,1) varies slightly from that expected from theory.

5.5 Cluster Size Distributions:

Under the assumption that the fractional concentration of particles within a certain size range $V \pm \Delta V$ (discrete) or $V \pm dV$ (continuous) is a function *only* of the normalized particle volume ($x = \frac{V}{s}$), we have[3]:

$$n(V,t)\frac{\Delta V}{M_0} = f(x)\Delta x \text{ (discrete)} \tag{5.147}$$

$$n(V,t)\frac{dV}{M_0} = f(x)dx \text{ (continuous)} \tag{5.148}$$

$$\Delta x = \frac{\Delta V}{s} \text{ (discrete)} \tag{5.149}$$

$$dx = \frac{dV}{s} \text{ (continuous)} \tag{5.150}$$

where:

$$M_0 = \sum_{all} n(V,t)\Delta V \ (discrete) = \int_0^\infty n(V,t)dV \ (continuous) \ (0^{th} \text{ moment}) \tag{5.151}$$

$$M_1 = \sum_{all} n(V,t)V\Delta V \ (discrete) = \int_0^\infty n(V,t)VdV \ (continuous) \ (1^{st} \text{ moment}) \tag{5.152}$$

or generally:

$$M_p = \sum_{all} n(V,t)V^p\Delta V \ (discrete) = \int_0^\infty n(V,t)V^p dV \ (continuous) \ (p^{th} \text{ moment}) \tag{5.153}$$

$$s = \frac{M_1}{M_0} \tag{5.154}$$

Rearranging leads to:

$$n(V,t) = \frac{M_0^{\,2}}{M_1} f(x) \tag{5.155}$$

or:

$$n(V,t) = M_1 s^{-2} f(x) \tag{5.156}$$

More generally, we can write [34,77]:

$$n(V,t) = M_1 s_p^{\,-2} f(x) \tag{5.157}$$

where:

$$s_p = \frac{M_p}{M_{p-1}} \tag{5.158}$$

$$x = \frac{V}{s_p} \tag{5.159}$$

This distribution is termed the "scaling distribution" [3, 84]. It can be separated into three distinct components. The first piece is the first moment of the size distribution, M_1; this is the total number of monomers in the system. If no particles are added to the system during the aggregation process, M_1 will be independent of time. The second piece is the inverse of the square of the average cluster volume, which varies with time. The third is a time independent function of the normalized particle volume. We see then that all of the time dependence of the size distribution is contained within the average cluster volume.

If we allow a system of particles to aggregate for sufficient time to obtain the scaling distribution, we can plot $n(V,t)s_p^{\,2}$ vs. $\frac{V}{s_p}$ and the resulting curve should be independent of time. Since aggregation within a system normally begins with a system of monomers, it will take some time before the system approaches this steady-state scaled

size distribution. After the system has reached this point, further plots should all lie along the same curve. This of course breaks down if gelation begins to set in, since the approach to gelation is marked by a change in the homogeneity constant. Here the above conditions for the scaling distribution fail.

For homogeneous aggregation kernels the scaling function for large x can be written in the following form as found by van Dongen & Ernst [84]:

$$f(x) = Ax^{-\lambda} e^{-\alpha x} \tag{5.160}$$

with λ the kernel homogeneity as defined above.

The scaling distribution has several important properties[77]:

$$M_i(t) = M_1 s_p{}^{i-1} m_i \tag{5.170}$$

with:

$$m_i = \int_0^\infty x^i f(x)dx = A\alpha^{\lambda-i-1}\Gamma(i+1-\lambda) = m_{i-1} \text{ (i}^{\text{th}}\text{ moment of scaling function)} \tag{5.171}$$

$$\alpha = p - \lambda \tag{5.172}$$

$$m_1 = 1 \text{ (by normalization)} \tag{5.173}$$

$$A = \frac{\alpha^{2-\lambda}}{\Gamma(2-\lambda)} \tag{5.174}$$

$$s_i = s_1 \frac{i-\lambda}{1-\lambda} \text{ (i}^{\text{th}}\text{ average size)} \tag{5.175}$$

Chapter 6 - Results: Aggregation in Aerosols:

Here we present the results of research into aggregation phenomena within aerosols. This regime is characterized by nonspecific particle interactions such as van der Waals, leading to irreversible aggregation on particle collision. The topic of Diffusion Limited Cluster Aggregation (DLCA) in two and three dimensions from initially dilute (low volume fraction) to dense (high volume fraction) is covered. Specific attention is given to kinetics, size distributions, and cluster morphologies, including superaggregate structures observed during gelation. An imminently useful scaling argument is presented and applied successfully to several regimes of motion, including the "Epstein" regime. Regime crossover from ballistic to Epstein is explored, unexpectedly yielding kinetic exponents nearly identical to continuum values for specific sets of system conditions.

6.1 Diffusion Limited Cluster Aggregation in Two-Dimensional Systems - Dilute to Dense:

6.1.1 Introduction:

For comparison to the work of other researchers in 3-dimensional DLCA systems [36-38], a series of 2-dimensional DLCA simulations were done. Simulations were run using the above described OLMC (Off-Lattice Monte Carlo) algorithm with $N_0 = 250{,}000$ monomers in a square PBC system box. The system sizes were adjusted to give a range of area fractions f_v from initially dilute (0.01) to dense (0.32); overall area fractions were $f_v = 0.01, 0.02, 0.04, 0.08, 0.16, and\ 0.32$. Simulation results were averaged over 5 trials for each area fraction, with $f_v = 0.04 - 0.32$ ending when $N_c = 10$ (number of clusters) and $f_v = 0.01, 0.02$ ending when $N_c = 100$ (due to computer time constraints). Parameters studied included kinetics, kernel homogeneity, and size-distributions of evolving aggregates.

6.1.2 Kinetics:

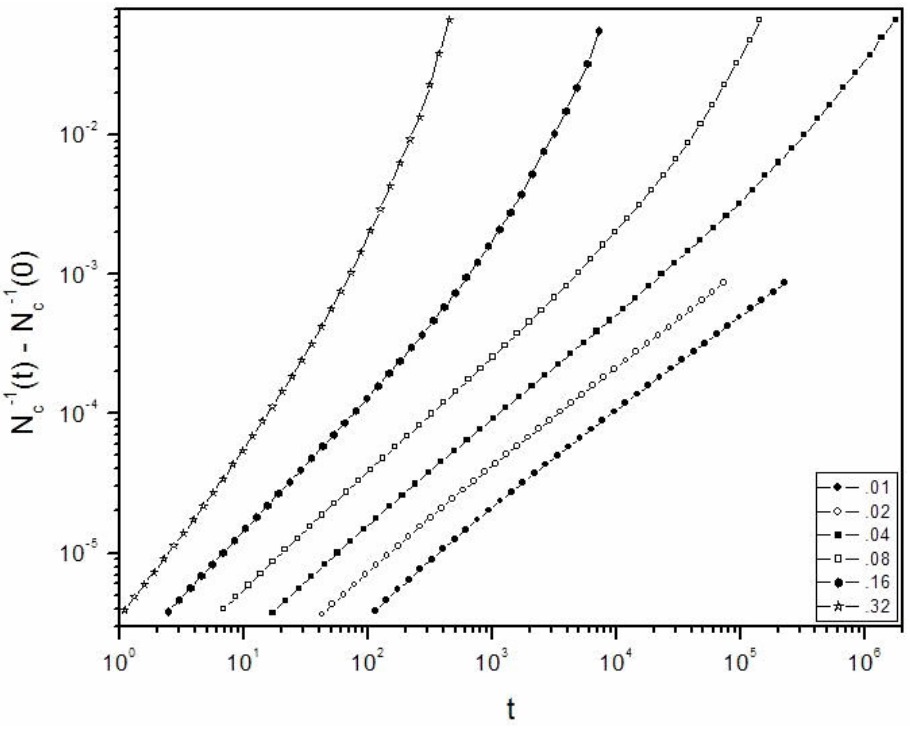

Fig 6.1: 2D DLCA kinetics for a range of volume fractions

Fig. 6.1 shows the results for 2d DLCA kinetics in terms of the scaled average cluster size: $s_{scale} = \frac{1}{N_c(t)} - \frac{1}{N_0}$ vs. t_{MC} for all area fractions. Results are shown beginning at a simulation time when the average cluster size N is 2. Previous to this time, as described earlier, linear kinetics are expected and observed regardless of the kinetic kernel.

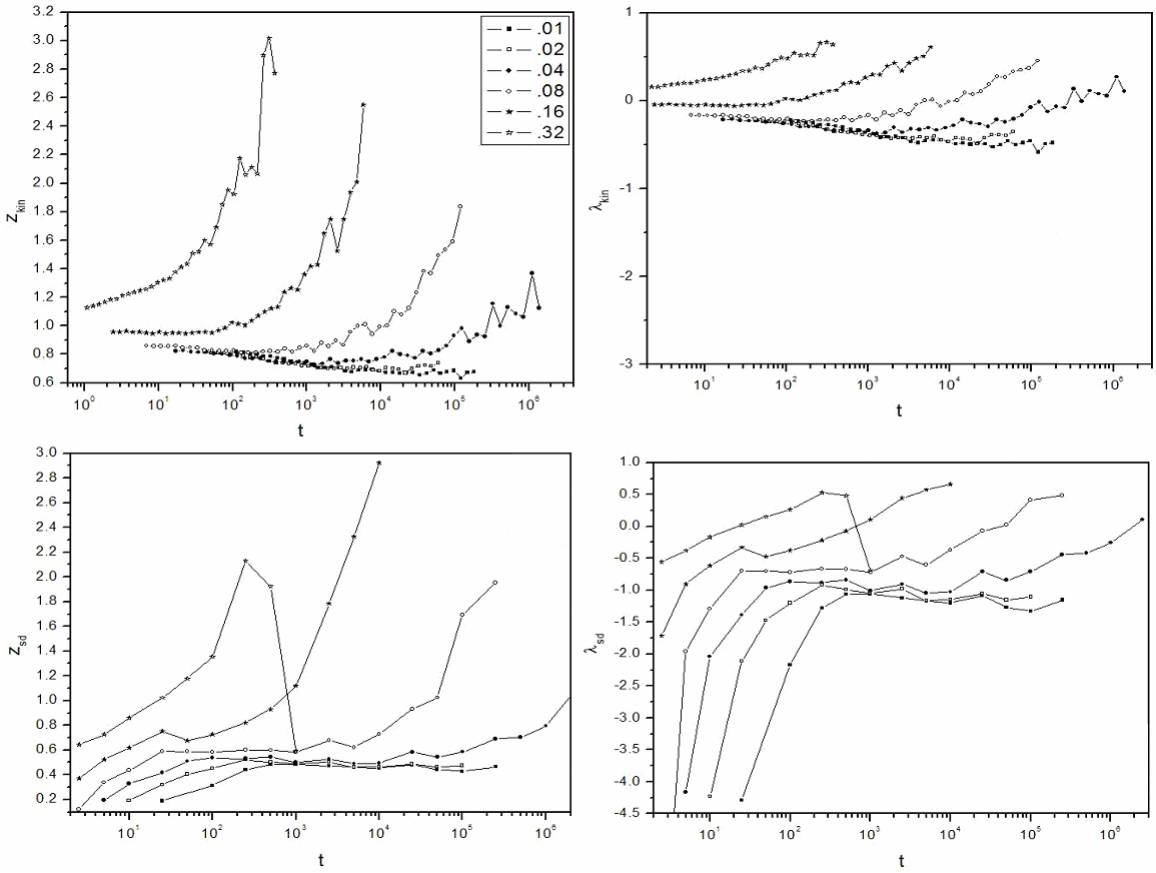

Fig 6.2: (a-d) (top left - bottom right) z and λ found from both kinetics and CSD data for 2D DLCA aggregation.

A corresponding graph of kinetic exponent z_{kin} vs. time is given in Fig. 6.2a, a graph of the time derivative of s_{scale} from Figure (1). As can be seen from Figure 6.2a, the value of z_{kin} begins in the range 0.8-0.9 for area fractions of 0.01 to 0.08; the systems are still evolving from their early time linear kinetics. In the case of $f_v = 0.01, 0.02$, z_{kin} falls to ≈ 0.7 as the aggregation proceeds; no increase in kinetics is seen at late times. Scaling arguments (above) yield an expectation for a steady-state value of $z \approx 0.59$ for 2d dilute-limit DLCA using $Df = 1.45$, the accepted value [37]. Recent MD simulations at intermediate f_v have also yielded $z \approx 0.69$, in agreement with these results [54]. For

$f_v = 0.04$, z starts with a slow descent to from $z \approx 0.8$ to $z \approx 0.75$ which then turns to a steady rise to $z \approx 1.2$ at late times. For $f_v = 0.08$ the kinetic exponent first falls slowly from $z \approx 0.85$ to $z \approx 0.80$ and then steadily rises to $z \approx 1.8$ at late times. As f_v is increased to 0.16 the initial $z \approx 0.95$ is maintained for some time before rising swiftly to ≈ 2.5 without any significant decrease. For $f_v = 0.32$, z starts at 1.1 and rises to ~ 3 monotonically. For the higher area fractions studied $(0.04 - 0.16)$, unexpectedly, there is a period of time for which the kinetics *is* power law in nature, with a z *higher than that expected in the dilute limit*.

Other researchers having studied DLCA aggregation in 3 dimensions also notice the same *enhancement in z* at late times as we do in our 2d simulations for $f_v \geq 0.04$ [40, 64]. Likely, the same enhancement would also have been observed in our case for $f_v = 0.01, 0.02$ if the simulations had been carried out to a later time. We, as they, attribute this to the significant amount of *cluster crowding* that occurs at late times in the system; as noted previously, this is inevitable due to the fact that $Df < d$ leading to gelation at late times.

Figure 6.2b shows the corresponding graph of the homogeneity constant:

$$\lambda_{kin} = \frac{1}{1 - z_{kin}} \tag{6.1}$$

obtained from cluster kinetics data. For the lowest area fractions (0.01,0.02), $\lambda_{kin}(t \to \infty) \approx -0.5$; scaling predictions place this value at ≈ -0.69. λ_{kin} for other area fractions follow the same general trend as that for z_{kin} given above:

6.1.3 CSD:

Cluster size distribution data was used to calculate the homogeneity constant (λ_{sd}) through fitting of size distribution data to the scaling form and values for the kinetic exponent (z_{sd}) using the relation:

$$z_{sd} = \frac{1}{1-\lambda_{sd}} \tag{6.2}$$

The corresponding graphs are shown in Figs. 6.2c and 6.2d. The trend of the z_{sd} for each value of f_v is very similar to that obtained from the kinetics data; one can easily see the kinetic exponent rising as the aggregation proceeds, the system proceeding from a relatively diffuse to cluster-dense state. This similarity is also seen in the trend of the λ_{sd}. However, z_{kin} seems to exceed z_{sd} by between 0.2 and 0.3 for area fractions $0.01 - 0.16$ and as much as 0.4 to 0.5 for area fraction 0.32. The "dilute-limit" value found for z_{sd} is ≈ -0.5 vs. $z_{kin} \approx 0.7$. In 3D, the agreement is better between the two [64], and it seems apparent that the mean-field estimate is less accurate in describing the 2D aggregation process. This is not entirely unexpected, as mean field predictions for critical exponents are known to work better at higher dimension, as in the Ising Model. One also notices the anomalous trend for area fraction 0.32 to have z_{sd} actually decrease at late times. This may have been brought about by the onset of gelation and worsening statistics as $N_c \to 0$. The trend for this downward turn can also be seen at the very end of z_{kin} for the same area fraction.

6.1.4 Scaling form:

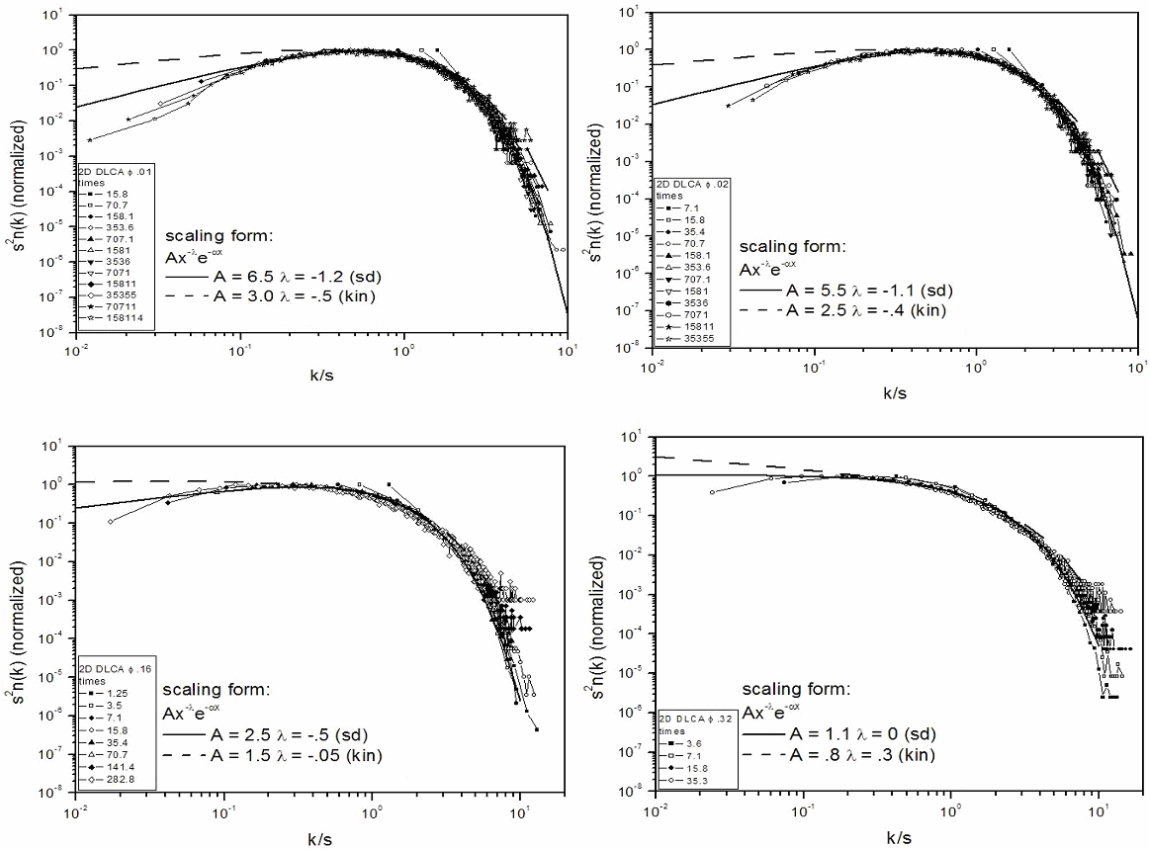

Fig 6.3: (a-d) (top left - bottom right) CSD with scaling form for various 2D DLCA volume fractions.

Cluster Size Distributions for the two highest and two lowest f_v values are shown in Figures 6.3(a-d). These distributions follow a scaling form as can be seen clearly when the vertical axis is $s^2n(k)$ and the horizontal axis is k/s where k is the cluster size (binned) and s is the average cluster size $\left(\frac{M_1}{M_0}\right)$. The solid and dashed lines for each area fraction represent lines fit to the scaling form $Ax^{-\lambda}e^{-\alpha x}$ where $x = \frac{k}{s}$ for the simulations using values for λ from the kinetics and cluster size distributions. The solid line represents the fit using λ_{sd} (size distribution data) and the dashed line represents the

fit using λ_{kin} (kinetics data). In all cases, the size distribution data seems to provide the best fit. This seems reasonable as the value of λ_{sd} obtained from the distributions would be expected to fit the cluster size distribution data better than λ_{kin}, which was obtained from the kinetics data.

Conclusion:

In summary, we see that the lowest area fractions in 2D DLCA give kinetic results in good agreement with both scaling predictions and the work of other researchers. Additionally, there is agreement between the kinetic and size-distribution data in the general evolution of the system. The mean-field approximation on which the relationship between the homogeneity and kinetic exponent is based is weaker in 2D than in 3D as evidenced by the slight but noticeable variance in steady state value of z and λ predicted.

6.2 *Kinetic and Morphological Studies of DLCA in Three Dimensions Leading to Gelation - Simulation and Experiment:*

6.2.1 Introduction:

Here we present the analysis of 3D DLCA Aggregation for a range of volume fractions from 0.001 to 0.200, specifically studying the kinetics and morphologies of clusters formed. The morphologies of clusters are analyzed using two of the above described techniques, namely the static structure factor and ensemble mass fractal dimension. In addition a third technique, *perimeter analysis*, is used and shown to give consistent results with those of the other two methods [85]. Results indicate a volume fraction dependent crossover from dilute DLCA type aggregates of $D_f \approx 1.8$ to dense percolated type gel superaggregates of $D_f = 2.6$ consistent with other simulation and experimental studies [64,86]. Our simulated systems are each comprised of $2 \cdot 10^5$ monomers.

6.2.2 Kinetics and Gelation:

In Fig 6.4 we display the growth of the scaled average cluster size for our range of volume fractions:

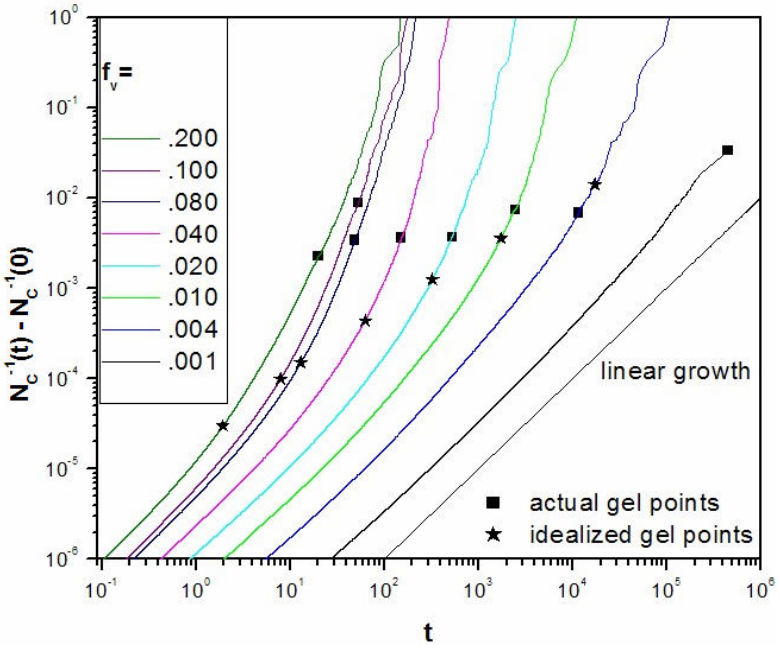

Fig 6.4: Kinetics of 3D DLCA at various f_v including ideal and actual gel points.

Actual and ideal gel points (based on N_{gel} from case 3 assumption in the gelation theory section above) are shown. As expected, the lowest volume fractions yield near linear growth, while at higher volume fractions, growth is linear for ever decreasing time intervals (if at all) due to the onset of cluster crowding; this is consistent with increased kinetics found in other simulation studies [40,64].

Note also that the ideal gel time underestimates the actual simulation value by a factor of ≈ 10 for the highest volume fraction (0.20), but becomes increasingly more accurate at lower volume fractions. Concurrently, the actual scaled average cluster size at gelation is higher than that predicted by the above *monodisperse* theory for the higher volume fractions. These two findings indicate that for high volume fraction systems, gelation is not well modeled as a process occurring in a monodisperse system but rather due to erratic growth of large clusters in systems with a high degree of *polydispersity*. By

the time gelation occurs, there are a few large clusters left with perhaps a small number of smaller clusters present. This is consistent with the picture of static site percolation in 3D[82]. For the lowest volume fractions modeled, there is good agreement between theory and simulation, indicating that our monodisperse theory is a good model of gelation in low volume fraction systems. This is perhaps fortunate as most experimental situations involve volume fractions that are significantly *below* those modeled here.

6.2.3 Df (Ensemble Method):

Using the above described ensemble method to determine Df, we plot in Fig 6.5 log-log R_g vs. N for 3 volume fractions, each at a point where $N_c = 192$ clusters remain in the system:

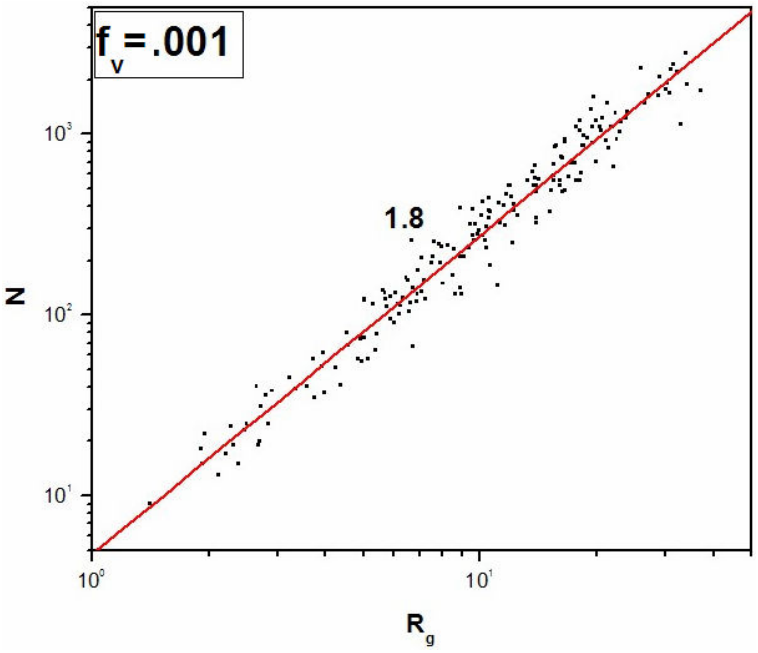
f_v =.001
1.8
N
R_g

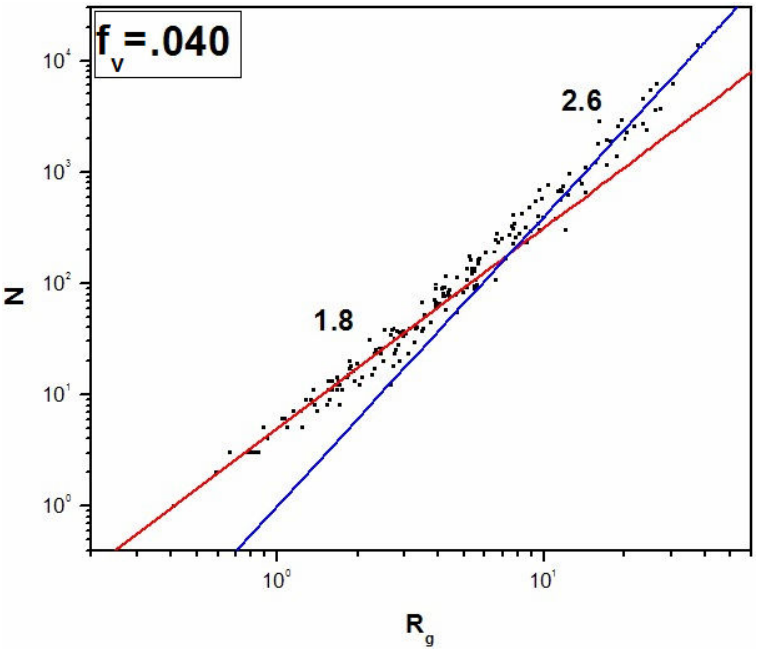
f_v =.040
2.6
1.8
N
R_g

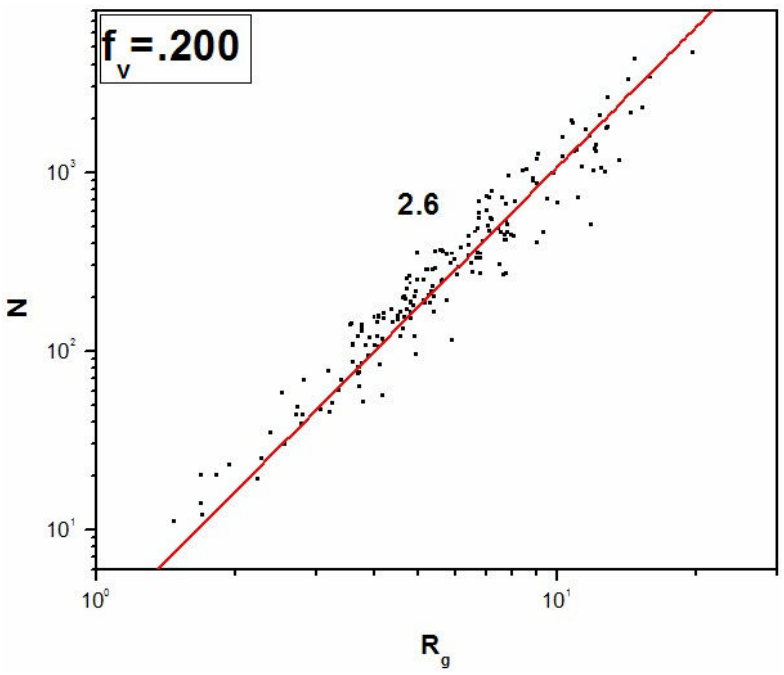

Fig 6.5: ensemble Df for $f_v = 0.001$ (top) ,0.040 (center) , and 0.200 (bottom) demonstrating the variance in Df with crowding.

For $f_v = 0.001$, the fractal dimension is consistently 1.8, in good agreement with 3D DLCA predictions. For $f_v = 0.040$, the fractal dimension exhibits a crossover from $Df \approx 1.8$ to $Df \approx 2.6$ at $R_g \approx 8d_0$. Theory (case 3 - section 5.3.1.3 above) yields an expected crossover at $R_g \approx 3.6d_0$, slightly below the simulation value; case 2 (section 5.3.1.2) assumptions give $R_{g,gel} \approx 7.1d_0$, a better agreement. This crossover indicates that for this volume fraction, clusters initially grow in a nearly dilute state, crossing over to a cluster-crowded state at later times, leading to gelation/percolation. For $f_v = 0.200$, the fractal dimension is $Df \approx 2.6$ for the entire range, exactly what we'd expect from site percolation[82]. Clusters at this volume fraction *never* have a chance to grow in a dilute

state; even the monomers are crowded from the very beginning, as is corroborated by the nonlinear kinetics results at this volume fraction.

6.2.4 Df (Structure Factor Method):

We display the structure factor for the gelled (system spanning) cluster for all simulated volume fractions in Fig 6.6:

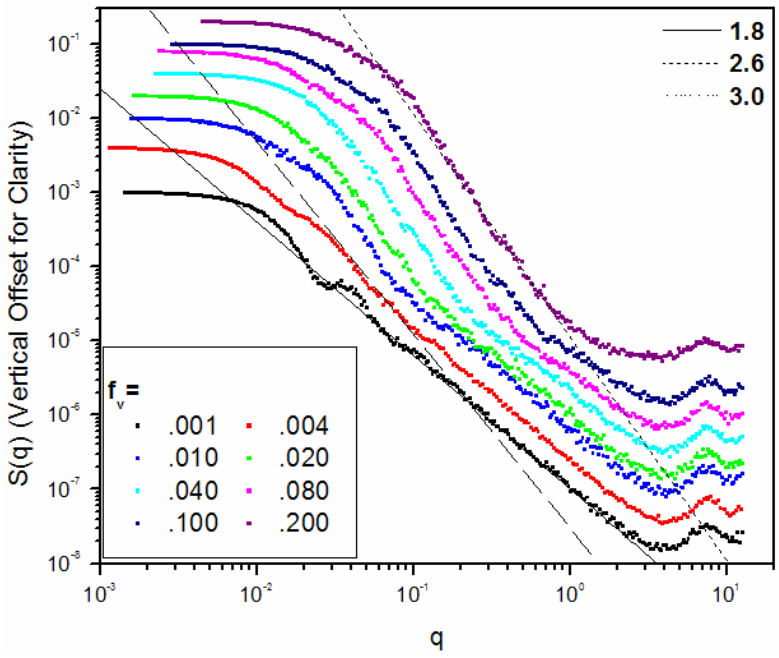

Fig 6.6: S(q) for gelled cluster for range of volume fraction in 3D DLCA

Results are consistent with those of the ensemble Df method. The lowest value of f_v show $D_f \approx 1.8$ over the entire q range, whereas at increasing volume fractions a crossover to $Df \approx 2.6$ occurs at increasing values of q (decreasing length scales), consistent with our picture of gelation. At the highest volume fractions, Df is seen to approach ≈ 3.0, higher than we would expect.

6.2.5 Df Crossover in Gelled Clusters:

Fig. 6.7(a-c) shows images of the gelled clusters for 3 different volume fractions:

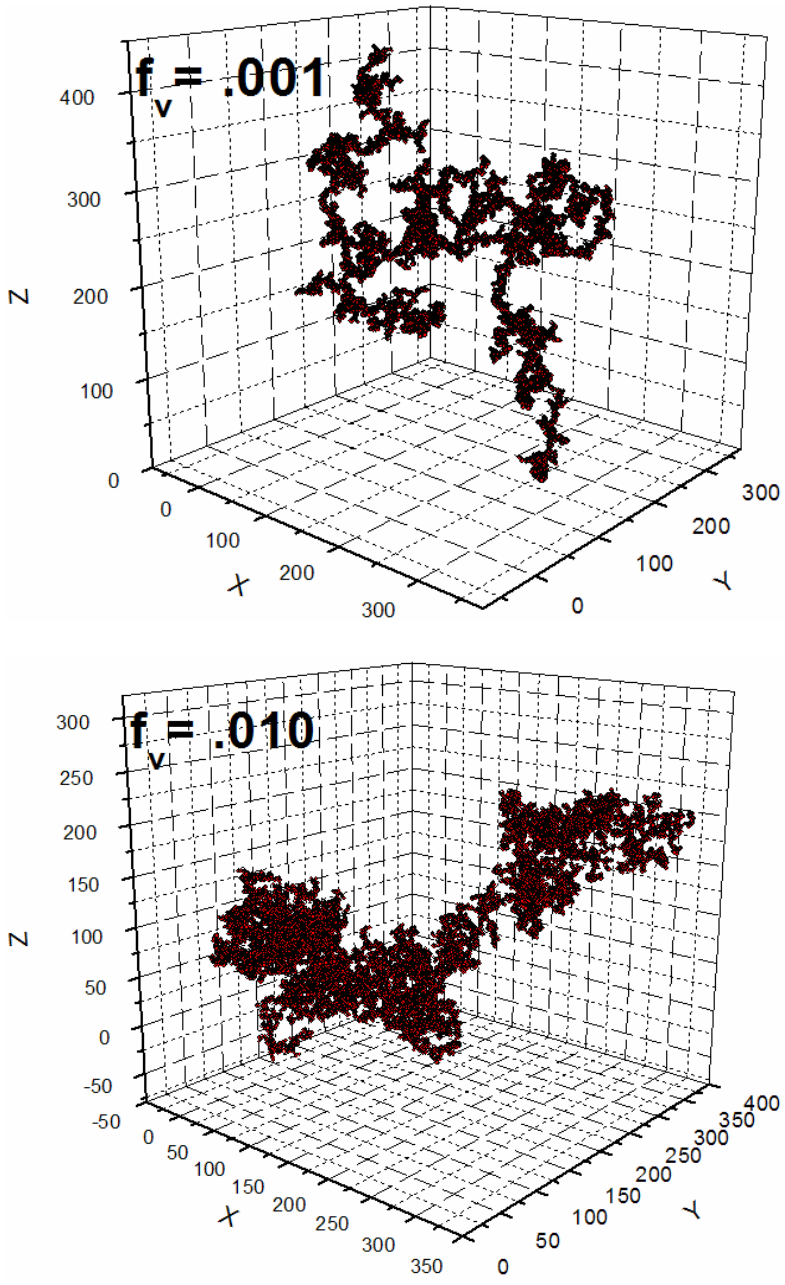

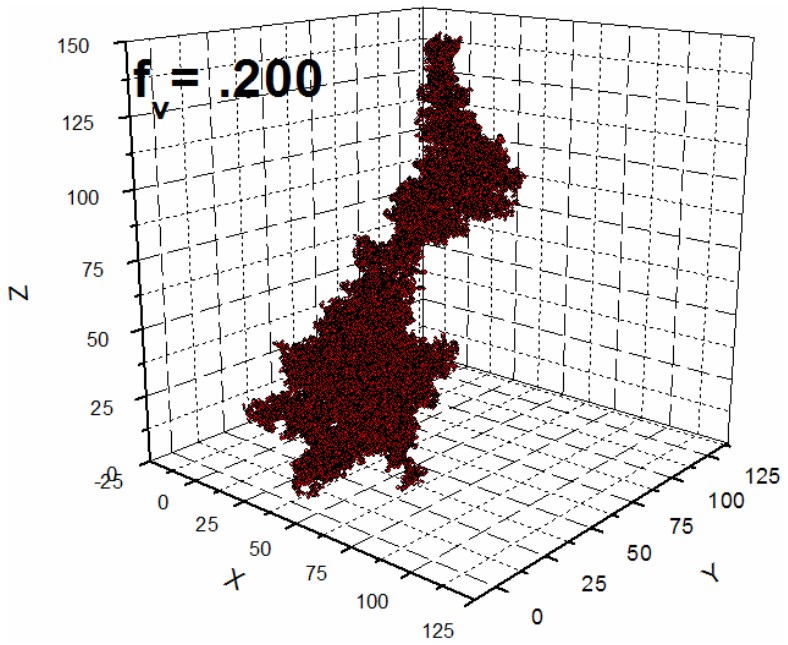

Fig 6.7: (a-c) (top-bottom) gelled clusters for various 3D DLCA volume fractions

6.2.5.1 Low fv (0.001):

Here we see the wispy aggregate characteristic of 1.8 fractals. The superaggregate structure is not obvious in the gelation cluster image, consistent with the kinetics and ensemble Df results. To see a crossover to 2.6 for Df would require a much larger system.

6.2.5.2 Intermediate fv (0.010):

The gelation cluster is not completely dense, indicating that this cluster is of lower fractal dimension on small length scales (1.8), and at large length scales has begun to exhibit the densely packed 2.6 fractal dimension of the superaggregate.

6.2.5.3 High fv (0.200):

The gelation cluster looks dense (2.6) on all length scales, as is corroborated by the structure factor, ensemble mass fractal dimension, etc.

6.2.6 Df (Perimeter Method):

6.2.6.1 Current Study:

Following the method of Jullien et. al. [85], the fractal dimension of clusters can be determined via a calculation of the perimeter fractal dimension D_p. D_p is determined by "gridding" a two-dimensional projection of the aggregate and calculating how many grid points ($N_{gridpoints}$) are needed to cover the perimeter of the projection over a range of grid sizes. Df is then found by the negative of the slope of a log-log plot of $N_{gridpoint}$ vs. gridsize. For $Df < 2$, Jullien et. al. [85] finds:

$$Df \approx D_p \tag{6.3}$$

while for $Df > 2$:

$$Df \approx 3 - (D_p - 1)^{\frac{2}{3}} \tag{6.4}$$

This method is shown in Fig 6.8 for $f_v = 0.200$. Also displayed in Fig 6.9 is an image of the gridding technique for $f_v = 0.200$, showing the perimeter points for the smallest gridsize (d_0).

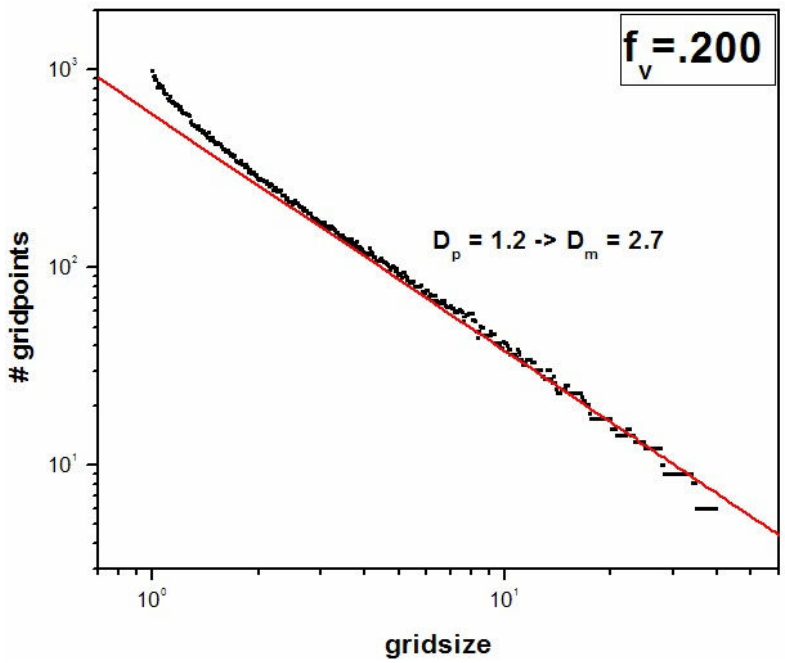

Fig 6.8: Perimeter Df for a f_v = 0.200 3D DLCA cluster

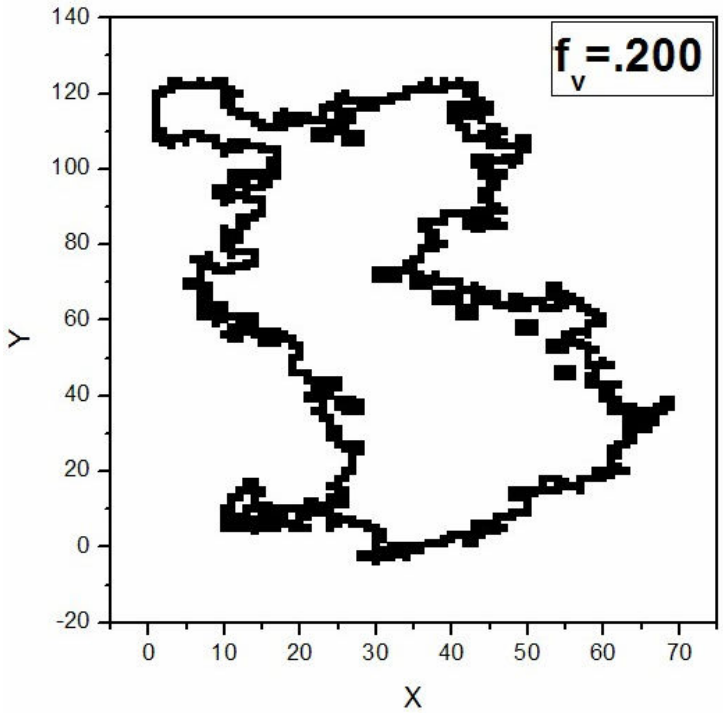

Fig 6.9: Gridding scheme for finding Dp for a f_v = 0.200 3D DLCA cluster

This analysis yields a calculated $Df \approx 2.7$, close to that found for this volume fraction from the ensemble method.

6.2.6.2 Experimental Study:

Below is a set of images Fig 6.10-6.11 from a TEM analysis of soot aggregates formed by explosion of hydrocarbon gases in a reaction chamber as reported by Dhaubhadel et. al. [9]. The first image is taken at the scale of hundreds of nm:

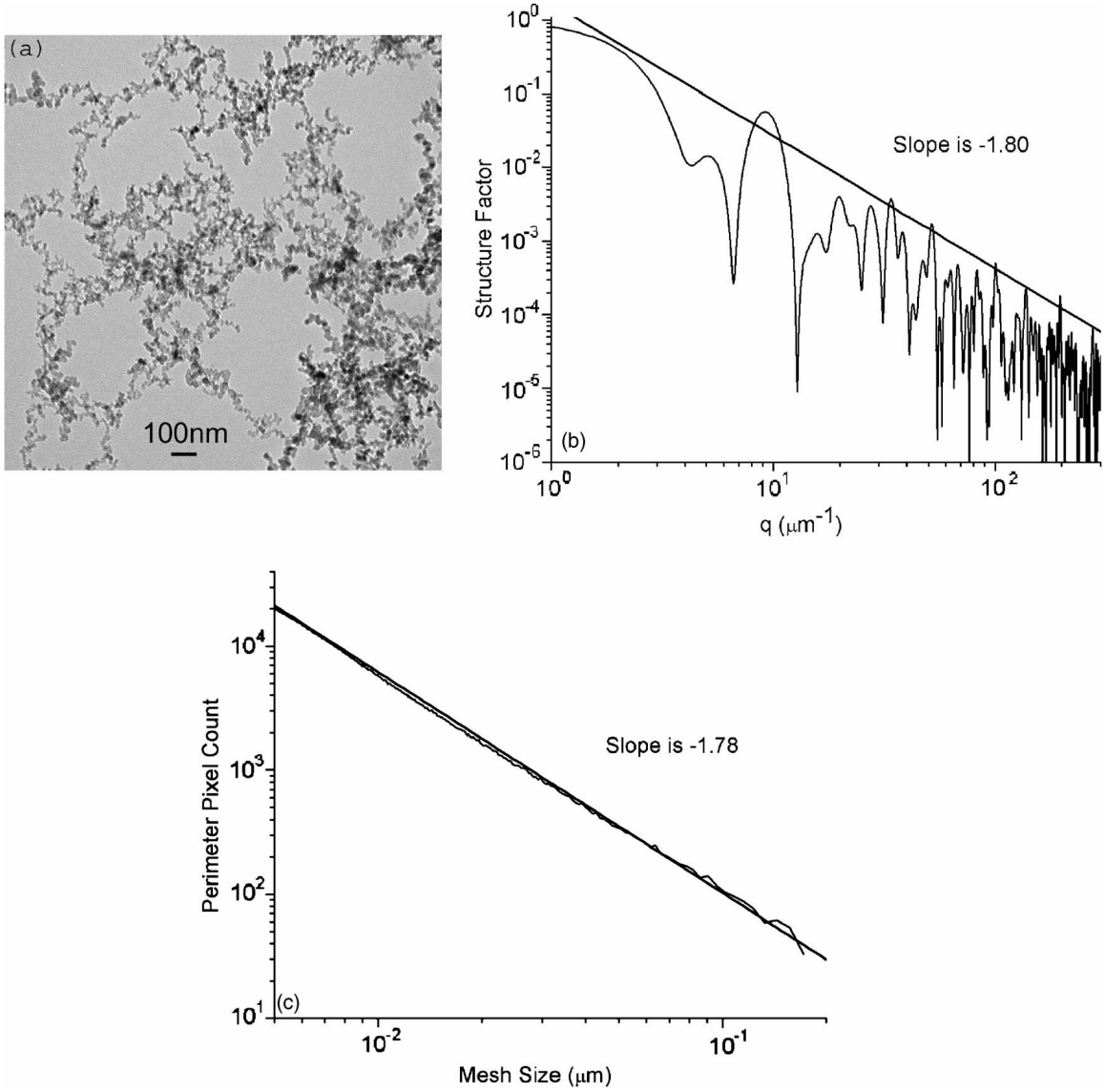

Fig 6.10: TEM at 100's of nm of explosion chamber soot along with structure factor and perimeter analysis. Stringy 1.8 Df fractals are obvious.

At this scale, $Df \approx 1.8$ fractals are apparent from both the structure factor and the perimeter analysis. At a larger scale (tens to hundreds of μm's) we see that Df has crossed over to a 3D percolation value near 2.5 from the structure factor and ≈ 2.4 from the perimeter analysis, using $D_p = 1.44$:

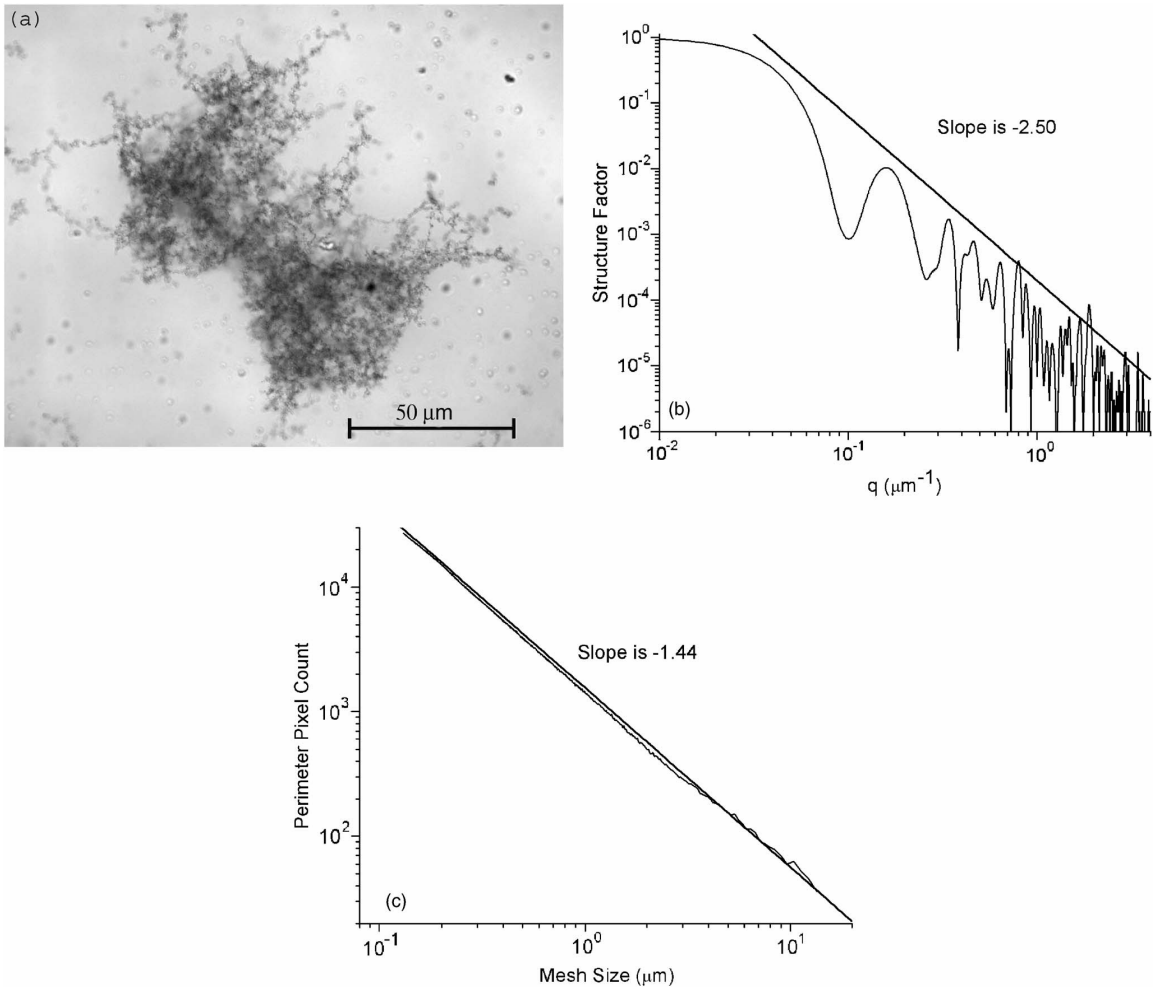

Fig 6.11: TEM at 10-100's of μm of explosion chamber soot along with structure factor and perimeter analysis. Bulky 2.6 Df percolated fractals can be seen.

Thus from simulation and experiment we see that when aggregation begins in a dilute state, aggregates grow with $Df \approx 1.8$, and as the system evolves to a cluster-dense state, the fractal dimension exhibits a crossover to $Df \approx 2.6$, consistent with the work of other researchers [64,86].

6.2.7 Conclusions:

Through our simulation of 3D DLCA aggregation in systems from initially dilute to dense, we see clear evidence of a crossover in fractal dimensions from cluster dilute (1.8) to cluster-dense (2.6) in good agreement with other simulation work[40,64] and experimental studies [9]. Theoretical predictions for the cluster size at crossover are in decent agreement with simulation results at low volume fractions.

6.3 *Diffusion Limited Cluster Aggregation in Aerosol Systems with Epstein Drag:*

6.3.1 Introduction:

Here we focus on cluster-cluster aggregation in the "Epstein regime", a diffusional regime where the diffusion coefficient is inversely proportional to the cluster cross-sectional area in the medium, thus free-molecular in nature. Results presented are from low volume fraction MC aggregation simulations in this regime (Epstein DLCA); these are the first such studies presented in the literature to our knowledge. Our findings indicate that aggregates grown under Epstein conditions have a fractal dimension of ~ 1.8, similar to that of continuum DLCA aggregates. The kinetic exponent z in the Epstein regime is found to be $z \approx 0.8$, lower than its value for both continuum DLCA ($z = 1$) and free-molecular BLCA ($z \approx 2$). Cluster size distribution data for Epstein systems are found to scale at large cluster sizes with exponents consistent with the kinetic data. From scaling arguments, we predict values for z and λ (kernel homogeneity) based on the mass/size dependence of the particle velocity and collision cross section. These predictions are seen to give accurate results for both dilute and *intermediate* values of particle volume fractions in current study of Epstein DLCA. Additionally, the scaling arguments also agree with work done by other researchers with various choices for the aggregation kernel.

6.3.2 Cluster-Dilute, Cluster-Dense, and Intermediate Systems:

As mentioned previously, recent work [40, 87-90] has shown that the particle volume fraction affects the aggregation process when the system becomes crowded. To describe "crowded" we use the mean cluster-cluster nearest neighbor distance R_{nn}. We then define a *cluster dilute regime* as one where the relative separation to size ratio is large, i.e., $\frac{R_{nn}}{R_g} \succ\succ 1$ and a *cluster dense regime* for which the separation is relatively small, i.e., $\frac{R_{nn}}{R_g} \geq 1$. In this work we also describe an *intermediate* regime which lies between the cluster dilute and cluster dense.

6.3.3 Regimes of Motion:

The motion of the clusters between inter-cluster collisions, whether diffusive or ballistic, affects the aggregation kernel. The aggregation kinetics, size distribution, and particle morphology are all functions of this motion.

To describe particle motion in a medium, hence the aggregation regime, the most commonly used parameter is the Knudsen number *Kn (*defined above). To a good approximation the mean free path of the medium is:

$$\lambda_m \approx \frac{1}{n_m} \tag{6.5}$$

, with n_m the medium molecule number density, which for a gas is dependent on the temperature and pressure [3].

An often overlooked parameter is the *diffusional* Knudsen number:

$$Kn_D = \frac{\lambda_p}{R} \tag{6.6}$$

, where λ_p is the persistence length of the particle. λ_p is the average distance over which a particle moves *effectively* in a straight line [32]. If one observes a particle's motion on a length scale much less than λ_p, the motion is essentially ballistic while for larger length scales, the path is diffusional (random-walker).

As noted by Oh and Sorensen, both $Kn \sim 0$ and $Kn_D \sim 0$ in the continuum [34]. Other researchers do not often directly refer to a specific condition on Kn_D for this regime. Many aggregation studies are carried out in the diffusive continuum regime. These include colloidal aggregation in a liquid medium and aerosol aggregation at relatively low temperatures (or high pressures) and/or large particle sizes.

As Kn increases from ~ 0 to higher values, the crossover from the continuum to Epstein diffusion occurs. This intermediate Kn regime is usually called the "slip regime" which can be described through the use of the Cunningham correction, C(Kn), to the Stokes-Einstein Diffusion law, introduced above where we write:

$$D = D_{SE}C(Kn) \approx D_{SE} + D_{Ep} \tag{6.7}$$

The approximation is good to within 4% of that given by the Cunningham correction over the entire Kn regime [35].

On the opposite extreme of Kn from the continuum is the free molecular regime $\left(Kn \succ\succ 1\right)$. Free-molecular particles can move either *diffusively* or *ballistically* between collisions with each other. Previous workers have claimed that a crossover between these two extremes occurs when $Kn_D \approx 1$ [30,32,34]. We find, however, that a better determination of this crossover is the comparison of λ_p to R_{nn}. We define a nearest neighbor Knudsen number as:

$$Kn_n = \frac{\lambda_p}{R_{nn}} \tag{6.8}$$

When $Kn_n < 1$, the motion of spherical particles in the free molecular regime is diffusive, with diffusion constant:

$$D_{E_P} = \frac{3}{8\rho R^2}\left(\frac{mk_B T}{2\pi}\right)^{1/2}\left(1+\frac{\pi}{8}\beta\right)^{-1} \tag{6.9}$$

We refer to this regime as the *Epstein regime*, characterized by $D \propto R^{-2}$.

When $Kn_b > 1$, the motion of spherical particles is ballistic, hence the *ballistic regime*.

The differences between the Epstein and ballistic regimes are just as important as their similarities. In both cases the resistance to the medium is free-molecular, with drag force proportional to particle cross sectional area. In the Epstein regime, however, the sum of molecular impacts with the particle *is* sufficient to appreciably alter the direction of cluster motion between collisions, thus leading to diffusional motion. A cluster in the ballistic regime still encounters drag, but the molecular impacts are insufficient to significantly alter the trajectory, hence effective straight-line motion between collisions results.

6.3.4 Mobility Radius:

To apply the diffusion constant and drag coefficient results for both regimes, which are written for spherical particles, to fractal aggregates, we replace the sphere radius R with an effective mobility radius R_m for the aggregate. R_m will be a function of monomer size and number of monomers per aggregate as:

$$R_m \propto r_0 N^x \tag{6.10}$$

which defines x.

Wang and Sorensen [71] made a comprehensive study of diffusive mobility for all Kn that both reviewed earlier work and presented new data for fractal aggregates. They concluded that when $Kn << 1$ and $N \geq 110$, $R_m \approx R_g \propto N^{\frac{1}{Df}}$. Hence, for $D_f = 1.8$, $x = 0.55$. However, when $N \leq 110$ a crossover to the $N = 1$ limit begins and then Wang and Sorensen concluded $x = 0.44 \pm 0.03$.

For the Epstein Regime, $Kn > 10$ and the free-molecular drag force F_{drag} on a cluster is proportional to its cross sectional area A_{CS} *as seen by the medium*. From this a mobility radius R_m can be defined as:

$$A_{CS} = \pi R_m^2 \tag{6.11}$$

Most particles have some degree of "drag screening". That is, part of the cluster shields other parts from direct contact with fluid flow and thus the influence of gas drag.

Wang and Sorensen [71] considered both mobility measurements for fractals and various studies of monomer-monomer screening within a cluster and consistently found value of:

$$x = 0.44 \pm 0.03 \tag{6.12}$$

By coincidence, this is the same value as found in the continuous limit for $N \leq 110$.

6.3.5 Scaling of the Aggregation Kernel:

Here we extend our simple scaling analysis from above to describe the dependence of the aggregation kernel on its variables. This functionality is quantified by λ which in turn determines the size distribution and kinetics functionalities on their

variables. We present results for all *motional* regimes and in two *concentration* regimes: dilute and intermediate.

As above, our scaling argument gives the collision kernel K as proportional to their relative collision cross-sectional area A and relative cluster velocity, v, yielding:

$$K \sim Av \text{ (see Eq. 5.5)} \tag{6.13}$$

consistent with the units of $\left[L^3 t \right]$. Here A is distinct from the cross-sectional area A_{CS} as seen by the medium molecules in mobility radius calculations; it instead refers to the effective area seen by another fractal particle during a collision process. One typically writes this as $A \sim R_g^2$ where R_g is the radius of gyration of a fractal cluster [83].

6.3.5.1 Ballistic Regime:

In the ballistic regime, described previously, one obtains $\lambda = 0.55$. This is translated into $z = 2.2$ (see Eq. (4)) in the dilute limit. This value of z is consistent with simulation results [49].

6.3.5.2 Diffusion Regime:

In the diffusive cases, whether in continuum or in Epstein regimes, v becomes a *characteristic velocity relevant for diffusion*:

$$v \propto \frac{D}{R_c} \tag{6.14}$$

where D is the diffusion constant and R_c is a characteristic diffusional length-scale. Diffusive particles do not have a unique velocity as such since they obey:

$$< x^2 >= 2dDt \tag{6.15}$$

However, if one uses a length scale of size R_c to measure the motion of a diffusive cluster, one would find that it takes time:

$$t_c = \frac{R_c^{\,2}}{2dD} \tag{6.16}$$

for the cluster to move *on average* a distance R_c from where the motion is observed to begin. This diffusive velocity represents a speed along the Brownian path using a "ruler" of length R_c. Thus the *diffusive velocity* using R_c as a length-scale can be defined as:

$$v = \frac{R_c}{t_c} = \frac{2dD}{R_c} \propto \frac{D}{R_c} \tag{6.17}$$

as given above.

Fig. 6.12: Diffusive path of a particle showing characteristic distance and time

In the dilute limit for $Kn \prec\prec 1$, R_g is the only length-scale in the system. In dilute-limit scaling, a particle is seen to exist in an isotropic "field" of other particles. We can think of this as a kind of collision probability density field surrounding a particle. Let r be the distance from the center of a particle. The collision probability density steadily rises from r = 0 to $r \approx 2R_g$ at which it approaches a constant value, dependent on the volume fraction of dispersed particles. In other words, the characteristic distance

required for collision to occur is a distance on the order of the particle diameter. Thus, for collisional purposes in the dilute limit, we use $R_c \propto R_g$ as the proper length scale. Thus $v \propto \frac{D}{R_g}$. The persistence length in the continuum is microscopic and R_{nn} is very large hence neither represents a valid length scale for this scaling. In addition, $A \propto {R_g}^2$ and $R_g \propto N^{\frac{1}{Df}}$. Thus:

$$K \propto DR_g \tag{6.18}$$

, a result originally derived by Smoluchowski in a more rigorous fashion. In this case $D \propto \frac{1}{R_m}$ and $R_m \propto R_g$ in the continuum limit. As a result $D \propto \frac{1}{R_g}$ which with $K \propto DR_g$ implies that K is a constant (independent of the particle mass or linear size), in turn leading to $\lambda = 0$ and $z = 1$ in the dilute limit of the continuum regime.

We can use a similar argument for computing λ and z in the Epstein regime. $K \propto DR_g$ is still satisfied as in the continuum case, but now:

$$D \propto \frac{1}{{R_m}^2} \tag{6.19}$$

holds. Since $R_m \propto N^x$ and $R_g \propto N^{\frac{1}{Df}}$, one finds

$$\lambda = \frac{1}{D_f} - 2x \text{ (dilute regime; Epstein)} \tag{6.20}$$

for the dilute-limit Epstein regime.

In many simulations of cluster-cluster aggregation, the system is not in the-asymptotically dilute range (defined by $R_{nn} \rightarrow \infty$) as monomer volume fraction is

typically $f_v \approx 0.01$ and rarely goes lower than $f_v = 0.001$. In the case of high initial volume fractions, the system is already monomer dense, and the dilute-limit predictions needs to be adjusted accordingly. Even at low initial volume fractions one should be aware that the system will become cluster dense ($R_{nn} \rightarrow R_g$) or crowded as the system aggregates. In order to determine the crowding of the system, we find the occupied volume of the clusters based on their perimeter radius, R_p. Since the volume occupied by a fractal particle is $V_{occ} \sim R_p^3$, using the relationship between R_g and R_p above one finds, $V_{occ} \sim R_g^3 \sim N^{3/Df}$. The total volume of the system occupied by particles goes as $V_{occ,tot} = N_c V_{occ} \sim N^{3/Df-1}$. The occupied volume fraction $f_{occ} = V_{occ,tot}/V_{system}$ increases without bound as the average particle size N increases. As f_{occ} approaches 1, the clusters begin to crowd each other and the system evolves from a cluster dilute to a cluster dense state.

Even before the system becomes cluster dense, R_{nn} quickly becomes a relevant length scale with respect to any given particle's motion, since it is this distance over which a cluster must diffuse in order to collide and aggregate with another cluster. At some intermediate time t where $0 < t < t(f_{occ,tot} = 1)$, one can estimate the characteristic diffusion velocity v as $v \propto \frac{D}{R_{nn}}$ with $R_{nn} \propto N_0^{-\frac{1}{d}}$ in d-dimensions. One can equivalently write $R_{nn} \propto N^{\frac{1}{d}}$, where N is the average cluster size. One then finds that in the intermediate regime of the continuum limit, $K \propto N^{\frac{1}{Df}-\frac{1}{d}}$ which yields

$$\lambda = \frac{1}{D_f} - \frac{1}{d}. \text{ (intermediate regime; Stokes Einstein)} \quad (6.21)$$

In the Epstein regime similar arguments yield

$$\lambda = \frac{2}{D_f} - \frac{1}{d} - 2x \text{ (intermediate regime; Epstein) (6.22)}$$

In the continuum limit, with $D_f = 1.8$ and $d = 3$, we obtain $\lambda = 0.22$ hence by Eq. 6.21, $z = 1.28$ in the intermediate regime. This value of the kinetic exponent z agrees well with recent simulation results [40].

As we show below, older simulation results [91] are also more consistent with the intermediate regime scaling than the dilute-limit scaling for various choices of the aggregation kernel. In a series of Monte Carlo simulations in two and three dimensions Meakin et al. [91] modeled cluster-cluster aggregation with particle diffusion constants $D \propto N^{\gamma}$ where γ is related to the kernel homogeneity λ as:

$$\lambda = \gamma + \frac{1}{D_f}. \tag{6.23}$$

For each γ used in their simulations they fit their kinetic data (average cluster mass vs. time) to a power law growth curve to find the associated kinetic exponent, which we denote as z_{MC}. From the known value of γ (hence λ) we compute the kinetic exponent z from our scaling arguments --- z_{dil} in the dilute limit and z_{int} in the intermediate regime. Our results listed in Table 6.1 clearly indicate that MC simulations for typical simulation monomer volume fractions ($f_v < 0.001$) do probe the intermediate scaling regime instead of the true dilute regime. Thus, one needs to analyze simulations data for kinetic exponents in the Epstein regime both in terms of dilute and intermediate scaling exponents. Note that both dilute and intermediate scaling assumptions break down when $\gamma > 0$ as the system enters the cluster dense regime too quickly.

γ	z_{MC}	z_{dil}	z_{int}
-3	0.33	0.29	0.31
-2	0.45	0.41	0.45
-1	0.8	0.69	0.82
-0.5	1.3-1.4	1.06	1.38

Table 6.1. In the first column, γ is the exponent for the mass dependence of the diffusion constant, $D \sim N^{\gamma}$. z_{MC} refers to the kinetic exponent as measured from a Monte Carlo simulation [92] using the indicated γ. z_{dil} and z_{int} are the dilute-limit and intermediate volume fraction theoretical predictions for the kinetic exponent using the corresponding γ.

In Table 6.2 we summarize the predictions for λ and z in the various regimes.

Regime	λ *(formula)*	Λ *(calculated)*	*z (calculated)*	*z(simulation)*
Ballistic	$(4\text{-}D_f)/2D_f$	0.55	2.2	~ 2.0
Continuum, dil.	0	0	1	1.0
Continuum, inter.	$(d\text{-}D_f)/dD_f$	0.22	1.28	1.25 ± 0.25
Epstein, dil.	$(1\text{-}2xD_f)/D_f$	-0.36	0.73	0.80 ± 0.02
Epstein, inter.	$(2d\text{-}D_f\text{-}2xdD_f)/dD_f$	-0.14	0.88	0.80 ± 0.02

Table 6.2. Predictions from our scaling theory as well as simulation results for the kinetic exponent in the various motional/concentration regimes. Here calculated values of λ are found from the corresponding scaling formula using $d = 3$ (3 dimensional aggregation) and the values for D_f and x determined in the simulations for each regime.

The fractal dimension of the aggregates, D_f, is 1.8 for continuum and Epstein regimes, 1.9 for BLCA. The value of the mobility radius exponent, x, was found to be 0.46 for the Epstein regime simulations. The calculated value for the kinetic exponent z is found from λ(calculated). We find good agreement for each of these regimes. A single value for z(simulation) is given for the Epstein regime (both dilute and intermediate) since our simulations only explored a monomer volume fraction of 0.001, as stated in the paper.

6.3.6 Simulation Models and Methods:

In order to evaluate our theoretical predictions, we have run a series of MC simulations for the Epstein Regime. We start our simulation with 10^5 monomers placed in a periodic cubical box of sufficient size to make the monomer volume fraction f_v = 0.001. At each MC step, one cluster is chosen according to standard MC prescription (at random with equal likelihood among all clusters) and moved a maximum distance of d_0 (one monomer diameter) with probability:

$$p_{move} = \frac{D_{clust}}{D_0} \tag{6.24}$$

along a spherically random direction. D_{clust} and D_0 are the Epstein diffusion constants of the cluster and monomer respectively. In the Epstein regime:

$$p_{move} = \frac{\pi d_0^{\,2}}{4A_{CS}} \tag{6.25}$$

, where A_{CS} is the cross sectional area of the cluster, ensuring that monomers move with probability unity. A_{CS} is determined by a separate subroutine within the program that calculates the projected area of the cluster in a plane normal to the direction of motion.

Cluster merging and time updates follow the procedure described earlier for MC simulations [40,64,91]. Our simulation results are averaged over a series of 10 runs.

The above method is the standard well-known prescription of Monte Carlo simulation of cluster-cluster aggregation modified for the Epstein regime. Using a variety of different kernels and within different motional regimes, the motion of both primary particles and fractal clusters is found to follow the correct diffusion law to a high degree of precision in all cases [4,40,91].

For the purpose of comparison simulations aggregation were also performed under continuum DLCA and ballistic limited cluster-cluster aggregation (BLCA) conditions in addition to those of Epstein DLCA. The continuum DLCA simulation method is as described previous, done identically to the Epstein but using:

$$p_{move} = \frac{D_{cluster}}{D_0} = \frac{R_{g0}}{R_g} \tag{6.26}$$

, where R_{g0}, R_g are the radii of gyration of the monomer and cluster respectively. The BLCA MC simulations have also been described in previous sections.

6.3.7 Cluster Projection and Mobility Radii Exponents:

The predictions given above for λ require knowledge of the exponent x relating the mobility radius to the cluster mass. For this purpose we display in Fig. 6.13 the log-log plots of A_{CS} vs. N for Epstein clusters as well as for continuum DLCA and BLCA. Linear chains are also included as a test of the procedure. A database of 10 clusters of size N for N = 10, 20, 40, …640 are generated for each kernel. For each cluster, 10^4 different, spherically random directions are chosen, and the cluster's projectional area normal to each direction is calculated. A grid scheme is used for this purpose with 15

grids per monomer diameter. The number 15 is chosen due to the fact that "gridding" a circle with grids 1/15 of a monomer diameter gives an area estimation that differs from the actual value by less than 0.1%. The $A_{CS}(N)$ for each kernel is an average over all the clusters of size N as well as each of the 10^4 directions for each cluster.

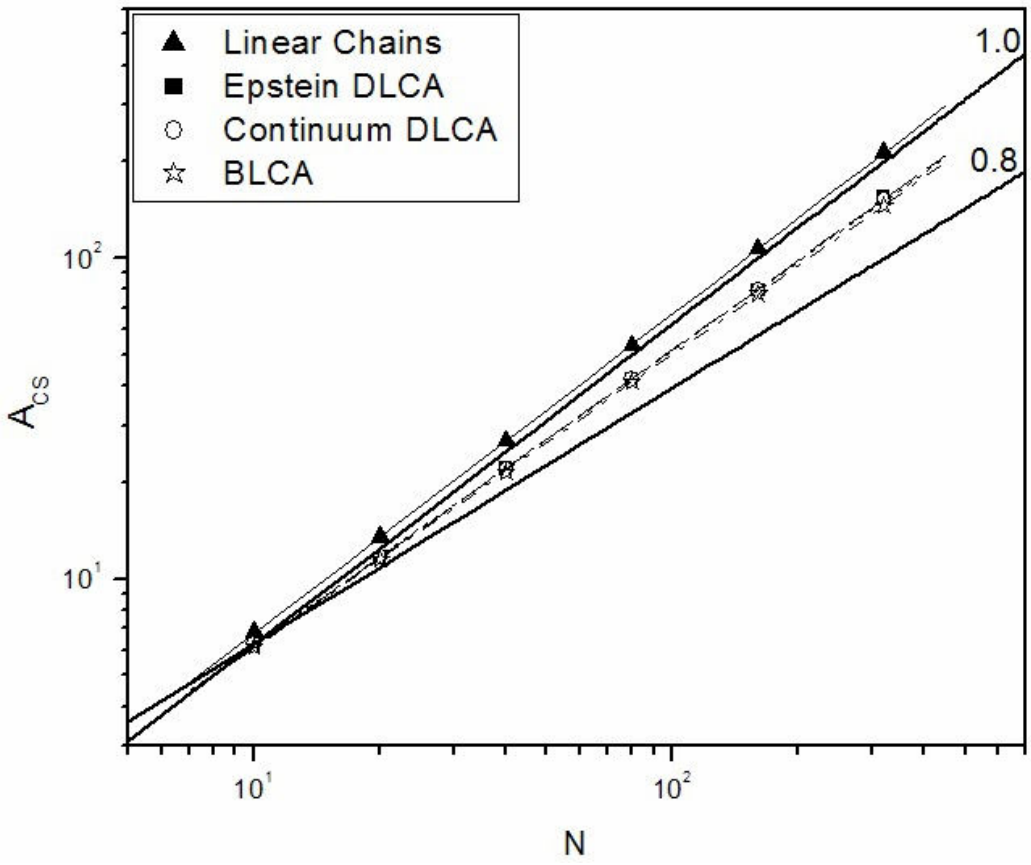

FIG. 6.13: Plot of the cluster projection A_{CS} vs. cluster particle number N. For Epstein and BLCA $A_{cs} = \pi R_m^2$ where R_m is the cluster mobility radius. Linear chains have a power law exponent of 0.995±0.001, very close to the expected value of 1.000. All aggregates have exponents of ~ 0.92 (Epstein DLCA 0.928±.005, continuum DLCA 0.921±.003, BLCA 0.916±.002).

The linear chains exhibit $A_{CS} \sim N^{1.0}$, hence $x = 0.5$. The exponent 1.0 *does not* indicate that no monomer-monomer screening occurs for linear chains; some degree of screening occurs for every projectional plane except those parallel to the line of the chain itself. What the value indicates is that the *average projectional cross-sectional area* as well as the amount of screening scale linearly with the size giving $x = 0.50$, as expected.

For fractal clusters produced by *each* of the aggregation kernels we find that $A_{CS} \sim N^{0.92}$, i.e. $x = 0.46$. Meakin et al. [92] in a series of simulations have found such a simple power law relationship between the cluster cross sectional area and the particle number with an exponent of $2x \sim 0.93$, very close to our finding of $2x = 0.92$. These results are also in agreement with the finding of Wang and Sorensen for aggregates grown in the laboratory at high *Kn* [93]. Recently, Mackowski found the hydrodynamic radius of clusters with $D_f = 1.7\text{-}2.0$ to scale with $x \sim 0.47$, also consistent with our results [94].

6.3.8 Simulation Results in the Epstein Regime:

6.3.8.1 Fractal Dimension:

In Fig. 6.14, we plot N vs. R_g (in units of monomer diameter) for the Epstein clusters that were used in the projection calculations (10 each of mass 10,20,40,..640). From the slope and intercept of this log-log plot we find $D_f = 1.80 \pm 0.06$ and $k_0 = 1.24 \pm 0.15$.

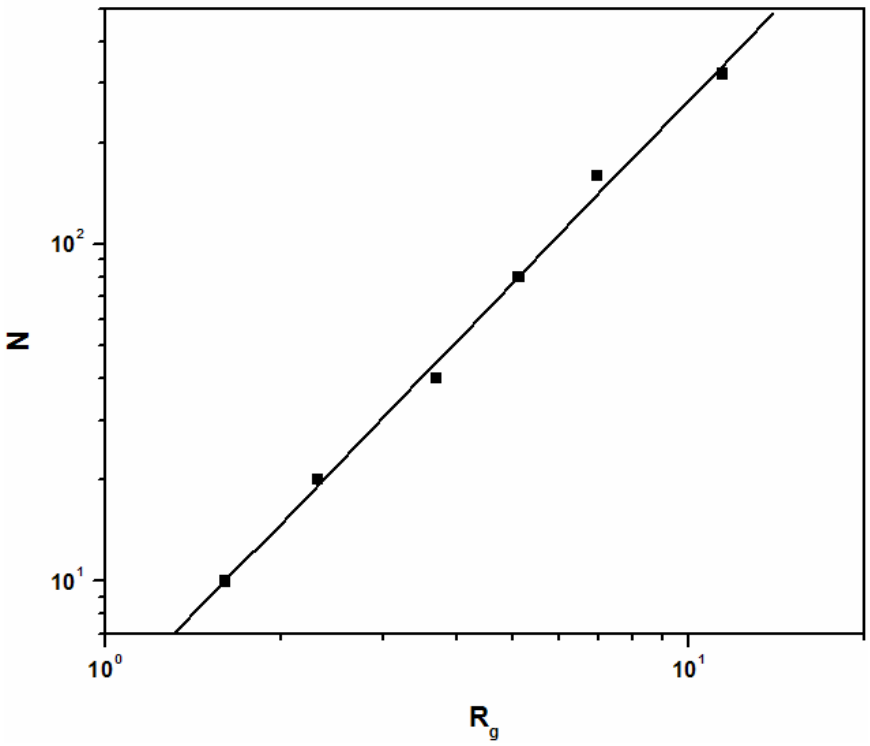

FIG. 6.14. The mass fractal dimension $D_f = 1.80 \pm 0.06$ for Epstein aggregates as found from the real space analysis of the ensemble of clusters. $k_0 = 1.24 \pm 0.15$.

An alternate method for finding D_f makes use of the reciprocal space calculation of the geometric structure factor of large clusters, described earlier. A legitimate range of magnitudes for $\boldsymbol{q}$ is set by the length scales of the simulation, namely the monomer diameter d_0 and the linear size of the system box L such that $\frac{2\pi}{L} < q < \frac{2\pi}{d_0}$. As stated earlier, at large wave vector q, the structure factor $S(q)$ of aggregates goes as q^{-D_f}, so D_f can be seen as the negative slope of a log-log plot of the structure factor of large clusters in the system at high q values [77]. Figure 6.15 shows the structure factor of the largest cluster in the system for the Epstein kernel at a time during the aggregation process

where $N_c = 97$. One can easily see that the structure factor curve for intermediate q values is well described by the fit line representing $S(q) \sim q^{-D_f}$ with $D_f = 1.82 \pm 0.03$.

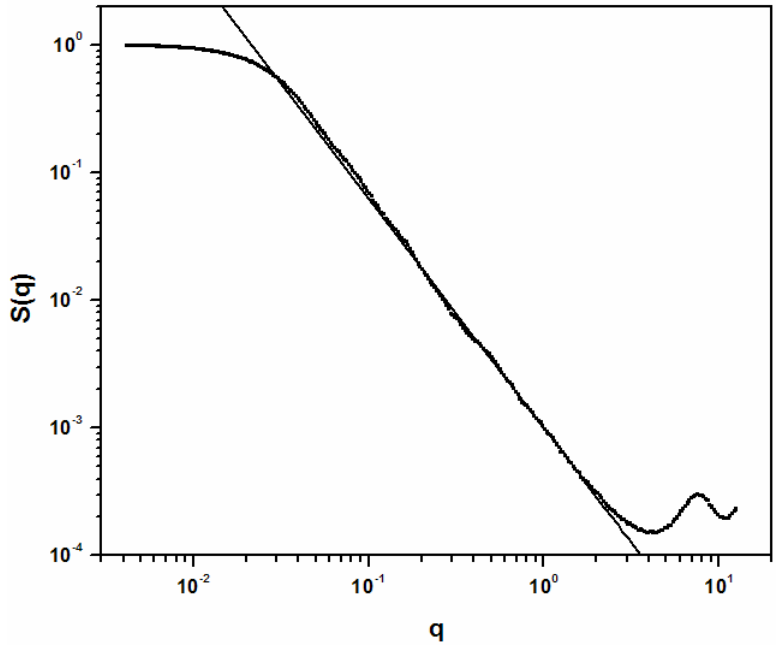

FIG. 6.15. The mass fractal dimension $D_f = 1.82 \pm 0.03$ for Epstein aggregates as found from a structure factor calculation for large aggregates in the system.

In Fig. 6.16 (a-d) we display images of the simulation box at various times in the simulation, showing the time evolution of the cluster morphologies for Epstein aggregates. Due to the similarity of the morphologies of clusters in all aggregation regimes (BLCA, continuum DLCA, Epstein DLCA) including D_f values that extend over the narrow range 1.8 to 1.9, morphologies alone cannot easily be used to distinguish the regime of aggregation.

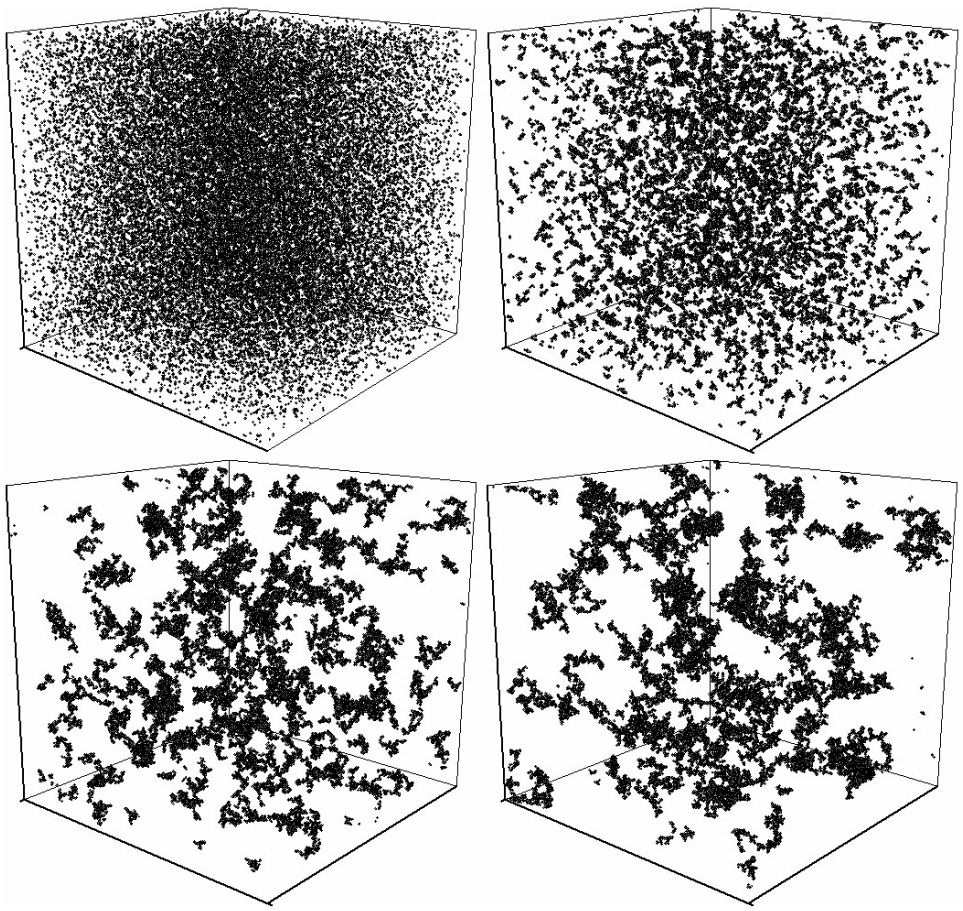

FIG. 6.16: (a-d)(top left-bottom right) Images of the system volume at various times during aggregation in the Epstein regime. The average size of clusters and time are for 4a ($N = 260$, $t = 2$), 4b ($N = 32$, $t = 9372$), 4c ($N = 512$, $t = 336751$), and 4d ($N = 2703$, $t = 2079152$).

6.3.8.2 Kinetics of Aggregation:

Figure 6.17 displays the results for the kinetics from our Epstein simulations. Here the scaled inverse cluster number is plotted vs. Monte Carlo time in a log-log plot. The slope of this curve (after the initial linear transient described earlier) is $z = 0.80 \pm 0.02$.

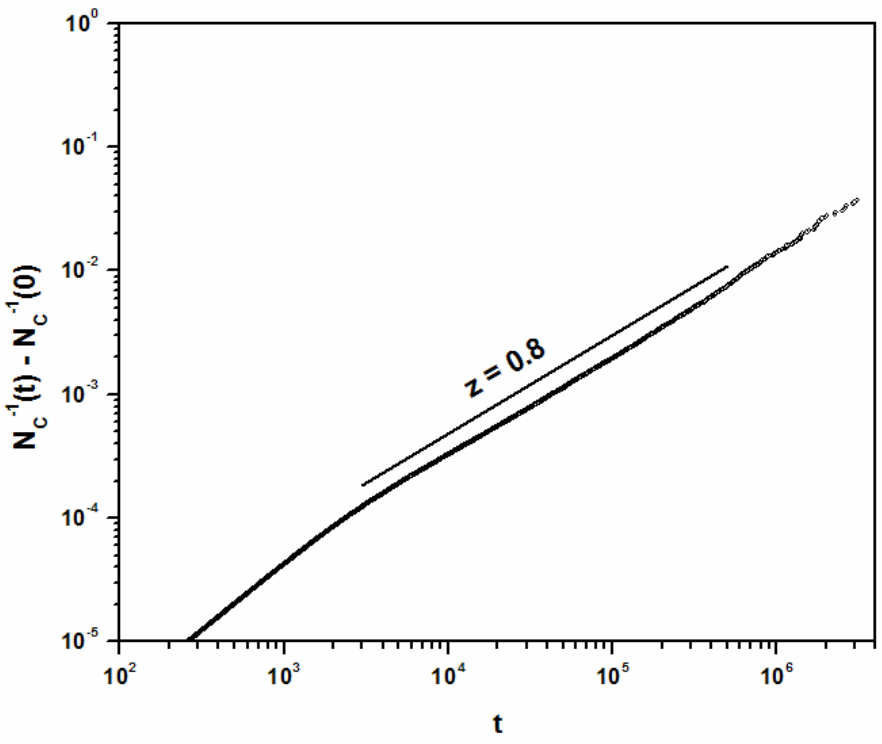

FIG. 6.17. The kinetic exponent starts with a transient value of $z = 1.0$ crossing over to a scaling regime value of $z = 0.80 \pm 0.02$, a value well supported by theoretical calculations.

Using the value of D_f determined above (1.8), scaling predictions yield $z = 0.73$ for the dilute limit and $z = 0.88$ for the intermediate regime. The kinetic exponent from the simulation is consistent with these two values. As predicted by our scaling arguments above, our simulation results verify that the kinetic exponent for the Epstein regime is both noticeably smaller than the continuum prediction of $z = 1$ and well below the free molecular value of $z = 2.2$.

In Table II we also display our calculated predictions for λ and z from our scaling theory along with simulation results for the kinetic exponent for the various motional/concentration regimes.

6.3.8.3 Cluster Size Distributions:

In Fig. 6.18 we have plotted the scaled size distributions for the Epstein regime for a number of simulation times. When the fit to the scaling form given above is made for the range $x > 1$ (large x), excellent agreement with the scaling form is found for all times. From the kinetics data above we found $z = 0.80 \pm 0.02$ corresponding to a λ value of -0.25 ± 0.03. Fitting of the cluster size distributions to the scaled form yields $\lambda = -0.3 \pm 0.1$, consistent with the kinetic results.

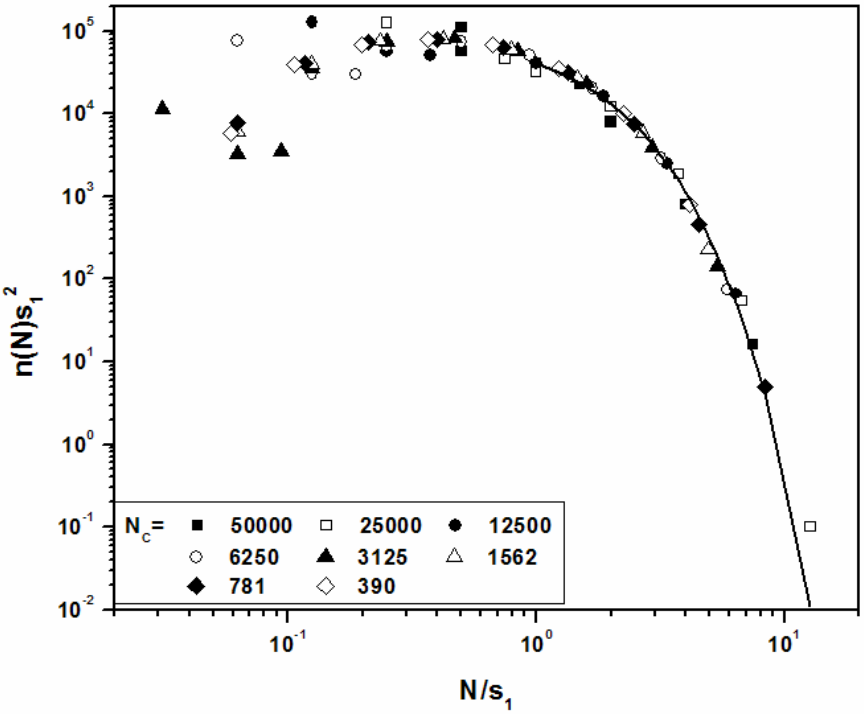

FIG. 6.18. Cluster size distribution data for a number of different times in the aggregation process. The system is initialized with 10^5 monomers and distributions are shown every time the number of clusters decreases by a factor of 2, down to $N_c = 390$ clusters left in

the system. The data for large $x = \frac{N}{s_1}$ is well described by the scaling form $Ax^{-\lambda}e^{-\alpha x}$ where $\alpha = 1-\lambda$ with $\lambda = -0.36 \pm 0.20$. The kinetics data yields $\lambda = -0.25 \pm 0.03$, in agreement with the size distribution data.

6.3.9 Conclusions:

MC simulations of dilute-limit Epstein DLCA aggregation have been carried out. We have found the mobility radius of Epstein aggregates calculated from cluster projectional areas to scale with the particle mass with an exponent of 0.464 ± 0.003, in good agreement with both the computer simulations and experimental work of other researchers.

Fractal dimensions for simulated Epstein aggregates were found to be 1.82 ± 0.03, close to that of continuum DLCA (~1.8) and BLCA (~1.9).

The kinetics exponent of aggregation in the Epstein regime from our simulations ($z = 0.80$) is consistent with our scaling arguments ($z = 0.73$-0.88). The cluster size distributions also agree well with both the kinetics and scaling results for large cluster sizes.

6.4 Motional Crossover from Ballistic to Epstein Diffusional in the Free-Molecular Regime:

6.4.1 Introduction:

Here we present the results of a theoretical/simulation study of the aggregation of dispersed particles in the free molecular regime to demonstrate the effect of *crossover* between ballistic and diffusive type motion which occurs due to cluster growth. Most aggregation simulations consider systems initialized with an ensemble of monomers whose motions between collisions with each other are well approximated by *either* ballistic (straight-line) or diffusive types. Due to the aggregates' evolving size, systems that initially aggregate in a ballistic fashion can exhibit a crossover to diffusive at later times through the evolution of Kn and Kn_n. Additionally, as the aggregates continue to grow, they can begin to crowd one another, and the motions of aggregates between collisions can again cross over to a ballistic type near system gelation. The kinetics of aggregation, resulting cluster size distributions, and aggregate morphologies can all be affected by these crossovers, and it is the results of these processes that we present here.

6.4.2 Persistence Length and Characteristic Time:

If the interparticle/external potential is *negligible* between particle collisions (as in the case of van der Waals forces), one can use the Langevin equation to determine the *characteristic time* over which the action of the above forces can alter the velocity of a particle. For particles of much greater mass than the medium molecules, a single collision with a medium molecule will not significantly alter the path of the dispersed

particle, so for short times the particle trajectory will be along a straight-line trajectory (ballistic). However, after many such collisions, the particle's direction of motion will inevitably become uncorrelated with its initial direction [30,32]. This idea is a continuation of the concept of mean free time/mean free path of a gas molecule in an ideal gas. This particle "mean free time" will be referred to as its *characteristic time* (t_c), and the corresponding "mean free path" is termed *persistence length* (λ_p) as mentioned previously. λ_p can be found by simple scaling in the Langevin Equation (rewritten here for convenience) in the following way:

$$m_p \frac{d^2\mathbf{x}_p}{dt^2} = \mathbf{F}_{drag} + \xi - \nabla U = f_{drag} \frac{d\mathbf{x}_p}{dt} + \xi - \nabla U \tag{6.27}$$

Here [=] means "has units of"

$$\frac{d^2 x_p}{dt^2} \left[=\right] LT^{-2} \tag{6.28}$$

$$\frac{dx_p}{dt} \left[=\right] LT^{-1} \tag{6.29}$$

$$\rightarrow \frac{f_{drag}}{m_p} \left[=\right] T^{-1} \tag{6.30}$$

$$\rightarrow t_c = \frac{m_p}{f_{drag}} \left[=\right] T \tag{6.31}$$

where M, L, and T are units of distance and time, respectively. One may complain that in the above argument, we are not calculating the characteristic time for the velocity *direction* to change but rather the *magnitude* of the velocity since the term used in the scaling is the drag force which is always *opposed* to the direction of motion. However,

similar arguments can be made using the stochastic thermal force ξ, by use of the time correlation given above in Eq. 2.6.

$$\frac{<\xi(t)\xi(t')>}{m_p^{\,2}} = 6k_B T f_{drag}\,\frac{\delta(t-t')}{m_p^{\,2}}\,[=]\,L^2T^{-4} \tag{6.32}$$

$$k_B T\,[=]\,ML^2T^{-2} \tag{6.33}$$

$$\delta(t-t')\,[=]\,T^{-1} \tag{6.34}$$

$$m_p\,[=]\,M \tag{6.35}$$

$$\rightarrow \frac{f_{drag}}{m_p}\,[=]\,T^{-1} \tag{6.36}$$

$$\rightarrow t_c = \frac{m_p}{f_{drag}}\,[=]\,T \text{ (as before)} \tag{6.37}$$

The stochastic force is *isotropic* and independent of particle velocity. The characteristic times calculated for the drag force and stochastic thermal force are identical. Of course this is not unexpected, as the fluctuation-dissipation theorem confirms that the correlation function of the fluctuating force will be linearly related to the friction coefficient, as we see in the correlation function for ξ given above. Therefore t_c is a measure of the time it takes for a particle's velocity *in a particular direction* to become completely uncorrelated with its previous value. If we are in the free-molecular regime, we find the characteristic time to be given by:

$$f_{drag} = 7.26\delta P\sqrt{\frac{m_g}{k_B T}}\,r_p^{\,2} \tag{6.38}$$

$$\rightarrow t_c = \frac{0.138}{\delta P}\sqrt{\frac{k_B T}{m_g}}\,\frac{m_p}{r_p^{\,2}} \tag{6.39}$$

In the continuum, we determine:

$$f_{drag} = 2.573 \frac{\sqrt{k_B T m_g}}{d_g^{\,2}} r_p \tag{6.40}$$

$$\rightarrow t_c = 0.3886 \frac{d_g^{\,2}}{\sqrt{k_B T m_g}} \frac{m_p}{r_p} \tag{6.41}$$

Using the above expression for t_c, we can get an idea of how far "on average" a dispersed particle can move along a ballistic trajectory before its motion becomes diffusive, the persistence length λ_p. Again assuming zero potential before contact, we know that the velocity of the dispersed particles is thermal in nature with (Eq. 2.12):

$$v_p = v_{rms} = \sqrt{\frac{3k_B T}{m_p}} \tag{6.42}$$

The persistence length is then given by the product of the characteristic time and the thermal velocity:

$$\lambda_p = v_p t_c \tag{6.43}$$

In the free molecular regime, this corresponds to:

$$\lambda_p = 0.2396 \frac{k_B T}{\delta P \sqrt{m_g}} \frac{\sqrt{m_p}}{r_p^{\,2}} \tag{6.44}$$

6.4.2.1 Spherical Particles:

For a spherical monomer, the following mass/radius relationship holds:

$$m_p = \frac{4\pi}{3} \rho_p r_p^{\,3} \quad (\rho_p \text{ is the particle density}) \tag{6.45}$$

Thus, in the free molecular regime:

$$\lambda_p = 0.4892 \frac{k_B T}{\delta P \sqrt{m_g}} \sqrt{\frac{\rho_p}{r_p}} \tag{6.46}$$

or alternatively:

$$\lambda_p = 0.6210 \frac{k_B T}{\delta P \sqrt{m_g}} \frac{\rho_p^{\frac{2}{3}}}{m_p^{\frac{1}{6}}} \tag{6.47}$$

We see then that for spherical particles (or coalescing aggregating particles), the persistence length goes as the $-\frac{1}{6}$. As the particles aggregate and the clusters grow in size they have shorter persistence lengths, becoming diffusive on ever decreasing length scales.

6.4.2.2 Fractal Aggregates:

The aggregation of spherical monomers produce extended fractal aggregates with the above described relationship between mass and radius of gyration, written here for cluster mass m_p instead of number of particles N:

$$m_p = m_0 k_0 \left(\frac{R_g}{r_0} \right)^{Df} = \frac{4\pi}{3} \rho_p k_0 r_0^{3-Df} R_g^{Df} \tag{6.48}$$

m_0 = mass of monomer

ρ = mass density of monomers

D_f (fractal dimension) = 1.8 for 3D DLCA (continuum & Epstein)

= 1.9 for 3D BLCA

= 2.1 for 3DRLCA [95]

k_0 = fractal precursor (~1.3 for DLCA)

Care must be used in calculating the drag force on a fractal aggregate, since the *radius* of a fractal aggregate used in the Langevin equation and drag calculations is not

uniquely defined (mass is). Experiment has shown that in the continuum regime, for DLCA aggregates: $r_m \sim R_g$ [31]. In the free molecular regime we have seen [27,31]:

$$A_{CS} = k_{A,N} r_0^{\,2} N^{2x} = \pi r_m^{\,2} \tag{6.49}$$

$$2x \approx 0.92 \text{ (for BLCA, DLCA type aggregates)} \tag{6.50}$$

$$k_{A,N} \approx 2.9 \tag{6.51}$$

$$r_m = \left(\frac{k_{A,N}}{\pi} \right)^{\frac{1}{2}} r_0 N^x = k_x r_0 N^x \tag{6.52}$$

$$x \approx 0.46 \tag{6.53}$$

$$k_x \approx 0.96 \tag{6.54}$$

In this case, the free molecular drag can be seen as:

$$F_D = -\frac{4\pi \delta n_g m_g v_g r_m^{\,2}}{3} v_p \quad \left(r_p \prec\prec \lambda_g \right) \tag{6.55}$$

$$f_D = \frac{4\pi}{\sqrt{3}} \delta k_x^{\,2} N^{2x} r_0^{\,2} P \sqrt{\frac{m_g}{k_B T}} \tag{6.56}$$

The characteristic time is then:

$$t_c = \frac{m_p}{f_D} = \frac{\sqrt{3}}{4\pi} \frac{1}{\delta k_x^{\,2} r_0^{\,2} N^{2x} P} \sqrt{\frac{k_B T}{m_g}} m_p \tag{6.57}$$

The persistence length is found to be:

$$\lambda_p = v_p t_c = \sqrt{\frac{3}{4\pi}} \frac{k_B T}{\delta k_x^{\,2} P \sqrt{m_g}} \sqrt{\frac{\rho_p}{r_0}} N^{\frac{1}{2}-2x} \tag{6.58}$$

The persistence length is seen to vary as the $\frac{1}{2} - 2x$ power of the aggregate mass. Since x was shown to be ≈ 0.46, this means $\frac{1}{2} - 2x \approx -0.42$. This decrease in λ_p with increasing m_p (or N) follows our intuition that large clusters diffuse on smaller length scales than small clusters do.

6.4.4 Rnn and Rnns

Another important parameter in determining the rate of aggregation of particles within a system is the nearest neighbor distance R_{nn} between particles. As defined previously, $Kn_n = \frac{\lambda_p}{R_{nn}}$, so that λ_p and R_{nn} can determine whether the system will exhibit diffusive type or ballistic type aggregation.

An important consideration here is that for the collision of two aggregates, we may not be as interested in knowing how far apart the *centers* of the clusters are as their *boundaries*, since it is at those boundaries that the aggregates will collide and form a new structure. We define a *nearest neighbor surface separation* distance R_{nns}:

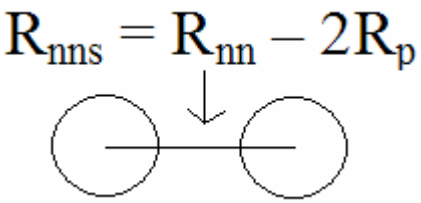

Fig 6.19: Visualization of nearest neighbor surface separation R_{nns}

$$R_{nns} = R_{nn} - 2R_p \tag{6.59}$$

$$R_{nns,ideal} = 2r_0\left[\left(\frac{f_{cp}}{f_{v0}}\right)^{\frac{1}{3}} N^{\frac{1}{3}} - \sqrt{1+\frac{2}{Df}}k_0^{-\frac{1}{Df}} N^{\frac{1}{Df}}\right] \quad (f_{cp} \approx 0.74 \text{ is closest packing fraction})$$

(6.60)

Eq. 6.60 introduces the mass scaling law into the nearest neighbor calculations in a way that is intuitively clear. The second term increases with decreasing D_f, meaning that less compact fractal aggregates (low D_f) fill the volume more efficiently and thus have smaller nearest neighbor surface separation distances. More compact structures, i.e. higher D_f, have larger surface separations.

We present a typical example:

$D_f = 1.8$, $f_{v0} = .001$, $k_0 = 1.3$

$$R_{nns} = r_0\left(18.09N^{\frac{1}{3}} - 2.51N^{\frac{5}{9}}\right) \tag{6.61}$$

$$\frac{dR_{nns}}{dN} = r_0\left(6.03N^{-\frac{2}{3}} - 1.39N^{-\frac{4}{9}}\right) \tag{6.62}$$

We plot these in Fig 6.20 with:

$$f(x) = R_{nns}(N) \tag{6.63}$$

$$g(y) = \frac{dR_{nns}(N)}{DN} \tag{6.64}$$

$$x = N \tag{6.65}$$

All distances are in units of the monomer radius, r_0.

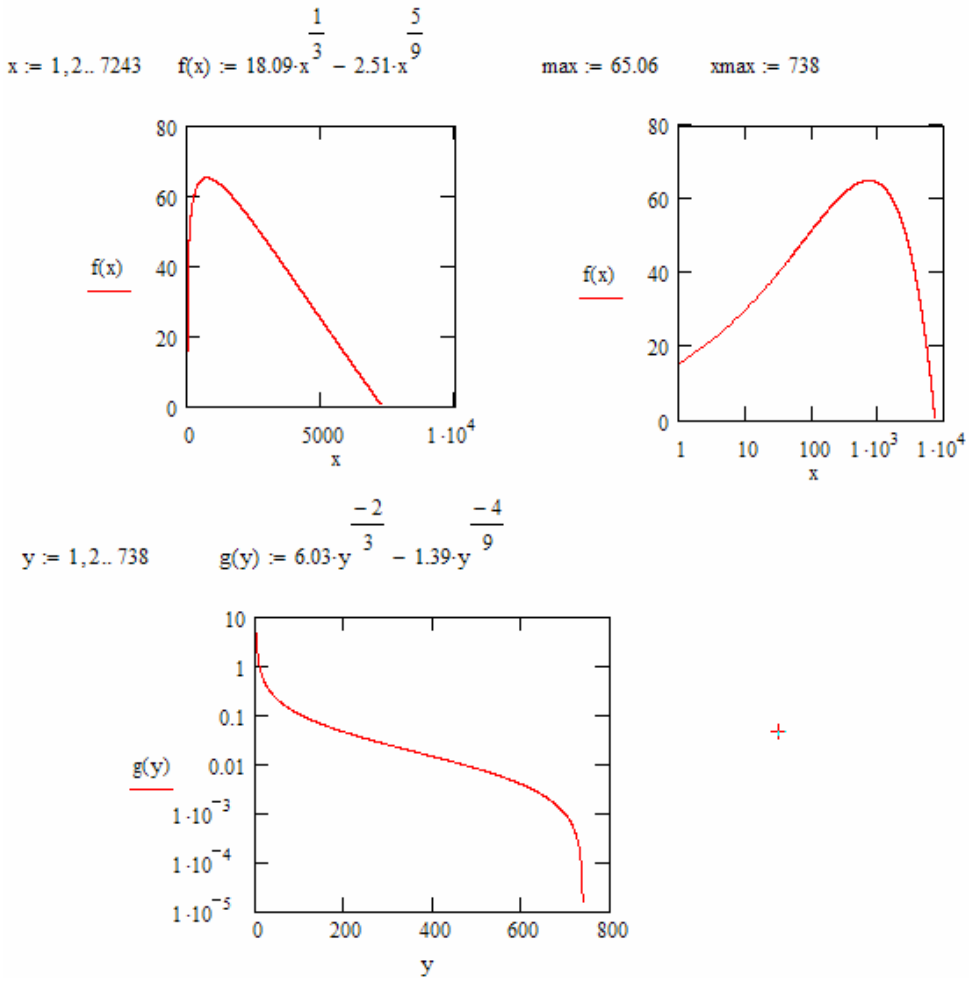

Fig 6.20: plots of R_{nns} and its derivative as function of cluster size.

It is easily seen that R_{nns} is not a monotonic function of the aggregate mass. The upper two plots are of R_{nns} as a function of N, one linear scale and one semilog for clarity. The top left shows both the presence of a maximum for R_{nns} and an approach to 0 as the aggregate mass approaches $N \approx 7200$. The maximum value of R_{nns} occurs and is determined from the lower graph of $g(y) = \dfrac{dR_{nns}(N)}{DN}$ which approaches 0 as the aggregate mass becomes $N \approx 740$. As the aggregate grows, R_{nns} initially *grows*, reaching a maximum value of $R_{nns,\max} \approx 65$ when the aggregate mass is $N \approx 740$. From

this point on, $R_{nns} \to 0$ with increasing mass. Near this point, the system would experience clear signs of cluster crowding and the onset of gelation due to the loss of free volume in which the clusters could move.

When $R_{nn} \succ\succ R_p$ we are justified in using the simplified expression for R_{nn} instead of the more complicated R_{nns} formula, as R_p then is a minor correction in the calculation of R_{nns}. This condition certainly holds for early times in low volume fraction aggregating systems.

We are reminded that in an infinite system of aggregates with $Df < 3$, it is inevitable for $R_{nns} \to 0$, as R_p grows without bound and has a larger exponent ($\frac{1}{Df}$) than R_{nn} ($\frac{1}{3}$). This approach to zero is marked by the crowding of clusters and the onset of gelation, where eventually all of the monomers are incorporated into a single system-spanning cluster. Since the most compact structure in a 3 dimensional space has $Df = 3$ (solid object), this provides a limiting case of growth of $R_{nns} \propto N^{\frac{1}{3}}$. This is exactly what happens in a system of coalescing liquid drops. Since the exponent for R_{nn} and R_p are equal, R_{nns} *does not* approach 0 with N, but rather continues to increase with the same power as R_{nn}.

For fractal aggregates in a finite system, gelation is not a certainty. It is possible for clusters to aggregate to the point where only a single cluster remains without the clusters ever crowding each other. A simple example illustrates this point. A system that starts with a very small number of monomers (i.e. 2) at a very low but fixed volume fraction will inevitably aggregate to form a single cluster, but the process will never be

limited by cluster crowding as the collision between the particles will be governed by the aggregation dilute-limit kernel up to the point where a single cluster is formed. At this point, the aggregation process will have ceased, and the remaining cluster will not span the system.

In any case, what we are interested in is the following: An aggregating system that starts in the ballistic regime will have aggregates whose persistence length λ_p starts at a value significantly larger than the mean interparticle surface spacing R_{nns}. This can be used as a definition for ballistic aggregation. As the aggregates grow, their λ_p values will shrink and R_{nns} values will *initially* increase. This will lead to a crossover at some point to a *diffusive* regime, where the motion of aggregates between collisions is that of random walkers. This happens for the simple reason that the growing clusters will diffuse on ever shrinking length scales even as they grow further apart, to the point that a cluster will change directions many times on average before colliding with another cluster. At some later time, λ_p and R_{nns} will again become approximately equal. This occurs when the clusters have grown large enough for the system begins to crowd and $R_{nns} \to 0$. For some brief period of time before gelation (and kinetic arrest), the kinetics may be well described as ballistic $\left(\lambda_p \succ\succ R_{nns}\right)$. The size distribution of the aggregates, however, *should not* have sufficient time to take on the characteristics of a ballistic type aggregation.

Here we consider a physical example. Using our previous values for the fractal dimension, prefactor, and volume fraction (same R_{nns}), we select some particle and medium parameters:

$r_0 = 50\text{nm}$

$P = 1\%\ P_{atm} = 1\text{kPa}$

$\rho = \rho_{water} = 1\text{gm/cc} = 10^3\ \text{kg/m}^3$

$m_g(N_2) = 4.65 \cdot 10^{-26}\ \text{kg}$

$k_B T(\text{room temp}) \approx 4.0 \cdot 10^{-21}\ \text{J}$

$$\rightarrow \lambda_p = \lambda_{p0} N^{\frac{1}{2}-2x} \approx 222.7 r_0 N^{-0.42} \tag{6.66}$$

In Fig 6.21 we plot (distances in units of r_0) :

$$f(x) = R_{nns}(N) \tag{6.67}$$

$$h(x) = \lambda_p(N) \tag{6.68}$$

$$x = N \tag{6.69}$$

$h(x) := 222.7 \cdot x^{-.42}$

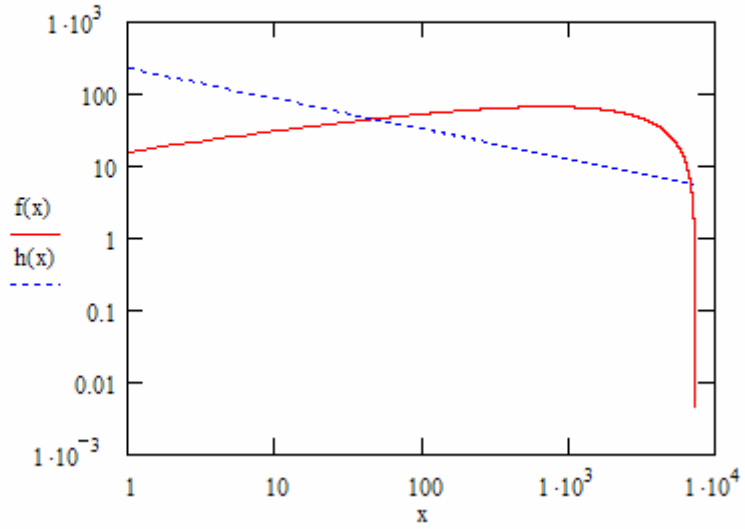

Fig 6.21: Plots of R_{nns} (f(x)) and λ_p (h(x)) as functions of cluster size for a specific set of system conditions.

The system initially starts in the ballistic regime with $\lambda_p \succ\succ R_{nns}$. As the system evolves, the growth of R_{nns} is dominated by the increase in the cluster separation R_{nn}, the size of the clusters being small comparatively. As the clusters grow, their persistence length decreases, which combined with the increasing R_{nns} leads to a regime crossover when $N \approx 47$. At this point, the system begins to become diffusive in nature as most clusters experience random changes in direction several times before colliding with other clusters. The finite initial volume fraction of monomers eventually becomes an important parameter in the evolution of this system as the average mass becomes $N \approx 1000$. At this point, the contribution to R_{nns} from the cluster perimeter radii attains a value on the order of R_{nn}, leading to a decrease in R_{nns} with increasing N; the surfaces of the growing clusters are getting closers. As the clusters continue to grow, it is their size that dominates R_{nns}. As N continues to increase, cluster crowding is inevitable, as is the crossover back to "ballistic" type kinetics near the gel point where λ_p, though small, becomes greater than R_{nns}.

The process of aggregation can be highly varied. In some sense, the regime of aggregation can be determined with 2 ratios between the four important parameters of the system: λ_g, R_p, λ_p, R_{nns}. The first ratio is the Knudsen Number $Kn = \frac{\lambda_g}{R_p}$, as defined previously. Kn describes the relationship between the motion of a particle or aggregate and the *medium,* namely the drag; $Kn \prec\prec 1$ indicates the continuum regime, and $Kn \succ\succ 1$ the free-molecular. The second ratio is the nearest neighbor Knudsen number, previously defined as $Kn_n = \frac{\lambda_p}{R_{nn}}$, which we redefine here as:

$$Kn_n = \frac{\lambda_p}{R_{nns}} \tag{6.70}$$

. When $Kn_n \succ\succ 1$, the motion of particles is ballistic. When $Kn_n \prec\prec 1$, the motion is diffusive. Kn_n describes the relationship between the motion of a particle or aggregate and *other particles or aggregates*.

Finally, R_{nns} as an individual parameter is useful in that $R_{nns} \to 0$ indicates the onset of cluster crowding/gelation.

6.4.4 Kinetics:

In the Epstein regime, the kinetic exponent is found to be z ~ 0.8 from Monte Carlo simulation [27]. From theory, we found z ~ 0.73 in the dilute limit [27].

The kinetic exponent for all three regimes (ballistic, Epstein, continuum) has been verified by computer simulation. The importance of the above arguments is that the evolution of the kinetic exponent from the ballistic to Epstein regimes might in fact pass from z ~ 2.2 (ballistic) to z ~ 0.8 through the range of z = 1.0 , a value normally indicative of *continuum* kinetics. A z of 1.0 in this case *would not* indicate continuum regime for aggregation, though the kinetics and resulting size distribution may be reminiscent of this. To resolve this, we need to make clear, then, whether or not the crossover from ballistic to Epstein regimes represents a sharp change in the kinetic exponent from ~ 2 to ~ 0.8 or a continuous one.

6.4.5 Simulation:

6.4.5.1 Procedure:

In order to resolve the above questions, we have carried out a series of Monte Carlo simulations of the aggregation of dispersed particles at low volume fraction in a gaseous medium. The varied parameter was the persistence length λ_p of the monomers. Adjusting this parameter has the same effect as varying the pressure of the gas in the aggregation chamber. With lower gas pressure, the initial persistence length of the monomers is higher, leading to more ballistic type aggregation. At higher gas pressures, diffusive motion and DLCA-type aggregation predominate. Specifically we study the kinetics, cluster size distributions, and morphologies of aggregates formed.

A dilute volume fraction of $f_v = 0.001$ was chosen for our simulations, with the number of monomers set to 10^5. Experimental systems often have volume fractions *significantly* lower than this value as well as particle numbers many orders of magnitude higher. It has been shown in previous simulations, however, that this volume fraction does represent reasonably well an approach to the "dilute-limit" (zero volume fraction) that is implied by the Smoluchowski coagulation equation [27,40,64]. The number of particles used, though not as high as we would desire, does allow us to see a developing size distribution that we can analyze and compare to theory.

The simulations generally follow the stand PBC MC prescription of particle placement and selection. After cluster selection a random number generator is used to determine whether the motion of this particle/cluster will be ballistic or diffusive. The probability is set such that the expectation value of the number of steps required for the particle to alter its direction of motion will yield a particle motion that *on average* persists ballistically for a distance equal to the persistence length. If ballistic, the particle is moved a distance proportional to its thermal velocity $\left(v \propto \frac{1}{\sqrt{N}} \right)$ in a direction parallel

to its previous direction, the *initial* direction of motion for the monomers having been set randomly. If the motion is found to be diffusive, the particle is moved a distance $r_{move} \propto D^{\frac{1}{2}}$ in a *random* direction, where $D \propto \frac{1}{A_{CS}}$ is the particle diffusion constant in the free molecular regime. In an earlier version of the program, the particle was set to move *exactly* the persistence length before changing directions, but this is unrealistic in that the thermal forces on the particle due to medium molecules are stochastic in nature. The persistence length measures the *characteristic* length for ballistic motion, not the exact length.

Here we need to clarify a point about time scales. Traditionally, in ballistic and diffusive MC simulations, one time unit represents the time it takes all monomers in the system to move on average 1 diameter (see Simulation Methods above). Since this simulation involves both ballistic and diffusive motions, we have to be careful about our time scaling. We can get an ideal about the time scale from our above equations for the Epstein drag force and our knowledge of the thermal velocity of the particles. The time required for monomer to move a distance $d_0 = 2r_0$ in the ballistic case is:

$$t_{0,b} = \frac{2r_0}{v_{p0,rms}} = \frac{4}{3}\sqrt{\frac{\pi\rho_p}{k_B T}} r_0^{\frac{5}{2}} \tag{6.71}$$

The time required *on average* for a monomer to move this distance in the diffusive case (Epstein) is found as follows:

$$< x^2 > = (2r_0)^2 = 6Dt_{0,d} = 6\frac{k_B T}{f_{drag,Ep}} t_{0,d} = \frac{6(k_B T)^{\frac{3}{2}}}{7.26\delta P\sqrt{m_g}} \frac{1}{r_0^{\,2}} t_{0,d} \tag{6.72}$$

$$\rightarrow t_{0,d} = 4.84\delta P \frac{\sqrt{m_g}}{\left(k_B T\right)^{\frac{3}{2}}} r_0^{\ 4} \tag{6.73}$$

What we are interested in is the ratio of these numbers:

$$\frac{t_{0,d}}{t_{0,b}} = 2.05\delta \frac{P}{k_B T}\sqrt{\frac{m_g}{\rho_p}} r_0^{\frac{3}{2}} \tag{6.74}$$

Using an example, we see that for:

$\delta = 1.36$

P = 1000Pa

T = 298K

$m_g(N_2) = 4.65 \cdot 10^{-26}$ kg

$\rho = 1000$ kg/m^3

$$\frac{t_{0,d}}{t_{0,b}} = 1 \rightarrow r_0 = 360nm \tag{6.75}$$

So, for this combination of parameters, our simulation would have the proper relative time scaling $\left(t_{0,d} = t_{0,b}\right)$ for both diffusive and ballistic motion for monomers with diameter of $\approx 0.7\,\mu$m. Of course, all of these parameters can be varied continuously. For a different set of particle/medium conditions, the time increment for a ballistic movement vs. a diffusive movement would have to be adjusted accordingly.

6.4.5.2 Morphologies/Fractal Dimension:

In Fig. 6.22 we display an example of the ensemble Df for $\lambda_{p0} = 10^3$ (ballistic case) at a time when the average cluster mass has grown to $N \approx 10^3$. D_f is measured to be 1.84 ± 0.03.

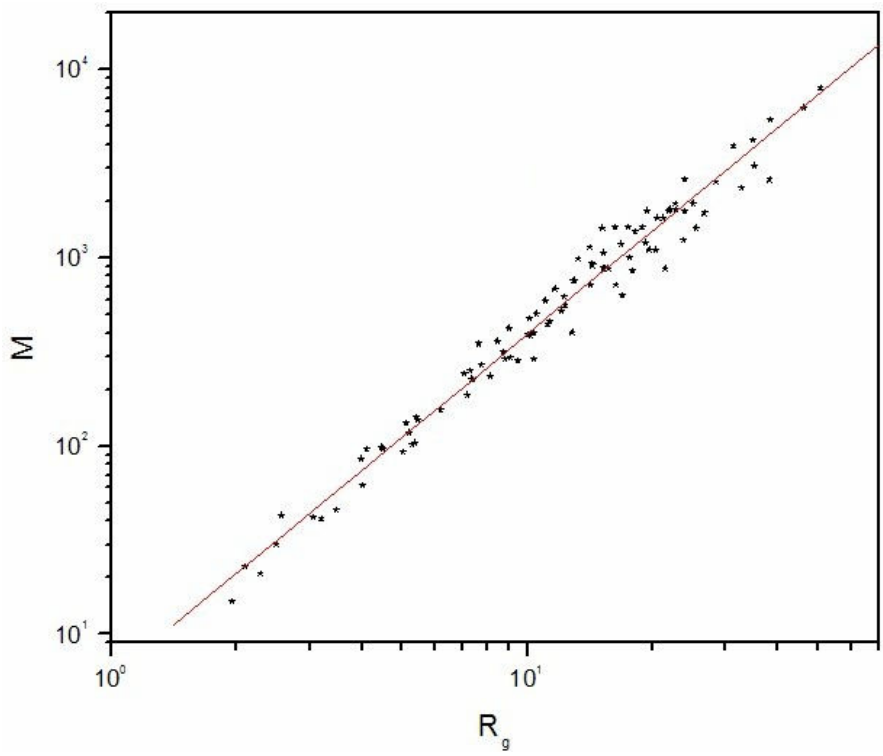

Fig 6.22: Ensemble Df for $\lambda_{p0} = 10^3$. Df is found to be 1.84 ± 0.03. Average cluster size is $N \approx 10^3$.

Fractal dimensions for all simulated values of λ_{p0} when $N \approx 10^3$ are shown in Fig. 6.23.

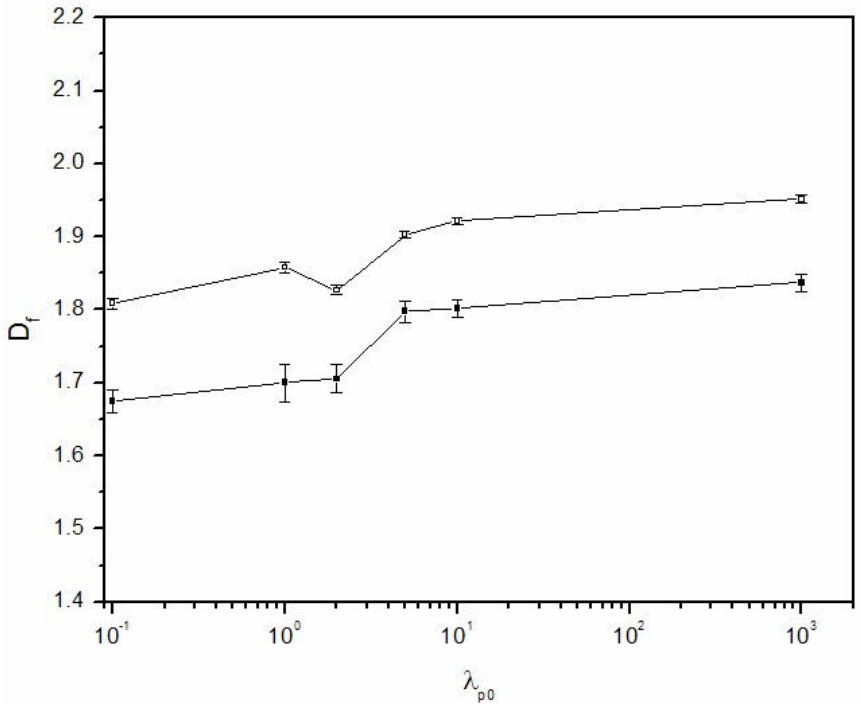

Fig 6.23: Ensemble Df (filled squares) and structure factor Df (open squares) for all values of λ_{p0} when $N \approx 10^3$. Standard error bars shown.

We notice a trend of increasing D_f with λ_{p0}. This is in agreement with our expectations that higher values of λ_{p0} lead to more ballistic type aggregation, with a known value of $Df \approx 1.9$ [41-43], and lower values of λ_{p0} lead to diffusive type aggregation for which the fractal dimensions is ~ 1.8, as seen in recent Monte Carlo simulations in the Epstein regime (free-molecular diffusive) [27].

In Fig. 6.24 we show the plots of the structure factor for our various choices of λ_{p0}.

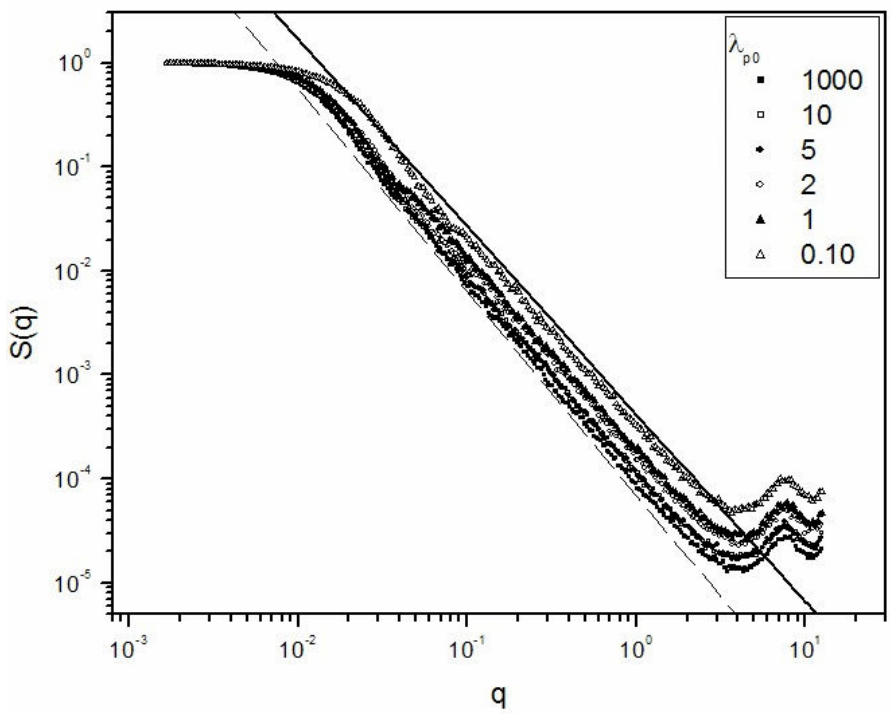

Fig 6.24: S(q) for all values of λ_{p0} when $N \approx 10^3$. The highest value of λ_{p0} (1000) gives a slope of ~ 1.95 (dashed fit line) while the lowest (0.1) gives ~ 1.80 (continuous fit line).

Notice that at higher values of the initial persistence length, the fractal dimension is seen to be ~1.95, again close to the known value of D_f for BLCA aggregates. At lower values of λ_{p0}, the fractal dimension is closer to 1.80, as expected for diffusive aggregation. This is perhaps more easily seen in Fig. 6.25 where $\frac{S(q)}{q^{-1.8}}$ is plotted vs. q, where one can more easily distinguish values of D_f near 1.8.

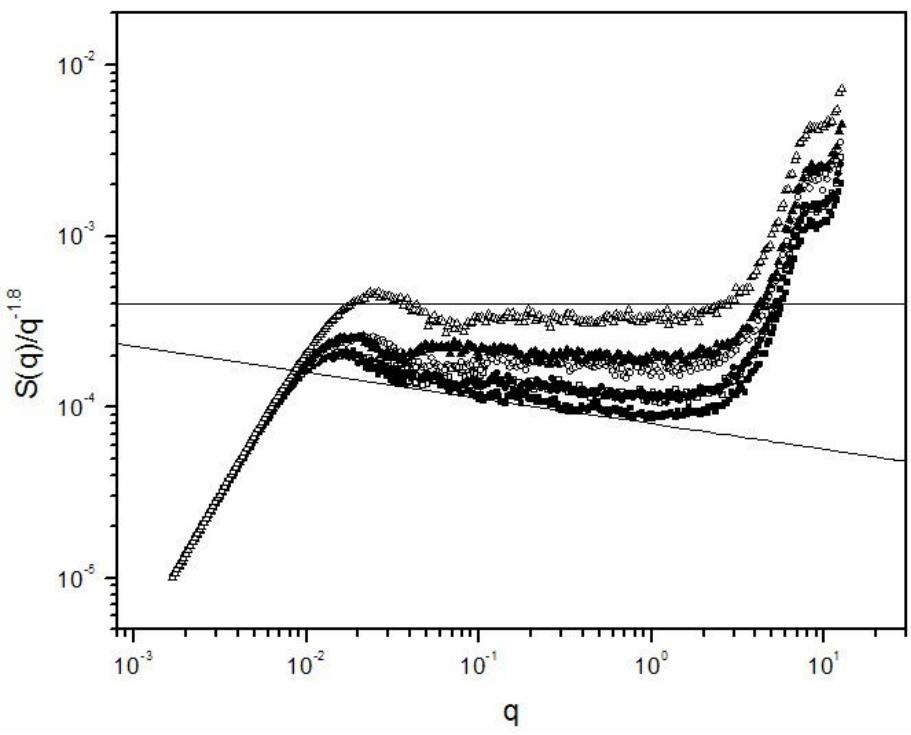

Fig 6.25: $\frac{S(q)}{q^{-1.8}}$ for all values of λ_{p0} when $N \approx 10^3$ plotted to more easily identify Df. The highest value of λ_{p0} (1000) gives Df ~ 1.95 while the lowest (0.1) gives Df ~ 1.80. Symbols follow definition from Fig 6.24.

Again in Fig. 6.23 we display the values of D_f with their error bars obtained from the structure factor for the all values of the initial persistence length. We see the same trend of increasing D_f with λ_{p0} that we observed with the ensemble method, with the structure factor yielding slightly higher values.

We conclude that D_f values throughout the whole regime of λ_{p0} are consistent with our expectations from previous DLCA, BLCA results.

6.4.5.3 Kinetics and Gelation:

As we vary the value of λ_{p0} from $1000d_0$ to $0.10d_0$, we find the kinetic exponent to evolve in a more or less continuous fashion. In Fig. 6.26 we display a plot of the scaled average cluster size vs. time for all values of λ_{p0}.

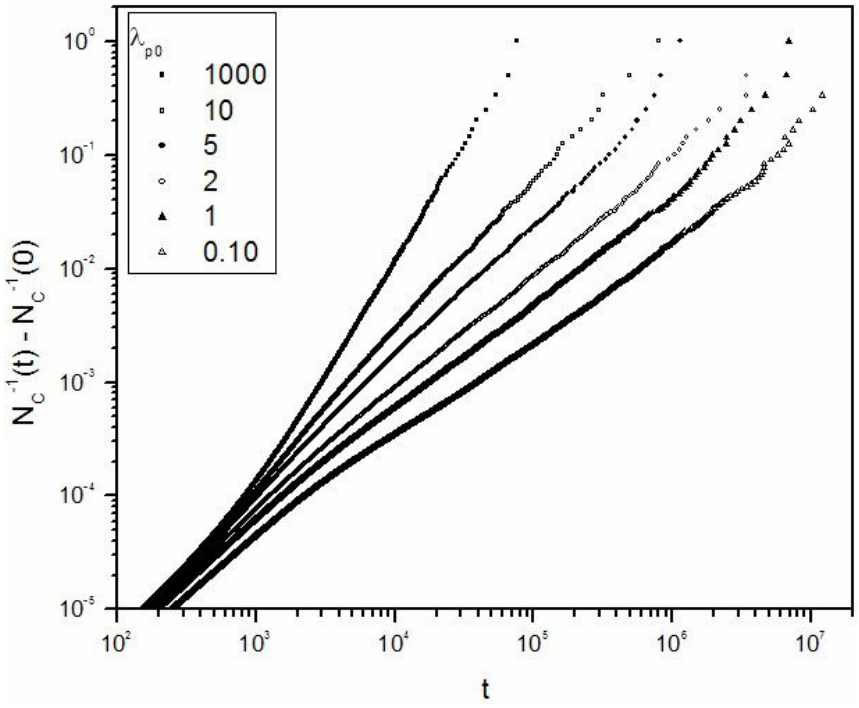

Fig 6.26: kinetics plots for all values of λ_{p0}. The highest value of λ_{p0} (1000) gives $z \sim 2$ while the lowest (0.1) gives $z \sim 0.80$.

For the largest $\lambda_{p0,}$ we clearly see the approach to $z = 2$ at late times, consistent with our BLCA predictions. In order to more easily distinguish the value of z, in Fig. 6.27 we plot the $\frac{S_{scale}}{t}$ vs. t, since most of our values lie near $z = 1.0$ (linear growth).

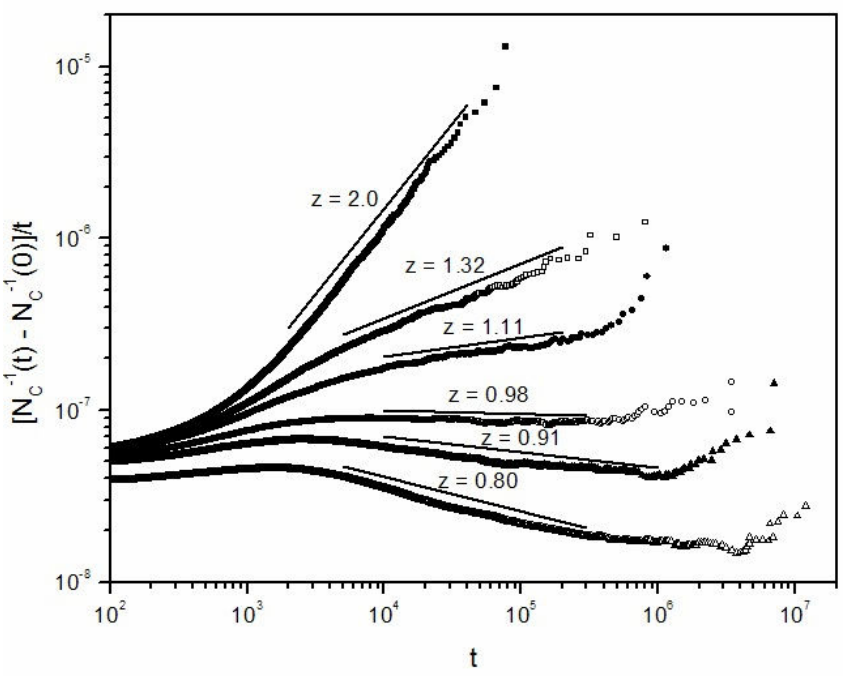

Fig 6.27: Fig 6.26: $\frac{S_{scale}}{t}$ for all values of λ_{p0} plotted to distinguish values of the kinetic exponent. The highest value of λ_{p0} (1000) gives z ~ 2 while the lowest (0.1) gives z ~ 0.80. Symbols indicate same values of λ_{p0} as in Fig 6.26.

For the lowest value of λ_{p0} (0.10), we obtain z ~ 0.80, in good agreement with both theory and recent simulation studies for the diffusive Epstein regime [27]. Interestingly, no sharp crossover appears in z for any choice of λ_{p0}. Rather, a smooth transition seems to be occurring, where intermediate value of λ_{p0} yield power law kinetics with exponents between the theoretically expected ~ 0.7-0.8 for Epstein and ~ 2 for BLCA. In fact, past the initial transient z = 1 which occurs before the average cluster size reaches 2, for λ_{p0} = 2 we find z ~ 1.0 for nearly the entire simulation. Thus we confirm that a kinetic exponent of ~1.0 *may not indicate continuum dynamics*. Rather, for the correct set of

conditions, z ~ 1.0 can be measured for aggregation in a rarified gas, intermediate between ballistic and Epstein conditions.

For several values of λ_{p0}, we see an enhancement in the kinetics at very late times, with the kinetic exponent increasing from its steady-state value. This is most clearly visible for λ_{p0} = 5, 1, 0.1. We see a hint of this enhancement at λ_{p0} = 10 and 2, but for a shorter period of time. It may be difficult to observe this enhancement in some circumstances because the statistics worsen when the average number of clusters in the system is less than about 10. Kinetic enhancement occurs, as discussed previously, due to the crowding of clusters and onset of gelation, and is confirmed by previous simulation studies by Fry et. al. [40]. In Fig. 6.28 we display the evolution of gel times with λ_{p0}. Also plotted are the times at which kinetic enhancement is observed to occur for various values of λ_{p0}.

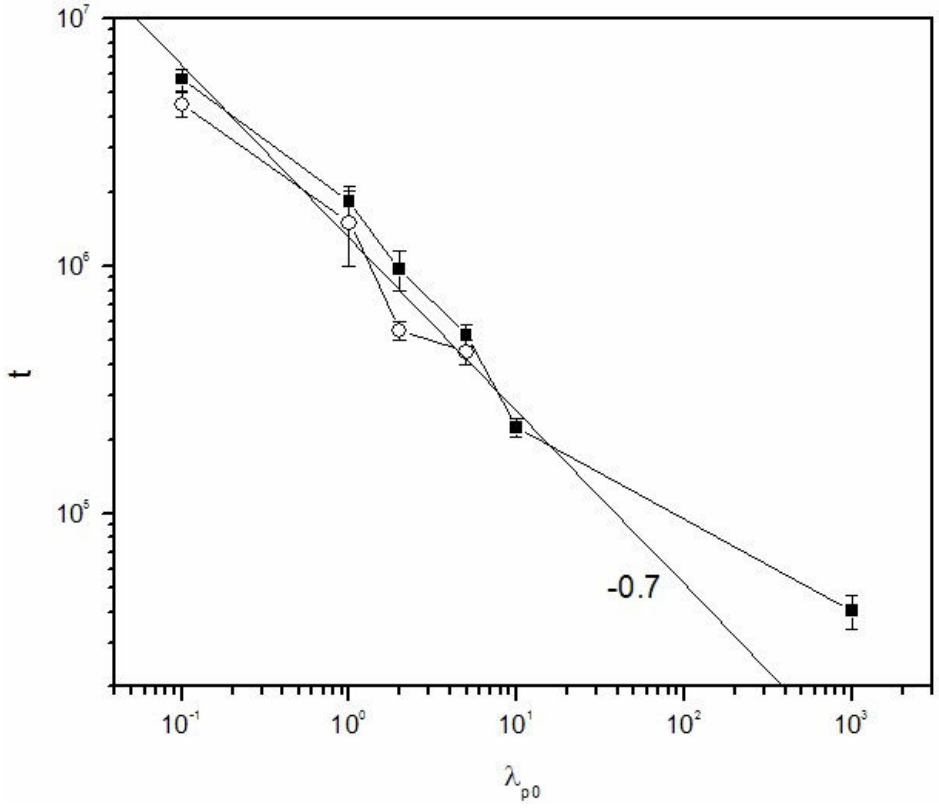

Fig 6.28: Gel times (squares) and time for kinetic enhancement to occur (circles) for all values of λ_{p0}.

Note that for small λ_{p0} (initially diffusive motions) the gel time can be quite large. We expect, but have not investigated that the gel time plateaus at very high values of λ_{p0}, indicating a limiting value of the gel time for *purely* ballistic aggregation (no medium). In the cases where we do see enhanced kinetics, we see a correspondence, also expected, between the value of the gel time for a particular choice of λ_{p0} and the point on the kinetic curves at which enhancement is seen to occur.

6.4.5.4 CSD:

Systems that begin as a collection of monomers aggregate and develop a size distribution which can be described at intermediate times ($0<t<t_{gel}$) by the scaling form given above in Eq. 5.157 [3,34,77]:

$$n(N,t) = M_1 s_p^{-2} \varphi(x) \tag{6.75}$$

In Fig. 6.29 we display the size distribution through plotting $s_p^2(t)n(N,t)$ vs. $x = \frac{N}{s_p}$ for $\lambda_{p0} = 10^3$, along with the fit curve to the scaling form.

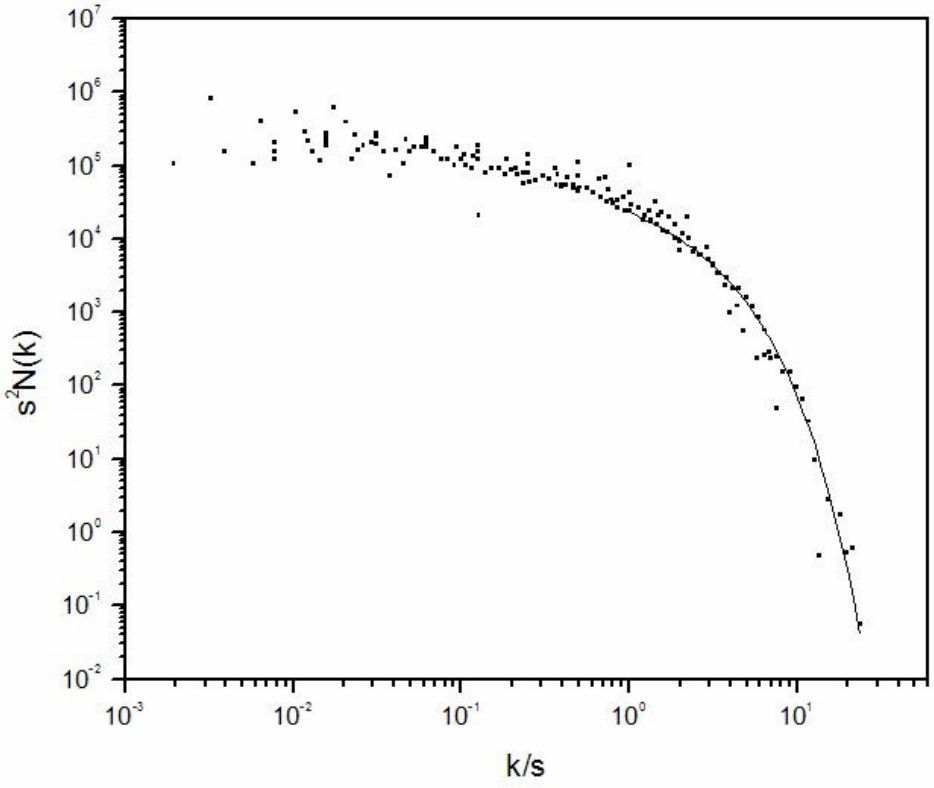

Fig 6.29: $s_p^2(t)n(N,t)$ vs. $x = \frac{N}{s_p}$ for $\lambda_{p0} = 10^3$, along with the fit curve to the scaling form.

The x>1 range is fit by the scaling form fairly well.

Since the kinetic exponent is related to the kernel homogeneity $z = \frac{1}{1-\lambda}$, we can calculate a kinetic exponent z_{csd} from the λ we find by fitting the size distribution to the above scaling form. We can compare z_{csd} to the corresponding z_{kin} from the kinetics data. We have done this in Figure 6.30.

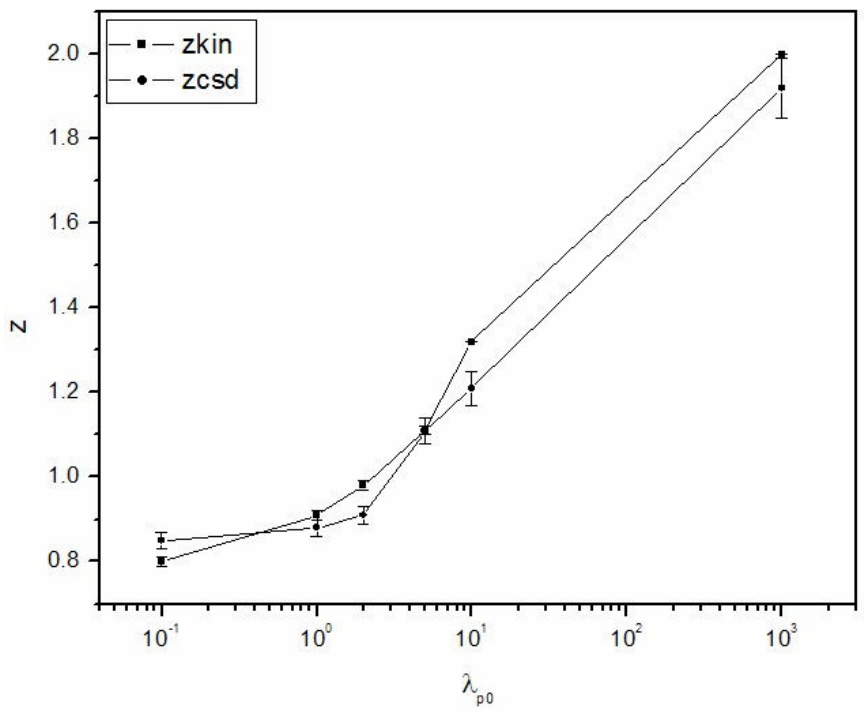

Fig 6.30: z from kinetics and CSD for all values of λ_{p0}

The agreement is rather good for the entire range of λ_{p0} and confirms that the homogeneity and kinetic exponent of the aggregation process evolve continuously from the ballistic values at high λ_{p0} to Epstein values at small λ_{p0}.

6.4.6 Conclusions:

We have performed simulations of the aggregation of particles in the free-molecular regime of particle motion, including the effect of crossover from ballistic to diffusive motion with a diffusion constant proportional to the particle cross-sectional area.

The fractal dimension of these aggregates is in agreement with previous findings for both free-molecular DLCA (Epstein Regime) [27] for low values of λ_{p0} and ballistic

aggregation for high values of λ_{p0}. Intermediate values of λ_{p0} have D_f between the ballistic and diffusive limits.

Kinetic exponents in this crossover regime are in good agreement with ballistic and free-molecular diffusive (Epstein) aggregation for the high and low values of λ_{p0} respectively. Interestingly, intermediate values for λ_{p0} do not begin with ballistic exponents gradually crossing over to diffusive. Instead for each value of λ_{p0}, a power law growth with time is seen to occur, with the value of z continuously changing as λ_{p0} is varied.

Cluster size distributions are seen to scale in accordance with theory, with homogeneity constants that are in good agreement with the kinetics data.

Finally, the idea of regime crossover is a realistic approach to the idea of aggregation in any number of circumstances due to the evolution of both Kn and Kn_n caused by the growth of particles during aggregation. Our findings indicating that continuum type dynamics ($z = 1$) can occur in aerosols under specific free molecular conditions, thus the kinetic exponent alone cannot distinguish free-molecular from continuum in this case.

Chapter 7 - Results: Aggregation in Colloidal Systems:

Here we present the results of research into a variety of topics related to aggregation in colloidal systems. We address the process of selective aggregation of binary mixtures of different sized colloidal particles coated with complementary chemical species(proteins) and the differences seen in kinetics and structural forms from those of standard DLCA models. Next, we present the results of simulations of DNA mediated colloidal aggregation, verifying the sharp temperature profiles observed by experimental researchers and analyzing the morphologies of structures seen at various temperatures. Finally we use a simplified model, the $\alpha - 2\alpha$ potential, to explore the effect of potential range and depth on systems resembling coulomb-screened solutions of proteins with high salt concentrations.

7.1 Selective Aggregation in Binary Colloids:

7.1.1 Introduction:

Much of the recent work in the field of aggregation has focused on tailoring the interaction between colloidal particles so that a greater control over the self-assembly of these particles (and hence their material properties) can be obtained. This can be achieved in several ways. One typical way to vary the interaction between charged colloidal particles is to add salt or surfactant solution of different molarities via the DLVO potential as mentioned above [96]. Another way to modify the interaction between colloidal particles is to induce a depletion interaction [97-99] by the addition of a non-adsorbing polymer (or a different sized colloid [100]). The strength and range of the interaction can be controlled in this case by changing the concentration and the length of the polymer chain. Depletion colloids are known to exhibit transient gel formation, reversible aggregation and eventual crystallization [101]. A different route has recently been taken by Hiddessen *et al.* [102] to control the assembly of *binary* colloidal particles. They introduce specific biomolecular cross-linking among smaller and larger diameter particles by coating these particles with complimentary biological proteins. These proteins behave as specific lock-and-key molecules and mediate adhesion only between two different sized colloidal particles but not among particles of the same size. A progressive series of structures from micelles to fractal-like elongated chains have been observed in the experiment as the ratio of the number of small to big particles was changed.

For a quantitative understanding of the structures formed in the above mentioned binary colloids, we have carried out a variation of the above OLMC DLCA model by considering a *bidisperse* system where a *selective* aggregation can occur only when two different-sized particles come into contact (those with complementary ligands). We should point out that our current study is totally different from past work in this context, where either (i) a non-selective aggregation among polydisperse particles was considered [103], or, (ii) a selective aggregation was studied among particles of the *same* size [104]. None of these previous studies seem to yield the variety of cluster morphologies observed in the Hiddessen *et al.* experiment. In contrast, our simulations reproduce much of the experimentally observed structures as a function of the ratio of the number of small to big particles. We also study quantitative measures of the aggregation process such as the kinetics of aggregation and cluster size distribution and compare our results to those for monodisperse off-lattice DLCA (and to some extent to RLCA) aggregation.

7.1.2 Model and Numerical Procedure:

In the model bidisperse system, we consider N_S = 20,000 small particles of radius r_s = 1 unit and a variable number (N_L) of large particles of radius r_L = 5 units. This closely resembles the particle sizes used in the experimental study of Hiddessen *et al.* who have used spheres of size 0.94 μm and 5.5 μm. Values of N_L are chosen to be 100, 200, 2000, and 10,000 for the number ratio $n_R = \frac{N_S}{N_L}$ to be 200, 100, 10, and 2, respectively. We chose these number fractions closely following the ones by Hiddessen *et al.* for a direct comparison of simulated cluster morphologies with experimental observations. Both the

small and large particles were randomly placed in a 2D simulation box of linear size L (in units of the *diameter* of the small particles) with a desired total area fraction of 10%.

Periodic boundary conditions were used in the simulation and the link-cell algorithm [40,64] was employed to significantly reduce computation time.

Particle selection and movement again follow standard MC prescription defined above with the following modifications. When a collision between two clusters occurred, a test was made to see whether the contact particles in the two clusters were of the same or different size. If the particles were of different sizes, the clusters were joined into one cluster and the aggregation process was allowed to continue. If the particles were of the same size, no joining occurred, and the clusters were permitted to diffuse away from one another in subsequent steps.

Besides the simulation being in 2D, the area fraction of 10% considered in the simulation is much larger than the volume fraction (typically 10^{-4} - 10^{-3}) used in the experimental study of Hiddessen *et al*. Our choice of an area fraction of 10% had much to do with the prohibitively long computer time taken for the observance of aggregation in a very dilute system. Still, even in our relatively dense case, the simulation shows remarkable qualitative similarity to the experimental results.

7.1.3 Results:

7.1.3.1 Morphologies and Df:

In Figs. 7.1(a-d) we display morphology of clusters obtained for various values of the number ratio n_R. For $n_R = 200$, we observe in Fig. 7.1a that the system quickly falls into a non-aggregating state where large particles are completely coated by small particles and no further aggregation takes place. Clusters in this case are either single

small particles or "micelles" with one large particle completely encased in small particles. This compares extremely well with experimental situation for a comparable value of n_R. One must be careful not to view the groupings of small particles together in this figure as clusters. Our simulation allows same size particles to come in contact but not to join into a cluster when they touch.

When n_R is decreased to 100 (fig. 7.1b), clusters involving more than a single large particle start forming. Predominantly the clusters involve only two large particles. Again, this is very similar to what was observed in the experiment. Larger clusters (up to 5 or more large particles) are seen when n_R is further decreased to 10 (Fig. 7.1c). It is interesting to note that the "cloud" of small particles seen in Fig. 7.1a and 7.1b has now been almost completely swept away by aggregation with large particles; almost all of the small particles are now involved in multiple particle clusters. The experiment also seemed to indicate this removal of stray small particles from the system.

For n_R =2, fractal clusters are readily formed as shown in Fig. 7.1d.

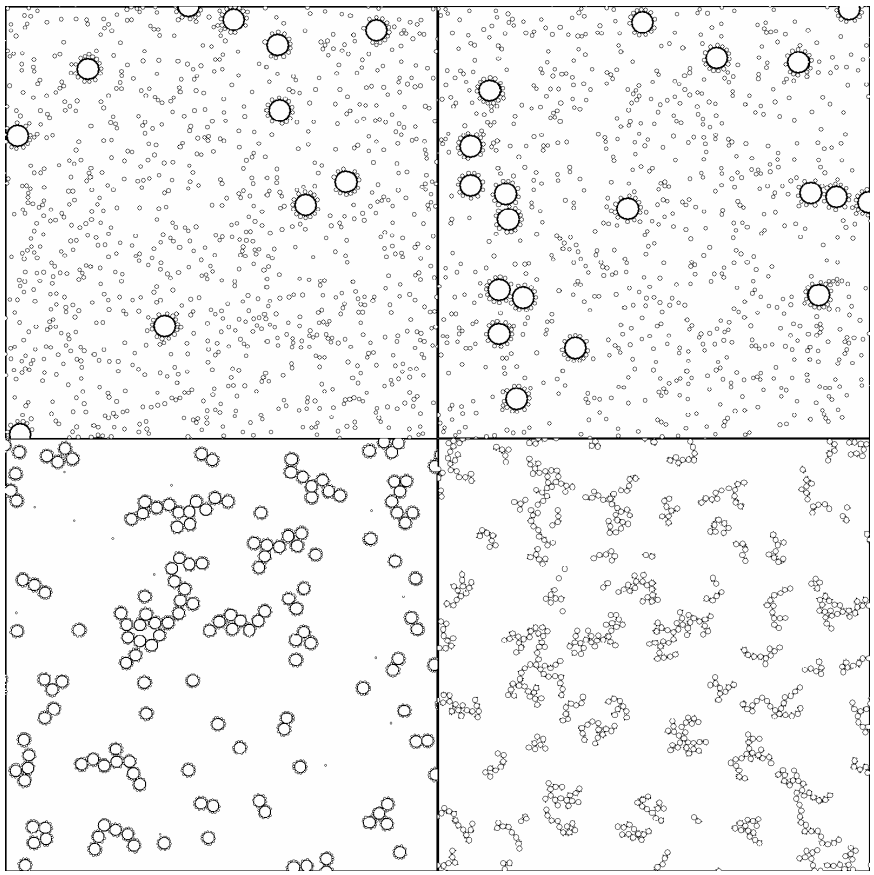

Fig 7.1:

a: (top left): Late time snapshots of 20,000 small particles with 100 large particles (number fraction 200:1). Notice the predominance of clusters containing only 1 large particle. The box dimensions are 420 x 420 in units of the *diameter* of the small particles. The current view is set to a 100 x 100 section. The apparent "clusters" of small particles alone are not actually clusters. The simulation allows small particles to touch each other but then diffuse away in later steps.

b: (top right): 20,000 small particles with 200 large particles (number fraction 100:1). In this situation most clusters contain only a few large particles. The box dimensions are 440 x 440. The current view is set to 100 x 100.

c: (bottom left): 20,000 small particles with 2000 large particles (number fraction 10:1). Notice the larger clusters containing several large particles as well as the almost complete absence of monomers. The box dimensions are 740 x 740. The current view is set to 200 x 200.

d: (bottom right): 20,000 small particles with 10,000 large particles (number fraction 2:1) at t = 12,650. Now we see many larger clusters containing several large particles and the complete absence of monomers. The box dimensions are 1450 x 1450. The current view is set to 400 x 400.

To quantify the fractal nature of these clusters, we have run the simulation for a much longer time (t = 1,997,850) than shown in Fig. 6.31d (t = 12,650). Such a late time (t = 1,997,850) configuration (Fig. 7.2) shows an ensemble of clusters quite similar to what has been observed in previous studies of 2d DLCA or RLCA models. The smaller particles cannot be seen in Fig. 7.2 but their presence becomes apparent when we zoom into one of the clusters (see Fig. 7.3).

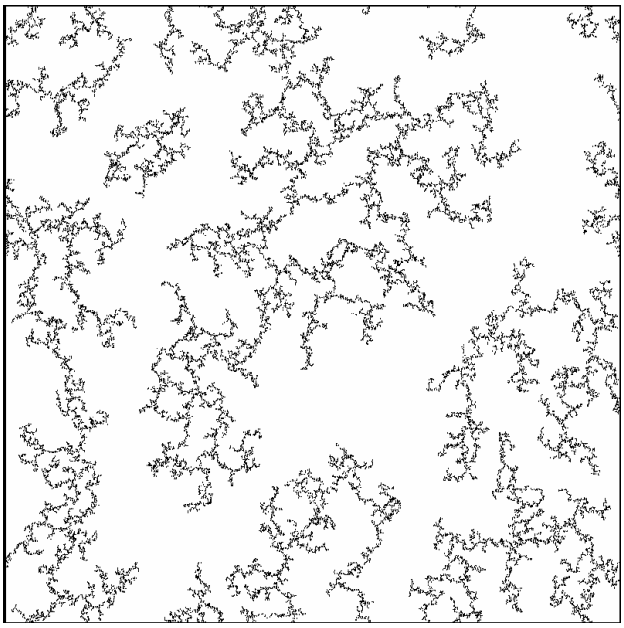

Fig 7.2: 20,000 small particles with 10,000 large particles (number fraction 2:1) at t = 1,997,850. We observe very large branched clusters containing hundreds of large particles as well as many small particles which at this scale are nearly invisible. The small particles act like glue for the large particles to stick together in clusters. The box dimensions are 1450 x 1450 as is the current view.

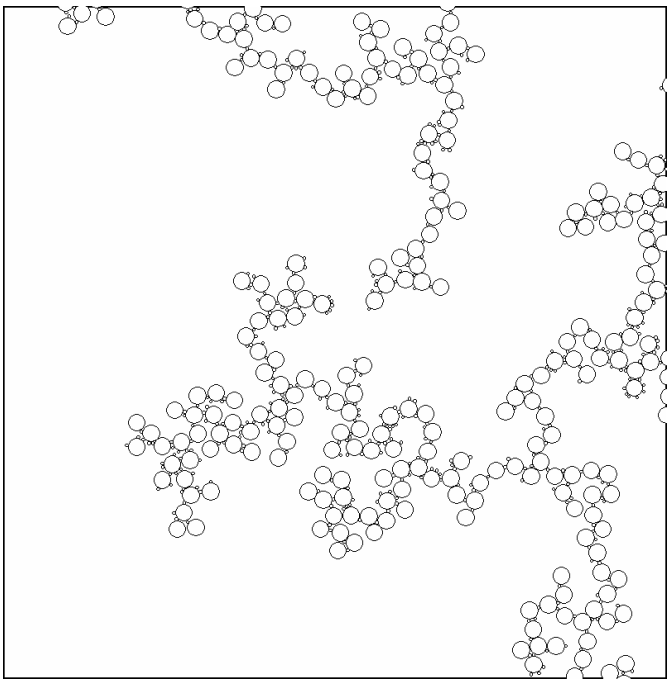

Fig 7.3: The same simulation as Fig. 6.32, but focused into a current view of 250 x 250. At this level of focus, we can see the small particles that were invisible in Fig. 6.32.

After being able to reproduce various cluster morphologies seen in the experiment, we now focus on the case for $n_R = 2$ and carry out a quantitative analysis of our results. First, we compute the fractal dimension of the ensemble of clusters in this case by plotting the mass M of a cluster versus radius of gyration R_g in an ensemble of clusters (Fig. 7.4). The fractal dimension of the clusters, D_f is then determined from the slope of such a log-log graph.

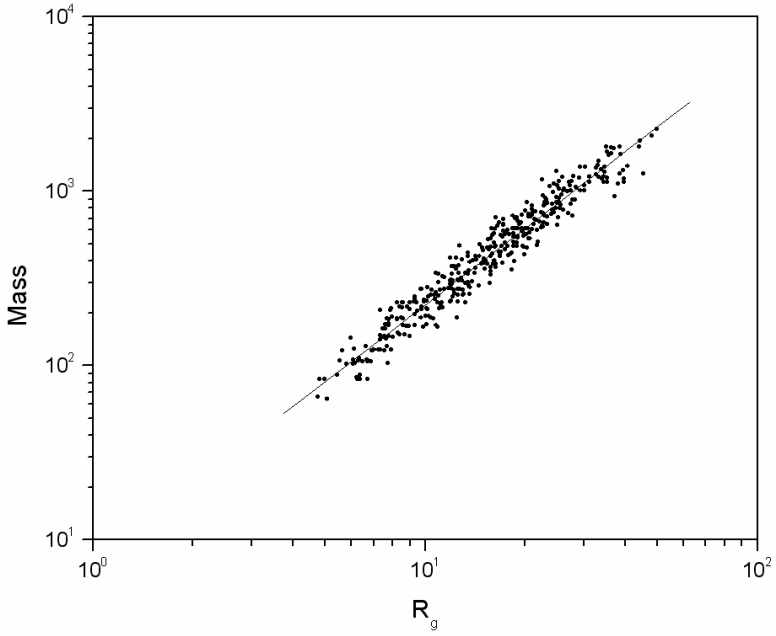

Fig 7.4: Fractal dimension of clusters formed with number fraction 2:1 at time t = 38,276 with N_c= 414. The value obtained from the slope of a linear fit to log(M) vs. log(R_g) is 1.46.

Fig. 7.5 is a graph of the evolution of D_f with time averaged over ten runs of the simulation. The value of D_f ranges from about 1.40 at t = 15,300 to 1.54 at t = 382,700.

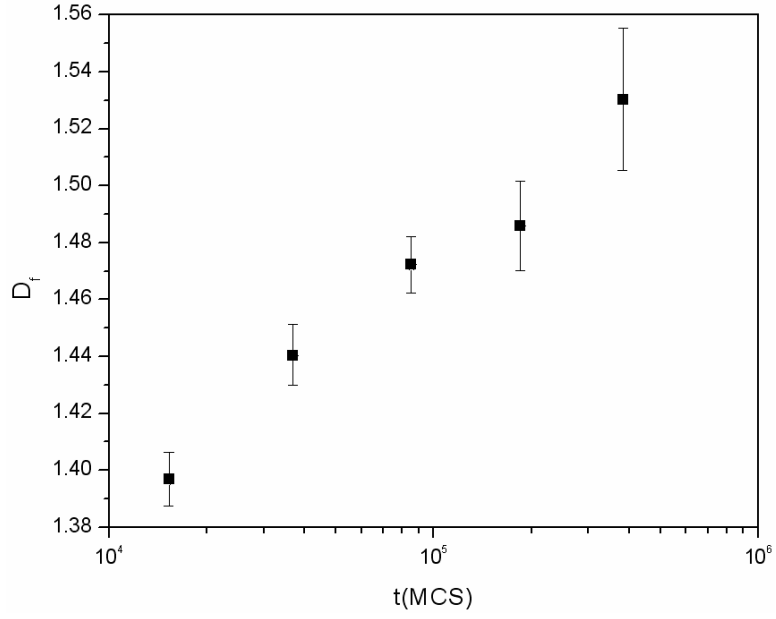

Fig 7.5: Fractal dimension vs. time in Monte-Carlo steps of clusters formed with number fraction 2:1 for times ranging from 10^4 to 10^6. The fractal dimension varies continuously from nearly 1.4 (similar to 2D DLCA of ~1.45) to a value of 1.54 consistent with 2D RLCA (D_f = 1.55) as the time evolves. All values were derived from a sample of ten runs. Error bars represent standard errors of values. The large standard errors at late times are due to a relatively smaller number of clusters in the system.

For early times, the value of the fractal dimension is similar to the accepted value for 2d DLCA [39]. This is remarkable given the selective nature of the aggregation process here. Although not all cluster collisions result in the formation of a new cluster, a sufficiently large number of these collisions produce aggregation at earlier times, presumably due to the availability of a large number of small particles at earlier times. In addition, the larger particles can be decorated by more than one small particles and this provides a considerably larger probability of aggregation than in past studies of selective aggregation with *same* sized particles [103], where the system behaves like a RLCA system over the entire evolution process. At later times, there are fewer small particles present in our system and now, most collisions do not lead to the formation of aggregates. It is possible then that the binary colloid system may cross over from a DLCA morphology at early times to an RLCA morphology at late times. The signature of this is present in the fractal dimension of the clusters which slowly increases from the 2d DLCA value of 1.4 and approaches the 2d RLCA [39] value of ~1.55.

7.1.3.2 Kinetics:

Results for the kinetics of aggregation is presented in Figure 6.36, where we show a log-log plot of the scaled average cluster size vs. time *t*.

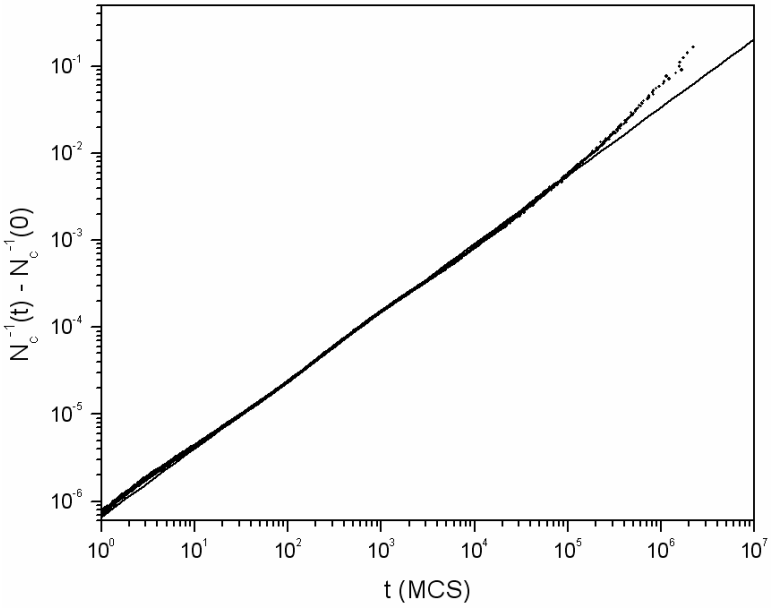

Fig 7.6: Graph of $N_c^{-1}(t) - N_c^{-1}(0)$ vs. t for $n_R = 2$. The straight line fit at the intermediate times yield the kinetic exponent $z = 0.74 \pm 0.05$.

The slope of this graph yields the kinetic exponent *z* [84]. The value obtained for z in this case is $z = 0.74 \pm 0.04$ in the intermediate time as shown by the straight line in the graph. Scaling arguments above [54,105] yield $z = 0.59$ in the dilute limit of 2d DLCA model. It is known, however, that the value of z increases from this dilute limit value as the system becomes dense due to cluster crowding [40,64]. Indeed, for intermediate times, the scaling argument yields $z = 0.67$ for the 2d DLCA model [54]. Even larger values of the kinetic exponent have been observed at intermediate times in simulations of 2d DLCA for larger area fractions [64]. There is also a hint of an increase of the kinetic exponent at later times in Fig.7.6 due to cluster crowding.

In contrast, one might expect that for larger values of n_R (n_R = 200,100, or 10), the system would enter a non-aggregating state at late times when further aggregation becomes impossible. In the case of number fraction n_R = 200, or 100 this is obvious, since each large particle can be surrounded only by a finite number of small particles. Once all of the large particles are completely surrounded, further aggregation halts. A corresponding slow down in kinetics is also observed for n_R = 10 (Fig. 7.7).

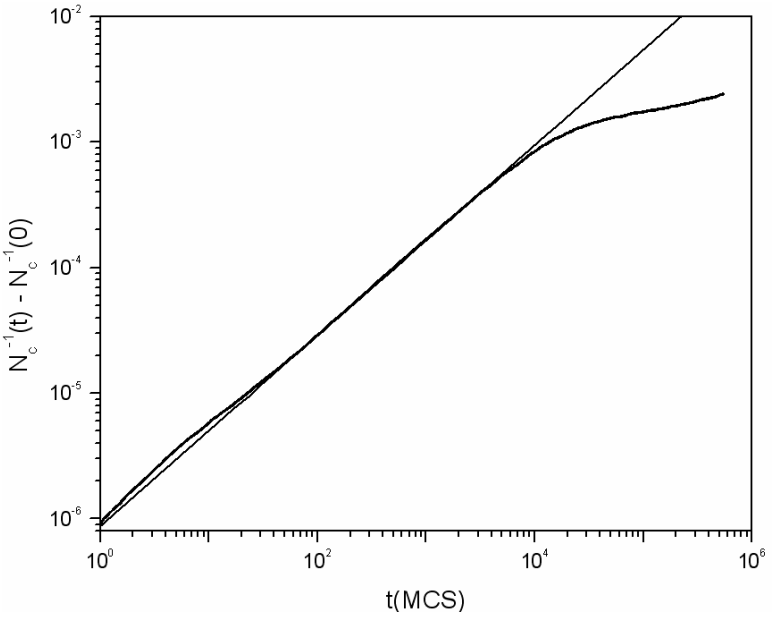

Fig 7.7: Same as in 7.6 except for n_R = 10. The straight line fit at the intermediate times yield the kinetic exponent $z = 0.74 \pm 0.05$. Note the slow down in the kinetics at late times.

Here, at intermediate times, the kinetic exponent is $z = 0.74 \pm 0.04$ as in the case of n_R = 2, but a distinct slowdown in the kinetics of aggregation is observed at late times. For n_R = 2 such a slowdown may occur but is difficult to observe in the simulations unless one considers late time studies in a very large system (with much larger number of particles but yet with a much smaller volume fraction). Likely, there is a critical number ratio,

dependent on the size ratio, for which kinetic arrest before gelation occurs. This remains a topic for further study.

7.1.3.3 CSD:

The similarity between the current simulation of binary colloids with $n_R = 2$ and 2d DLCA is further explored by computing cluster size distributions. In Fig. 7.8 we show the cluster size distribution at various times.

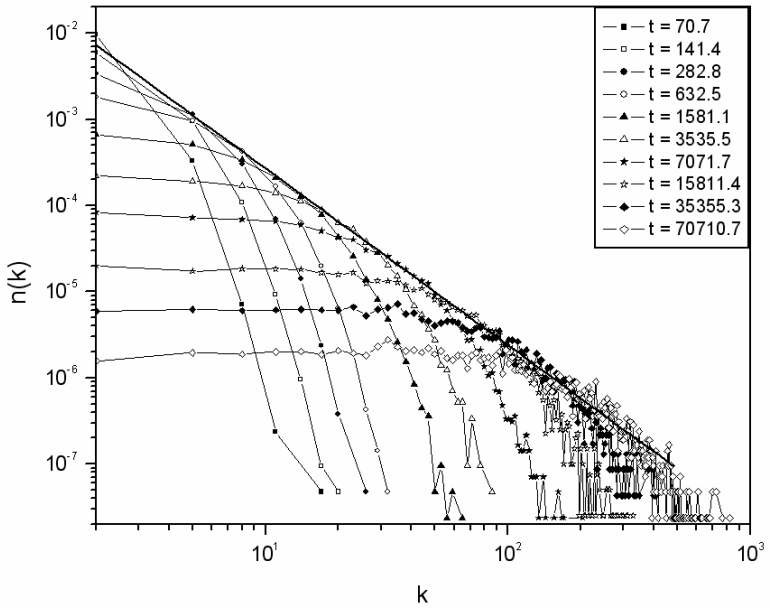

Fig 7.8: Cluster size distributions for various times during the simulation along with the common tangent line. The slope of the tangent line is -2.05 in good agreement with theory.

The common tangent line is included as well, yielding a slope of ~ -2.05, in good agreement with theoretical predictions [91]. In Fig. 7.9 we plot the scaled (and normalized such that the maximum value of the function is unity) cluster size distribution.

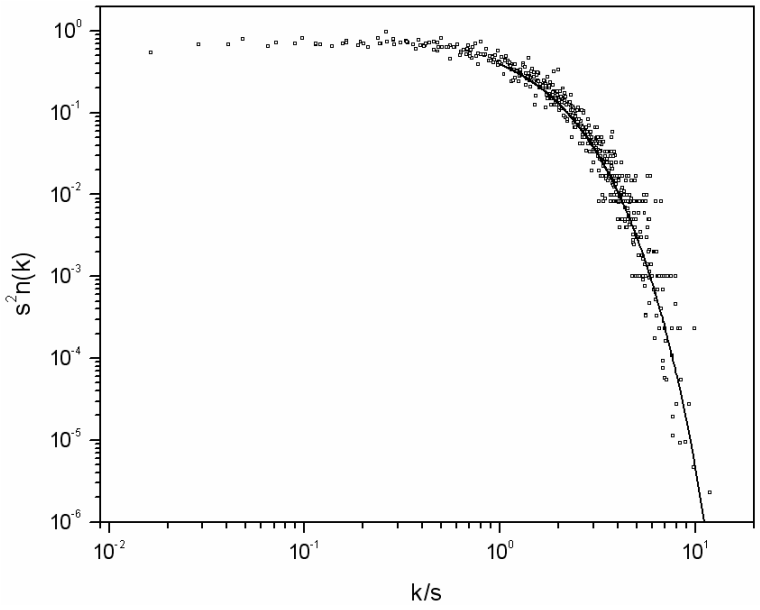

Fig 7.9: Scaled cluster size distributions along with the theoretical form (solid line) expressed in Eq. (1.1) with λ = - 0.35 and α = 1.35.

This graph demonstrates that a scaling form works well for the current simulations. For DLCA, the scaled cluster size distribution can be expressed as the scaling form given above in Eq 5.160 [34,84]:

$$\Phi(x) = Ax^{-\lambda}e^{-\alpha x}, \tag{7.1}$$

for large values of *x,* where $\lambda = 1 - z^{-1}$, and $\alpha = p - \lambda$. p = 1 is the order of the *average cluster size* we are using (s_p above). In our simulations, $p = 1$ and if we consider $z = 0.74$, we find $\lambda = -0.35$, and $\alpha = 1.35$. Fig.5 shows that Eq. (6.76) with these values of λ and α fit the scaled cluster size distribution quite well for large values of *x*.

7.1.4 Conclusions:

In summary, we have carried out a simulation study of selective aggregation in binary colloids with two different sized particles. By varying the number fraction of the

large to small particles, we have been able to reproduce the morphological characteristics of the clusters observed in experimental work of Hiddessen *et al.* The appearance of micelles, small clusters, and much larger branched structures depending on the number fraction of large to small particles follows almost exactly the same pattern as reported in the experiment. In addition, we have compared aggregation in binary colloids with the DLCA model by considering the fractal dimension, kinetic exponent, and cluster size distribution. The fractal dimension for the 2:1 number fraction starts out with a 2d DLCA value but crosses over to a larger value suggesting a DLCA to RLCA crossover in cluster morphology at late times. The kinetic exponent and the cluster size distribution, however, are consistent with 2d DLCA results. Further investigation of selective aggregation is certainly warranted, and a number of parameters are available to be adjusted in the search for a detailed understanding of this process. Those parameters include overall system volume fraction, size ratio of large to small particles, and number fraction. The determination of the conditions under which the system may enter a non-aggregating state is another alluring topic for further study. In addition, a fragmentation probability can also be imposed on the clusters which might lead to a steady-state *crystalline* morphology.

7.2 Aggregation-Fragmentation in a Model of DNA-Mediated Colloidal Assembly:

7.2.1 Introduction:

Here we present results from an OLMC simulation of DNA-mediated colloidal assembly. In this simulation, aggregation-fragmentation of a *binary* mixture of colloidal particles are studied through a simplified model of base-pair hybridization between complementary DNA strands attached to the particles. Bonding between monomers is modeled as a simple temperature sensitive A/B type interaction, where type A and B monomers can only bond to the opposite type (no A/A or B/B attachments allowed). The actual chemistry of base-pair hybridization is not included in the model.

To control the assembly of colloidal and nanoparticles in a totally novel yet effective way, several groups [22,102,106-111] have introduced *specific* biomolecular cross-linking among particles by coating these particles with complimentary biological complexes. Often these complexes are proteins or DNA molecules which behave as specific lock-and-key and mediate attractive interaction only between specific colloidal particles. A selective aggregation is induced by coating species *A* and *B* with single-strand DNA molecules (ssDNA) along with the addition of target ssDNA which can form links only between a pair of *A* and *B* type colloidal particles. The association between hybridized DNA strands is reversible upon heating above a 'melting' temperature T_m. On one hand, the DNA-driven assembly of nanoparticles can be used as building blocks of complex materials synthesis, and, on the other, the assembly can be used to detect mutations in specific DNA sequence. For both of these applications, one needs to

quantitatively understand how the dissolution of the DNA-driven assembly depends on the size of the particles and on the surface density and interaction strength (which might be controlled by changing the dielectric properties of the surrounding medium) of the DNA molecules. The morphology of the assembly as a function of this large set of variables is extremely important to understand to control the material properties (such as optical and electronic properties of gold nanoparticle assembly). Moreover, if the dissolution of the assembly is very sharp, one can possibly map DNA sequences on the macroscopic phase behavior of the nanoparticle assembly.

There is a wealth of experimental data on dissolution of DNA-linked nanoparticle assemblies. For example, Jin *et al.* [22] have analyzed the dependence of the dissolution temperature on the size of the particles and on the surface density and interaction strength of the DNA molecules. As the DNA coverage is increased one obtains higher dissolution temperature. Below the dissolution temperature the particles aggregate into a gel-like state, while even slightly above the dissolution temperature, the gel comes apart into much smaller clusters. The sharpness of the dissolution temperature strongly indicates that *multiple* DNA linkers are formed between each pair of particles. A mean-field model introduced by Lukatsky and Frenkel [21] reproduces the experimental observation of a sharp dissolution temperature. However, this mean-field model completely ignores cluster morphology and thus cannot provide a detailed description of the assembly or the dissolution process.

As a first step toward providing a detailed theoretical understanding of the morphology and dissolution of DNA-mediated colloidal assemblies, we have carried out computer simulations of reversible aggregation of a binary mixture of colloidal particles

through a simple model of base-pair hybridization between complementary DNA strands attached to the particles. The morphological structures of the clusters formed as well as the kinetics of growth are analyzed in our two-dimensional simulations. The parameters varied in this work include the coverage of DNA molecules on the particles, the number of possible DNA linkers between pairs of particles, the temperature, and the overall area fraction of colloidal particles. The fractal dimension and kinetic growth exponents for clusters formed near the melting temperature agree with those seen previously for two-dimensional diffusion-limited cluster aggregation (DLCA) models [64,91]. At intermediate temperatures, the clusters appear more compact, exhibiting the signs of local order. At higher temperatures, formation of large clusters is not favorable under the action of temperature-dependent fragmentation and the system eventually reaches a steady state consisting of a collection of small aggregates. In all cases studied, the temperature profiles are sharp, indicating that the selective hybridization process provides a highly sensitive measurement tool. The kinetics curves obtained from simulations are comparable to those of 2D DLCA in the case of lower temperatures, while for intermediate temperatures, a complicated behavior is observed and a possible explanation based on coordination number and local order is offered. Steady state behavior of the average cluster size at higher temperatures is analyzed in terms of a mean-field aggregation-fragmentation model [112,113].

7.2.2 Model and Numerical Procedure:

We model the experimental situation where species A and B are coated with ssDNA and the addition of target ssDNA can form links only between a pair of A and B type colloidal particles. The temperature dependent free-energy difference $\varepsilon(T)$ of a

double-stranded DNA molecule connecting a pair of *A* and *B* type colloidal particles is considered to have a form:

$$\varepsilon(T) = s\,k_B\,(T - T_m) \tag{7.2}$$

in the model [21] where T_m is the 'melting' temperature of the target DNA, k_B is the Boltzmann's constant, and $s = 10$. This expression represents the first term in the expansion of the exact free energy [114]. Lukatsky et. al. [21] refer to the work of Rouzina and Bloomfield [114], who report the entropy difference between the two states (helix and coil) as 25 cal/mol*K (or $12.5k_B$), modeled by Lukatsky et. al. as ~$10k_B$. This is translated into a probability of forming a bond between a pair of *A* and *B* type colloidal particles as:

$$p = \exp[-\varepsilon(T)/k_B T] \tag{7.3}$$

, while the probability of a previously formed bond being severed is *1-p,* following standard Metropolis MC methods. When $T \leq T_m$, the interaction is irreversible (*p = 1),* but as *T* is increased, fragmentation of clusters can take place.

To study the formation of DNA mediated assembly of colloidal particles, we use a modified OLMC algorithm. Initially, 10^4 unbonded particles (monomers) of each type (*A* and *B* with complementary DNA strands) are placed at random in a square box with PBC. We have considered several monomer area fraction (f_a) ranging from $f_a = 0.01$ *to 0.40*. Clusters are selected and moved according to standard MC methods (see above) within the continuum regime. After each unitary increment of MC time, a test is made for all system particles to determine what changes in bonding with neighbors have occurred. Particles of type *A* are allowed to bind only to particles of type *B*. For this to occur, the surfaces of the two particles must lie within a certain cutoff distance (in our case *0.1*

times the monomer diameter). A bond formed at some time *t*, is allowed to break at a later time with probability *1-p,* as previously mentioned. For each simulation, the total number of bonds for each particle (b_t) is set to a fixed value, as well as the maximum number of bonds between any two neighboring particles (b_n). The constraints (b_t and b_n) come from geometrical limitations in 2 dimensions and not from any chemical considerations of DNA itself. For example, in the case of $b_t = 10$ and $b_n = 3$, a specific particle may make up to *10* bonds with neighboring particles of the opposite type, with up to *3* of those bonds with a particular neighbor (Figure 7.10).

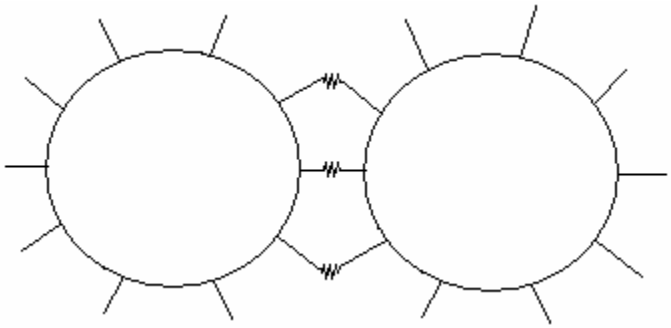

Fig 7.10: Bonding between 2 monomers in a simulation with $b_t = 10$ and $b_n=3$. DNA linkers are assumed to be distributed approximately symmetrically over the surface of the monomers, limiting the number of possible "linker" contacts between monomers.

At $T = T_m$, only aggregation can take place as bond breaking is not possible. When $T > T_m$, formation and severing of bonds between particles can take place and evolution of the system is controlled by both an aggregation and fragmentation kernel. The aggregate structures formed in our simulations are, as in the case of normal DLCA/RLCA type simulations, "free-floating", that is not attached to an underlying substrate. Therefore, we ignore particle/substrate type interactions.

7.2.3 Results:

7.2.3.1 Morphologies:

In Figure 7.11, we show snapshots of the structures formed for temperatures T= *1.00, 1.02, 1.04* , and *1.05* respectively in units of T_m. These images are taken at a late-time in each simulation; late-time refers to a time at which the cluster number has reached a plateau. In each case the monomer area fraction is $f_a = 0.10$ with $b_t = 10$ and $b_n = 3$.

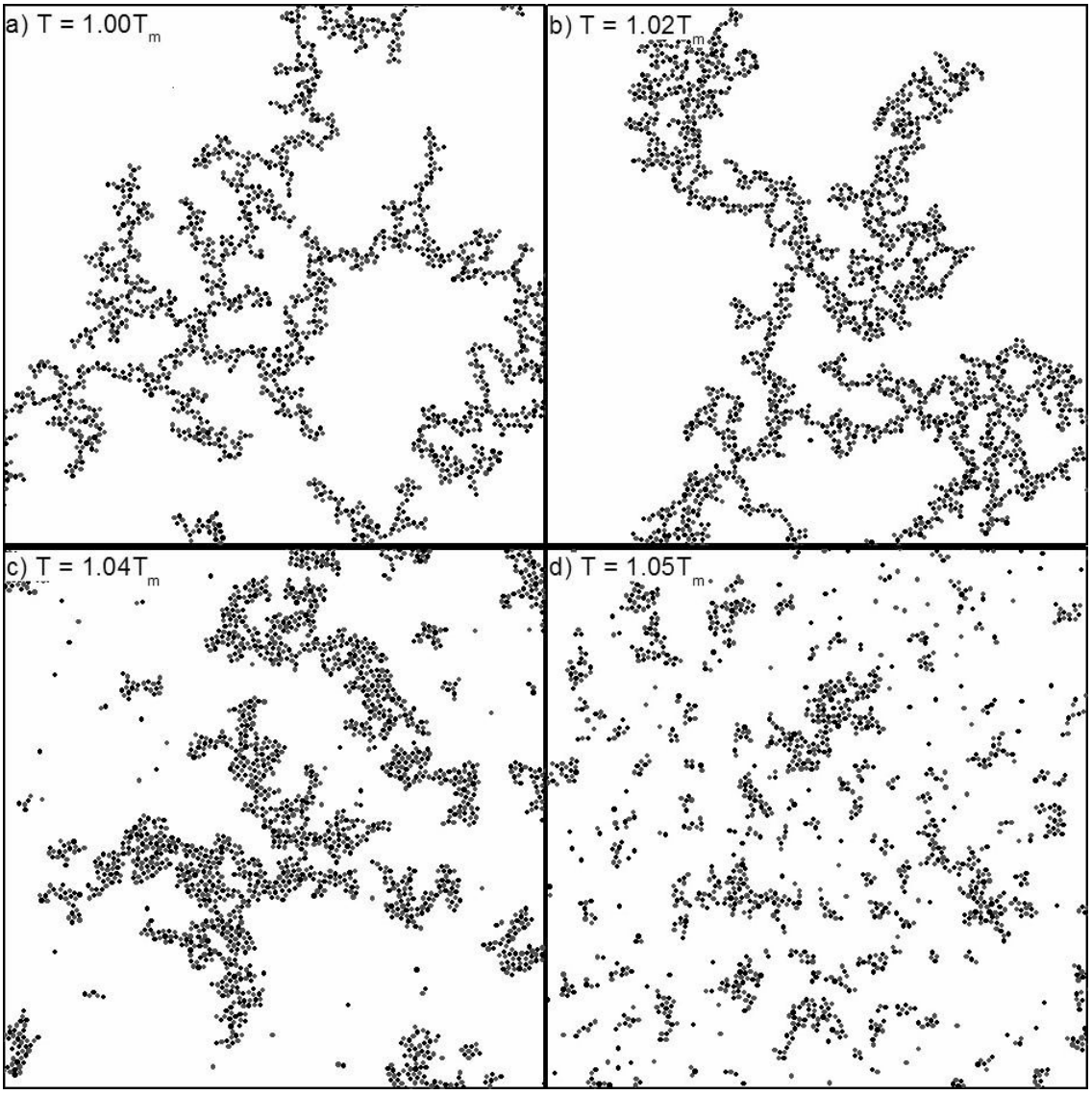

Fig 7.11:

a (upper-left): Late-time (t = 24, 444) snapshot of a system at the DNA 'melting' temperature T_m. At this temperature only aggregation events occur and a gel-like morphology is observed. Here $b_t = 10$, $b_n = 3$, and $f_a = 0.1$.

b (upper-right): Same as in a) except $T = 1.02T_m$ and t = 98, 349. In comparison to the aggregation-only morphologies seen at T_m, the clusters here begin to exhibit some compactification and local ordering due to fragmentation and reaggregation.

c (lower-left): Here $T = 1.04T_m$ and t = 93, 905. A higher degree of compactification is observed, and local ordering becomes more clear. Some of the clusters have begun to dissolve as can be seen by the presence of monomers and smaller clusters.

d (lower-right): Now $T= 1.05T_m$ and t = 949, 489. Fragmentation is highly pronounced here as can be seen by the proliferation of small clusters. The whole system is on the verge of dissolution.

Cluster formation at the melting temperature ($T = T_m$) is *irreversible* and the fractal morphology of the system is quite similar to DLCA aggregates in two dimensions (Fig. 7.*11d*). The binary nature of the interactions between particles does not seem to alter the overall structure of the aggregates [25].

As shown in Fig. 7.12, the fractal dimension of these clusters rises from a value of $\approx$ *1.40* to over *1.50*.

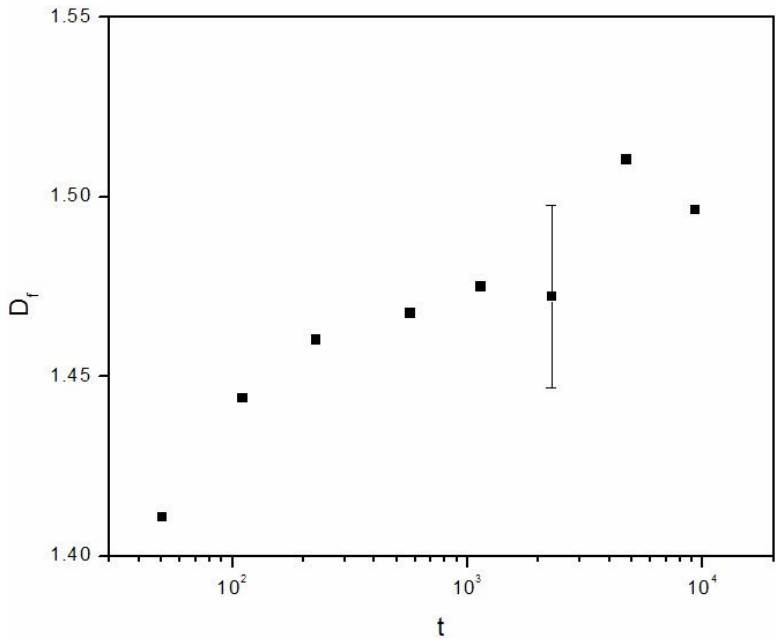

Fig 7.12: Evolution of the fractal dimension D_f with time in the case of an overall area fraction of f_a = 0.10 with bonding configuration b_t=10 and b_n=3 at the melting temperature T_m. The clusters begin to form with a fractal dimension close to that of 2d-DLCA value (D_f = 1.4) and evolve toward a higher value, closer to the 2d-RLCA value (D_f = 1.55). A "characteristic" error bar is shown. Error bars for other data points are of similar magnitude.

At later times, many collisions between clusters do not lead to an *A-B* binding hence aggregates do not form in every collision. It is possible then that the binary colloid system may cross over from a DLCA morphology at early times to a reaction-limited (RLCA) morphology at late times [25, 104]. The signature of this is present in the fractal dimension of the clusters which slowly increases from the lower value of *1.4*, passes through *1.45* (the accepted 2d DLCA value) and approaches the 2d RLCA value [39] of *1.55*.

As the temperature is increased from T_m, fragmentation of clusters becomes possible; as a result, the aggregation process becomes reversible. At a temperature of $T = 1.02T_m$, for example, we begin to notice the onset of compactification of the clusters. Visual inspection of cluster morphology at various times suggests that this process occurs due to a sequence of fragmentation and subsequent reaggregation. The branches of the clusters formed at this temperature are thicker than in the $T = T_m$ case. Even though some fragmentation is allowed at this temperature, clusters are still large and extended with very few monomers or smaller clusters existing at late times. When the temperature is further increased to $T = 1.04T_m$, clusters become even more compact and a local ordering among monomers becomes noticeable by visual inspection of the morphological images, indicating the beginning of crystallization. Bands of alternating type particles are also noticeable. The presence of compact clusters in the system at this temperature is reflected in the increased value of the fractal dimension D_f as shown in Fig. 7.13, which climbs significantly past the final value for the irreversible, $T = T_m$, case (*1.50-1.55*) to a value above *1.60*.

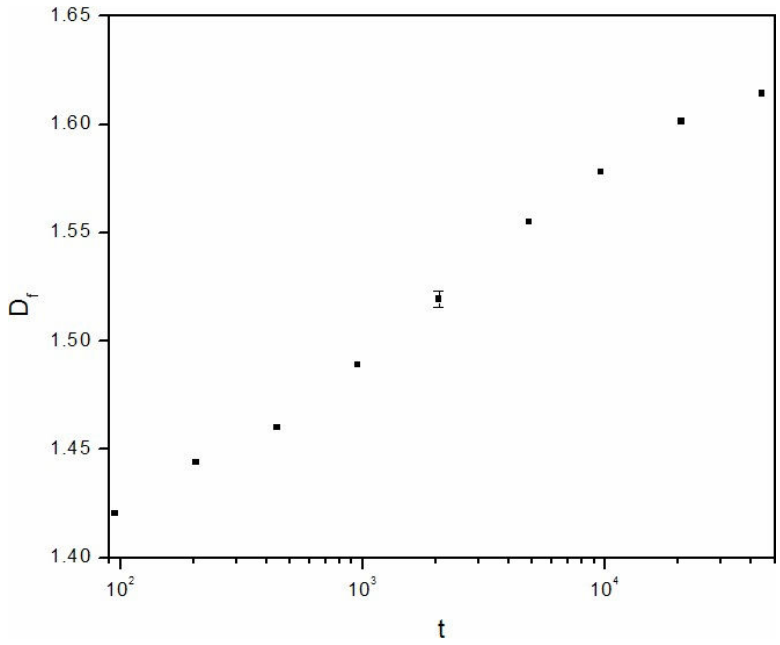

Fig 7.13: Same as in Fig. 7.12 except T = 1.04T_m. The compactification of the clusters seen in Fig. 7.11c is reflected in the increasing value of the fractal dimension D_f. It begins at a value close to the accepted 2d-DLCA value of 1.4 and continues to rise past 1.6, indicating the formation of more compact clusters at late times. Beyond this temperature, steady-state clusters are too small for fractal dimension curves to have much meaning. A "characteristic" error bar is shown. Error bars for other data points are of similar magnitude.

However, at $T = 1.04\ T_m$, we also observe that very large clusters present at lower temperatures do not exist any longer. The system is composed instead of monomers, dimers, and a variety of other small clusters coexisting with some larger clusters. Finally, by $T = 1.05\ T_m$, fragmentation dominates at late times and does not allow large clusters to form. We have confirmed this by starting out with an initial configuration containing several very large clusters and then running the simulations for $T = 1.04$ and $T = 1.05$. In

each case, the large clusters dissolved, leaving behind systems that were nearly identical to those formed from an initial configuration of monomers at those temperatures. From our studies it is possible to estimate the *dissolution* temperature (T_{dis}) of the whole assembly. For the values of b_t and b_n considered here, $T_{dis} \approx 1.05\ T_m$.

In Figure 7.14, we display a plot of the number of monomers left in the system at late times, $N_m\ (t_{late})$ vs. the scaled temperature $(T-T_m)/T_m$ for the bonding configuration $b_t=10$ and $b_n=3$ at various area fractions.

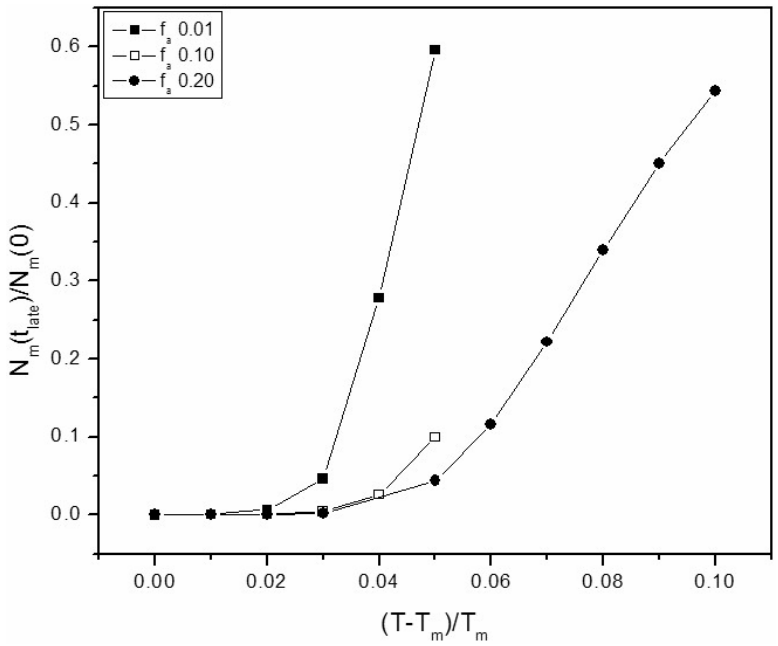

Fig 7.14: Plot of the number of monomers left in the system at late times vs. the scaled temperature $(T-T_m)/T_m$ for the bonding configuration $b_t=10$ and $b_n=3$ for various area fractions. Notice the sharp temperature profiles.

Due to computer time limitations, some of the simulations had not completely reached a steady state by the latest times available to us. In cases where the steady state cannot be reached within a reasonable amount of computer time, the temperature is close to the

melting temperature and the evolution process is dominated by aggregation. However in most of those cases, aggregation had nearly eliminated the presence of monomers in the system by the latest time and further time evolution will be unlikely to alter N_m (t_{late}) significantly. Note that the temperature profile in Fig. 7.14 is sharp in the case of area fraction $f_a = 0.01$ and becomes less sharp as the area fraction is increased. Such sharp dissolution temperature profiles are already seen in experiments. The decreased sharpness at higher area fractions perhaps originates from the stability of large clusters in a high degree of packing environment such as for $f_a = 0.10$ and 0.20. More bonds would have to be broken, on average, to dissociate a particle from its parent cluster in such cases and the transition from a gel-like phase to a dispersed, small-cluster phase becomes more gradual with temperature.

Similar random fractal and compact cluster morphology is observed at various temperatures for other values of b_t and b_n. As expected, the dissolution temperature depends on b_t and b_n. This is demonstrated in Fig. 7.15 where we fix the area fraction to be $f_a = 0.01$ and vary b_t and b_n.

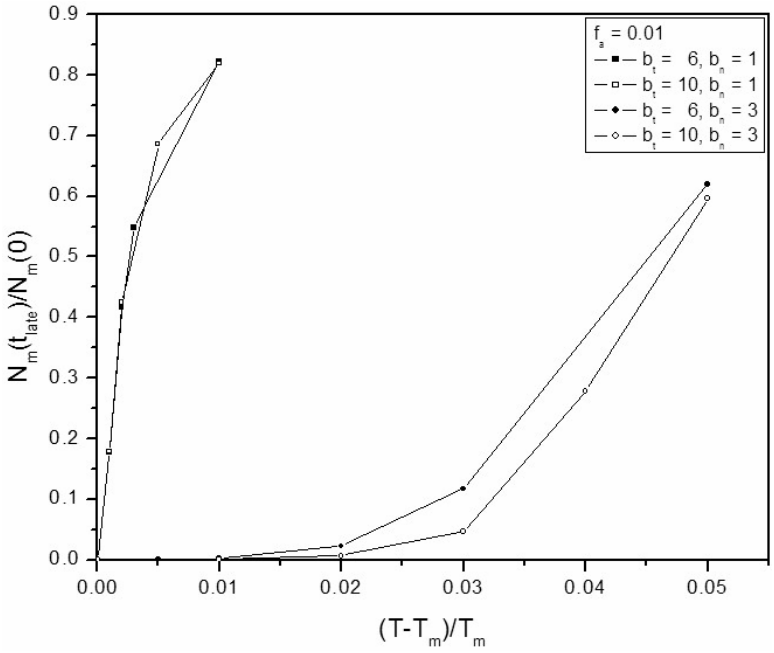

Fig 7.15: Here we fix the area fraction at $f_a = 0.01$ and vary b_t and b_n. The dissolution temperature increases as one increases b_t. When $b_n = 1$, the value of b_t does not change the dissolution phase-diagram appreciably when $b_n = 1$. Even for $b_n > 1$, the effect of b_t on the dissolution phase diagram is still marginal.

The dissolution temperature increases as one increases b_t. When $b_n = 1$, only one bond is allowed between each pair of *A* and *B* particles, and the dissolution temperature of the whole assembly (T_{dis}) is very close to the DNA 'melting' temperature T_m. In this case, any single bond breaking splits a fractal cluster (of average coordination ≈ 2) into two. One would expect then that the value of b_t would not change the dissolution phase-diagram appreciably when $b_n = 1$. This is clearly demonstrated in Fig. 7.15. Even for $b_n > 1$, the effect of b_t on the dissolution phase diagram is still marginal. It is thus essential to have multiple DNA linking between each pair of *A* and *B* particles to have a large

dissolution temperature. This result of our simulation agrees quite well with experimental observations [22,106,107].

7.2.3.2 Kinetics of Growth:

In Figs. 7.16 and 7.17 we show the scaled average cluster size versus time in a log-log plot for the $b_t = 10$, $b_n = 3$ bond configurations at monomer area fractions $f_a = 0.01$ and $f_a = 0.10$, respectively, with temperatures T ranging from T_m to $1.05T_m$.

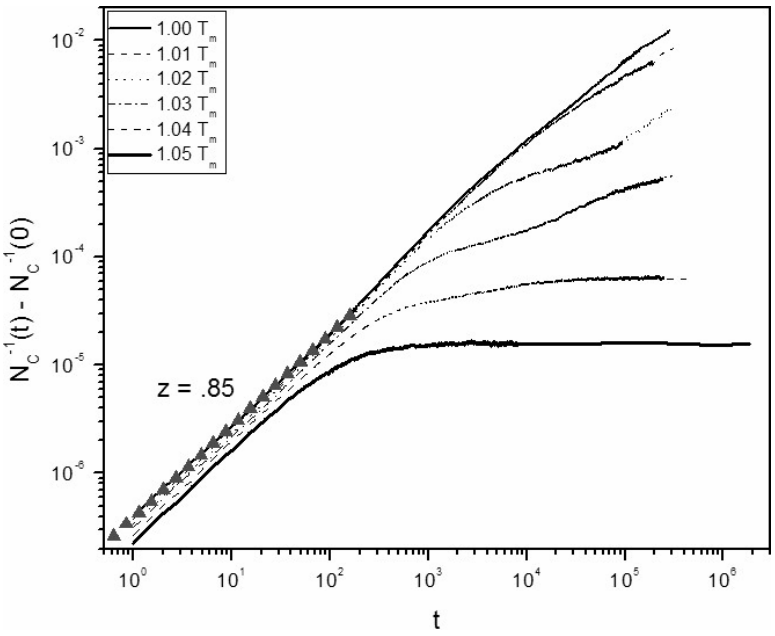

Fig 7.16: Kinetics graph showing a log-log plot of inverse cluster number vs. time (slope = z , the kinetic exponent) for the case of area fraction $f_a = 0.01$ and bonding configuration $b_t = 10$, $b_n = 3$ at various temperatures. As can be seen in the graph, all curves start with $z \approx 0.85$. As time progresses, the higher temperature kinetics reach steady-state values, whereas the kinetic behavior is complicated at intermediate temperatures showing the appearance of inflection points.

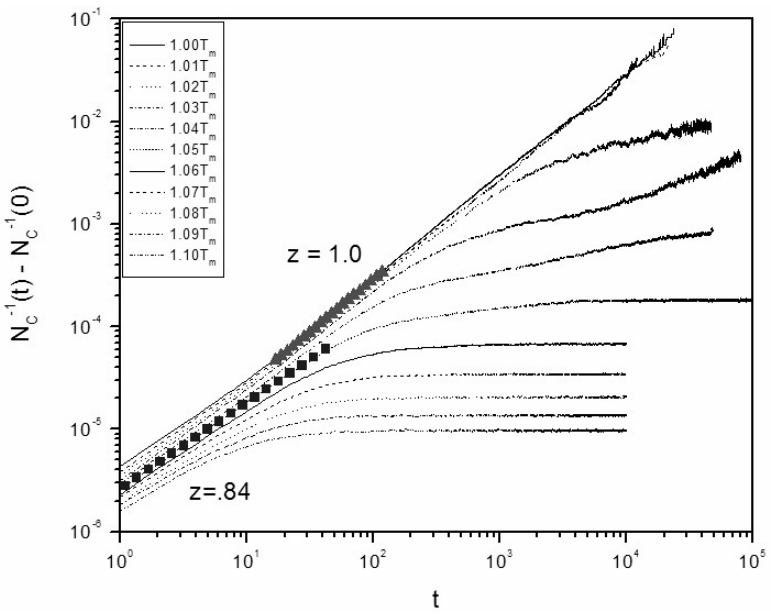

Fig 7.17: Same as in Fig 6.46, but for area fraction $f_a = 0.10$. At lower temperatures the early time value of $z \approx 0.84$ increases to a higher value of $z \approx 1$ at intermediate times. This is consistent with the cluster crowding picture for 2d DLCA. Again, higher temperature kinetics reach steady-state values, whereas the kinetic behavior is complicated at intermediate temperatures.

For each area fraction f_a and temperature T, the early time kinetic exponent $z \approx 0.85$, is consistent with 2d DLCA at these area fractions [91]. This indicates that at early times fragmentation does not play an important role in the cluster evolution process.

At $T = T_m$, the aggregation process is irreversible and one might expect to see the same value of the kinetic exponent z throughout the evolution process. However, one needs to consider two different mechanisms that can change the kinetic exponent even in the irreversible case. First, it is known for the DLCA model that cluster crowding increases the kinetic exponent at late times. Second, as mentioned before, most collisions

do not lead to the formation of aggregates at late times for the binary aggregation model studied here. This leads to a slow down in the late time growth kinetics, particularly for smaller area fractions. Signature of such a slow down at late times is clear for $f_a = 0.01$ when $T = T_m$. For $f_a = 0.1$, z increases from 0.85 ± 0.03 to about $1.00 \pm .02$ at intermediate times before showing a *hint* of slowing down at late times. This increase in the kinetic exponent at intermediate times is consistent with the cluster crowding picture developed for the DLCA model [40].

As the temperature is increased from T_m, fragmentation becomes important at late times and the system should approach a steady state. This steady state is readily reached at higher temperatures while it takes extremely long times for the system to reach the steady state near T_m. For temperatures near T_m such as for $T = 1.03\ T_m$, kinetic curves show the presence of inflection points, not observed in traditional aggregation-fragmentation models. To investigate the mechanism behind the inflection point, we focused on the behavior of the kinetic curves for $T = 1.03\ T_m$ by setting $f_a = 0.01$ and $b_n = 3$ but varying b_t from *3* to *10*. These results are shown in Fig.7.18.

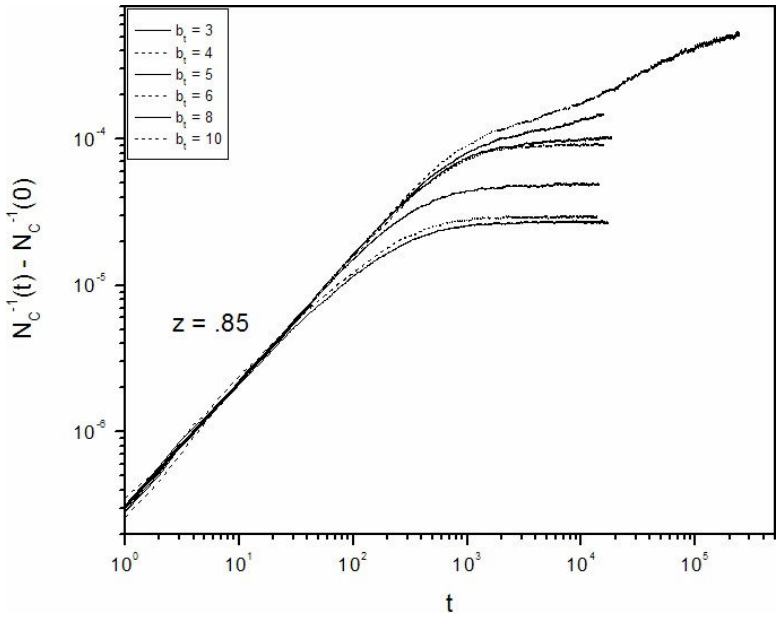

Fig 7.18: Kinetics curves for an overall area fraction of $f_a = 0.01$ and $b_n = 3$. Here b_t is varied from 3 to 10. For values of $b_t > 8$, inflections points can be seen in the kinetic graphs.

The inflection points are not observed in the cases of $b_t < 8$. In addition, we notice that the higher the total number of bonds allowed per particle, the larger the final cluster size.

One possibility is that the inflection points are related to the geometry of the clusters as compactification takes place in stages during the aggregation process. To test this hypothesis, we plot in Fig. 7.19 the time evolution of the average coordination number.

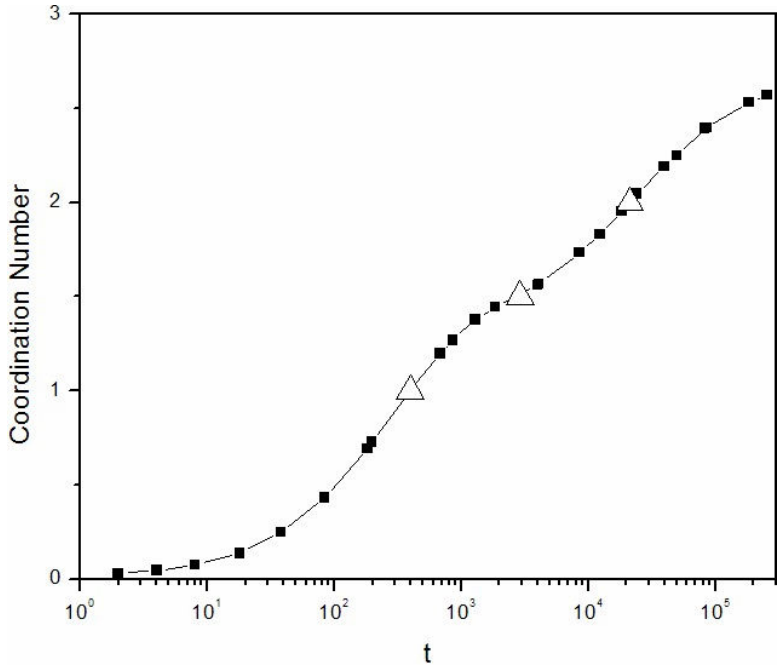

Fig 7.19: A plot of the coordination number (with opposite-typed particles) for an overall area fraction of $f_a = 0.01$ and bond configuration $b_t=10$ and $b_n=3$ at an intermediate temperature of $1.03T_m$. Inflection points occur in similar positions to those seen in the kinetics data (t = 400 ,4000, 40000) shown by the triangles.

We define the coordination number of a particle as the number of opposite type neighbors it has within the cutoff distance of the bonding interaction. The coordination number exhibits similar inflection points previously observed in the kinetics graphs at roughly the same times (*400, 4000*, and *40000* Monte Carlo steps). The average radius of gyration for clusters and the average nearest neighbor distance also show similar inflection points indicating the geometric origin of the inflection points. The first inflection point occurs almost exactly where the average coordination number crosses the value of one and the third one near the value of two. The coordination number seems to approach the steady-state value of three with time, corresponding to a tightly packed arrangement of particles. As a reference, we point out that the average coordination number of a system of dimers is 1 and large chains or DLCA type clusters is 2. The average value of 3 indicates a structure that is more compact than normal DLCA type fractal aggregates. This corroborates the cluster morphologies we have observed at intermediate temperatures. Our results indicate that the inflections in the kinetic graphs are related to a geometric rearrangement of particle positions with time, where at certain stages of packing, the average coordination number crosses integer (or possibly half integer) values, allowing more neighbor particles (of a different type) to fit next to a particular particle. At these times, the bonds available to a particular particle start to become shared among the now higher number of different type neighbors, leading to the changes in the aggregation behavior. This restructuring may represent a sort of "punctuated equilibria" for this aggregation-fragmentation system, where aggregate bonding configurations stay relatively fixed for long periods of time but are separated by brief periods of bond

restructuring. Of course this is not entirely surprising considering the geometrical constraints of spherical packing. Our cutoff length for the bonding of two opposite type monomers is quite short, only allowing bonding at near contact for the monomer surfaces. The "stringy" DLCA aggregates of coordination number of 2 collapse as temperature exceeds the melting temperature due to the cyclic process of aggregation and fragmentation. This, of course, leads eventually to additional contacts between monomers as the aggregate structures seek free energy minima. These new contacts then become available sites for bonding.

Since the inflection points indicate a restructuring of the growing clusters to fit in more neighboring particles, they are sensitive to the values of b_t and b_n. In Fig. 7.20, we show another set of cluster growth kinetics for $f_a = 0.01$ and for $b_t = 6$ and $b_n = 3$.

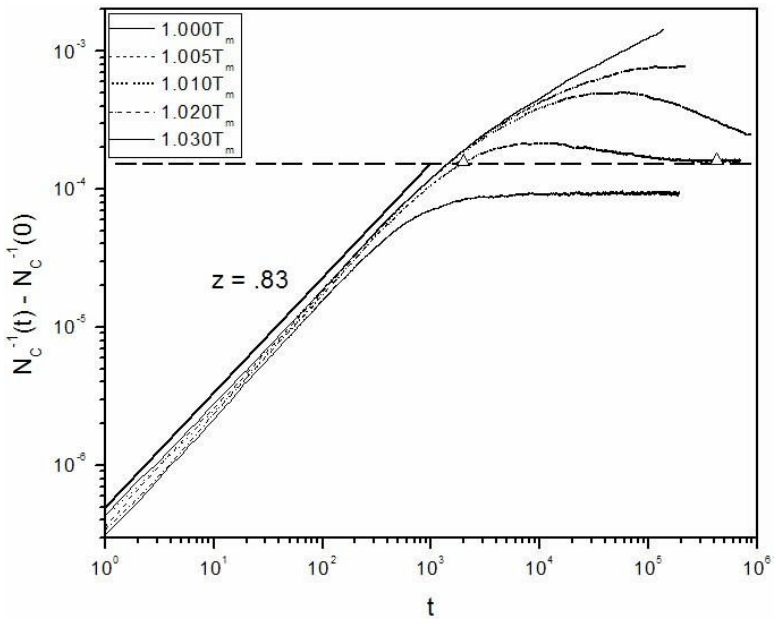

Fig 7.20: Kinetics curves for an overall area fraction of $f_a = 0.01$ with $b_t = 6$ and $b_n = 3$. Here the temperature is varied from T_m to $1.03T_m$. The dashed horizontal line indicates the inverse cluster number corresponding to an average cluster size of 4. The triangles represent two points on either side of the peak (at t = 1977 and t = 426080, respectively)

in the kinetics curve where the average cluster size in the system are similar to each other.

The early time growth exponent is consistent with previous results ($z \approx 0.83$) but now the growth kinetics is *not* monotonous at finite temperatures. We again suspect that this is due to the compactification of the clusters. To demonstrate this we show snapshots of the cluster morphology for $T = 1.02$. We chose two times ($t = 1{,}977$ and $t = 426{,}080$) placed around either side of the peak of the cluster size distribution such that the number of remaining clusters is approximately equal (denoted by two triangles on the graph). The horizontal line in Fig. 7.20 represents the value of the inverse cluster number when the average cluster size is 4 monomers. In Fig. 7.21a, we see a sampled section of the box, showing the state of aggregation at $t = 1977$ with *4840* clusters remaining in the system.

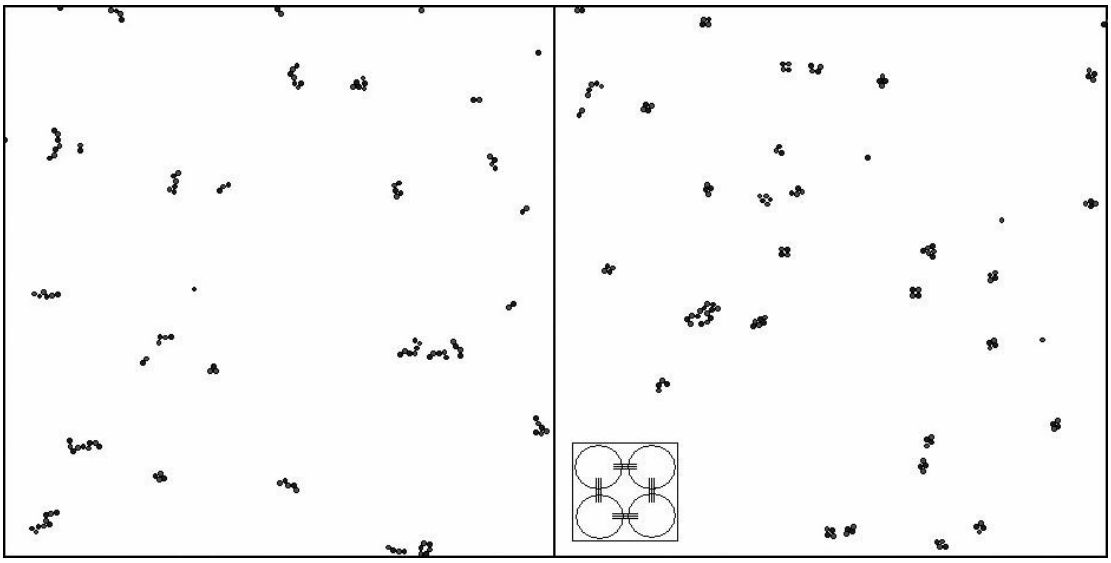

Fig 7.21:

a (left): A sample section of the system morphology for the case referred to in Fig. 7.20 with t = 1977. The aggregates here are small but appear as the "stringy" precursors of DLCA-like aggregates.

b (right): A sample section of the system morphology for the case referred to in Fig. 7.20 with t = 426080. The aggregates here are more compact than the previous case, and a proliferation of tetramers is apparent. The inset represents a possible stable bonding configuration (for $b_t = 6$ and $b_n = 3$) leading to these 4-particle clusters.

We observe that clusters, although small, have the somewhat stringy appearance of small DLCA-like aggregates. This is not altogether surprising since the kinetic growth curves for the $T = T_m$ (pure aggregation case) and $T = 1.02\ T_m$ are not significantly different from each other at this time. However, by $t = 426,080$, the above curves are noticeably different and the appearance of the clusters for $T = 1.02\ T_m$ is significantly altered as can easily be seen in Fig. 7.21b. Here the total number of clusters is very close to that of the previous time (*4749*), but the clusters are far more compact. In fact, the system seems to be dominated by tetramers. In the inset, a possible stable tetramer bonding configuration is shown in which particles have used all available bonds. This may explain why in the case of $b_t = 6$, $b_n = 3$ case, the system is driven toward these *4*-particle clusters at temperatures above the melting temperature. Of course, it may still be possible to develop larger stable aggregates at temperatures closer to the melting temperature. However, the amount of computer time needed to observe this would be enormous since some of our simulations have taken several weeks to reach completion, and possibly two more decades of time would be required to observe this effect.

7.2.3.3 Scaling Behavior at the Steady State:

The steady-state value of the cluster size can be related to the homogeneity constants for aggregation (λ) and fragmentation (α). The homogeneity exponents are expressed through the behavior of the aggregation and fragmentation kernels (Eqns. 5.21 5.22) when the clusters aggregating of fragmenting are scaled in size by a factor of *a*:

$$K(ai,aj)=a^{\lambda}\,K(i,j) \text{ and } F(ai,aj)=a^{\alpha}\,F(i,j) \tag{7.4}$$

As above (Eq. 5.31), one can obtain a steady state value s_0 for the average cluster size:

$$s_0=\left(\frac{M_1\,a\,k_c}{b\,k_f}\right)^{y} \tag{7.5}$$

where *y* is a scaling exponent which can be written in terms of λ and α in the following way:

$$y = (2-\lambda+\alpha)^{-1} \tag{7.6}$$

As M_1 represents the monomer area fraction f_a, one can compute the value of *y* by determining how the steady-state cluster size scales with the monomer area fraction. Since the value of the aggregation homogeneity constant λ is given by:

$$\lambda = 1-\frac{1}{z} \tag{7.7}$$

one can calculate α from the simulation, the fragmentation homogeneity constant. The value of α would be important to understand how the fragmentations take place in the clusters.

One noteworthy point is that for higher temperatures in our simulation, the steady-state average cluster size s_0 is not a very large number. Since s_0 evolves from a value of 1 (the system starts as a dispersion of monomers) it becomes important then to

consider s_0 -1 (instead of s_0) in our scaling analysis. Figs. 7.22 and 7.23 portray log-log plots of s_0-1 versus the area fraction f_a for two different sets of parameters of the model.

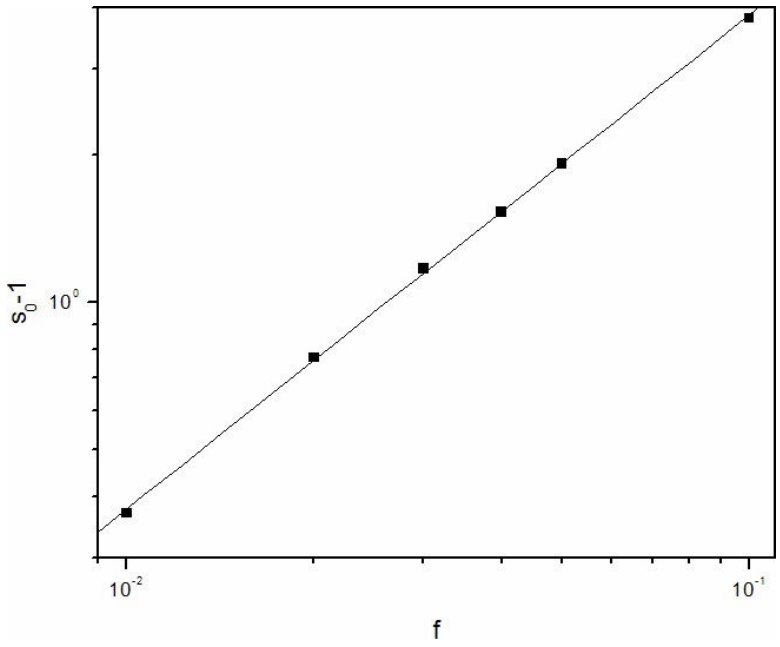

Fig 7.22: log-log plot of the steady-state scaled value of the average cluster size vs. overall area fraction in the case of $T = 1.003T_m$ with a bonding configuration of b_t=3 and b_n=1. A best fit line passes very near all data points, indicating the fact that scaling does work well in this case. The line has a slope of 1, yielding a fragmentation kernel exponent α of –1, assuming λ = 0, and z = 1.

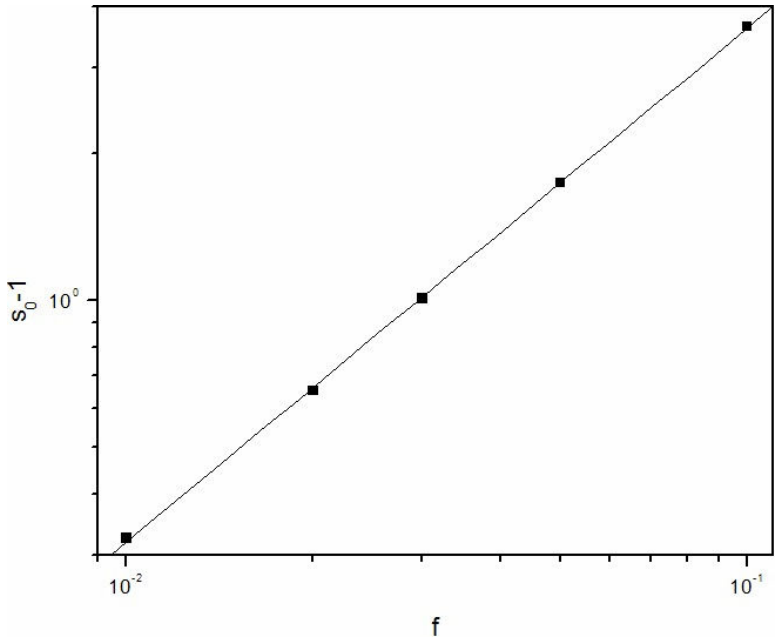

Fig 7.23: Same as in Fig. 7.22 except T = 1.05T_m with a bonding configuration of b_t = 10 b_n=3. The line has a slope of 1, yielding a fragmentation kernel exponent α of -1, assuming λ=0, and z=1.

Scaling seems to work quite well in each case yielding $y = 1.0 \pm 0.05$. If we use the late time (average cluster size > 4) value of $z \approx 1$ for the kinetic exponent, we obtain $\alpha \approx -1$. These findings suggest that the fragmentation kernel decreases for larger clusters with a power law of exponent -1 for all of the bonding configurations and temperatures studied. This would indicate that larger clusters come apart more slowly than smaller clusters, leading to the interpretation that fragmentation is occurring at the surface of the clusters.

7.2.4 Conclusions:

In conclusion, we have carried out an off-lattice Monte Carlo simulation of DNA-mediated colloidal assembly where aggregation-fragmentation of a binary mixture of colloidal particles are studied through a simple model of base-pair hybridization between

complementary DNA strands attached to the particles. A number of important insights can be obtained from these simulations. The morphologies of the aggregates we have observed are highly temperature sensitive, varying from DLCA-like aggregates near the DNA melting temperature to aggregates with local ordering (and hint of crystallization) at intermediate temperatures. Of course, to observe the details of local crystal ordering in 2D, a more robust model may be required, considering that such effects tend to be thermodynamic in nature. Thermal considerations only come into play in our model through the diffusion constant of clusters and the probability of a cluster move being accepted, as mentioned above. Finally the whole system dissolves into very small clusters at slightly higher temperatures. The sharpness of the temperature profiles seen in the morphologies is quantified by the number of unattached monomers left in the system at late times as a function of temperature. Simulation results agree with experimental observation of sharp temperature profiles for DNA-mediated aggregation. The kinetics of growth shows an early time agreement with 2d DLCA results followed by a more complicated growth behavior. An increase in the kinetic exponent corresponding to cluster crowding at high area fractions is observed. Interestingly, we have also observed inflection points and a negative kinetic exponent under certain conditions, results attributed to compactification of clusters above the melting temperature. This conclusion is supported by the increase in mass fractal dimension with time as well as the evolution of coordination number and its correspondence to the inflection points observed in the kinetics. Finally, the steady-state behavior of the average cluster size indicates that over a wide range of bonding configurations, the fragmentation of clusters happens at the surface.

Further study into these intriguing systems is certainly warranted, as DNA mediated colloidal aggregates can exhibit a wide variety of morphological forms, possibly leading to the development of new and diverse types of novel materials in addition to their potential use for detection of small discrepancies in DNA coding.

7.3 A Short-Range Model for Protein Aggregation in Highly Salted Solutions:

7.3.1 Introduction:

Two of the important parameters that mediate aggregation in particulate systems are the range and depth of the interaction potential between primary particles. As stated earlier, the DLVO potential allows some adjustment of these via the choice of dispersed particle material, salt concentration, temperature, etc [24,54]. However, the DLVO potential, combining vdW interaction with Yukawa-type electrostatic screening, lacks the short-range nature necessary to model such systems as simple proteins in high salt concentration solutions. These protein interactions are highly chemically specific and though often quite strong, tend to extend over much smaller length scales than those accounted for by DLVO type interactions. Appropriate short range attractive potentials have been used in combination with long-range screened Coulomb repulsion to study equilibrium cluster phases and low-density arrested disordered states in the context of sterically stabilized colloidal systems with depletion interactions [116]. However, under a high salt concentration, the long range Yukawa-type potential can be almost completely eliminated, leaving only the short range attractive potential to control the aggregation mechanism. One such short-range potential is the $\alpha - 2\alpha$ potential, an extension of the Lennard-Jones potential defined above. This potential has the form [116]:

$$E = 4\varepsilon\left[\left(\frac{\sigma}{r}\right)^{2\alpha} - \left(\frac{\sigma}{r}\right)^{\alpha}\right] \tag{7.8}$$

As in the LJ form, the depth of this potential is ε. As α increases, the *range* of the potential shrinks. Some examples are shown in Fig 7.24:

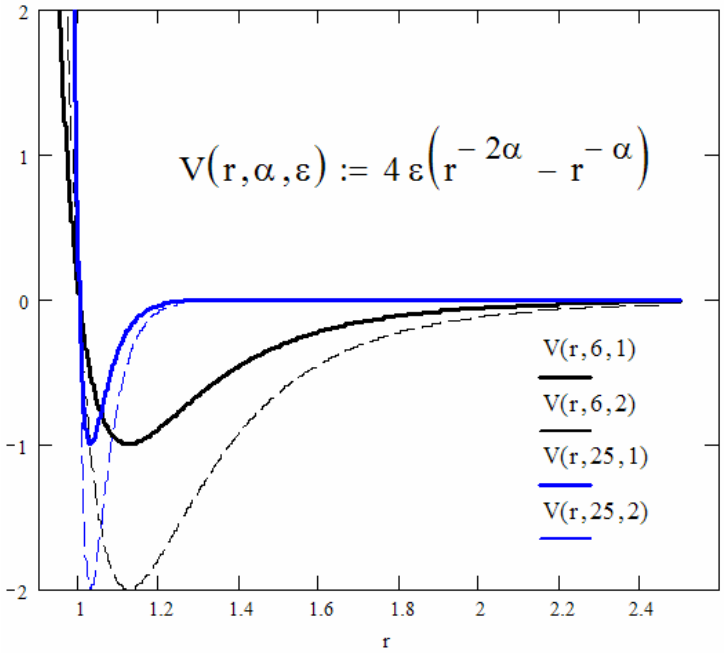

Fig 7.24: the $\alpha - 2\alpha$ for several choices of α and ε.

7.3.2 Simulation:

Using the BD code and procedure described earlier with the $\alpha - 2\alpha$ potential, we have simulated the aggregation of particles in 2D interacting under the above potential for two volume fractions (0.05 and 0.20) with two different values of α (6 and 12) and two values of ε (4 and 7 in units of k_BT). This potential represents a *minimum model* of the aggregation of simple proteins such as lysozyme under strong electrostatic screening brought on by high salt concentrations [15] for which the range of interaction is small.

7.3.3 Morphologies:

We show below in Figures 7.25 & 7.26 late time (6400 time steps) images of the system with various selections of α, ε, and f_v.

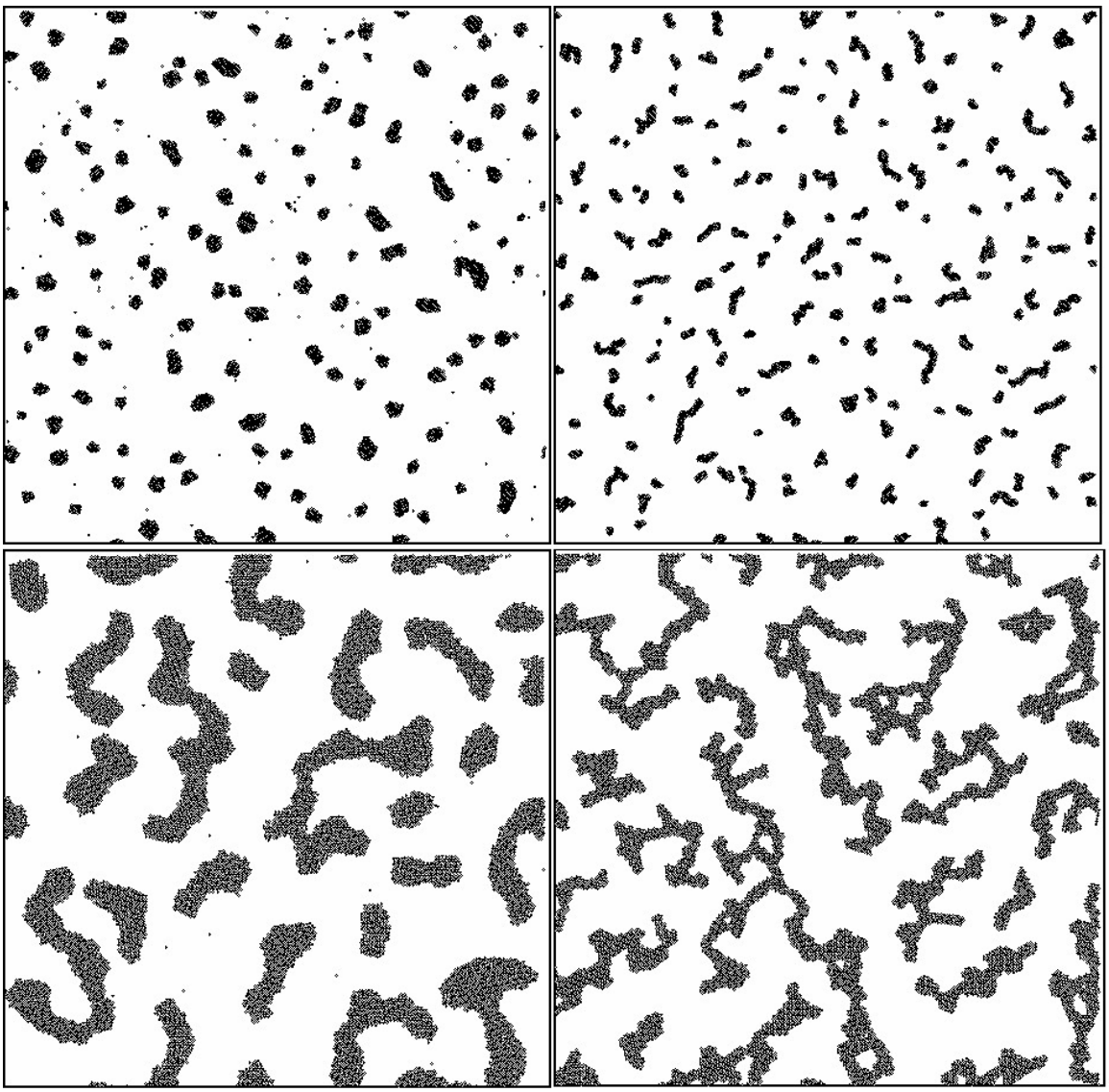

Fig 7.25:

(a)-top left: $\alpha = 6, \varepsilon = 4, f_v = 0.05$ Small compact clusters - a few monomers

(b)-top right: $\alpha = 6, \varepsilon = 7, f_v = 0.05$ Small, slightly branched clusters - no monomers

(c)-bottom left: $\alpha = 6, \varepsilon = 4, f_v = 0.20$ Large, thick, slightly branched clusters - a few monomers

(d)-bottom right: $\alpha = 6, \varepsilon = 7, f_v = 0.20$ Large, thin, highly branched clusters - no monomers

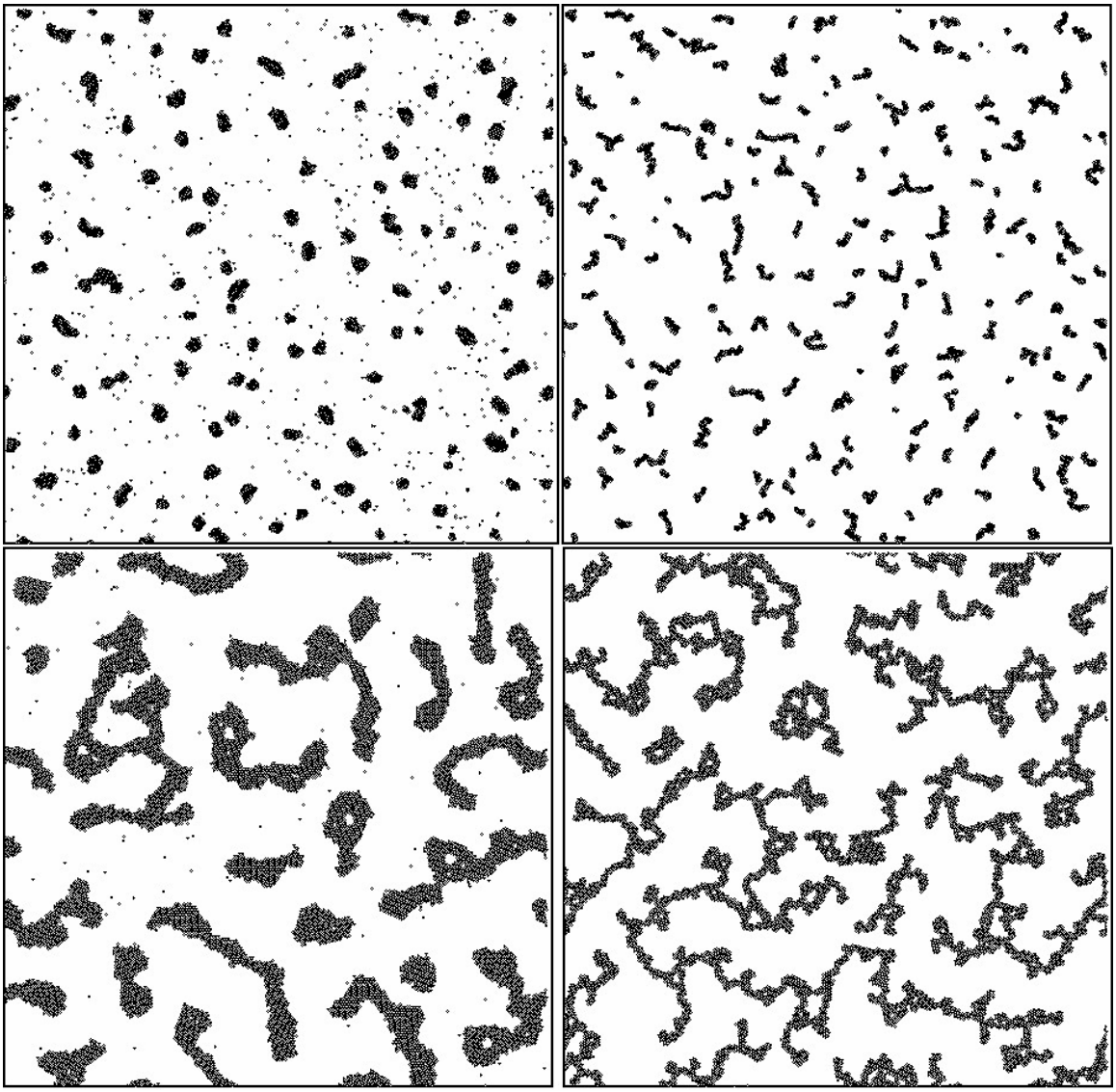

Fig 7.26:

(a)-top left: $\alpha = 12, \varepsilon = 4, f_v = 0.05$ Small compact clusters - large number monomers

(b)-top right: $\alpha = 12, \varepsilon = 7, f_v = 0.05$ Small, slightly branched clusters - no monomers

(c)-bottom left: $\alpha = 12, \varepsilon = 4, f_v = 0.20$ Large, thick, slightly branched clusters -moderate number monomers (thinner than for $\alpha = 6$)

(d)-bottom right: $\alpha = 12, \varepsilon = 7, f_v = 0.20$ Large, thin, highly branched clusters present - no monomers (thinner than for $\alpha = 6$)

The morphologies of these systems are similar to those seen by Chakrabarti, Fry, and Sorensen [54] who studied a DLVO type potential with a secondary minimum in the potential of $4k_BT$ and $7k_BT$. Similar agreement is found with the structures seen by Skjeltorp [55] whose experimental findings indicated that polystyrene spheres aggregating in two dimensions with a DLVO potential with secondary minimum depth = $4k_BT$ produce structures that are crystalline on small length scales and fractal on large length scales with Df = 1.48-1.49. Our results agree with Chakrabarti et al. at $4k_BT$ and 20% volume fraction, namely the presence of compact clusters in "equilibrium" with a background gas of monomers at $4k_BT$ well-depth. We also note that for the shorter range $\alpha = 12$, a more abundant gas phase is present. Additionally, at $7k_BT$, clusters have a complex morphology, showing crystalline type structure at small length scales and 2D fractal structure at larger length-scales, with the shorter range potential leading to thinner branches. The limiting case of a contact potential is expected to yield results similar to the standard DLCA model where the average coordination number of particles in a cluster is 2. To clarify these points we display two of these these "fat-fractal" structures in Fig 7.27 along with their structure factors in Fig 7.28:

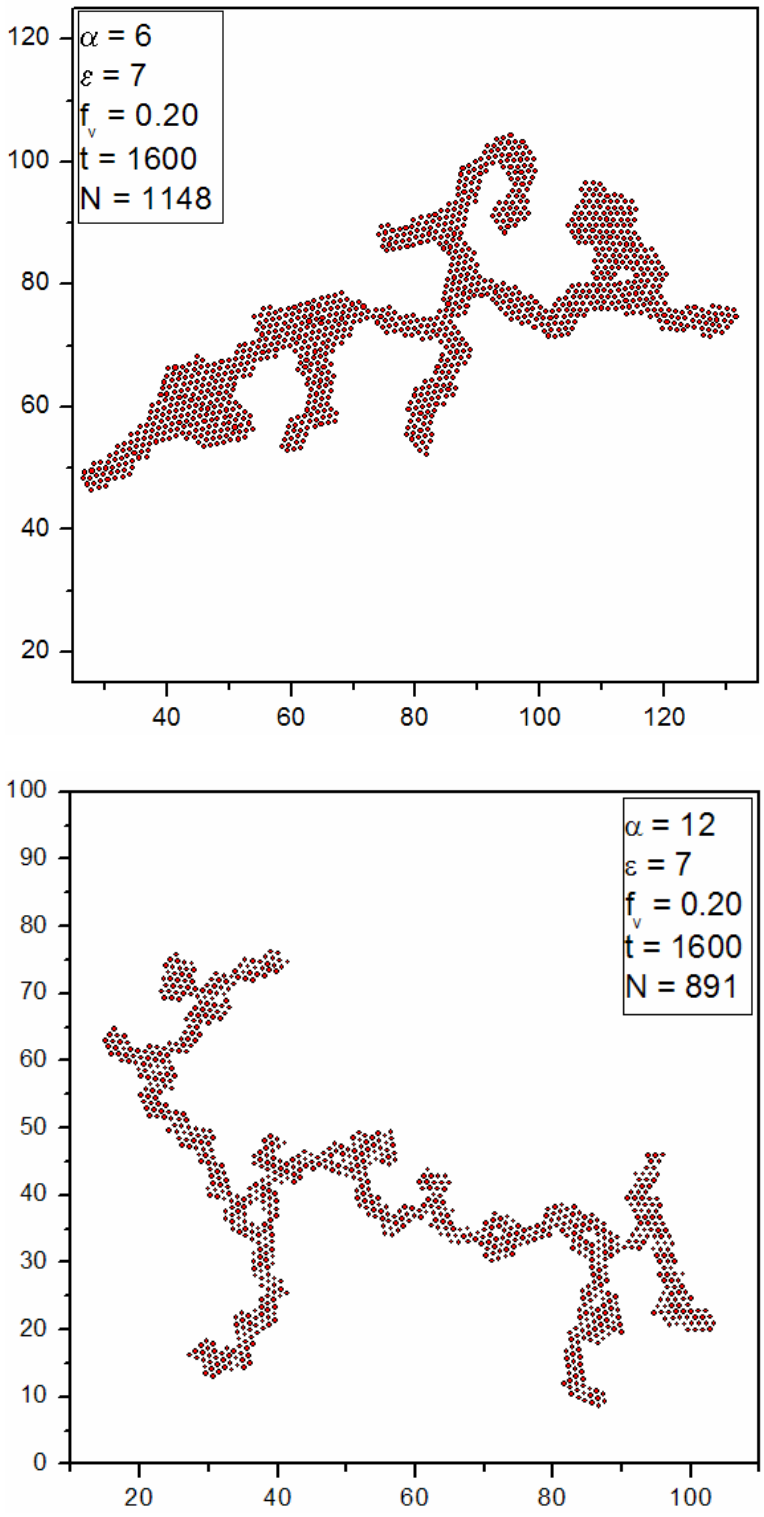
α = 6
ε = 7
f_v = 0.20
t = 1600
N = 1148
120
100
80
60
40
20
40
60
80
100
120
α = 12
ε = 7
f_v = 0.20
t = 1600
N = 891
100
90
80
70
60
50
40
30
20
10
0
20
40
60
80
100

Fig 7.27:

a) top: size $N = 1148$ cluster for $\alpha = 6, \varepsilon = 7, f_v = 0.20$ Notice the crystal ordering at small length scales and the branched fractal structure at large length scales.

b) bottom: size $N = 891$ cluster for $\alpha = 12, \varepsilon = 7, f_v = 0.20$ at $t = 1600$ similarly showing different morphologies at different length scales. With increased α(decreased range), the structures are more ramified as evidenced by thinner branches.

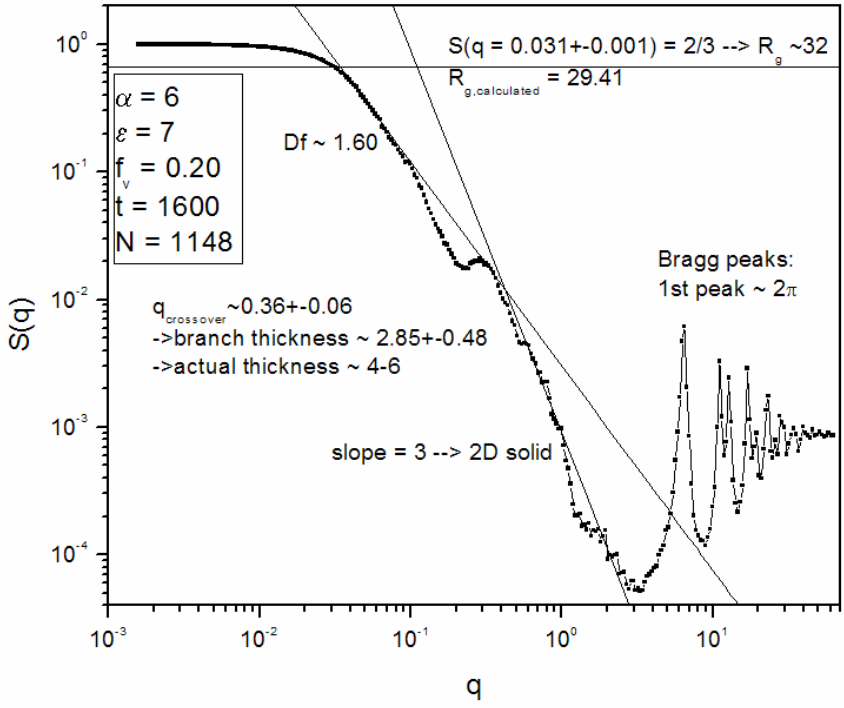

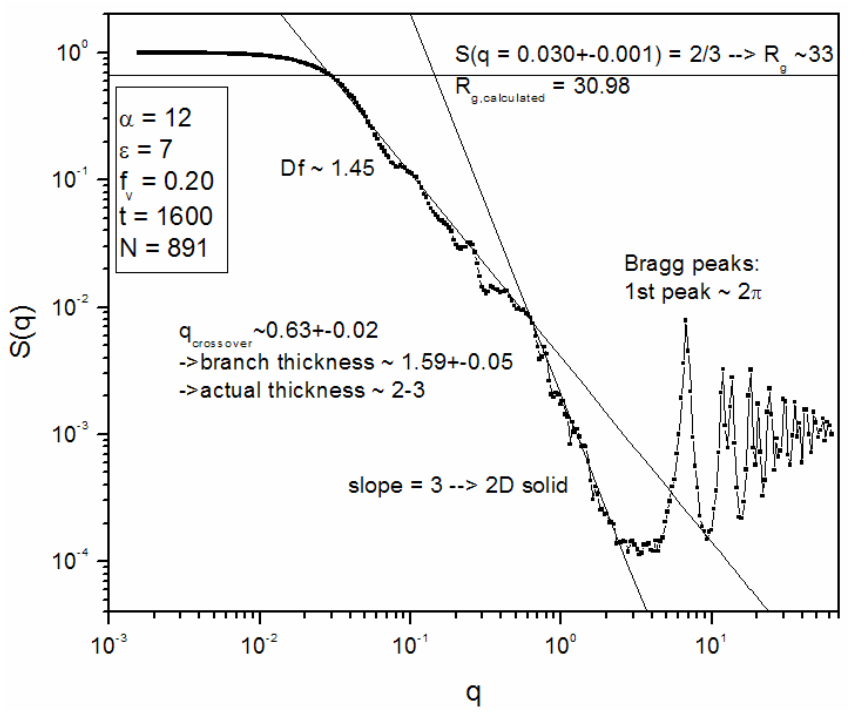

Fig 7.28:

a) top: Structure factor for cluster from Fig 7.27a

b) bottom: Structure factor for cluster from Fig 7.27b

From the graphs of the structure factor, we make a number of observations. The presence of the Bragg peaks at high q values corroborates our observation of a closest-packed crystal lattice at small length scales. The slope of 3 for the intermediate q-range indicates that the cluster is seen as solid 2D object at this length scale, again indicating the observed solid structure of the branches. For q values below this, there is a crossover at some point to a fractal type structure (correlated with cluster branch thickness), with a shift to Df in the standard DLCA range of ~ 1.45 for $\alpha = 12$ and ~1.60 for $\alpha = 6$. Chakrabarti et al. saw similar variations in Df as a function of the *depth* of the potential

well instead of the range. Though not comprehensively analyzed here, it is obvious from Figs. 7.25 and 7.26 that we find similar trends as functions of the well depth.

The effect of the range of the potential is seen in branch thinning for the shorter range potential ($\alpha = 12$), leading to more DLCA like behavior, which is of course the limit of short range, being a *contact-only* potential. Range is also observed to effect the abundance of the gas phase present in the system, which is not entirely unexpected.

7.3.4 Conclusion:

We have successfully demonstrated a two-dimensional minimum model for physical systems with short-range attractive potentials, such as lysozyme-like proteins in highly salted solutions where charge interactions are almost completely screened and the aggregation is controlled almost completely through very short-range lock-key type chemical interactions . A variety of complex structures can be observed. This model produces similar structures to more complicated and longer ranged forms, such as DLVO [54], though the branched structures seen for the shorter range potential tend to be thinner No known morphological studies of these experimental systems have been done to our knowledge, leading to an alluring topic for further research.

Chapter 8 - Conclusions:

The goal of this work has been to come to a better understanding of the process of aggregation in aerosols and colloids. To this end, we have examined a wide range of seemingly unrelated physical systems, coming to the realization that much about aggregation is indeed universal.

The fractal nature of structures formed by the aggregation of clusters has been surprisingly consistent from one regime to the next, with the fractal dimension varying little between the two diffusion limited (continuum and Epstein ~1.8) and ballistic limited (~1.9) models. Additionally, we have seen that under the action of nonspecific potentials (vdW and short range $\alpha - 2\alpha$) as well as other highly specific interactions (selective complementary proteins, ssDNA), Df *at some length scale* is remarkably resistant to change, despite our expectations to the contrary. Interestingly, we have also seen complex structures composed of short-range crystalline forms which evolve at large length scales into fractal structures. Additionally, we have observed the crossover in Df (1.8-2.6) that occurs as a system evolves from cluster dilute to cluster dense on its way to gelation in three dimensions.

Through a simple yet powerful scaling model we have been able to predict the aggregation kernel homogeneity and through it, the kinetic exponent for the entire spectrum of motional regimes. We have been the first in both theory and simulation to demonstrate that aggregation in the Epstein regime yields a kinetic exponent of 0.8, unexpectedly less than that of the continuum regime value of 1. Continuing in this vein, we have demonstrated the effect of crossover between ballistic and Epstein regimes that occurs due to the growth of clusters on the kinetics of aggregation, surprisingly yielding

near-continuum kinetics in very non-continuum conditions. We have additionally explained how the nearest neighbor separation becomes an important parameter in determining the kinetic exponent at intermediate volume fractions for all systems. In various cases we have seen and appropriately interpreted interesting kinetic behavior brought on either by kinetic arrest (selective binary colloids) or cluster fragmentation (ssDNA), with the latter actually producing an unexpected nonmonotonic growth in the average cluster size under certain conditions.

We have consistently correlated measured size distributions with kinetics data, verifying the connection between the two implied by the homogeneity of the aggregation kernels for the Smoluchowski Equation.

We have successfully used mathematical models to predict the gel point of simulated low volume fraction DLCA systems, while seeing the need for better models to explain the discrepancy found at initially high volume fractions.

In many ways, much remains to be done. For this no apology is made. This research has answered some questions, and it has brought others to light. Already, others are taking the knowledge we have gained by this research and continuing this work on into the area of Nanoparticles studies, an entirely new field of research, one bringing together scientists from a host of diverse fields. We leave it to them to lead the way from here.

References:

[1] www.wordreference.com/definition/aggregation

[2] H. Firoozmand, B.S. Murray, and E. Dickinson, Langmuir, **23**, 4646 (2007).

[3] S.K. Friedlander, *Smoke, Dust and Haze*, (Oxford University Press, Oxford, 2000).

[4] F. Family and D. P. Landau, *Kinetics of Aggregation and Gelation,* (North-Holland, Amsterdam, 1984).

[5] G. Wurm , J. Blum, Icarus, **132,** 125 (1998).

[6] J. Blum, et. al., Phys. Rev. Lett. **185**, 2426 (2000).

[7] R. Jullien, R. Botet, and P. M. Mors, Faruday Discuss. Chern. SOC., **83**, 125 (1987).

[8] A. Y. Kim, K.D. Hauch, J.C. Berg, J.E. Martin, and R.A. Anderson, J. Coll. Int. Science, **260** (1), 149 (2003).

[9] R. Dhaubhadel, F. Pierce, A. Chakrabarti, and C. M. Sorensen, Phys. Rev. E. **73**, 011404 (2006).

[10] current research in progress by author

[11] G. Urbina-Villalba, J. Mol. Struc-theochem., **769** (1-3), 171 (2006).

[12] R. D. Tweney, Perspectives on Science, **14.1**, 97 (2006).

[13] A. E. Gonzalez, G. Odriozola, and R. Leone, Eu. Phys. Journ. E., **13** (2), 165 (2004).

[14] A. E. Gonzalez, Phys. Rev. E., **74** (6), 061403 (2006).

[15] M. H. Lee, E. M. Furst, Phys. Rev. E., **74** (3), 031401 (2006).

[16] H. Park, S. Kim, H. S. Chang, Jour. Aerosol Sci., **32** (11), 1369 (2001).

[17] S. M. Dammer, D. E. Wolf, Phys. Rev. Lett, **93** (15), 150602 (2004).

[18] L. S. Matthews, T. W. Hyde, IEEE Trans. on Plasma Sci., **32** (2), 586 (2004).

[19] P. Bartlett, R. H. Ottewill, P. N. Pusey, Phys. Rev. Lett., **68** (25), 3801 (1992).

[20] N. Hunt, R. Jardine, P. Bartlett, Phys. Rev. E., **62** (1), 900 (2000).

[21] D. B. Lukatsky, D. Frenkel, Phys. Rev. Lett., **92** (6), 068302 (2004).

[22] R. C. Jin, G. S. Wu, Z. Li, C. A. Mirkin, and G. C. Schatz, Jour. Am. Chem. Soc., **125** (6), 1643 (2003).

[23] M. Li, S. Mann, Jour. Mat. Chem., **14** (14), 2260 (2004).

[24] J. N. Israelachvili, *Intermolecular and Surface Forces: With Applications to Colloidal and Biological Systems,* (Academic Press, London,1992).

[25] F. Pierce, A. Chakrabarti, D. Fry, and C. M. Sorensen, Langmuir, **20**, 2498 (2004).

[26] F. Pierce, C. M. Sorensen, and A. Chakrabarti, Langmuir, **21**, 8992 (2005).

[27] F. Pierce, C. M. Sorensen, and A. Chakrabarti, Phys. Rev. E. **74**, 021411 (2006).

[28] to be published by author "Simulation of the Aggregation Process during Ballistic to Diffusional Crossover in the Free-molecular regime"

[29] A. Einstein, *De "Investigations on the theory of the brownian movement."*, (Dover Publ., New York, 1956).

[30] N. A. Fuchs, *The Mechanics of Aerosols,* (Pergamon, Oxford, 1964).

[31] G. M. Wang and C. M. Sorensen, Phys. Rev. E., **60**, 3036 (1999).

[32] B. Dahneke, *Theory of Dispersed Multiphase Flow*, (Academic Press, New York, 1983).

[33] G. M. Hidy, *Aerosols: An Industrial and Environmental Science,* (Academic Press, Orlando, 1984).

[34] C. Oh , C. M. Sorensen, J. Aerosol Sci., **28**, 937 (1997).

[35] C. M. Sorensen and G. M. Wang, Aerosol Sci. Technol., **33**, 353 (2000).

[36] P. Meakin, J. of Sol-Gel Sci. & Tech., **15**, 97 (1999).

[37] P. Meakin, Phys. Rev. Lett., **51**, 1119 (1983).

[38] M. Kolb, R. Botet, and R. Jullien, Phys. Rev. Lett., **51**, 1123 (1983).

[39] F. Family, P. Meakin, and T. Vicsek, J. Chem. Phys., **83**, 4144 (1985).

[40] D. Fry, T. Sintes, A. Chakrabarti, and C. M. Sorensen, Phys. Rev. Lett., **89** (14), 148301 (2002).

[41] A. Hasmy, J. of Sol-Gel Sci. & Tech., **15** (2), 137 (1999).

[42] P. Meakin, J. Colloid Interface Sci., **102**, 505 (1984).

[43] G. W. Mulholland, R. J. Samson, R. D. Mountain, and M. H. Ernst, Energy Fuels, **2**, 481 (1988).

[44] F. London, Trans. Faraday SOC., **33**, 8 (1937).

[45] J. E. Lennard-Jones, Proceedings of the Physical Society, **43**, 461(1931).

[46] http://en.wikipedia.org/wiki/Lennard-Jones_potential

[47] W. L. Jorgensen, J. D. Madura, and C.J. Swenson, J. Am. Chem. Soc., **106**, 6638 (1984).

[48] H. Sellers, A. Ulman, Y. Shnidman, and J. E. Eilers, J. Am. Chem Soc., **115,** 9389 (1993).

[49] W. L. Jorgensen, J. Phys. Chem, **90,** 6379 (1986).

[50] T. K. Xia, J. Ouyan, and U. Landman, Phys. Rev. Lett., **69** (13), 1967 (1992).

[51] W. D. Luedtke, U. Landman, J. Phys. Chem., **100** (32), 13323 (1996).

[52] W. D. Luedtke, U. Landman, J. Phys. Chem. B., **102**, 6566 (1998).

[53] J. M. Victor, J. P. Hansen, Trans. Faraday Soc. II, **81,** 43 (1985).

[54] A. Chakrabarti, D. Fry, and C.M. Sorensen, Phys. Rev. E., **69**, 031408 (2004)

[55] A. T. Skjeltorp, Phys. Rev. Lett., **58**, 1444 (1987).

[56] M. Y. Lin, H. M. Lindsay, D. A. Weitz, R. C. Ball, R. Klein, and P. Meakin, Phys. Rev. A., **41** (4), 2005 (1990).

[57] D.A. Weitz, J.S. Huang, M.Y. Lin, and J. Sung, Phys. Rev. Lett., **54**, 1416 (1985).

[58] J.E. Martin, J.P. Wilcoxon, Phys. Rev. Lett., **61**, 373 (1988).

[59] J.E. Martin, J. Wilcoxon, and J. Odinek, Phys. Rev. A., **43**, 858 (1991).

[60] A. E. Gonzalez, F. Martinez-Lopez, A. Moncho-Jorda, and R. Hidalgo-Alvarez, Jour. Coll. Int. Sci., **246** (2), 227 (2002).

[61] A. E. Gonzalez, F. Martinez-Lopez, A. Moncho-Jorda, et al., Physica A- Stat. Mech., **333**, 257 (2004).

[62] P. Meakin, R. Jullien, Jour. Chem. Phys., **89** (1), 246 (1988).

[63] P. Meakin, Phys. Rev. A., **38** (9), 4799 (1988).

[64] FRY D THESIS KANSAS STATE : 2003

[65] M. P. Allen and D. J. Tildesley, *Computer simulation of liquids*, (Clarendon Press, Oxford, 1989).

[66] N. Metropolis, A. W. Rosenbluth, M. N. Rosenbluth, A. H. Teller, and E. Teller, Jour. Chem. Phys., **21** (6), 1087 (1953).

[67] A.Einstein, Ann. Phys., **17**, 549 (1905).

[68] W. F. Vangunsteren, H. J. C. Berendsen, Mol. Phys., **45** (3), 637 (1982).

[69] J. M. Sancho, M. S. Miguel, S. L. Katz, and J. D. Gunton, Phys. Rev. A. **26** (3), 1589 (1982).

[70] C. Scherer, Brazilian Jour. Phys. **34** (2A), 442 (2004).

[71] A. Sierou, J. F. Brady, Jour. Fluid Mech., **448**, 115 (2001).

[72] L. Verlet, Phys. Rev., **159**, 98 (1967).

[73] M. Smoluchowski, Z. Phys., **17**, 585 (1916).

[74] M. Deaconu, E. Tanre, Ann. Scuola Norm. Sup. Pisa, **29,** 549 (2000).

[75] J. Bertoin, The Annals of Applied Probability, **12**(2), 547 (2002).

[76] J. B. McCleod, Proc. London Math. Soc., **3** (14), 445 (1964).

[77] C. M. Sorensen, Aerosol Sci. Technol., **35**, 648 (2001).

[78] C. M. Sorensen, G. C. Roberts, J. Colloid Interface Sci. **186**, 447 (1997).

[79] B. Mandelbrot, *The Fractal Geometry of Nature*, (W H Freeman & Co, San Francisco, 1982).

[80] A. Guinier, G. Fournet, C. B. Walker, and K. L. Yudowitch, *Small Angle Scattering of X-Rays*, (Wiley, New York, 1955).

[81] G. Porod, Kolloid Z., **124**, 83 (1951).

[82] D. Stauffer and A. Aharony, *Introduction to Percolation Theory*, (Taylor & Francis, London, 1992).

[83] M. Zurito-Gotor, D. E. Rosner, J. Colloid Interface Sci. **255**, 10 (2002).

[84] P. G. J. van Dongen, M. H. Ernst, Phys. Rev. Lett., **54**,1396 (1985).

[85] R. Jullien, R. Thouy, and F. Ehrburger-Dolle, Phys. Rev. E., **50**, 3878 (1994).

[86] D. Fry, A. Chakrabarti, W. Kim, and C. M. Sorensen, Phys. Rev. E., **69**, 061401 (2004).

[87] C. M. Sorensen, W. B. Hageman, T. J. Rush, H. Huang, and C. Oh, Phys. Rev. Lett., **80**, 1782 (1998).

[88] C. M. Sorensen, W. Kim, D. Fry, and A. Chakrabarti, Langmuir, **19**, 7560 (2003).

[89] W. Kim, C. M. Sorensen, and A. Chakrabarti, Langmuir, **20**, 3969 (2004).

[90] W. G. Kim, C. M. Sorensen, D. Fry, and A. Chakrabarti, J. Aerosol Sci., **37**, 386 (2006).

[91] P. Meakin, T. Vicsek, and F. Family, Phys. Rev. B., **31**, 564 (1985).

[92] P. Meakin, B. Donn, and G. W. Mulholland, Langmuir, **5**, 510 (1989).

[93] G. M. Wang and C. M. Sorensen, Aerosol Sci. Technol., **34**, 297 (2001).

[94] D. W. Mackowski, J. Aerosol Sci., **37**, 242 (2006).

[95] A. E. Gonzales, Phys. Rev. Lett., **71** (14), 2248 (1993).

[96] R. Hunter, *Foundations of colloid science*, (Clarendon Press, Oxford, 1987).

[97] S. Asakura, F. Oosawa, J. Chem. Phys., **22**, 1255 (1954).

[98] A. Vrij, Pure Appl. Chem., **48**, 471 (1976).

[99] R. Verma, J. C. Crocker, T. Lubensky, and A. G. Yodh, Macromolecules, **33**, 177 (2000).

[100] E. K. Hobbie, Phys. Rev. Lett., **81**, 3996 (1998).

[101] V. J. Anderson, H. N. W. Lekkerkerker, Nature, **416**, 811 (2002).

[102] A. Hiddessen, S. Rodgers, D. Weitz, D. Hammer, Langmuir, **16**, 9744 (2000).

[103] G. Bushell, R. Amal, J. Colloid Interface Sci., **205**, 459 (1998).

[104] P. Meakin, S. Miyazima, J. Phys. Soc. Jpn., **57**, 4439 (1988).

[105] M. Kolb, Phys. Rev. Lett., **53**, 1653 (1984).

[106] T. A. Taton, C. A. Mirkin, and R. L. Letsinger, Science, **289**, 1757 (2000).

[107] C. A. Mirkin, R. L. Letsinger, R. C. Mucic, and J. J. Storhoff, Nature, **382**, 607 (1996).

[108] V. T. Milam, A. L. Hiddesen, J. C. Crocker, D. J. Graves, and D. A. Hammer, Langmuir **19**, 10317 (2003).

[109] S. Cobbe, S. Connolly, D. Ryan, L. Nagle, R. Eritja, D. J. Fitzmaurice, Phys. Chem. B, **107**, 470 (2003).

[110] E. T. Kisak, M. T. Kennedy, D. Trommeshauser, and J. A. Zasadzinski, Langmuir, **16**, 2825 (2000).

[111] N. C. Seeman, Nature, **421**, 427 (2003).

[112] F. Family, P. Meakin, and J. M. Deutch, Phys. Rev. Lett., **57**, 727 (1986).

[113] C. M. Sorensen, H. X. Zhang, T. W. Taylor, Phys. Rev. Lett., **59**, 363 (1987).

[114] I. Rouzina, V. A. Bloomfield, Biophys. J., **77**, 3242 (1999).

[115] R. P. Sear, Current Opinion in Coll. & Int. Sci, **11**, 35 (2006).

[116] F. Sciortino, S. Mossa, E. Zaccarelli, and P. Tartaglia, Phys. Rev. Lett., **93** (5) 055701 (2004).